



Faculté de Médecine



Inserm

La science pour la santé
From science to health



Université de Lille
Faculté de Médecine
Année 2024

THESE

Pour l'obtention du grade de
DOCTEUR DE L'UNIVERSITE DE LILLE

Spécialité : NEUROSCIENCES- MED

Présentée par
Chirine (EL) KATRIB

**Biopsie virtuelle de la maladie de Parkinson :
Vers une meilleure compréhension des marqueurs
neuroradiologiques grâce à l'étude de modèles
animaux.**

Soutenance le 02 Février 2024

Directeur de thèse : **Dr Nacim Betrouni**
Co-directrice de thèse : **Dr Charlotte Laloux**

JURY

Pr. David Devos -----	Président du Jury
PU-PH, Université de Lille	
Dr. Marianne Amalric -----	Rapporteuse
Directeur de recherche, Université de Marseille	
Dr. Patrice Péran -----	Rapporteur
Directeur de recherche, INSERM, Université de Toulouse	
Dr. Benjamin Dehay -----	Examineur
Directeur de recherche, INSERM, Université de Bordeaux	
Dr. Nacim Betrouni -----	Directeur de thèse
Chargé de recherche, INSERM, Université de Lille	
Dr. Charlotte Laloux -----	Co-directrice de thèse
Ingénieure de recherche, Université de Lille	



Faculté de Médecine



Inserm

La science pour la santé
From science to health



Lille University
Faculty of Medicine
Year 2024

THESIS

For the degree of
Philosophiae Doctor, PhD

Discipline: NEUROSCIENCE- MED

Presented by
Chirine (EL) KATRIB

**Virtual biopsy of Parkinson's disease:
towards a better understanding of neuroradiological
markers through animal model studies.**

Thesis defense held on February 2nd, 2024

PhD supervisors:
Dr Nacim Betrouni
Dr Charlotte Laloux

JURY

Pr. David Devos -----	Jury President
<i>Professor of Pharmacology, Lille University</i>	
Dr. Marianne Amalric -----	Thesis examiner
<i>Research director, Marseille University</i>	
Dr. Patrice Péran -----	Thesis examiner
<i>Research director, INSERM, Toulouse University</i>	
Dr. Benjamin Dehay -----	Thesis examiner
<i>Research director, INSERM, Bordeaux University</i>	
Dr. Nacim Betrouni -----	Thesis director
<i>Researcher, INSERM, Lille University</i>	
Dr. Charlotte Laloux -----	Thesis co-director
<i>Researcher, Lille University</i>	

ACKNOWLEDGMENTS/REMERCIEMENTS

À mon père[†]

***“As long as our brain is a mystery, the universe, the reflection of the structure of the brain
will also be a mystery.”***

— Santiago Ramón y Cajal

INDEX

PROLOGUE	7
LIST OF MAIN ABBREVIATIONS	8
LIST OF FIGURES	10
LIST OF TABLES	12
List of Annexes	12

PART ONE: INTRODUCTION & STATE OF THE ART

1 Chapter 1: Parkinson's disease	14
1.1 Pathophysiology and symptomatology of PD	16
1.1.1 Prodromal phase (pre-motor) (Stage 1 & 2)	17
1.1.2 Early phase (Stage 3).....	20
1.1.3 Advanced or mid-phase: diagnosis (Stage 4)	22
1.1.4 Late phase (Braak stage 5 & 6).....	23
1.1.5 Asymmetry in PD.....	26
1.2 Therapeutic approaches in PD	26
1.2.1 Symptomatic therapies	26
1.2.2 Preventive or curative therapies (DISEASE MODIFYING TREATMENTS).....	31
1.3 Diagnosis of PD	35
1.3.1 Diagnostic criteria: MDS scores for motor and non-motor symptoms.....	35
1.3.2 Diagnostic and prognostic Biomarkers of PD: current status	37
2 Chapter 2: Animal models of Parkinson's disease	41
2.1 Neurotoxic models.....	42
2.1.1 6-OHDA	42
2.1.2 MPTP	43
2.2 Transgenic models	45
2.3 Alpha-synuclein models: from physiology to pathology.....	46
2.3.1 Alpha-synuclein in physiological conditions: structure & role.....	46
2.3.2 Alpha-synuclein in pathological condition	49

2.3.3	Viral overexpression and spreading models of alpha-synuclein.....	50
3	Chapter 3: Magnetic resonance imaging & PD	53
3.1	Magnetic Resonance Imaging	54
3.1.1	Basics of MR Images.....	54
3.1.2	Types of MRI acquisitions	55
3.2	Post-processing and Analysis of MR imaging.....	60
3.2.1	Structural and quantitative MRI	60
3.2.2	Functional MRI	63
3.2.3	Radiomics and texture features.....	64
3.3	MRI in Parkinson’s disease: from clinical routine to research and preclinical exploration	66
3.3.1	Structural changes in MRI in PD.....	66
3.3.2	Quantitative MRI analysis in PD.....	66
3.3.3	Diffusion Tensor Imaging (DTI) in PD	67
3.3.4	Magnetic Resonance Spectroscopy (MRS) in PD	67
3.3.5	Texture features in PD	68
3.3.6	Functional connectivity in PD.....	68
3.3.7	New MRI sequences for PD.....	69
	RATIONAL	61

PART TWO: MATERIAL & METHODS

1	ANIMAL MODELLING AND EXPERIMENTAL DESIGN	76
1.1	Animal experimentation	76
1.1.1	Stereotactic surgery – model creation.....	77
1.1.2	Experimental design.....	79
2	BEHAVIOURAL EVALUATION	80
2.1	Stepping test - Sensori-motricity, forelimb akinesia.....	81
2.2	Actimetry - Spontaneous locomotricity	82
2.3	Openfield (OF) - Spontaneous locomotricity & anxiety.....	82
2.4	Elevated plus maze (EPM) - Anxiety.....	83
2.5	Y-maze Spontaneous alternation test - Working memory	84
2.6	Morris water maze (MWM) – Visuospatial learning & memory and mental flexibility.....	84
2.7	Touchscreen tests	86

2.7.1	Operant conditioning	86
2.7.2	Paired visual discrimination task.....	87
2.7.3	Paired visual discrimination task - Reversal learning – Cognitive flexibility	88
2.7.4	5 choice serial reaction time task - Attention	88
2.8	Sucrose consumption test.....	90
3	MAGNETIC RESONANCE IMAGING EXPLORATIONS.....	92
3.1	Structural T2-weighted (T2w) imaging	92
3.1.1	Acquisition.....	92
3.1.2	T2w image analysis	92
3.1.3	Voxel based morphometry (VBM)	93
3.1.4	ROI-based analysis	94
3.2	T2* weighted imaging.....	96
3.2.1	Image acquisition	96
3.2.2	T2* image analysis	96
3.3	Resting-state functional imaging (rs-fMRI).....	98
3.3.1	Image acquisition	98
3.3.2	Rs-fMRI analysis	98
4	HISTOPATHOLOGY	102
4.1	Brain tissue collection	102
4.2	Immunohistochemistry.....	102
4.2.1	Dopaminergic neurons.....	102
4.2.2	Alpha-synuclein deposits	103
4.2.3	Neuroinflammation markers	103
4.3	Iron histochemistry	103
4.4	Histological quantification	104
4.4.1	Stereology	104
4.4.2	Striatal TH quantification	104
4.4.3	Alpha-synuclein quantification	105
5	STATISTICAL ANALYSES	107
 PART THREE: RESULTS		
1	Chapter ONE:.....	110

Behavioural characterization of the AAV alpha-synuclein model: a focus on the cognitive and neuropsychiatric phenotype, and the underlying changes in brain tissue. 110

1.1	Background and aims.....	110
1.1.1	Specifics of the model.....	110
1.1.2	Beyond the motor symptomatology.....	111
1.1.3	Aims and study design	112
1.2	Motor phenotype.....	113
1.2.1	Spontaneous locomotor activity	113
1.2.2	Sensori-motor activity.....	113
1.3	Cognitive phenotype	114
1.3.1	Working memory	114
1.3.2	Visuo-spatial learning and memory	115
1.3.3	Visual discrimination.....	116
1.3.4	Attention	116
1.3.5	Mental Flexibility.....	117
1.4	Neuropsychiatric phenotype	118
1.4.1	Anxiety in EPM	118
1.4.2	Depressive-like behaviour.....	119
1.5	Histopathology.....	119
1.5.1	Dopaminergic Neurodegeneration: assessment of the lesion's extent.....	119
1.5.2	Alpha-synuclein propagation	120
1.5.3	Preliminary results: phospho-alpha-synuclein, aggregates and inflammation markers. .	122
1.6	Discussion.....	124
1.7	Conclusion.....	128

2 Chapter TWO:..... 129

Imaging characterization of the AAV alpha-synuclein model: structural and functional alterations linked to behavioural phenotype and histopathology. 129

2.1	Background and aims.....	129
2.1.1	Neuroimaging in preclinical PD	129
2.1.2	The AAV alpha-synuclein model's validated characteristics: what is left?	130
2.1.3	Aims and study design	131
2.2	Structural changes	131
2.2.1	Voxel based morphometry (VBM)	132

2.2.2	ROI-based volumetry	132
2.3	Iron accumulation	134
2.4	Functional connectivity	134
2.5	Discussion.....	136
2.5.1	Imaging and behavioural phenotype	136
2.5.2	Imaging and histopathology.....	137
2.5.3	Asymmetry.....	138
2.6	Conclusion.....	138
3	CHAPTER THREE:.....	146
	Beyond conventional imaging analyses: Exploration of texture features as finer imaging markers to spatially correlate with the histopathological signature.....	146
3.1	Background and aims.....	146
3.1.1	Radiomics in Neurodegenerative diseases	146
3.1.2	MRI Texture features in PD: from clinical findings to preclinical investigations	147
3.1.3	Aims: Top-down exploration in our model	148
3.2	Results and Correlations	150
3.2.1	Texture features and behavioural parameters	150
3.2.2	Texture features and neurodegeneration	151
3.2.3	Texture feature and alpha-synuclein deposits.....	151
3.3	Discussion.....	152
3.4	Conclusion.....	154
4	Chapter FOUR:.....	156
	Application of the 3-facet methodology in toxin-based models of PD. Preliminary results and proof of concept.....	156
4.1	Background and aims.....	156
4.1.1	Description of the selected toxin-based models	156
4.1.2	Study design & aims:.....	158
4.2	Behavioural evaluation	159
4.2.1	Motor and sensorimotor evaluations	159
4.2.2	Cognitive evaluation	161
4.2.3	Neuropsychiatric evaluation	163
4.3	Imaging evaluation.....	164
4.3.1	Structural MR imaging	164

4.3.2	R2* Iron accumulation	164
4.4	Histopathology	166
4.4.1	Dopaminergic degeneration	166
4.4.2	Iron accumulation and inflammation?.....	167
4.5	Discussion.....	167
4.5.1	MPTP model.....	167
4.5.2	6OHDA model	168
4.5.3	Toxin-based versus AAV alpha-synuclein animal model?.....	169
4.6	Conclusion.....	170

PART FOUR: DISCUSSION & CONCLUSION

GENERAL DISCUSSION	172
From Preclinical studies... ..	172
AAV alpha-synuclein model: 3-facet characterization and model limitations.....	172
Experimental design: methodological limitations and improvement strategies.....	174
MR Imaging versus Histology: Originalities and challenges.....	175
Translational validity of preclinical observations.....	177
... to Clinical repercussions.....	178
Diagnostic, prognostic and imaging biomarkers of PD	178
Alpha synuclein and PD.....	178
The promise of Multimodal imaging in PD.	179
CONCLUSION.....	182
REFERENCES	184
ANNEXE.....	212
ENGLISH ABSTRACT
ENGLISH ABSTRACT for non-scientists.....
RESUME FRANCAIS
Résumé grand public

PROLOGUE

Neurodegenerative diseases are caused by common cellular and molecular mechanisms including specific types of neuronal dysfunction and degeneration and protein aggregation (Jellinger et al. 2010). Therefore, only a post-mortem autopsy with the generation of a histopathological profile of the brain allows a definitive diagnosis of these diseases. Additionally, the presence of concomitant and mixed pathology and symptomatology complicates the diagnosis and discrimination between different subtypes of these diseases, whether it's Lewy body dementia, vascular dementia, frontotemporal dementia, Alzheimer's, Parkinson's, Multiple System Atrophy (MSA) or progressive supranuclear palsy (PSP) (Dugger et al. 2014). However, with the rapid development of various non-invasive brain imaging techniques, as well as state-of-the-art machine learning analyses on big data from large cohorts of patients, these pathological changes in the brain have the potential to be inferred even without autopsy, and a specific and differential diagnosis has become possible. But the question remains: Can we consider certain imaging as biomarkers for the diagnosis of these diseases?

A biomarker is a measurable indicator that reflects the biological state of a specific disease or physiological process. Biomarkers can be molecules, such as proteins, lipids, or nucleic acids, or they can be physiological measurements that indicate the presence, progression, or response to treatment of a disease. Biomarkers can be used in clinical practice for diagnosis, monitoring disease progression, assessing treatment efficacy, and predicting patient outcomes (Biomarkers Definitions Working Group, 2001).

The common emphasis is that a biomarker should provide objective evidence of the underlying biological process and should be reliable, valid, sensitive, specific, and easily measurable (Fuentes-Arderiu 2013). There has been some debate in the scientific community, regarding the use of imaging features as biomarkers. While imaging features can provide valuable information about the structural or functional changes associated with a disease, there is a concern that they may not directly reflect the underlying biological process, but rather are the indication of a downstream consequence of the disease. Therefore, some researchers have argued that imaging features should not be considered biomarkers. Ultimately, and as will be revealed during the course of this dissertation, certain imaging features can provide valuable information about the biological processes of a disease and should be considered as biomarkers.

In this context, the following manuscript as the aim of my thesis will be to decode the possible role of non-invasive imaging as biomarkers allowing a virtual biopsy of the brain in the context of neurological diseases, specifically Parkinson's disease, using animal models.

LIST OF MAIN ABBREVIATIONS

α-syn	Alpha-synuclein
AAV	Adeno-Associated Virus
ASYN	Alpha synuclein group
BBB	blood-brain barrier
BG	Basal Ganglia
BOLD	Blood Oxygen Level
CSF	cerebrospinal fluid
CTRL	control group
DaT	dopamine transporter
DTI	Diffusion tensor imaging
EPI	Echo-planar imaging
EPM	Elevated plus maze
FA	Fractional Anisotropy
FC	functional connectivity
GFAP	glial fibrillary acidic protein
GLCM	grey-level co-occurrence matrix
GM	Grey matter
h-α-syn	A53T-human-alpha-synuclein
i.p.	intraperitoneal
IBA1	ionized calcium-binding adapter molecule 1
LB	Lewy bodies
L-DOPA	Levodopa
MCI	mild cognitive impairment
MD	Mean Diffusivity
MFB	medial forebrain bundle
MPTP	1-methyl-4-phenyl-1,2,3,6-tetrahydropyridine
MRI	Magnetic Resonance Imaging

MRS Magnetic Resonance Spectroscopy

MSA multiple system atrophy

MWM Morris water maze

NAA N-acetyl aspartate

OF Openfield test

PD Parkinson's disease

PET positron emission tomography

PFF pre-formed alpha-synuclein fibrils

PSP progressive supranuclear palsy

PVD Paired visual discrimination task

QSM Quantitative Susceptibility Mapping

ROI Region of Interest

Rs-fMRI Resting-state Magnetic Resonance Imaging

SA Spontaneous alternation test

SN, *SNpc* Substantia Nigra *pars compacta*

SPECT single-photon emission computed tomography

ST Striatum

T1wi spin-lattice relaxation time T1-weighted image

T2wi spin-spin relaxation time T2-weighted image

TH Tyrosine hydroxylase

VBM Voxel based morphometry

VBR Voxel based relaxometry

WM White matter

5CSRT 5-choice serial reaction time task

6-OHDA 6-hydroxydopamine

LIST OF FIGURES

Figure 1. Parkinson's disease's first descriptions.

Figure 2. Pathological hallmarks of Parkinson's disease.

Figure 3. The different pathways affected in Parkinson's disease and leading to non-motor symptoms.

Figure 4. Simplified representation of the basal ganglia (BG)-thalamocortical circuit.

Figure 5. The evolution of anatomopathological characteristics and clinical symptoms associated with Parkinson's disease over time.

Figure 6. Illustration of alpha-synuclein structure.

Figure 7. Schematic depiction of alpha-synuclein aggregation pathway.

Figure 8. Overview of the different characteristics of the animal models of PD.

Figure 9. Overview of different brain MRI modalities, and data analysis techniques.

Figure 10. Overview of the methodological processes in Radiomics' analysis.

Figure 11. 3-facet methodology design and principal objective of this thesis project.

Figure 12. Coronal section of Rat brain atlas depicting the stereotactic coordinates of nigral injections

Figure 13. Experimental design.

Figure 14. Illustration of the different tests used to evaluate motor activity in an animal model.

Figure 15. The Elevated Plus Maze test for Anxiety evaluation.

Figure 16. The spontaneous alternation test for working memory evaluation.

Figure 17. The Morris Water Maze test for Visuospatial learning and memory.

Figure 18. The Touchscreen visual discrimination, cognitive flexibility and attentional tasks.

Figure 19. Rat brain MR images pre-processing pipeline.

Figure 20. Generation of an $R2^*$ map from a multi-echo $T2^*$ sequence.

Figure 21. Schematic illustration of the data analysis pipeline used for rs-fMRI.

Figure 22. Illustration of the striatal tyrosine hydroxylase quantification.

Figure 23. Adaptation of the QUINT workflow for histological analysis.

Figure 24. Spontaneous locomotor and sensorimotor activity evaluation in COGSYN 2021.

Figure 25. Visuo-spatial learning and memory evaluation in the Morris Water Maze test.

Figure 26. PVD and 5CSRT touchscreen tasks.

Figure 27. Analysis of the reversal paradigm accounting for mental flexibility.

Figure 28. Assessment of anxious-like behaviour in the Elevated Plus Maze test.

Figure 29. Evaluation of dopaminergic neurons in the dorsal striatum and Substantia nigra pars compacta of ASYN and CTRL rats.

Figure 30. The evaluation of human alpha-synuclein (h- α -syn) propagation in ASYN group.

Figure 31. Assessment of asymmetrical neurodegeneration and alpha-synuclein accumulation in ASYN animals.

Figure 32. Assessment of alpha-synuclein phosphorylation and markers of neuroinflammation in the AAV alpha-synuclein model.

Figure 33. Dopaminergic denervation and attentional deficits.

Figure 34. MRI structural changes and alpha-synuclein spreading in ASYN model.

Figure 35. Evaluation of Iron accumulation in ASYN model.

Figure 36. Functional connectivity between brain regions in ASYN animals compared to CTRL at 18-weeks p.i.

Figure 37. Major steps of radiomics pipeline.

Figure 38. Texture features comparison of the Substantia Nigra in ASYN versus CTRL animals.

Figure 39. Schematic view of the proposed texture working hypothesis in animal models of PD.

Figure 40. Toxin-based model experimental design.

Figure 41. Spontaneous locomotor evaluation of toxin-based models.

Figure 42. Sensorimotricity and Forelimb akinesia evaluation of toxin-based models.

Figure 43. Analysis of the alternation score in the Y-maze spontaneous alternation test in toxin-based models.

Figure 44. Visuospatial learning, memory and cognitive flexibility evaluation of toxin-based models in the MWM test.

Figure 45. Evaluation of anxiety in MPTP and 6OHDA rats.

Figure 46. Variation of R2* values (in toxin-based models).

Figure 47. Evaluation of dopaminergic neurons in the Substantia nigra pars compacta (A) and the dorsal striatum (B) of toxin-based models.

LIST OF TABLES

Table 1. MRI in clinical versus preclinical PD

Table 2. The evaluation of behavioural phenotype in 3 cohorts of the AAV α -synuclein model.

Table 3. Multimodal MRI evaluation in 3 cohorts of the AAV α -synuclein model.

Table 4. Volumetric measures of selected ROIs in ASYN versus CTRL groups overtime.

Table 5. Functionally grouped regions used for VBM, fMRI and h- α -syn histological analyses.

Table 6. List of Texture features computed, together with a description of their significance, equations and models.

LIST OF ANNEXES

Table 1: Therapeutic Options for Treating Non-Motor Symptoms of Parkinson's Disease.

Table 2. AAV-based alpha-synuclein overexpression rodent models.

Table 3. Alpha-synuclein deposit scores.

Annex 4. Overview of behavioural results of cohorts 2020, 2021, 2022

Annex 5. *Article 1 Submission* MRI Evaluation of AAV α -Synuclein Model of Parkinson's Disease is associated with α -Synuclein propagation

Annex 6. *Article 2 Submission* Textural features of magnetic resonance imaging correlate with tissue changes in a human alpha-synuclein overexpression model of Parkinson's disease

PART ONE

INTRODUCTION & STATE OF THE ART

1 CHAPTER 1: PARKINSON'S DISEASE

History & Epidemiology

Parkinson's disease (PD) and its symptoms were first described in detail in 1817 in James Parkinson's clinical essay "An essay on the shaking palsy" (Figure 1). Based on six cases, he described involuntary tremulous motions accompanied by reduced muscular power in his patients. He also noted a tendency to bend the trunk forward and to switch from a walking to a running pace. Although Parkinson's essay is now recognized as the true founding work describing the disease, it received little attention when it was first released. Indeed, it was not until sixty years later that Jean Martin Charcot, a French neurologist, further described the specific symptomatology of the pathology, distinguishing different types of PD, and recognized the importance of Parkinson's work, naming the condition "Parkinson's disease" (Walusinski, 2018). Parkinson's initial observations described only the motor aspect of the disease, even stating that the senses and intellect were not affected. The first description of non-motor symptoms, including cognitive disorders, only emerged in 1882, following the work of Benjamin Ball, who reported the case of a patient who developed hallucinations, and two other cases who developed irritability and depression (Fénelon et al. 2021).

Today, PD is the most common neurodegenerative disorder after Alzheimer's disease, with a prevalence of 1.7% in the population over 65 years old (Samii et al. 2004), which increases almost exponentially with age, reaching a peak after 80 years old (Pringsheim et al. 2014). It is currently believed to affect up to 10 million people worldwide. Moreover, given the ageing of the population, and due to the increase in life expectancy, the number of people with PD is expected to increase by more than 50% by 2030 (Kalia, L.V., and Lang, 2015).

Characterised by a triad of motor symptoms consisting of bradykinesia, resting tremors, and rigidity, PD is also accompanied by other symptoms, including neuropsychiatric disorders. These

non-motor symptoms may appear before the motor symptoms, which only manifest after 50-60% of dopaminergic denervation within the Substantia Nigra pars compacta (SNpc) (Bernheimer et al. 1973; Greffard et al. 2006). This progression of symptom appearance reflects a slow neurodegenerative process that manifests in the evolution of PD over several different characteristic phases.

In this chapter, I will first detail the neurophysiological impairments and associated symptoms that characterise the different phases of PD. I will then focus on the existing and eventual therapeutic strategies to manage PD. Finally, I will detail the process of diagnosing PD, allowing for the implementation of these strategies.

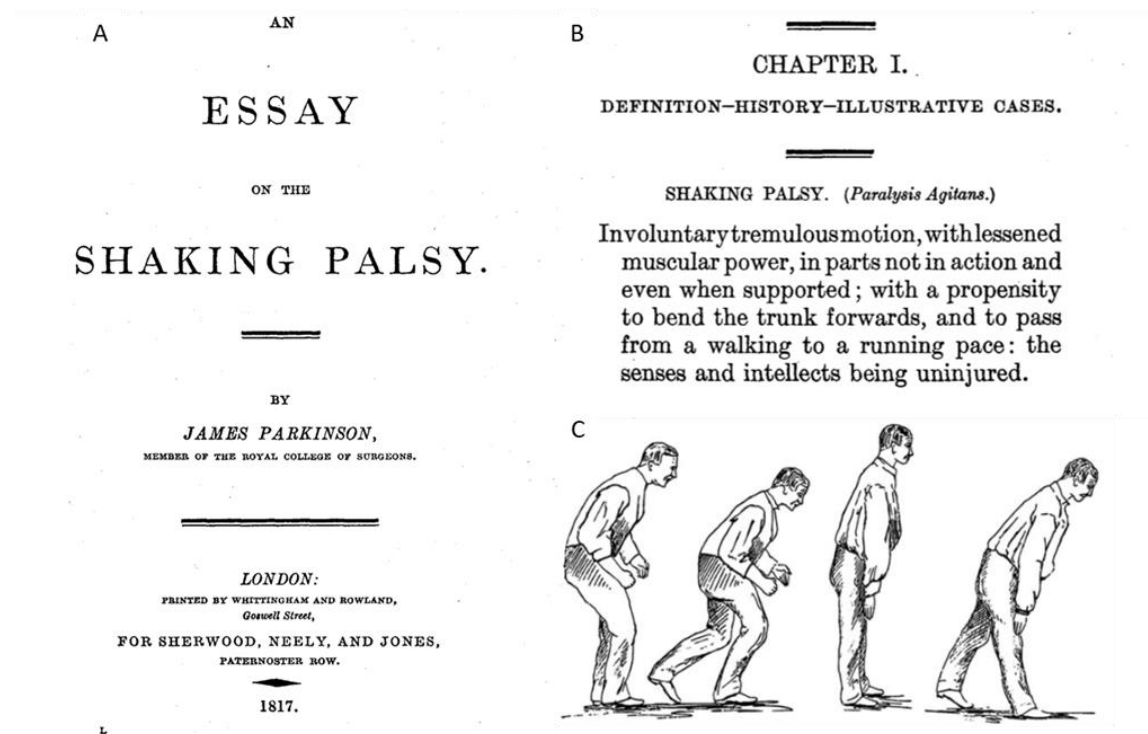


Figure 1. Parkinson's disease's first descriptions. A. Preface of "An Essay on the Shaking Palsy" by Dr. James Parkinson (1817). B. Extract from the first page of "An essay on the Shaking Palsy" describing the characteristic motor tremors of PD. C. Jean-Martin Charcot's drawing (1888) illustrating a "typical" Parkinson's disease with a flexed posture (left) and a Parkinsonian variant that included the absence of tremor and an extended posture (right). Adapted from Goetz, 2011

1.1 PATHOPHYSIOLOGY AND SYMPTOMATOLOGY OF PD

Although PD is mostly diagnosed in elderly people, as previously mentioned, it is a slow-progressing neurodegenerative disorder that starts several years before a probable diagnosis can be made. In addition, confirmation of the diagnosis can only be made post-mortem and relies on the presence of two markers: degeneration of dopaminergic neurons in the SNpc and the presence of intraneuronal inclusions of alpha-synuclein (α -syn) aggregates, known as Lewy bodies (LB) in different brain areas (Figure 2). Thus, Braak and colleagues proposed a classification

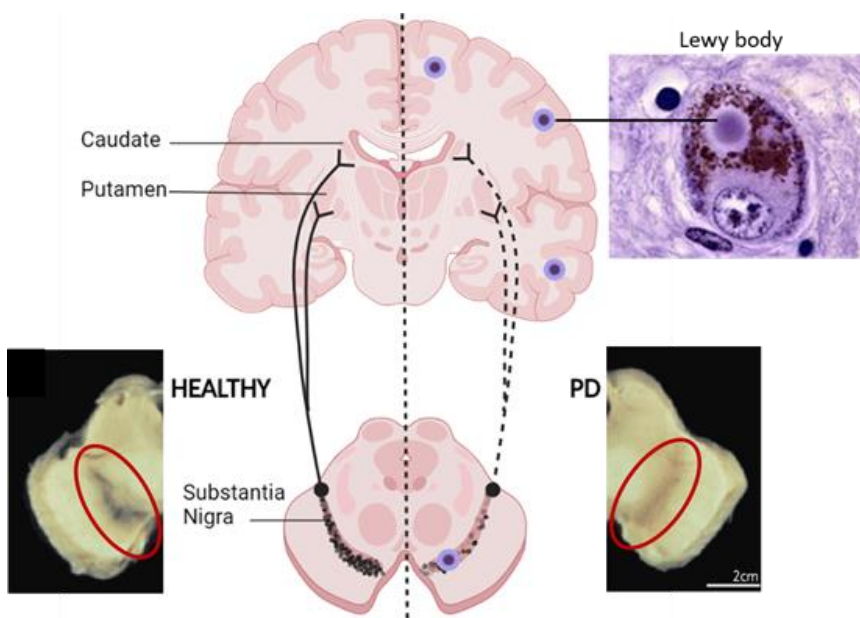


Figure 2. Pathological hallmarks of Parkinson's disease. Reduction of neuromelanin pigment in the substantia nigra pars compacta (SNpc) in a patient with PD (on the right) compared to a normal individual (on the left). Immunohistochemical labeling of Lewy bodies in a dopaminergic neuron of the SNpc. Fibrils made of insoluble polymers of α -synuclein are deposited in the neuronal body, forming round lamellated eosinophilic cytoplasmic inclusions (Fig. generated by Biorender; photos from Double et al. 2011; Mandel et al. 2010)

of the evolution of PD based on the rostro-caudal extension of Lewy body appearance, allowing for different stages of the disease to be distinguished, known as the Braak theory (Braak et al. 2003). This classification, widely supported by histological observations, constitutes the current consensus. It divides PD into six anatomopathological stages corresponding to four clinical phases: the prodromal phase, the early phase, the advanced or mid-phase, and the late phase (summarised in Figure 5).

1.1.1 Prodromal phase (pre-motor) (Stage 1 & 2)

The onset of the disease or stage 1 is characterised by the accumulation of alpha-synuclein in the neurons of the olfactory bulb and the dorsal motor nucleus of the vagus and glossopharyngeal nerves (Figure 3). Indeed, according to Braak, the olfactory system being in constant contact with the outside, could represent an entry point for toxic environmental factors such as pesticides whose impact on the development of PD is now recognized (Hawkes et al. 2007).

The vagus and glossopharyngeal nerves are mixed nerves that belong to the autonomic nervous system and autonomously regulate the functioning of most of our vital functions such as blood pressure, heart rate, respiration, and swallowing. In addition, the vagus nerve is also linked to the enteric system and provides almost all of the extrinsic innervation of the digestive tract. Thus, preclinical models of PD in mice, using overexpression of alpha-synuclein in the brain, show an accumulation of alpha-synuclein aggregates in the gastrointestinal tract (Wang et al. 2012). Moreover, it has been shown that injection of misfolded alpha-synuclein within the mouse gut leads to protein migration to the brain and the development of characteristic PD symptoms, thus supporting the hypothesis of Braak and colleagues that PD could start peripherally (S. Kim et al. 2019).

The involvement of the olfactory bulb leads to very early hyposmia in 70 to 90% of Parkinson's patients (Herting et al., 2008). Moreover, the involvement of mixed nerves can cause various non-specific symptoms ranging from constipation, given the link between the vagus nerve and the intestine, to hypotension, swallowing problems, or heart rhythm disorders (Dickson et al. 2009; Pfeiffer, 2011).

Stage 2 of the prodromal phase is characterised by the progression of Lewy body accumulation to the lower structures of the brainstem and the more significant involvement of the vagus nerve (Figure 3). Indeed, the lower parts of the pedunculopontine nucleus, the locus coeruleus, and the

raphe nucleus are affected, thus respectively impacting the cholinergic, noradrenergic, and serotonergic systems (Figure 3).

Histological studies conducted in Parkinson's patients have shown that the locus coeruleus may be the most affected structure in PD, with neuronal losses of up to 83% (Zarow et al., 2003). Damage to the pedunculopontine nucleus leads to rapid eye movement (REM) sleep behaviour disorder (RBD), which, with a prevalence of up to 70% in Parkinson's patients, is one of the most predictive early symptoms of PD (Adler et al., 2011; J. Zhang et al., 2017). Thus, cohorts of individuals with isolated RBD represent a major interest in studying early phases of PD. In addition, damage to the noradrenergic and serotonergic systems will lead to the appearance of neuropsychiatric symptoms (Figure 3B,C). Among them, depression seems to be the most common, with a prevalence ranging from 50 to 90% of Parkinson's patients depending on the studies considered (Aarsland et al. 2012; Poewe & Seppi, 2001; Reijnders et al. 2008). In PD, depression is characterised by sadness, pessimism, desperation, and may be accompanied by anxiety. However, unlike classical depression, guilt is rarely present (K. R. Chaudhuri et al. 2006; Ehrt et al. 2006). Thus, it has a major impact on the functional capabilities and quality of life of the patients. Despite this, depression is often not taken into account in Parkinson's patients and therefore undertreated (K. R. Chaudhuri & Schapira, 2009; Leentjens, 2004). Moreover, at a late stage, this lack of consideration is further exacerbated as the patient communicates little and/or may be affected by cognitive impairments.

Although anxiety can be considered one of the symptoms of Parkinsonian depression, it can also exist independently (Menza et al. 1993; Thobois et al. 2010). It can manifest itself in different ways, ranging from generalised anxiety disorders to forms of panic attacks or phobic symptoms. Like depression, anxiety disorders appear to be under-evaluated and undertreated in patients with PD, mainly due to imprecise diagnosis and overlap of symptoms with motor and cognitive characteristics (Gallagher et al., 2014; Weisskopf et al. 2003). However, anxiety is frequently

present in patients with a prevalence of approximately 40%, compared to 5-15% in the general population (Pontone et al., 2009, 2011, 2019).

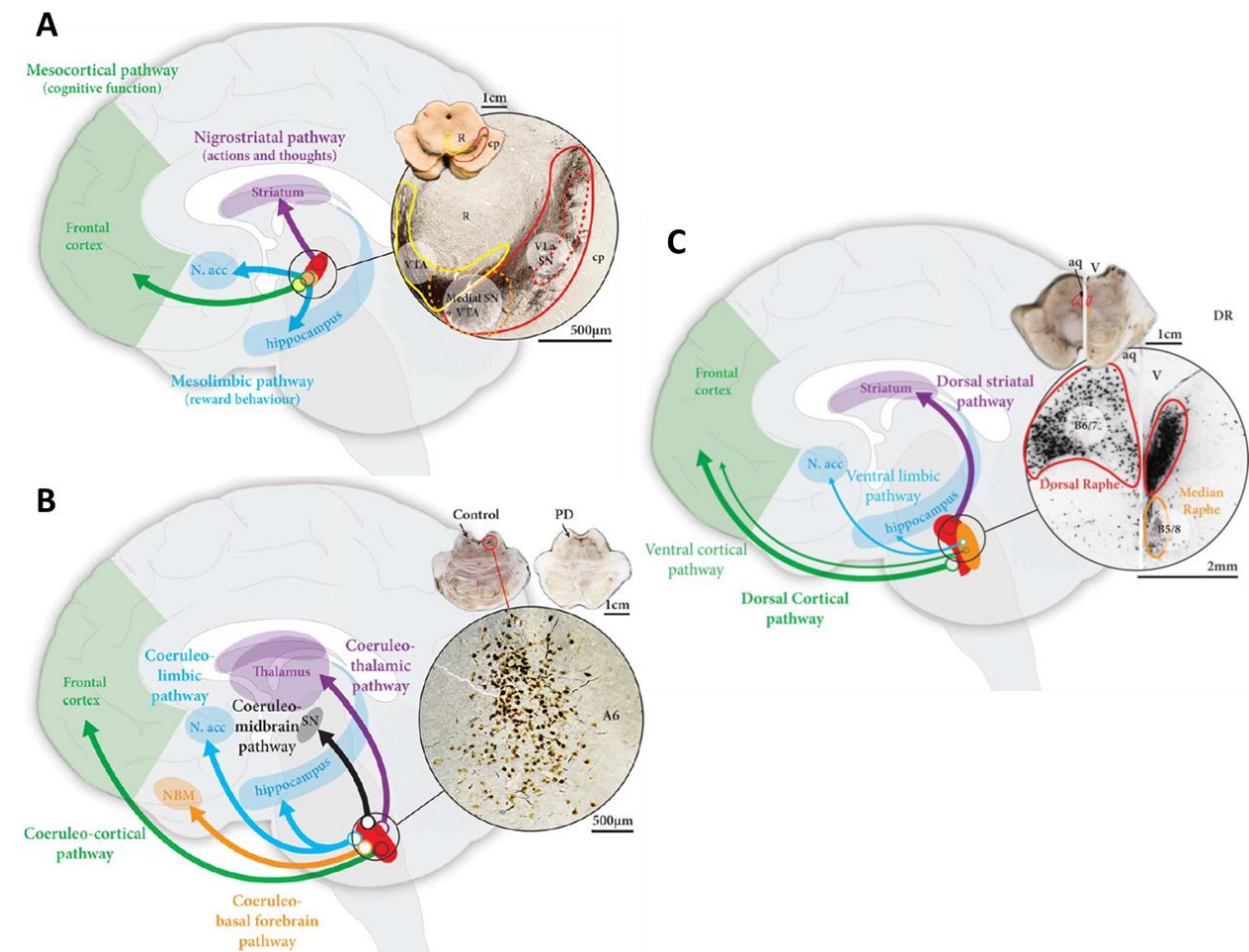


Figure 3. The different pathways affected in Parkinson's disease and leading to non-motor symptoms. A. Dopaminergic pathways. SNpc (in red) projects to the striatum; medial SN and VTA (in yellow) project to the limbic and cortical regions. B. Noradrenergic pathways. A6 noradrenaline neurons in the locus coeruleus (in red), innervate the SN, thalamus, and the cholinergic nucleus basalis of Meynert (NBM). C. Serotonergic pathways. Dorsal raphe projects to the striatum and cortex, whereas the median raphe projects to the limbic regions and cortex. N. acc: nucleus accumbens. (Adapted from Halliday et al. 2014)

1.1.2 Early phase (Stage 3)

Stage 3 is characterised by a greater accumulation of alpha-synuclein in the previously mentioned nuclei, but also by the involvement of non-thalamic grey nuclei such as the Meynert nucleus and the amygdala (Figure 3). The Meynert nucleus represents the major cholinergic innervation of the cortex and the amygdala, and would play a role in cortical arousal and cognitive functions (D. J. Lee et al. 2020). Within the amygdala complex, the central and basolateral nuclei are the main nuclei affected.

Finally, it is during this phase that the first characteristic damage to the dopaminergic system of PD appears, initially affecting the caudal and ventrolateral parts of the SNpc (Figure 3A). This neuronal death results in an imbalance within the basal ganglia (BG). The BG are a set of subcortical structures composed of four main nuclei: the striatum (or putamen), the pallidum subdivided into internal (GPi) and external (GPe) segments, the SNpc and the subthalamic nucleus (STN) (Figure 4). The striatum is considered the main input structure of the circuit since it receives strong dopaminergic innervation from the mesencephalon, many excitatory glutamatergic afferents from the cerebral cortex as well as from the thalamus (Bolam et al. 2000).

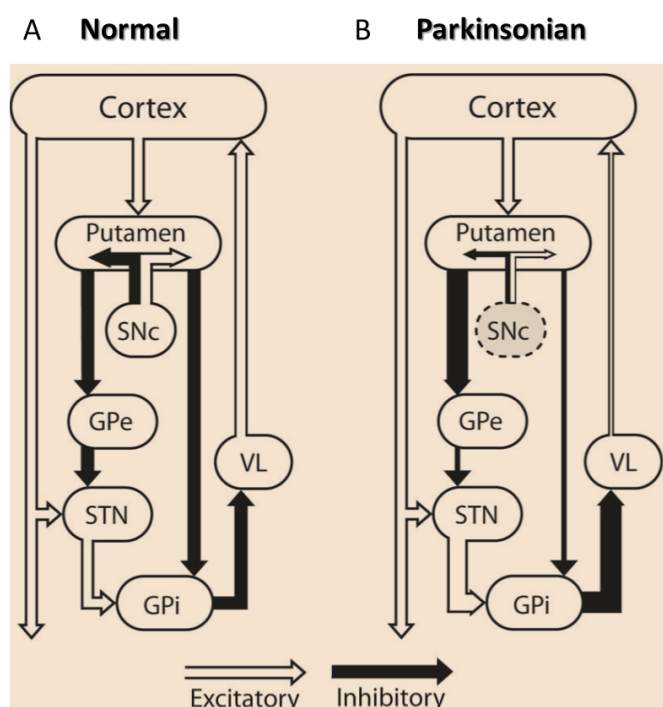


Figure 4. Simplified representation of the basal ganglia (BG)-thalamocortical circuit. A. Under physiological conditions. B. in PD context. SNc, substantia nigra, pars compacta; VL, ventrolateral nucleus of the thalamus; GPe, globus pallidus internus; GPi, globus pallidus externus; STN, sub-thalamic nucleus. (Adapted from Vitek et al. 2019).

The notion of direct and indirect pathways is based on the subdivision of neurons according to their projections and molecular signatures; dopamine having an opposite function in these 2 pathways (J. Park et al. 2020).

The direct pathway is formed by neurons that project to the GPi. Activation of dopamine receptor 1 (D1) by dopamine will promote inhibition of the GPi (Figure 4). The tonic inhibition exerted by these two output structures on the pre-motor thalamic networks will therefore be lifted, contributing to movement initiation by activating the motor cortex (Bolam & Smith, 1990). The indirect pathway is formed by neurons that project to the GPe, whose neurons in turn project to the STN. Neurons in the indirect pathway express dopamine receptor 2 (D2). Dopamine will lead to inhibition of the D2 receptors of neurons expressing it, allowing the inhibition of the GPe to be lifted, reinforcing its inhibitory effect on the STN, thus decreasing the glutamatergic excitation of the STN on the output structures. While the indirect pathway has an inhibitory influence on movement, dopamine induces a release of thalamic and cortical inhibition and thus also promotes movement elaboration (Parent & Cicchetti, 1998). However, in order to limit the effects of BG imbalance, compensatory mechanisms are put in place and the characteristic motor symptoms of PD appear only after 70 to 80% denervation at the level of the striatum.

Alternatively, although these lesions are compensated in the early phase, they can lead to other types of symptoms, particularly psychiatric ones such as apathy. Described for the first time in the context of PD by E. Brissaud who reported states of indifference and lack of reaction in Parkinson's patients (Prange et al. 2018), apathy has long been considered a simple symptom of depression. It wasn't until the 1990s that it was recognized as a full-fledged syndrome (Marin et al. 1991). Characterised by a loss of motivation expressed at the behavioural, cognitive, and emotional levels, apathy is manifested by:

- A decrease in goal-directed behaviours (reduced productivity, effort, initiative, perseverance, socialisation, leisure activities, and projects).
- A decrease in the emotion accompanying goal-directed behaviour (emotional blunting, absence of emotional response).

Although it can be associated with depression (Kirsch-Darrow et al. 2006), apathy in Parkinson's disease is mainly expressed alone and with a prevalence of up to 70% according to several studies (Starkstein & Brockman, 2011; Kirsch-Darrow et al. 2006). It differs notably from depression by the absence of negative or suicidal thinking and emotional distress (Marin 1990). Thus, apathy significantly reduces the quality of life of patients and severely impacts the lives of their loved ones (Benito-León et al. 2012).

1.1.3 Advanced or mid-phase: diagnosis (Stage 4)

During stage 4, the synucleinopathy process intensifies within the nuclei already affected in stage 3. In addition, the anterior and posterior intralaminar thalamic nuclei, which project to the striatum and cortex, begin to be affected. This stage also includes damage to the anteromedial temporal cortex, an area involved in transferring data from sensory associative areas to the prefrontal cortex via inputs from the limbic system. On the other hand, depletion of dopaminergic neurons progresses and now reaches the rostral, dorsal, and median regions of the SNc, leading to more significant striatal denervation. It is at this time, between the third and fourth stages, that the first motor symptoms of PD appear, allowing for diagnosis (Figure 5).

Known as the "motor triad," akinesia, resting tremors, and rigidity are the three main motor symptoms of PD (Samii et al. 2004).

Akinesia is defined as slowness and lack of spontaneous movements. Patients have difficulty with fine motor tasks such as buttoning a shirt and have a change in speech with a quiet and monotonous voice (hypophonia), increased saliva due to infrequent swallowing, or loss of facial expression (hypomimia) (Williams & Litvan 2013). Akinesia is the most disabling motor symptom in PD and can be observed quickly by the clinician because it is asymmetric (Miller-Patterson et al. 2018). Generally, it leads to reduced arm swing in the patient (Sterling et al. 2015).

Resting tremors are characterised by involuntary, rhythmic and alternating movements of one or more body parts movements. Their frequency can vary from low (4–5 Hz) to high (8–10 Hz). They are apparent in the most distal part of a limb, usually in the hand if the upper limb is involved, but they can also be observed in the feet, chin, or jaw. They occur during periods of rest or inactivity and disappear during voluntary action (Helmich et al. 2012).

Rigidity results from excessive muscle tension that prevents them from relaxing during movement. This hypertonicity affects the fluidity of movements, which become jerky, leading to the phenomenon of "cogwheel rigidity." Initially affecting the upper limbs, it then becomes generalised, leading to the appearance of postural problems, with the patient becoming stiff, hunched forward, and head down (Xia & Mao 2012).

Although tremors are often identified as a key feature of PD by clinicians and the public, their presence is not necessary for a diagnosis of PD, which is based more on akinesia and rigidity. In fact, nearly 10% of Parkinson's patients will never present tremors (Jankovic, 2008).

1.1.4 Late phase (Braak stage 5 & 6)

The following late phase is characterised by the spread of alpha-synuclein aggregates to almost the entire brain. Stage 5 is therefore defined as the beginning of the involvement of the neocortex and prefrontal cortex (Pavese et al. 2011). At this stage, the loss of dopaminergic neurons is such that the substantia nigra appears macroscopically pale (Braak et al. 2003; Braak & del Tredici, 2008). Finally, phase 6 involves the entire neocortex and primary somatosensory and motor areas.

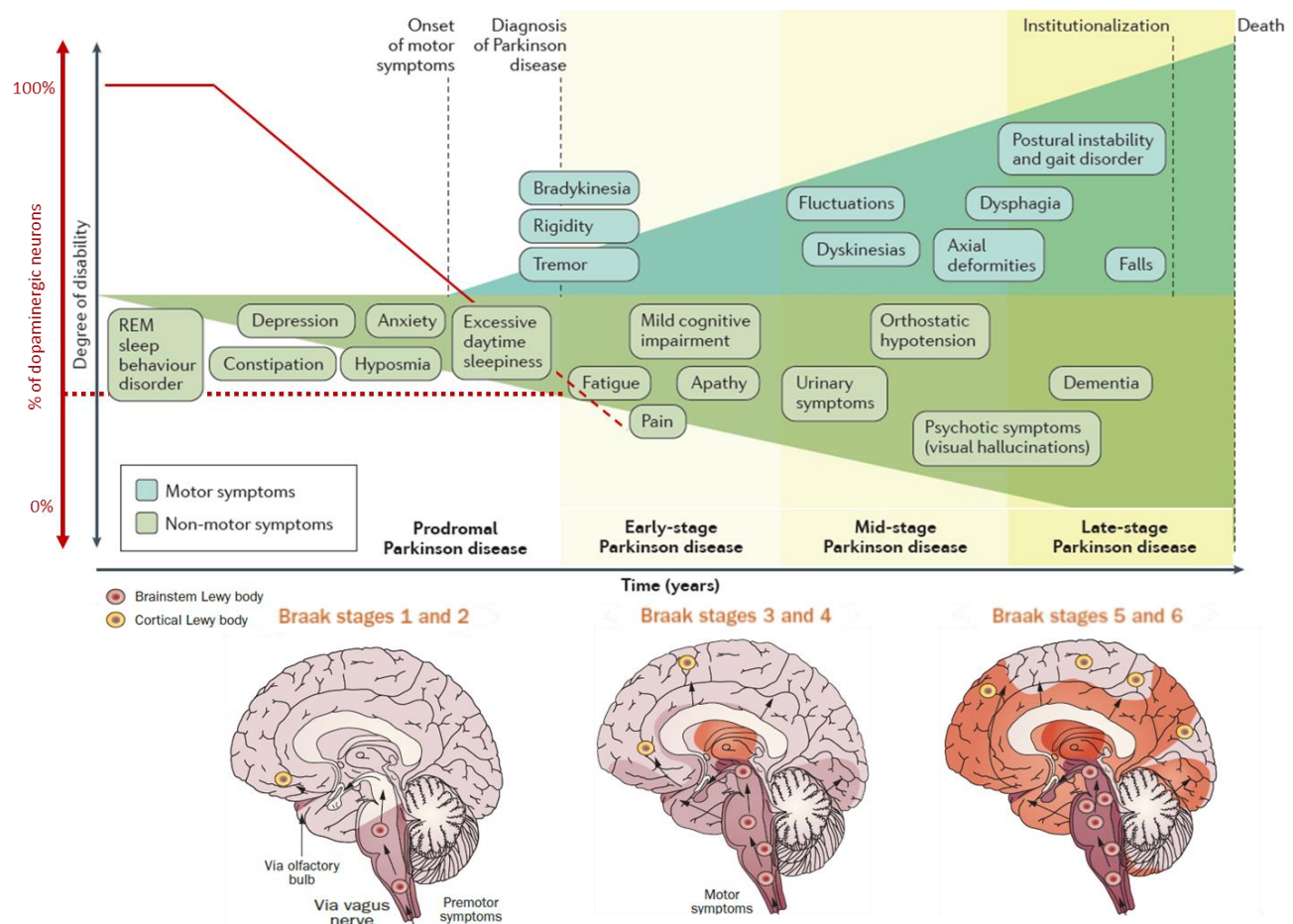


Figure 5. The evolution of anatomopathological characteristics and clinical symptoms associated with Parkinson's disease over time. Diagnosis of PD occurs with the onset of motor symptoms, but is preceded by several years of dopaminergic degeneration, alpha-synuclein and Lewy body accumulation, as well as non-motor symptoms. (Adapted from Poewe et al. 2017 & Doty et al. 2012)

This widespread involvement of the cortex is clinically manifested by the onset of dementia. With a prevalence ranging from 24 to 31% in Parkinson's patients (Aarsland et al. 2008), dementia appears 10 to 15 years after diagnosis. Amongst the many aspects of dementia, the most frequently encountered are cognitive deficits, memory impairment, difficulties in paying attention and processing information, visuospatial and executive dysfunctions (Goetz et al. 2009). In addition, 20% to 30% of patients may also experience hallucinations, most often visual (Diederich et al. 2009).

The Braak staging system, which closely corresponds to the original classification of Lewy body disorders proposed by Kosaka and colleagues (Kosaka et al. 1975), is now widely validated and accepted (Braak et al. 2005; Dickson et al. 2010; Dijkstra et al. 2014; Kingsbury et al. 2010).

However, this system is only adapted to patients whose disease is characterised by a slow progression, a long duration, and mainly motor symptoms, with dementia appearing only at a very advanced stage. Indeed, about 15% of Parkinson's patients do not fit into this classification. In particular, some patients do not have any involvement of the dorsal nucleus of the vagus nerve, the starting point of the Braak hypothesis (Attems & Jellinger, 2008; Kalaitzakis et al. 2008), nor do they show signs of rostro-caudal progression of the pathology (Kalaitzakis et al. 2008; Zaccai et al. 2008).

Furthermore, some patients with significant alpha-synuclein aggregation in the brain express few or no classic PD symptoms (Parkkinen et al. 2008). This confirms the wide heterogeneity of Parkinson's disease on both physiopathological and symptomatic levels. However, despite several presented hypotheses, there is still no consensus on the different subgroups of PD.

The reasons why some patients do not follow the Braak progression pattern are not known and remain to be elucidated. In addition, this classification is based solely on the propagation of alpha-synuclein aggregation, whereas this propagation appears weakly correlated with neuronal death, one of the major characteristics of PD (Blesa et al. 2018; Surmeier et al. 2017).

Therefore, many critical evaluations of the Braak hypothesis have since been formed. In 2008, Burke and colleagues highlighted the fact that there is still no confirmed correlation between Braak stages and the clinical severity of PD (Burke et al. 2008).

If robust correlations between the clinical progression of PD and other morphological changes, not available in the current Braak staging system, are discovered by future studies, then the staging systems we now use must be revised accordingly (Jellinger, 2010).

1.1.5 Asymmetry in PD

It is widely acknowledged that clinically, PD patients present with asymmetric motor symptoms. This asymmetry occurs from disease onset, in both sporadic and hereditary forms of the disease (Djaldetti et al. 2006). Studies have been able to associate it with more severe contralateral nigrostriatal degeneration, observed both in histopathology (Kempster et al. 1989; only one study) and in imaging (J. Wang et al. 2015). Another study showed that cortical degeneration in PD also differs between cerebral hemispheres (Claassen et al. 2016). Researchers have hypothesised that this hemispheric lateralization could be due to handedness, and one study was even able to associate the dominant hand-side with more severe symptoms (Van der Hoorn et al. 2011). However, the causal effects of handedness are still very much under debate.

Ultimately, asymmetries of the nigrostriatal dopamine system, which are exacerbated in disease context, could simply be related to general asymmetries in motor preference in humans (de la Fuente-Fernández et al. 2000), or a combination of several factors (genetic, environmental, accumulation of different pathological mechanisms...), which are too numerous to fully characterise, as Djaldetti and colleagues suggested.

1.2 THERAPEUTIC APPROACHES IN PD

Unfortunately, the treatments currently available for Parkinson's disease only treat symptoms, and cannot slow down, reduce, or stop the progression of the disease. However, several approaches being currently developed offer hope for a cure for Parkinson's disease.

1.2.1 Symptomatic therapies

1.2.1.1 *Pharmacological strategies*

Given the central role of the degeneration of dopaminergic neurons in the development of motor symptoms of Parkinson's disease, the first strategies used have involved supplementing the missing dopamine in the brain.

➤ **L-DOPA**

Unlike dopamine, its precursor, Levodopa (L-DOPA) is able to cross the blood-brain barrier (BBB) and is now the reference molecule for the treatment of Parkinson's disease. Its use as a first-line treatment allows for effective improvement of motor symptoms, particularly akinesia and rigidity (Morgan & Fox, 2016). However, taking L-DOPA does not slow down or stop the degenerative process. After several years of treatment, its effectiveness diminishes, leading to therapeutic escape (treatment failure). This is characterised by "on-off" type motor fluctuations, accompanied by involuntary abnormal movements called dyskinesias (Vijayakumar & Jankovic, 2016).

Although the origin of these L-DOPA-induced dyskinesias is not yet fully understood, they are primarily due to two phenomena: repeated L-DOPA doses resulting in pulsatile stimulation of dopaminergic receptors leading to their hypersensitization and the inability of the nigrostriatal pathway to store and convert L-Dopa into dopamine as the neurodegenerative process progresses (Carta et al. 2007; Iravani et al. 2012).

Interestingly, fragmented dosing or the use of a pump allowing for prolonged and continuous release of L-DOPA and stabilisation of its concentration has shown effectiveness in reducing these fluctuations (Antonini et al. 2010). Furthermore, delaying the introduction of L-DOPA treatment via the use of other molecules such as dopaminergic agonists, could limit these side effects and allow for the longest possible period of effectiveness (Chung et al. 2018).

➤ **Dopamine agonists**

There are two families of dopamine agonists based on their origin. The first family, known as old-generation agonists derived from ergot, such as bromocriptine, have affinity for both dopamine D2 receptors and serotonin receptors, which gives them good efficacy but also leads to the occurrence of side effects (Borovac, 2016). In order to address this lack of specificity, non-ergot-derived agonists, such as Pramipexole, which bind more specifically to dopamine receptors (D2/D3), have been developed (Holloway et al. 2000; Reichmann et al. 2006).

One of the most used dopamine agonists is apomorphine, which is very potent, activates all dopamine receptors, and significantly reduces the patient's tremor and dyskinesia (Carbone et al. 2019). It remains the only drug with efficacy comparable to that of L-DOPA. The development of an apomorphine infusion pump therapy has significantly ameliorated patients' quality of life (Drapier et al. 2016).

Furthermore, dopamine agonists have a longer half-life than L-DOPA, which leads to more stable dopaminergic stimulation and thus avoids the appearance of motor fluctuations and dyskinesias (Rascol et al. 2000; Stocchi, 2009). Unlike L-DOPA, they do not need to be converted into dopamine and are therefore not dependent on the number of remaining dopaminergic neurons (Samii et al. 2004). Thus, they are often prescribed as a first-line treatment, particularly in young patients, in order to delay the use of L-DOPA (Goldenberg, 2008). They can also be prescribed in addition to L-DOPA to reduce its doses and, and therefore limit its side effects.

However, in the long run, dopamine agonists can lead to the development of a heterogeneous group of side effects called impulse control disorders. In fact, dopamine agonists act as psychostimulants in PD patients and therefore lead to the appearance of stereotypies, abuse of dopaminergic treatment, as well as various impulsive/compulsive disorders (compulsive shopping, pathological gambling, hypersexuality...) (Atmaca, 2014; K.R. Chaudhuri & Schapira, 2009).

➤ Dopamine

The use of Dopamine as treatment has long been avoided, since as mentioned before, it does not cross the BBB, in addition to being a highly oxidizable molecule. However, recently, our lab has developed a new method of continuous intracerebroventricular (i.c.v.) administration of anaerobic dopamine to the brain, thereby overcoming the risk of oxidation. It first showed success in a preclinical study by restoring motor function and inducing an increase of dopaminergic neurons in MPTP mice (Laloux et al. 2017). An additional study in a non-human primate model of PD also proved successful and confirmed safety and efficacy of this type of administration as well as the absence of dyskinesia or behavioural sensitization (Moreau et al. 2020). Currently, an ongoing clinical trial (DIVE – NCT04332276), performed at the University/hospital of Lille, is yielding very promising results in PD patients, with i.c.v. Dopamine administration via a catheter connected to a pump implanted in the abdomen.

This new therapy could help overcome the pharmacological drawbacks of L-DOPA which is known to trigger motor fluctuations, dyskinesia, and other non-motor complications (Devos et al. 2017).

➤ Non-dopaminergic agents

Since PD does not only affect the dopaminergic system, pharmacological agents targeting the glutamatergic, GABAergic, serotonergic, noradrenergic, and cholinergic systems may be recommended in addition to dopaminergic therapy. This approach may be useful in treating postural instability or tremors, which are generally poorly improved by dopaminergic therapy (Fox, 2013).

It is also important in the treatment of non-motor symptoms such as selective serotonin reuptake inhibitors (SSRI), serotonin and norepinephrine reuptake inhibitors (SNRI), benzodiazepine and other anti-depressants (Annexe Table 1).

Ultimately, considering the heterogeneity of the disease mentioned earlier, therapy of Parkinson's disease must be individualised and tailored to the needs of every particular patient (Jancovik & Poewe 2012).

1.2.1.2 Surgical approaches

The therapeutic escape associated with pharmacological approaches has been a real challenge for clinicians, leading them to seek new therapeutic tools.

As mentioned before, the degeneration of dopaminergic neurons in PD leads to the appearance of motor symptoms through significant dysfunctions within the basal ganglia (Turner & Desmurget 2010). Thus, the degeneration of dopaminergic neurons in the SNpc generates, at the level of the indirect pathway, a strong inhibition of the globus pallidus externus, resulting in hyperactivity of the subthalamic nucleus and a decrease in movements (Parent & Hazrati 1995). It has therefore been suggested that the inhibition of the relay nucleus, the STN, could be effective in limiting the effects of degeneration and managing associated motor symptoms. Consequently, unilateral lesion approaches were first developed in primates showing good results on motor symptoms but causing abnormal movements of the contralateral limbs to the lesion (Bergman et al. 1990).

A reversible surgical approach, consisting of electrically stimulating the STN, was then proposed. The first studies showing that high-frequency stimulation (HFS) of the STN induced a spectacular functional improvement in motor symptoms, similar to that observed after administration of L-DOPA, but without inducing motor fluctuations and/or dyskinesias, were conducted in parkinsonian monkeys (Benazzouz et al. 1996). Subsequently, the transfer of this technique to patients revealed similar effects, thus restoring their autonomy (Krack et al. 2003; Limousin et al. 1995, 1998). Although it represents the reference tool for overcoming therapeutic escape associated with dopa-therapy, deep brain stimulation (DBS) remains reserved for patients under 70 years of age, still dopa-sensitive, and presenting motor fluctuations. Therefore, the eligibility criteria concerns less than 5% of PD patients (Artusi et al. 2020). In addition, recent studies in

animals and patients have reported the appearance of undesirable neuropsychiatric side effects associated with HFS, which could be caused both by stimulation and by the reduction of associated treatments (Castrioto et al. 2014; Lhommée et al. 2012; Vachez et al. 2020). However, the real link between the appearance of these disorders and HFS is currently debated: is the appearance of these behavioural disorders linked to the reduction of dopaminergic treatments, made possible by the efficacy of HFS-STN, or to a direct effect of HFS-STN? (Castrioto et al. 2014; Thobois et al. 2010).

1.2.2 Preventive or curative therapies (DISEASE MODIFYING TREATMENTS)

The strategies described above, which currently constitute the reference treatments for PD, are only symptomatic. While they do improve motor and sometimes non-motor symptoms, they can also lead to significant complications in the long run. Therefore, curative strategies based notably on cell therapy, gene therapy, or pharmacological approaches have been considered for development.

1.2.2.1 *Cellular therapy*

Cellular therapy, based on the transplantation of stem cells to replace degenerated neurons in areas affected by PD, has been considered since the 1980s (Bjorklund & Stenevi, 1979). To date, the main types of cells that have been tested in this approach are embryonic stem cells, neural stem cells, and mesenchymal stem cells. Although initial studies of embryonic stem cell grafts showed improvement in motor disorders in animals and a small number of patients (Yang et al. 2011), these results were subsequently nuanced by studies that did not show efficacy, especially in older patients (Freed et al., 2011). Indeed, despite an increase in dopaminergic release observed by functional imaging in grafted patients, no beneficial effect was demonstrated in clinical signs. In addition, some studies report transmission of the host's degenerative process to the graft, even leading to the appearance of Lewy bodies (Kordower et al. 2008).

Unfortunately, the use of other sources of stem cells, such as neural or mesenchymal stem cells, has also led to difficulties in clinical translation due respectively to technical difficulties related

to their collection and their limited proliferation and differentiation capacity (Jang et al. 2020). Thus, current research is mainly focused on other sources of cells with a higher potential for proliferation and differentiation, and most importantly, posing less ethical dilemmas. Indeed, induced pluripotent stem cells derived from somatic cells (e.g. fibroblasts), have molecular and morphological characteristics common to embryonic stem cells and differentiate similarly (Barker et al. 2017; Kikuchi et al. 2011). Moreover, the efficacy and safety of transplanting these cells have recently been reported in humans through initial results showing stabilisation or even improvement of motor and psychiatric symptoms after 18 months (Doi et al. 2020; Schweitzer et al. 2020). Although further studies are necessary, these results suggest that curative cellular therapy could be implemented in the future for patients with PD.

1.2.2.2 *Genetic therapy*

Given the difficulties in replacing lost DA neurons, gene therapy strategies have been developed. A first approach has been to attempt to limit the degenerative process or generate axonal regrowth through the use of neurotrophic factors, primarily glial cell line-derived neurotrophic factor (GDNF) or its analog neurturin, which have been evaluated in animals through adeno-associated virus (AAV) injections. It has been shown that the beneficial effects of GDNF on the nigrostriatal pathway were similar whether it was injected before (Kirik et al. 2000), after (Rosenblad, 1999; Rosenblad et al. 1997), or at the same time as the DA lesion (Rosenblad, 1999). These observations have highlighted the neuroprotective and regenerative properties of GDNF and its potential application in de novo patients. However, the first clinical trials of locally induced neurotrophic factor release using AAV within the nigrostriatal pathway, whether GDNF or neurturin, did not confirm the beneficial effects observed in animals in Parkinson's patients (Sullivan & O'Keeffe, 2016). GDNF even proved toxic in 10% of treated patients (Marks et al. 2010). In a lesson learned review, Jeffrey Kordower stipulates that despite the promising trophic factor potential, the challenge remains to distribute it appropriately to the brain regions that need it. He also reminds us that the most important aspect is to appreciate the stage of the

disease for which they are intervening. A recent study of his also showed that the neurtrn gene therapy did not have any effect on Lewy pathology (Chu et al. 2020).

Following deep brain stimulation (DBS), another approach aimed to reduce the hyperactivity of the STN present in Parkinson's patients by locally increasing the synthesis of gamma-aminobutyric acid (GABA), via the injection of AAV encoding for the glutamate decarboxylase (GAD) gene, the enzyme that limits its synthesis. Although clinical studies have shown an improvement in motor symptoms in patients resulting in an average 23.1% reduction in the UPDRS score, it remained lower than that achieved with the HFS, thus limiting the prospects of using this new approach (Kaplitt et al. 2007; LeWitt et al. 2011).

In recent years, a new approach to directly act on the dopamine synthesis pathway to restore sufficient striatal DA concentration has gained some attention. Dopamine synthesis relies on the cascade action of tyrosine hydroxylase (TH). This enzyme converts L-tyrosine to L-3,4-dihydroxyphenylalanine (L-DOPA), using guanosine triphosphate cyclohydrolase (GCH1) as a cofactor, as well as amino acid decarboxylase (AADC). Clinical trials allowing for the administration of a lentivirus containing the genes encoding for TH, AADC, and GCH1 named ProSavin® within the striatum have been conducted (Palfi et al., 2014). They began in humans less than 10 years ago and showed an improvement in motor symptoms 12 months after injection (Palfi et al. 2014). However, the longitudinal follow-up of the first treated patients showed that after 4 years, and with the progression of the disease, these effects tend to stagnate (Palfi et al., 2018). This can be explained by the fact that, like L-Dopa, this technique is dependent on remaining dopaminergic neurons, which continue to degenerate over the course of the disease.

Finally, given the pathogenic role of alpha-synuclein in PD, several strategies targeting its clearance or aggregation are currently being developed. Among them, immunotherapy, whether active, inducing the development of immunity against alpha-synuclein through the injection of a vaccine such as PD01 in the Affitope® project, or passive, via direct injection of antibodies

directed against alpha-synuclein, represents the most advanced strategy (W.G. Meissner, 2018), with phase II clinical trials currently underway (Jankovic, 2018; Schwab et al., 2020).

1.2.2.3 Potential pharmacological approaches

Amongst several possible therapeutic agents, recent explorations of anti-apoptotic factors and antioxidant molecules such as coenzyme Q10 presented with encouraging results in preclinical trials. However, none of these agents have shown promising results in patients (Tarazi et al. 2014). Furthermore, the evaluation of creatine supplementation in a cohort of over 1000 patients to address the mitochondrial energy deficit encountered in Parkinson's disease (PD) did not show superior efficacy to that of placebo (Kiebert et al. 2015).

In recent years, the low incidence rate of PD observed in diabetic patients treated with insulin sensitizers such as thiazolidinediones (TZDs) compared to other treatments (Brauer et al. 2015) has led to the hypothesis that these molecules may have therapeutic or protective potential in PD. To date, the use of TZDs such as the molecule MSDC-0160 in preclinical studies has shown a slowing of the progression of motor disorders that may be related to a neuroprotective effect of the molecule (Peelaerts et al. 2020).

Last but not least, our laboratory has explored for years the potential of iron chelation as a therapeutic modality for PD (Devos et al. 2014). Indeed, systematic and progressive iron accumulation in the SN is another conspicuous feature of PD pathophysiology (Mochizuki & Yasuda 2012). Despite very promising preclinical and clinical results, a large randomised clinical trial recently showed that Deferiprone, an anti-ferroptotic iron chelator agent, reduced iron accumulation, but was not associated with any benefits in PD patients (Devos et al. FAIRPARK-II 2022).

In conclusion, although promising results have been obtained in recent years, the major obstacle to the validation of the various aforementioned approaches is the too-late application of these

strategies in humans (Stocchi, 2013). Indeed, these approaches are only proposed once the diagnosis is established, thus in phases where the degenerative process is already well advanced, greatly limiting their outcome. These observations demonstrate the complete necessity of diagnosing PD as early as possible, in order to allow for better patient management, but also to access a time window compatible with the development and application of neuroprotective and curative strategies (Kilzheimer et al. 2019).

1.3 DIAGNOSIS OF PD

Currently, the diagnosis of Parkinson's disease relies entirely on the evaluation of motor clinical signs, which appear when the degeneration of dopaminergic neurons in the substantia nigra pars compacta exceeds 50-60%, leading to an 80% depletion of dopamine in the striatum (Mou et al. 2020). In addition, beyond its late establishment, the diagnosis of Parkinson's disease is made difficult by the existence of confounding pathologies such as multiple system atrophy (MSA) or progressive supranuclear palsy (PSP). The clinical examination, which allows for the diagnosis and monitoring of the progression of the disease, is mainly based on the use of symptom assessment scales and imaging techniques (Perlmutter, 2009).

As mentioned in the prologue, it is very important to note that to date, the only unambiguous way to confirm the initial diagnosis of Parkinson's disease is by reporting the concurrent presence of Lewy bodies and degeneration of the mesencephalic dopaminergic system in post-mortem analysis of the patient's brain (Marsili et al. 2018).

1.3.1 Diagnostic criteria: MDS scores for motor and non-motor symptoms

Historically, one of the first scales that was developed was the Hoehn and Yahr scale (Hoehn & Yahr, 1967), dividing Parkinson's disease into 5 stages ranging from the presence of unilateral signs resulting in minimal or no functional disability (stage 1), to the use of a wheelchair, or even

total loss of autonomy (stage 5). Although this scale is based on a simple classification system, it is reliable and quick to master and remains commonly used in parallel with other scales to describe the progression of Parkinson's disease symptoms.

Subsequently, the improvement in knowledge of PD's symptomatology led to the development of new multidimensional scales. Among them, the Unified Parkinson's Disease Rating Scale (UPDRS), developed in the 1980s to standardise and homogenise diagnostic criteria, whether evaluated by an expert or not, is divided into 4 sections. These are based on interviews or clinical observations, evaluating the mental state, daily routine activities, and motor abilities of patients. Today, recognized and used worldwide, its predictive value, evaluated retrospectively through post-mortem histological analysis, is about 76% (Hughes et al. 1992).

However, it is lacking in the evaluation of non-motor dysfunctions of the disease that can appear in the early stages. These deficits impair the quality of life of patients as much as the motor disorders (K.R. Chaudhuri et al. 2006), so the use of UPDRS is often supplemented by other scales such as the Hamilton scale or the PDQ39 which respectively evaluate depression or the patients' quality of life (Peto et al. 1998; Su et al. 2021).

Moreover, the UPDRS was revised in 2007 by the Movement Disorder Society (MDS), in order to better take into account all symptoms of the disease (Goetz et al. 2008). This new scale, called MDS-UPDRS, consists of 4 parts:

- I: Non-motor Experiences of Daily Living
- II: Motor Experiences of Daily Living
- III: Motor Examination
- IV: Motor Complications

Each part contains several items that can be scored from 0 (normal) to 4 (severe), leading to a maximum score of 272 (Annex). The part dedicated to non-motor daily conditions accounts for 52 points.

Although this revised version does not improve diagnostic performance, it allows for better evaluation of motor and non-motor signs, particularly under treatment.

More recently, the MDS has proposed new diagnostic criteria for PD (Postuma et al. 2015). The first step is to look for the presence of signs indicating a parkinsonian syndrome (slowness plus stiffness and/or tremor), followed by verification of the presence of additional criteria and the absence of exclusion criteria and red flags (Annex). The first multicenter evaluation of this method show that it can detect parkinsonian patients with around 95% sensitivity and 80% specificity (Postuma et al. 2018).

To date, the MDS-UPDRS represents the most commonly used tool for PD evaluation. However, diagnosis remains late because it is mainly based on the onset of motor symptoms. Indeed, a study reports increasing diagnostic accuracy with the progression of PD, ranging from 53% to 88% when symptoms have been present for more than 5 years (Adler et al. 2014). In addition, specificity problems persist regarding confounding diseases that we have addressed. To try to overcome this problem, complementary examinations to motor analysis, based notably on genetic tests and imaging methods are suggested.

1.3.2 Diagnostic and prognostic Biomarkers of PD: current status

As mentioned before, the diagnosis of PD based on clinical criteria can be challenging due to the presence of overlapping symptoms with other neurodegenerative disorders. Therefore, diagnostic and prognostic biomarkers are essential for accurate and early diagnosis, as well as prediction of disease progression, to allow for effective treatment and management of the disease.

Biomarkers are biological indicators that can provide objective measures of disease onset, progression, and response to therapy. In the case of PD, three main types of biomarkers have been identified:

1.3.2.1 *Genetics tests*

The identification of genetically defined forms of Parkinson's disease that differ from sporadic forms in various clinical aspects has challenged the traditional view of the disease as a unified entity, and has introduced a biological definition of subtypes within the Parkinson's disease spectrum (Tolosa et al. 2021).

Recent advancements in gene sequencing and genomics have enabled the rapid discovery of genetic causes and risk variants of the disease, revealing a highly complex genetic architecture involving both common and rare risk variants (Blauwendraat et al. 2020).

Mutations in at least 20 genes including SNCA, LRRK2, PARK2, PINK1, DJ-1 and GBA are now known to cause familial PD, which constitutes up to 15% of PD cases. These mutations have helped shed light on the underlying molecular basis of neurodegenerative processes (Fereshtehnejad et al. 2017). Additionally, over 90 genetic risk loci for the more common sporadic form of the disease have been identified, and these genes have been found to converge on common pathways related to mitochondrial homeostasis, cell death machinery, inflammatory signalling, intracellular trafficking, and endosomal-lysosomal dysfunction (Bandres-Ciga et al. 2020).

Genetic testing is increasingly used in clinical practice, particularly for patients with early onset of disease, family history, and those from high-risk populations. The identification of specific genetic forms of the disease can also provide opportunities for patients to participate in clinical trials targeting these specific forms of neurodegeneration. More importantly, genetic information has revealed that Parkinson's disease is phenotypically diverse. This diversity emphasises potential targets for disease-modifying interventions and suggests the possibility of using machine-learning algorithms to predict patient subgroups, age at onset, and clinical features (Nalls et al. 2015). These insights will also have an impact on the development and application of disease-modifying therapies, as shown by ongoing clinical trials targeting the GBA pathway or LRRK2 function (Tolosa et al. 2020).

1.3.2.2 Cerebrospinal fluid and blood tests

Although the link between brain deregulations and peripheral modifications visible in biofluids is not always evident, the search for biomarkers in biofluids has recently emerged to develop new diagnostic tools for neurodegenerative diseases.

Available evidence indicates that CSF and blood biomarkers that closely reflect the underlying mechanisms of Parkinson's disease, such as α -synuclein species, lysosomal enzymes, markers of amyloid and tau pathology, and neurofilament light chain, have the potential to be useful for both diagnosis and prognosis of PD (Parnetti et al. 2019).

In particular, a decrease in alpha-synuclein concentration in the CSF has been suggested as a possible early biomarker of the disease (Gao et al. 2015). However, this concentration is not correlated with the progression of PD. Although the decrease may be an indirect indicator of changes in the balance between secretion, solubility, or elimination of alpha-synuclein in the brain, other biomarkers more directly linked to alpha-synuclein aggregation and disease progression are needed (Mollenhauer et al. 2019). Additionally, other markers of Parkinson's disease's physiopathology have been identified in the CSF, such as indicators of mitochondrial deregulations, fatty acid metabolism, or energy metabolism in general (Öhman & Forsgren, 2015; Trezzi et al. 2017; Trupp et al. 2014; Willkommen et al. 2018).

Research is also being conducted on blood α -synuclein species and neurofilament light chain, which could serve as non-invasive tools for both early and differential diagnosis of Parkinson's disease versus atypical parkinsonian (Magdalinou et al. 2015).

Interestingly, comparative analyses of blood (plasma or serum) and CSF samples have shown common deregulations and similar performance in discriminating PD patients from healthy subjects (Plewa et al. 2021; Stoessel et al. 2018; Burté et al. 2017; Zhao et al. 2018). This distinction has the potential to be made in the earliest stages of PD. Indeed, metabolomic studies report mitochondrial alterations associated with oxidative stress in patients with non-motor symptoms similar to those observed in the early stages of PD, such as REM sleep disorders or neuropsychiatric disorders (Quinones & Kaddurah-Daouk, 2009).

Ultimately, larger independent studies are needed to further validate the use of CSF and blood biomarkers to improve the accuracy of Parkinson's disease diagnosis and prognosis (Parnetti et al. 2019).

1.3.2.3 Imaging (other than MRI)

Imaging techniques, which have been constantly improving for several years, are a robust diagnostic tool as well as a fundamental research instrument. I will focus in this chapter on molecular imaging, apart from Magnetic Resonance Imaging (MRI) which will be described in detail as the core of the thesis subject in Chapter 3.

In clinical practice, nuclear imaging constitutes a powerful method to detect *in vivo* changes in the brain at molecular level. It is mainly based on two approaches: positron emission tomography (PET) and single-photon emission computed tomography (SPECT).

The most common SPECT brain imaging in PD context is DaTscan, which allows visualisation of dopamine transporter (DaT) function in the striatum (caudate and putamen) (Gayed et al. 2015). In PD patients, DaTscan has shown a decrease in presynaptic dopamine reuptake sites (DaT) in the striatum, illustrating dopaminergic denervation (Fuente-Fernández 2012; Bega et al. 2021). This technique has mainly allowed the differentiation of PD from non-degenerative forms of parkinsonism, such as essential tremor, vascular and drug-induced parkinsonism (Jennings et al. 2004).

As for PET scan, different tracers are used to show disease-related changes in specific brain functions. For example, [18F]FDG is used to monitor glucose metabolism, which has a specific pattern in PD patients, including an increased metabolism of the thalamus, globus pallidus, putamen, cerebellum and pons, and a decreased metabolism of the occipital, temporal, parietal, and frontal cortices (Meles et al. 2017, 2020).

Other tracers such as [18F]FDOPA or [18F]FMT allow monitoring of the L-aromatic amino acid decarboxylase (AADC) enzymatic activity. Indeed, AADC converts L-DOPA to dopamine, and so it shows an indirect reflection of dopamine synthesis, storage and turnover. In PD patients, [18F]FDOPA showed reduced uptake in both the caudate and putamen of the striatum (Holtbernd et al. 2015; Akamatsu et al. 2017).

Similar approaches have been developed for the serotonergic and cholinergic systems, which are both affected in PD, and considered by most to be essential in the appearance of non-motor symptoms. For example, using a radioligand to visualise serotonin transporter binding, a study has shown that serotonergic alterations were more prevalent in apathetic PD patients compared to non-apathetic patients, indicating that serotonergic degeneration has a prominent role in neuropsychiatric symptoms of early PD (Maillet et al. 2016).

In summary, the constant improvement of clinical scales and different imaging methods now allows the diagnosis of the disease in about 90% of cases with a margin of error of about 20% (Rizzo et al. 2016). Nevertheless, the diagnosis remains late and limits patient care as well as the development of curative therapies. It appears necessary to develop diagnostic tools that are easily usable in the early stages of PD, even before the onset of motor symptoms, to stratify patients and devise a precision-medicine protocol for individual treatment strategies.

To do so, the use of animal models mimicking the different phases of PD, including the prodromal phase, is essential, to better understand the characteristics of these early stages of the disease, in order to find earlier and more adequate biomarkers.

2 CHAPTER 2: ANIMAL MODELS OF PARKINSON'S DISEASE

The development of animal models has proven essential to study the aetiology and pathophysiology of Parkinson's disease (PD), as well as to evaluate the effects of different types of treatments.

There is a wide consensus that no animal model is a perfect representation of the human disease, but there has been a development of highly valid models of PD, with good construct, face, and predictive validity. Indeed, a good animal model of PD must reflect the disease's aetiology, by

presenting a progressive lesion in the nigrostriatal pathway, preferably age-dependent. It should replicate the disease's phenotype as observed in humans. And it should represent translational human-animal correlations of therapeutic outcomes. It should also be reproducible, and not induce too many alterations in vital functions to avoid high mortality rates. The first models developed relied on the use of neurotoxins such as 6-hydroxydopamine (6-OHDA) in rats and 1-methyl-4-phenyl-1,2,3,6-tetrahydropyridine (MPTP) in mice and non-human primates. Furthermore, the identification of genetic mutations in certain familial forms of PD has led to the development of transgenic animal models such as the A53T- α -synuclein model. The development of relevant animal models remains active, particularly through the use of various neurotoxins such as pesticides and herbicides (paraquat, rotenone), which are recognized as risk factors for PD even though their characterization remains weak to this day (Berry et al. 2010; Bonneh-Barkay et al. 2005; Kamel, 2013; Xiong et al. 2012). In this chapter, I will discuss in detail the animal models that were used in the context of my thesis, namely the alpha-synuclein rat, the 6-OHDA rat, and the MPTP rat.

2.1 NEUROTOXIC MODELS

2.1.1 6-OHDA

6-OHDA was the first neurotoxic agent specific to catecholaminergic neurons, used to reproduce the characteristic motor symptoms of Parkinson's disease (PD) in animals (Ungerstedt, 1968). 6-OHDA does not cross the blood-brain barrier (BBB) and therefore must be directly administered intracerebrally in the areas of interest to induce degeneration. This neurotoxin penetrates dopaminergic and noradrenergic neurons through monoamine reuptake transporters, making the lesions non-specific. Therefore, a solution containing selective noradrenergic reuptake inhibitors (e.g., desipramine) is often injected in parallel to limit degeneration to dopaminergic neurons (Bové & Perier, 2012; Drui et al. 2014). Once internalised within neurons, 6-OHDA induces cell death by oxidative stress, inhibiting complex I of the mitochondrial chain and producing reactive oxygen species (Rodriguez-Pallares et al. 2007; Schober, 2004).

Initially injected bilaterally into the SNpc to induce severe to total loss of dopaminergic neurons, it has been used to demonstrate a symptomatology mimicking PD, including the presence of akinesia and catalepsy. However, these levels of lesions were also associated with severe adipsia and aphagia, causing significant weight loss in animals that could lead to their death, which led to limiting the use of this type of lesion (Campos et al. 2013). Subsequently, unilateral injections into the SNpc or the medial forebrain bundle (MFB) were preferred because they lead to the appearance of akinesia and rigidity of the contralateral limbs to the lesion, as well as rotation following the injection of dopaminergic agents such as apomorphine (Bezard et al. 1998; Tieu, 2011). Although simpler, this unilateral loss does not represent the entirety of the physiopathology and symptomatology of PD. Indeed, these models are primarily used for the study of motor disorders and therefore advanced phases of PD (Masini et al. 2021).

Thus, in order to study the other phases of PD and associated disorders, models of partial bilateral lesions have been developed. The use of lower doses of 6-OHDA leads to the appearance of characteristic non-motor symptoms, among others, early phases of PD such as apathy, anxiety, and depression (Drui et al. 2014; Favier et al. 2017). In addition, in this model, the administration of treatments commonly used in the clinic such as pramipexole or L-dopa corrects these disorders, giving it good predictive value (Drui et al. 2014; Favier et al. 2014).

Due to its isomorphism, predictive validity, and ease of use, the 6-OHDA rat model has allowed multiple advances in understanding the pathophysiological mechanisms of PD and in the development of therapeutic or neuroprotective strategies (Favier et al. 2014, 2017; Kirik et al. 2000). However, despite all its advantages, this model also has limitations because it does not reproduce the progressive nature of degeneration or the accumulation of alpha-synuclein and Lewy bodies characteristic of PD (Decressac et al. 2012).

2.1.2 MPTP

The 1-methyl-4-phenyl-1,2,3,6-tetrahydropyridine (MPTP) was discovered in 1976 when a group of young Californians consumed it by mistake and developed severe motor symptoms similar to

those observed in Parkinson's disease (PD) (Davis et al. 1979; William Langston et al. 1983). Post-mortem examination of their brains revealed a loss of DA neurons in the SNpc. It was then suggested to use this neurotoxin to create animal models of PD (W. Langston et al. 1984). MPTP has the advantage of easily passing through the blood-brain barrier (BBB) and can therefore be administered systemically.

After passing through the BBB, MPTP is transformed into 1-methyl-4-phenyl-1,2-dihydropyridinium (MPDP+) by monoamine oxidase B (MAO-B) in astrocytes (Chiba et al. 1984; Markey et al. 1984). MPDP+ then spontaneously oxidises to 1-methyl-4-phenylpyridinium (MPP+), which is extremely toxic (Castagnoli et al. 1985). Once taken up by glial cells, MPP+, like 6-OHDA, is captured by dopaminergic transporters, internalised into dopaminergic neurons, and leads to neuronal death via similar processes to those of 6-OHDA, mainly oxidative stress and mitochondrial dysfunction.

Given its systemic administration, MPTP intoxication is used in many species such as mice, monkeys, dogs, and cats (Bezard et al. 1998).

Like 6-OHDA, it has been shown that MPTP leads to rapid and significant loss of dopaminergic neurons (Bezard et al. 1998). However, new protocols based on injections of lower but repeated doses have been developed to induce progressive loss of neurons and thus mimic the characteristic neurodegenerative process of PD (Ballanger et al. 2016). In non-human primates, MPTP injection leads to motor symptoms very similar to those observed in PD patients, such as bradykinesia, often progressing to akinesia, rigidity, and sometimes tremors (Bezard & Przedborski, 2011). Moreover, these disorders can be corrected by treatment such as L-dopa or dopaminergic agonists (Veyres et al. 2018).

It is important to note that, for comparable doses, systemic administration of MPTP in rats does not produce dopaminergic degeneration. This resistance is due in particular to the large amount of peripheral MAO-B that transforms MPTP into MPDP+ even before it crosses the BBB (Giovanni et al. 1994; Schmidt & Ferger, 2001).

An interesting MPTP rat model was however developed by bilaterally injecting MPTP in the SNpc directly to avoid its peripheral transformation. This model was shown to have learning and

memory impairments, independently from any motor deficits (Da Cunha et al. 2001). It was then suggested that this model constitutes an interesting approach to an early phase of PD, with a lower percentage of dopaminergic loss, and only very mild motor deficits, but with a robust impairment of habit learning and spatial working memory (Ferro et al. 2005). Interestingly, the MPTP bilateral rat model represented a good alternative to the much more severe 6OHDA bilateral rat model, which was known to cause a more widespread cell loss, which is not limited to dopaminergic neurons, as well as a more intense body weight loss and higher mortality rate which made longitudinal and multimodal studies more difficult to perform.

2.2 TRANSGENIC MODELS

Other models are based on the genetic modifications found in familial forms of PD. The first mutations highlighted were those observed in the SNCA gene encoding alpha-synuclein (A53T, A30P, E46K, H50Q, and G52D mutations) (Polymeropoulos et al. 1997).

A mouse model over-expressing human wild-type alpha-synuclein driven by the murine Thy-1 promoter was also developed in 2002, and shown to reproduce many features of sporadic PD, including changes in dopamine release, alpha-synuclein pathology, neuroinflammation, and deficits in motor and nonmotor functions, manifested in PD (Chesselet et al. 2012).

Several other genes related to PD were also identified such as parkin, DJ-1, PINK1, and LRRK2 (Cookson, 2012; Selvaraj & Piramanayagam, 2019; Chia et al. 2020).

Complete deletion of the PINK1 gene in mice (PINK1 KO mice) leads to a decrease in striatal dopamine release (Kitada et al., 2007), only in aged animals, which is interesting given that PD is an age-related disease.

Similar results are observed with LRRK2, Parkin, and DJ1 gene knockouts (Sanchez et al. 2014). However, despite the presence of motor symptoms in these animals, neuronal loss is often lower than that observed in PD (less than 50%) (Creed & Goldberg, 2018; Sanchez et al. 2014). On the other hand, when transposed to rats, genetic models reproduce the characteristic symptoms of PD as well as the progressive nature of neurodegeneration (Creed & Goldberg, 2018), which

makes them relevant for studying the prodromal phase of PD or for developing neuroprotective strategies.

However, these models do not reproduce all the markers of PD, particularly the presence of Lewy bodies. Since these pathophysiological mechanisms are rarely present in animal models, they have been the subject of separate models, notably based on the accumulation of alpha-synuclein, which has led to a renewed interest in genetic models.

2.3 ALPHA-SYNUCLEIN MODELS: FROM PHYSIOLOGY TO PATHOLOGY

As mentioned in the first chapter, alpha-synuclein in its different forms plays a central role in synucleinopathies, notably Parkinson's disease. In this part, we will describe its role and structure under physiological then pathological conditions, and why alpha-synuclein overexpression and spreading constitute an interesting approach in modelling Parkinson's disease.

2.3.1 Alpha-synuclein in physiological conditions: structure & role

Alpha-synuclein is a small protein composed of 140 amino acids in humans. It was first identified in 1988 in the nucleus and presynaptic terminals of neurons from an electric ray (torpedo) (Maroteaux et al. 1988). This protein, as well as beta-synuclein, were later found in humans, with predominantly cerebral expression, although it is also strongly expressed in the blood (Jakes et al. 1994). Alpha-synuclein can be found intracellularly or associated with the membrane and localised in the brain at the presynaptic level. The synuclein family consists of three proteins: alpha-synuclein, beta-synuclein, and gamma-synuclein. These proteins are coded by three distinct genes, particularly the SNCA gene located on chromosome 4 (Chen et al. 1995). Alpha-synuclein is part of what is called intrinsically disordered proteins, meaning that it does not have a defined three-dimensional structure in solution (Weinreb et al. 1996).

The primary structure of this protein is artificially divided into 3 domains (Figure 6A). The N-terminal end of alpha-synuclein is composed of amino acids 1 to 60 which can form an alpha-helical structure that can bind phospholipid vesicles (Davidson et al. 1998). Interestingly, the A30P mutation associated with PD prevents the formation of this helix while the A53T mutation tends to promote it (Jensen et al. 1998). The central region of alpha-synuclein, called "NAC" for "Non-Amyloid β Component," comprises amino acids 61 to 95. This part of the protein is highly hydrophobic, and is capable of assembling into beta sheets and promoting the aggregation of alpha-synuclein to form the skeleton of fibers (Rodriguez et al. 2015). Finally, the C-terminal end of alpha-synuclein corresponds to amino acids 96 to 140. This end can bind to its own NAC domain (Binolfi et al. 2006), which inhibits the aggregation of alpha-synuclein. Therefore, the truncation of this C-terminal end strongly promotes the nucleation and elongation of the fiber protein assembly (Gallardo et al. 2020).

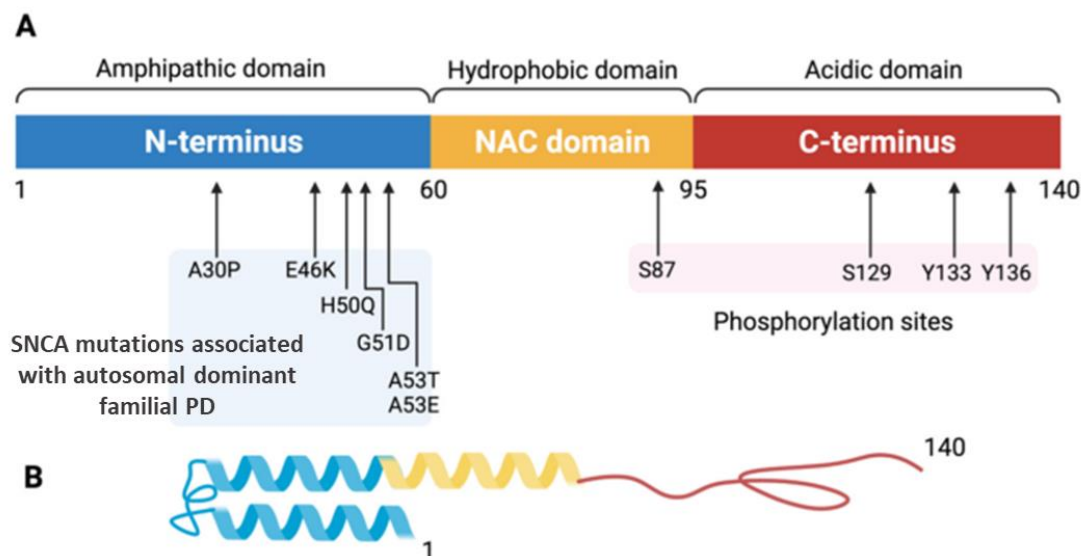


Figure 6. Illustration of alpha-synuclein structure. A. Representation of the three domains of alpha-synuclein with mutation and phosphorylation sites. B. Tertiary structure of the α -synuclein monomer. (Adapted from Fan et al. 2021).

The native state of alpha-synuclein is still widely debated. Most studies suggest that under physiological conditions, alpha-synuclein exists in different conformations with dynamic equilibrium. Different states of the protein (monomeric, oligomeric, transiently folded) could

coexist. Furthermore, the existence of multiple interaction partners of alpha-synuclein also influences its folding, making the study of this protein even more difficult (Dehay et al. 2016).

The physiological roles of alpha-synuclein are not yet fully understood. The conformational flexibility of this protein allows it to interact with many ligands, giving it multiple functions (Villar-Piqué et al. 2016):

- **Regulation of synaptic vesicle traffic** by promoting the assembly of the SNARE complex, which is essential for the release of neurotransmitters (Burré et al. 2010), hence, making alpha-synuclein involved in synaptic plasticity and learning (Burré, 2015).
- **Control of dopaminergic biosynthesis** by inhibiting the tyrosine hydroxylase enzyme (Perez et al. 2002; Lou et al. 2010), and by decreasing dopamine reuptake through DAT down-regulation (Wersinger and Sidhu, 2003).
- **Chaperone activity** to multiple proteins such as PKC (Protein Kinase C), the pro-apoptotic protein BAD (Bcl-2-Associated Death promoter), or the ERK protein (Extracellular signal-regulated kinases) (Ostrerova et al. 1999, Souza et al. 2000)
- **Interaction with the mitochondria** of dopaminergic neurons by modulating their membrane potential, calcium homeostasis, cytochrome c release and ATP production (Perez, 2020).
- Nuclear alpha-synuclein is also involved in the **regulation of gene expression** (Pinho et al. 2019), and can also have an anti-apoptotic role by downregulating the expression of the delta protein kinase C (Jin et al. 2011).

Ultimately, despite these multiple roles of alpha-synuclein, the protein is considered essential but not necessary, since triple knock-out for alpha-, beta-, and gamma-synuclein allows the generation of viable and fertile mice. However, these mice present significant age-dependent neuronal dysfunctions suggesting a preponderant role of alpha-synuclein in maintaining normal brain activity during ageing. Premature death of these triple-KO mice is also observed (Greten-Harrison et al. 2010). Conversely, overexpression of alpha-synuclein leads to progressive degeneration of dopaminergic neurons similar to that observed in PD (Mochizuki et al. 2006).

Therefore, maintaining a balanced physiological amount of alpha-synuclein appears necessary to avoid the development of synucleinopathies during ageing.

2.3.2 Alpha-synuclein in pathological condition

Under pathological conditions, alpha-synuclein can adopt a structure rich in beta sheets, which persists and promotes its aggregation (Rodriguez et al. 2015). The amount of alpha-synuclein in the brain depends on the balance between three phenomena: synthesis, clearance, and aggregation. If any one of these three processes is altered or unbalanced, such as the multiplication of the SNCA gene, or proteasome failure (less degradation of alpha-synuclein), or even increased oxidative stress, abnormal forms of alpha-synuclein are promoted to form stable toxic species (De Mattos et al. 2020). Indeed, abnormally folded alpha-synuclein exposes hydrophobic regions on its surface that are usually buried. These exposed hydrophobic surfaces tend to aggregate in order to minimise their interactions with the aqueous environment.

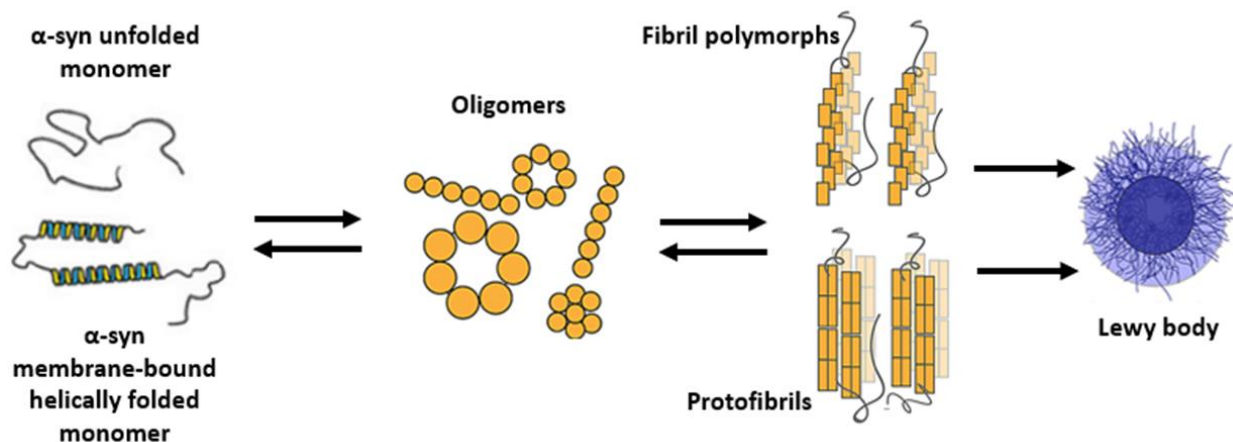


Figure 7. Schematic depiction of alpha-synuclein aggregation pathway. α-Synuclein monomers exists in different forms isoforms. They can undergo substantial structural changes, resulting in the formation of small oligomeric species that can be stabilized by β-sheet interactions, which then form higher-molecular-weight insoluble protofibrils. Those can also polymerize into amyloidogenic fibrils and other fibril polymorphs found in Lewy bodies. Both oligomeric and fibrillar species have been demonstrated to be neurotoxic. However, the mechanisms regulating these conformational changes from a normal to a pathological form remain unknown. (Adapted from Dehay et al. 2015 & Gadhe et al. 2022).

Misfolded alpha-synuclein therefore functions like a primer to recruit other monomers. And when their intermolecular interactions are sufficient, amyloid fiber polymerization becomes irreversible, because the fibers become strongly resistant to cellular machinery clearance pathways (Brundin et al. 2010).

The formation of alpha-synuclein aggregates leads to cellular toxicity (Alam et al. 2019). Indeed, these aggregates are first capable of trapping other macromolecules (proteins, lipids) and thus preventing their normal functioning. Moreover, these aggregates disrupt cellular ion homeostasis and proteostasis. Additionally, alpha-synuclein fibers can compromise the integrity and function of cellular organelles (endoplasmic reticulum, Golgi apparatus, mitochondria, lysosomes) (Flavin et al. 2017). Finally, these fibrillar assemblies promote degeneration by inducing chronic inflammation (Gustot et al. 2015).

Genetically, we know that three-point mutations in α -synuclein (A53T, A30P, and E46K) cause familial PD (Gasser, 2009, Lees et al. 2009). Mutations (A53T, A30P, E46K) or increased levels (triplication or duplication) of alpha-synuclein lead to aggregation and fibrillization. Features common to sporadic PD such as nitric oxide (NO), reactive oxygen species (ROS), and mitochondrial dysfunction also lead to alpha-synuclein aggregation. (Dawson et al. 2010). This suggests a vicious cycle phenomenon involving this protein, where its accumulation and aggregation can both be the origin of cellular homeostasis dysfunction but also its consequence. But in both cases, alpha-synuclein remains at the core of the pathophysiological processes of Parkinson's disease and other synucleinopathies, making alpha-synuclein animal models essential for the study of the pathology.

2.3.3 Viral overexpression and spreading models of alpha-synuclein

As mentioned before, the development of mutant mouse lines has shown that the accumulation of alpha-synuclein is accompanied by a decrease in striatal DA, the formation of Lewy bodies, and some motor dysfunction (Giasson et al. 2002; Masliah et al. 2000; Thiruchelvam et al. 2004), but

not significant degeneration of nigrostriatal pathway neurons (Fernagut & Chesselet, 2004; Jagmag et al. 2016). Since these mutant models do not reproduce the characteristic anatomopathology of PD, other models based on exogenous administration of the mutated protein have been developed.

Among the various strategies tested, bilateral injection of adeno-associated viruses (AAVs) into the SNpc inducing overexpression of alpha-synuclein has been shown to induce progressive death of dopaminergic neurons and loss of striatal dopaminergic terminals in rats (Bourdenx et al. 2015; Kirik et al. 2002; Decressac et al. 2012; Caudal et al. 2015; Ip et al. 2017), allowing for the study of the different phases of the disease in the same animal (Oliveras-Salvá et al. 2013). Depending on the form of alpha-synuclein used (wild type or A53T mutated), the loss of dopaminergic neurons in the SNc is on average 57% and 51% after 4 weeks, and 82% and 60% after 10 weeks of vector expression, respectively, for the wild type and A53T mutated form (Ip et al. 2017; J. Lu et al. 2015).

Given the progressive nature of the degenerative process, the first behavioural manifestations observed in this model are the appearance of non-motor symptoms after 3 weeks, such as depression or anxiety, and olfactory deficits (Caudal et al. 2015; Petit et al. 2013), followed by the expression of motor alterations 10 weeks after injection, mimicking more advanced phases of the disease (Bourdenx et al. 2015; Caudal et al. 2015; Decressac et al. 2012; Ip et al. 2017; Oliveras-Salvá et al. 2013).

More recently, other approaches have focused on studying the propagation of alpha-synuclein through intracerebral or systemic administration of pre-formed alpha-synuclein fibrils (PFF) (Patterson et al. 2019). Similar to the use of AAV, it leads to progressive degeneration and the appearance of motor and non-motor symptoms after several months (S. Kim et al. 2019; Patterson et al. 2019; Paumier et al. 2015; Shimozawa et al. 2017). Interestingly, it would also illustrate Braak's hypothesis, as discussed in chapter 1, that PD is initiated in the peripheral nervous system. Indeed, the injection of alpha-synuclein PFF into the intestine produces alpha-synuclein aggregation and significant progressive degeneration of dopaminergic neurons in the SNpc, accompanied by characteristic motor and non-motor symptoms of PD, such as psychiatric

disorders (Kim et al. 2019). Developed very recently, this model is still subject to a lack of consensus on the protocol for using alpha-synuclein PFF, which leads to relatively variable phenotypes depending on the protocols (Polinski, 2021).

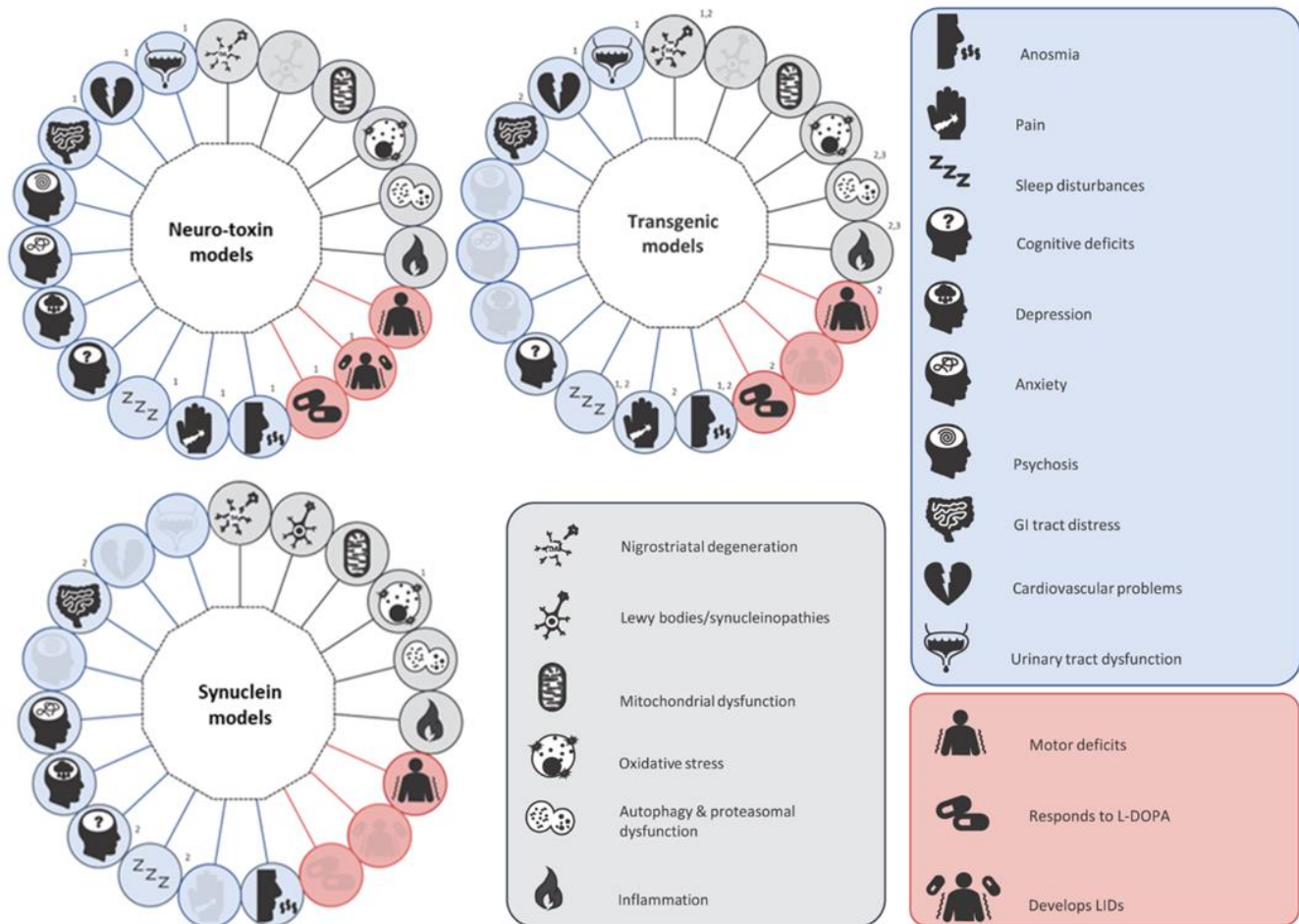


Figure 8. Overview of the different characteristics of the animal models of PD, detailed in Chapter 2. It summarizes the key pathological, pathogenic and symptomatic features present in neurotoxic, transgenic and alpha-synuclein models. The absence of a feature is greyed out. (Adapted from Lama et al. 2021).

To conclude this chapter, it is important to note again that Parkinson's disease can be emulated by a wide array of animal models, none of which completely recapitulate the entire disease's spectrum and complexities. In fact, each of these models offers its own advantages and disadvantages for studying different aspects of the disease, including the aetiology, pathology,

pathogenesis, and symptomatology (Figure. 8) . The choice of animal models should always depend on the researchers' main objectives, and the question they want answered.

3 CHAPTER 3: MAGNETIC RESONANCE IMAGING & PD

Magnetic Resonance Imaging is a relatively recent non-ionizing imaging technique based on the principle of Nuclear Magnetic Resonance (NMR), discovered in 1938 by Isaac Rabi, and for which he was awarded the Nobel Prize in Physics in 1944. It uses the phenomenon of relaxation of nuclear angular moments (or spins), discovered by Bloch and Purcell who described in 1946 the effect of spin precession when subjected to an external magnetic field. It turns out that, when placed in a magnetic field, certain nuclei such as ^1H , ^{13}C , and ^{17}O , possessing a non-zero spin, have the ability to absorb electromagnetic waves and then emit a wave of the same type during relaxation. These works earned Bloch and Purcell the Nobel Prize in Physics in 1952.

But the medical application was born from the work of Paul Lauterbur, who determined the spatial distribution of spins in 1974 by applying a gradient to the magnetic field (Lauterbur 1973), and Peter Mansfield, who developed the Echo-Planar Imaging (EPI) sequence which greatly reduces the image acquisition time (Stehling et al 1991). The latter shared the Nobel Prize in Medicine in 2003.

Since then, the technique has greatly developed, with technological improvements (high field, cryogenic probes, gradient improvements, etc.) as well as new sequences opening up new applications (diffusion imaging, CEST, functional imaging, etc.).

In this chapter, we will present these different techniques and their operating principles concisely. Particular attention will be paid to the methods used during this thesis.

3.1 MAGNETIC RESONANCE IMAGING

3.1.1 Basics of MR Images.

Magnetic Resonance Imaging (MRI) is a key modality for studying the brain, since it relies on the magnetic resonance phenomenon of water protons, which represent around 80% of the brain. To generate images, a static magnetic field is employed to disturb the magnetic moments of protons in the hydrogen nucleus from their equilibrium position, and their relaxation process is observed to generate an induced electronic signal. Although protons are initially arranged randomly, they align with the magnetic field, resulting in net magnetization towards the field direction (Balafar et al. 2010).

The intensity and length of the MRI signal are contingent upon three factors: the proton density (ρ), the spin-lattice relaxation time (T_1) which indicates how quickly the net magnetization recovers its equilibrium state, and the spin-spin relaxation time (T_2) during which magnetization components gradually diminish to zero (Brown et al. 2004). By manipulating these parameters, it is possible to acquire three distinct images of a single body, namely T_1 -weighted, T_2 -weighted, and ρ -weighted images. Based on its specific properties, a brain T_1 -weighted MRI enhances the signal of fatty tissues and suppresses the signal of water. Conversely, a brain T_2 -weighted MRI enhances the signal of water (Kawahara & Nagata, 2021) (figure).

An MR image represents the spatial layout of the MR signal, with two or three spatial dimensions, such as a slice or volume. Additionally, MR images capture a moment in time and could therefore represent the temporal dimension of a disease's progression (Kennedy et al. 2002). This temporal dimension is also used to characterise functional properties of MR parameters, especially in functional MRI (fMRI), which monitors changes in blood oxygenation in the brain resulting from neural activation.

Images are acquired at specific resolutions, with each voxel representing the average MR signal over a three-dimensional volume within the subject. The resolution (size) of the voxel can be different in each of its three dimensions. The image intensity of a voxel includes both the desired

MR signal and the noise contributed by the imaging device. The amount of signal compared to noise in the acquisition is termed the signal-to-noise ratio (SNR). There is an intrinsic theoretical limit to sensitivity for each MR property, so the acquisition parameters can be optimised to provide the best possible SNR per image. Indeed, there is a minimally acceptable net SNR necessary to create a clinically and diagnostically useful image.

Finally, the digital nature of MR images and their utility for computerised image analysis allow for quantification of morphometric properties, including quantitative variations in brain anatomy (Frank et al. 2021).

3.1.2 Types of MRI acquisitions

3.1.2.1 *Structural MRI*

Structural brain MRI acquisitions are the easiest and fastest types of sequences that allow for a detailed visualisation of the anatomy of the brain (Glasser & Essen 2011).

As mentioned earlier, there are two types of structural images that can be acquired: The T1-weighted images which provide high contrast between grey matter, white matter, and cerebrospinal fluid (CSF), commonly used to identifying structural abnormalities such as tumours and cysts (Figure 9A). And the T2-weighted images that provide high contrast between different types of soft tissue, including brain parenchyma, CSF, and oedema, and which are useful for identifying structural abnormalities such as demyelination, inflammation, and ischemia. There is also Fluid-attenuated inversion recovery (FLAIR) imaging, which is a type of T2-weighted imaging that suppresses the signal from CSF, making it easier to visualise brain parenchyma abnormalities.

3.1.2.2 *R2*, QSM, Neuromelanin*

Quantitative MRI techniques such as R2* mapping and quantitative susceptibility mapping (QSM) are important tools for measuring tissue properties in the brain.

R2* mapping measures the effective transverse relaxation rate of tissue, which is influenced by the local magnetic field inhomogeneities caused by tissue microstructure and iron content (Figure 9B). R2* mapping can be used to assess tissue iron content (Haacke et al. 2005), as well as other tissue properties such as myelin content and demyelination.

Quantitative susceptibility mapping (QSM) is a technique that measures the magnetic susceptibility of tissue, which is influenced by the magnetic properties of tissue constituents such as iron, calcium, and other metal ions (Wang & Liu 2015). QSM can be used to visualise and quantify iron deposition in the brain, as well as other pathologies such as calcification and haemorrhage.

Both R2* mapping and QSM are typically acquired using gradient-echo MRI sequences, which are sensitive to the magnetic susceptibility effects of tissue. These sequences are often combined with advanced post-processing algorithms such as sophisticated modelling and image reconstruction techniques to enable accurate and reliable quantification of tissue properties (Bagnato et al. 2018).

3.1.2.3 Diffusion Tensor Imaging (DTI)

DTI (Diffusion Tensor Imaging) is a specialised type of MRI sequence that provides information about the diffusion of water molecules in tissues, particularly in the white matter of the brain. DTI can reveal the direction and magnitude of water diffusion, allowing for the visualisation of white matter tracts (Figure 9C).

In DTI, multiple diffusion-weighted images (DWIs) are acquired from different directions, and the diffusion tensor, which is a mathematical representation of water diffusion, is calculated from the DWIs. As a result, several measures can be derived, such as fractional anisotropy (FA), mean diffusivity (MD), and axial and radial diffusivity, which provide information about the microstructural properties of the white matter (Basser et al. 1994; LeBihan et al. 2012; Assaf & Pasternak 2008). DTI has been widely used in research and clinical settings to investigate various neurological and psychiatric disorders that involve white matter abnormalities

3.1.2.4 Magnetic resonance spectroscopy (MRS)

Brain Magnetic Resonance Spectroscopy (MRS) enables the measurement of the concentration of different biochemical compounds in the brain. It utilises the same principles of nuclear magnetic resonance as MRI, but instead of imaging, it detects the signals produced by specific metabolites in the brain (Öz et al. 2014).

During MRS, a single voxel is placed in a specific location in the brain, and a radiofrequency pulse is applied to excite the hydrogen atoms of the metabolites in the tissue (Figure 9D). The resulting signal is then measured and analysed to determine the concentrations of different metabolites, such as N-acetyl-aspartate (NAA), creatine (Cr), choline (Cho), and myo-inositol (ml) (Soares et al. 2009).

NAA is considered a marker of neuronal health and viability, while Cr is involved in energy metabolism, Cho is a marker of cell membrane turnover, and ml is a marker of glial activation. Changes in the concentration of these metabolites are indicative of different pathologies, such as brain tumours, neurodegenerative diseases, and psychiatric disorders.

MRS has several advantages, such as its non-invasiveness and high specificity to certain metabolites. However, it also has some limitations, such as its low spatial resolution and the need for specialised expertise for data analysis.

3.1.2.5 Functional MRI

Functional magnetic resonance imaging (fMRI) measures the changes in blood oxygen level-dependent (BOLD) signals in response to neuronal activity in the brain (Figure 9E). It has become a widely used method for investigating the functional organisation of the brain in both healthy and disease contexts. The basic principle of fMRI is the fact that when a brain region becomes active, there is an increase in blood flow and oxygen consumption in that area. This leads to a localised increase in the concentration of deoxyhemoglobin, which is paramagnetic and affects

the magnetic field in the vicinity. By measuring changes in the magnetic field, fMRI can indirectly detect neuronal activity in the brain (Buxton 2009 book).

There are several types of fMRI sequences, but the most commonly used are gradient-echo echo-planar imaging (EPI) and spin-echo EPI. Gradient-echo EPI is sensitive to changes in both $T2^*$ and $T2$, whereas spin-echo EPI is primarily sensitive to changes in $T2$. Gradient-echo EPI is more commonly used due to its higher sensitivity to BOLD contrast.

During fMRI acquisition, the participant could be in a resting state hence resting state fMRI (rs-fMRI), or is asked to perform a task or stimulated with a sensory input to activate specific brain regions. The BOLD signal changes are then analysed using statistical methods to identify brain regions that show significant activity during the task or stimulus (Logothetis 2008).

fMRI has been used to study a wide range of cognitive functions, including perception, attention, memory, language, and emotion, as well as to investigate the neural basis of various neurological and psychiatric disorders. It has also been used to study the developing brain, as well as to track changes in brain function over time in response to various interventions.

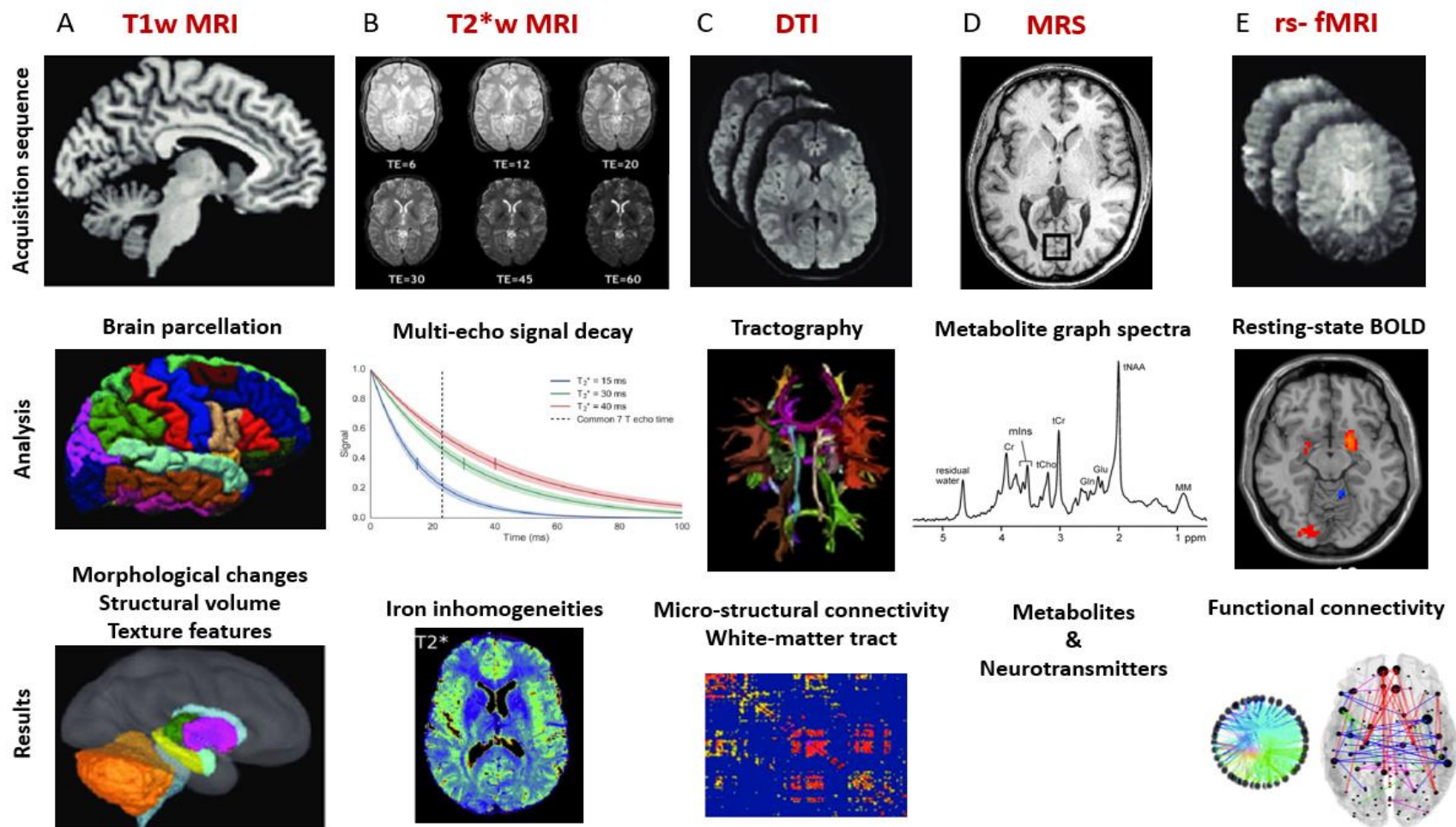


Figure 9. Overview of different brain MRI modalities, and data analysis techniques *detailed in 3.1.2* (Images from Gandy et al. 2021; Péran et al. 2007; Gracien et al. 2020; Öz et al. 2014; Hollander et al. 2017).

3.2 POST-PROCESSING AND ANALYSIS OF MR IMAGING

3.2.1 Structural and quantitative MRI

A few pre-processing steps are common to most MRI sequence analyses, including:

- Image Registration: Image registration involves aligning and comparing two or more images to determine their spatial correspondence. This technique is used to fuse multiple imaging modalities or align a patient's MRI scan with a template brain image for group analysis. Various registration algorithms exist, including rigid, affine, and non-linear registration methods.
- Image Segmentation: Segmentation involves dividing an image into different regions or segments based on its intensity, texture, or shape. This technique is used to separate different tissues or structures of interest in the brain, such as grey matter, white matter, and cerebrospinal fluid.

Atlases are used to aid in MRI image segmentation, by providing a reference or template for the identification and extraction of structures of interest. Atlases can be generated from individual images or from a population of images, and can be used to define regions of interest based on their location, shape, and intensity.

There are several different types of atlases used in MRI image segmentation, including:

- Anatomical atlases, generated from a population of MRI images and are used to define the location and boundaries of anatomical structures.
- Functional atlases, generated from functional MRI (fMRI) data and are used to identify regions of the brain that are activated during specific tasks or functions.

- Probabilistic atlases, generated from a population of MRI images and are used to define the probability of a voxel (3D pixel) belonging to a particular structure (Mazziotta et al. 2001). Probabilistic atlases can be used to segment structures that have variable boundaries or that are difficult to define using traditional methods.
- Statistical atlases, generated from a population of MRI images and are used to define regions of interest based on their statistical properties (Fenchel et al. 2008). Statistical atlases can be used to segment structures that have subtle or diffuse abnormalities, such as white matter lesions or cortical atrophy.

The use of atlases in MRI image segmentation has been shown to improve the accuracy and reproducibility of segmentation results, particularly for structures that are difficult to define using traditional segmentation methods.

3.2.1.1 VBM

Voxel-based morphometry (VBM) is a computational technique for analysing MRI data, allowing the investigation of differences in brain anatomy between groups of individuals. VBM works by segmenting the brain into small, three-dimensional units called voxels and comparing the density or volume of grey and white matter in each voxel between groups (Ashburner et al. 2000).

VBM is commonly used to study the brain in a variety of clinical and research settings, including studies of neurological and psychiatric disorders, ageing, and brain development. It has been used to identify structural changes in the brains of individuals with conditions such as Alzheimer's disease, multiple sclerosis, and schizophrenia, as well as to investigate the effects of environmental factors such as stress and drug abuse on brain structure.

The VBM method was first introduced by John Ashburner and Karl Friston in 2000. Since then, there have been many variations and improvements to the technique, including the use of different types of MRI scans (such as T1-weighted, T2-weighted, and diffusion-weighted scans),

different algorithms for segmenting the brain, and different statistical methods for analysing the data (Good et al. 2001; Mechelli et al. 2005).

One commonly used software package for VBM analysis is SPM (Statistical Parametric Mapping), which is available for free download from the Wellcome Trust Centre for Neuroimaging at University College London. Other software packages for VBM analysis include FSL (FMRIB Software Library) and CAT (Computational Anatomy Toolbox) (Gazer et al. 2022).

3.2.1.2 ROI

Region of Interest (ROI) analysis is a method used to analyse brain MRI data by focusing on specific regions of the brain that are hypothesised to be involved in a particular cognitive or clinical function. In ROI analysis, the researcher manually selects a region or multiple regions of interest on the MRI image and extracts quantitative measures such as grey matter volume, cortical thickness, or functional activity from the selected region.

ROI analysis has been widely used in clinical and cognitive neuroscience research, as it allows for the examination of specific regions or networks of the brain that are thought to be involved in a particular function or disorder. The method can be applied to structural, functional, and diffusion MRI data.

One of the advantages of ROI analysis is that it can be used to test specific hypotheses without the need for correcting for multiple comparisons across the entire brain. However, it is important to select the ROIs based on *a priori* hypotheses or anatomical/functional landmarks, to avoid data-driven biases.

3.2.1.3 Volumetry

Volumetry involves measuring the total volume of grey matter, white matter, and cerebrospinal fluid in specific regions of the brain. This method provides information about the size of different brain structures and can be used to study changes in brain volume over time (Giorgio & De Stefano 2012).

3.2.1.4 *Cortical thickness*

Cortical thickness analysis involves measuring the distance between the grey matter and white matter surfaces of the cortex. This method allows for the measurement of changes in the thickness of the cortex in different regions of the brain (Dahnke et al. 2013).

3.2.2 Functional MRI

Functional magnetic resonance imaging (fMRI) data can be analysed using different methods, including:

- **General Linear Model (GLM)** – which is the most common method used in fMRI analysis. It involves modelling the relationship between the fMRI signal and experimental variables using statistical models. GLM-based analysis allows for the identification of brain regions that show significant changes in response to a given task or stimulus.
- **Independent Component Analysis (ICA)**, which involves decomposing the fMRI data into a set of spatially independent components, which can then be used to identify different brain networks involved in the task or stimulus.
- **Seed-based correlation analysis**, which involves selecting a seed region of interest (ROI) and correlating its time series with the time series of other brain regions. This allows for the identification of brain regions that show functional connectivity with the seed ROI.
- **Network analysis**, which involves using graph theory to model the functional connectivity between different brain regions, hence allowing the identification of brain networks involved in tasks or impairments.

3.2.3 Radiomics and texture features

Machine learning techniques are used to analyse large datasets and make predictions based on patterns in the data. In MRI analysis, machine learning algorithms can be used for image segmentation, classification of brain regions, prediction of disease progression, and identification of biomarkers (Davatzikos et al. 2019).

Radiomics is a field of medical imaging that involves the extraction and analysis of large amounts of quantitative features from radiographic images, with the aim of providing improved diagnostic and prognostic information for a variety of diseases (Aerts et al. 2014; Gillies et al. 2016). Radiomics uses machine learning and statistical methods to identify patterns and associations between image features and clinical outcomes, and can be applied to a range of imaging modalities, including magnetic resonance imaging (MRI), computed tomography (CT), and positron emission tomography (PET).

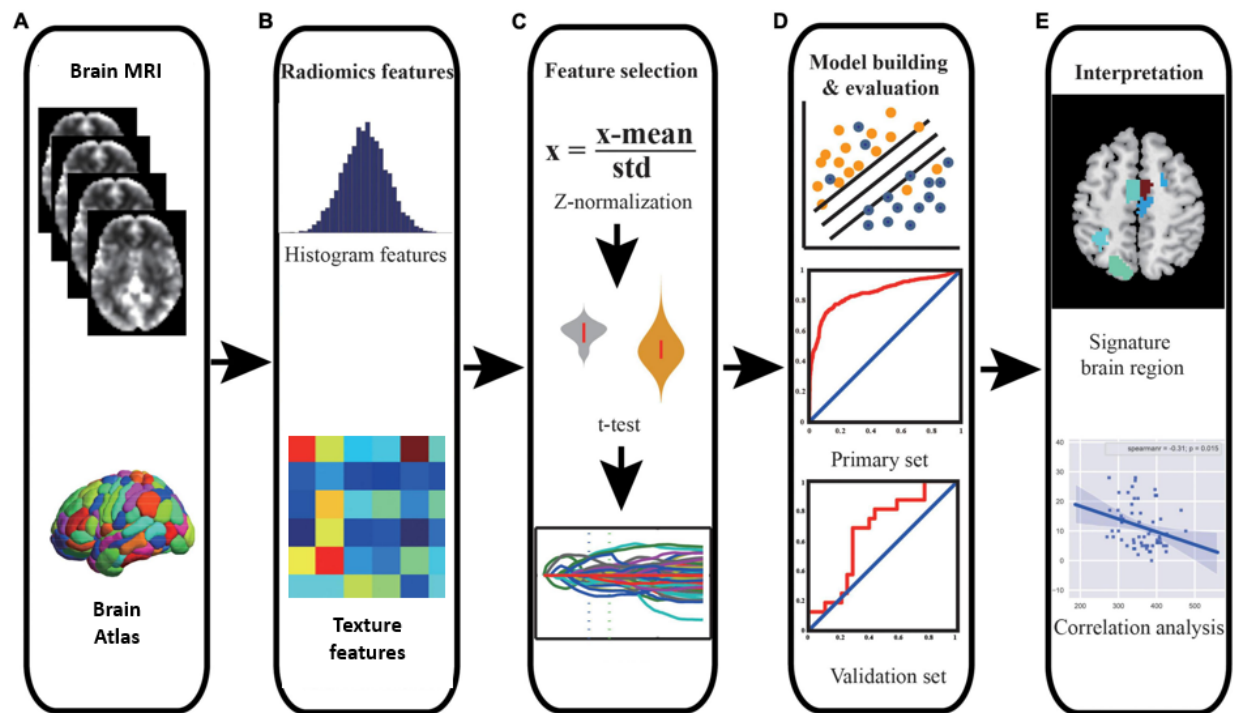


Figure 10. Overview of the methodological processes in Radiomics' analysis. (adapted from Shi et al. 2022).

Amongst the quantitative data extracted when using the comprehensive Radiomics' approach are texture features. They are a set of quantitative metrics that describe the spatial distribution of voxel intensities within an image. In brain imaging, texture features can be used to characterise the heterogeneity and complexity of brain tissues. These features can be extracted from various imaging modalities, including MRI and CT, and have been shown to provide useful information for diagnosis, prognosis, and treatment planning in various neurological disorders such as brain tumours and dementia.

Texture features can be categorised into first-order and second-order statistics. First-order texture features include measures of intensity histograms, such as mean, median, mode, variance, skewness, and kurtosis. These features describe the distribution of pixel/voxel intensities within an image or region of interest (ROI). Skewness measures the asymmetry of the intensity distribution, while kurtosis describes the degree of peakedness or flatness of the distribution.

Second-order texture features, on the other hand, describe the spatial relationships between pixels/voxels within an image. These features are derived from the grey-level co-occurrence matrix (GLCM), grey-level run length matrix (GLRLM), and grey-level size zone matrix (GLSZM). GLCM measures the frequency of co-occurring pairs of pixel/voxel intensities at specific distances and directions, while GLRLM and GLSZM measure the length and size of connected regions with similar intensities.

In brain imaging, texture analysis has been used to investigate various neurological disorders. For example, studies have shown that texture features derived from MRI can differentiate between healthy controls and patients with Alzheimer's disease or mild cognitive impairment (MCI) with high accuracy (Wu et al. 2018; Liu et al. 2020). Similarly, texture features derived from MRI have been used to differentiate between different subtypes of multiple sclerosis (Kuchling et al. 2018). Texture analysis has also been applied to fMRI data to investigate changes in functional connectivity in patients with schizophrenia (Sprooten et al. 2013).

3.3 MRI IN PARKINSON'S DISEASE: FROM CLINICAL ROUTINE TO RESEARCH AND PRECLINICAL EXPLORATION

3.3.1 Structural changes in MRI in PD

Morphological exploration of PD brain tissue is done using T1-weighted sequences. These images have yielded very promising results in distinguishing a PD profile and measuring its evolution (Heim et al. 2017).

Voxel-based morphometry (VBM) studies have identified reduced grey matter (GM) in the frontal lobe, right hippocampus, left anterior cingulate and superior temporal gyri as well as the limbic lobe, in PD patients compared to controls (Summerfield et al. 2005; Gao et al. 2017). A reduction of striatal volumes was also reported in PD patients (Pitcher et al. 2012). Corticometry showed cortical thinning in the orbitofrontal, prefrontal, and occipito-parietal cortex in PD subjects (Tinaz et al. 2011; Jubault et al. 2011; Chaudhary et al. 2021).

Interestingly, the evaluation of SN volume had differing results between studies, with some reporting an increase in SN volume using a 3D 7T MRI, others a decrease, or no change (Kwon et al. 2012; Minati et al. 2007; Péran et al. 2010).

In animal models, structural changes have not been widely explored. One of the rare studies using VBM in animal models showed grey matter atrophy in a unilateral 6OHDA rat model, consistent with what is observed clinically (Westphal et al. 2016).

3.3.2 Quantitative MRI analysis in PD

As mentioned earlier, these techniques are based on multi-echo T2* weighted acquisitions, which allow the production of R2* and QSM quantitative maps. The latter are related to ferritin-induced field inhomogeneities in the brain tissue. Increased R2* relaxation rates of SN were

observed in PD patients and this was correlated with the worsening of their motor symptoms (Péran et al. 2010; Ulla et al. 2013; Wieler et al. 2016).

A study comparing the diagnostic accuracy of QSM and R2* analysis showed a higher performance of QSM in discriminating between control subjects and patients with PD, the latter having significantly higher values of QSM and R2* in the Substantia Nigra (Murakami et al. 2015). A quantitative MRI analysis showed increased QSM in the SN of an MPTP mouse model, indicating the accumulation of iron in the substantia nigra (Guan & Feng 2018).

3.3.3 Diffusion Tensor Imaging (DTI) in PD

As mentioned earlier, DTI allows the quantification of brain microstructural integrity using different parameters such as Fractional Anisotropy (FA) which corresponds to the degree and the direction of the diffusion, and Mean Diffusivity (MD), which corresponds to the overall displacement of water molecules within brain tissue. The degeneration of white matter tracts along which water moves, increases MD and decreases FA. Studies have shown a reduced FA in the SN of PD patients (Cochrane et al. 2013; Vaillancourt et al. 2009), as well as an increase of MD in olfactory tracts (Scherfler et al. 2006; Rolheiser et al. 2011).

The use of DTI in the 6OHDA rat model has shown a decrease in FA values and increase in MD values in the substantia nigra, similar to results observed in PD patients (Monot et al. 2017; Soria et al. 2011; Van camp et al. 2009).

3.3.4 Magnetic Resonance Spectroscopy (MRS) in PD

In PD, reduced N-acetyl aspartate (NAA), which is an indicator of neuronal health and integrity, was observed in the putamen, the globus pallidus, the temporoparietal and the posterior cingulate cortex (Guan et al. 2017; Cao et al. 2017). Other metabolites were evaluated in PD context, such as choline, which is a marker of membrane turnover, osmoregulation and inflammation; myo-inositol, which is a marker of gliosis, demyelination and osmoregulation; and

Creatine (Cr), which is stable enough in healthy brains to use as reference spectrum, resulting in different reported levels and some inconsistencies (Firbank et al. 2002; Gröger et al. 2013).

Other studies using MRS techniques showed a decrease in NAA in the striatum and cortex of 6OHDA models, also similar to PD patients (Coune et al. 2013; Houne et al. 2010).

3.3.5 Texture features in PD

In our laboratory, the application of radiomics has shown that texture features in the hippocampus, amygdala and thalamus, correlated with slight cognitive changes in PD patients with different cognitive phenotypes (Betrouni et al. 2020). Texture features measured in the Substantia Nigra, the Putamen, the Caudate nucleus and the thalamus, were significantly associated with clinical scores for motor handicap as well (Betrouni et al. 2021). *(More details on the use of Texture feature-based analysis in Results Chapter 3.1 Background)*

3.3.6 Functional connectivity in PD

The majority of functional imaging studies in PD patients and animal models were done in resting state (Prodoehl et al. 2014).

Studies reported increased connectivity between the putamen and the supplementary motor area (SMA) in early-stage PD patients, which was interpreted as a compensatory mechanism for impaired motor control (Helmich et al. 2010). Others showed general reduced cortical-subcortical sensorimotor connectivity (Sharman et al. 2013). On the other hand, some studies focused on the cerebellum activity reported an increased cerebellar connectivity in PD patients with mild cognitive impairment and with dyskinesia (Cerasa et al. 2016; Tuovinen et al. 2018).

In animal models, functional connectivity (FC) changes have been explored in the nigrostriatal pathway, with decreased FC found in the interhemispheric striatum and ipsilateral cortices of 6-OHDA rats injected in the medial forebrain bundle (MFB) (Monnot et al. 2017; Westphal et al.

2017). Additionally, decreased FC was reported between the ipsilateral primary motor cortex and contralateral thalamus in the intrastriatal 6-OHDA model (Perlberg et al. 2018), and decreased FC was observed in corticocortical and striatocortical connections of 6-OHDA-injected rats (Zhurakovskaya et al. 2019). The interpretation of the decreased FC was generally related to direct lesioning effects. Conversely, increased FC was found between the striatum and the subthalamic nucleus and in the thalamus of both hemispheres in 6-OHDA rats injected in the MFB or striatum (Monnot et al. 2017; Westphal et al. 2017). Moreover, increased FC was observed between the ipsilateral striatum and the globus pallidus of 6-OHDA rats injected in the striatum (Perlberg et al. 2018). These findings suggest compensatory mechanisms and reorganisation, which have also been observed in PD patients. In a presymptomatic PINK1 knockout rat model, changes in rs-fMRI connectivity were observed in the basal ganglia and other regions, such as the amygdala, cortex, septum, and pons (Cai et al. 2019). They also showed decreased connectivity between the thalamus and striatum and increased connectivity within the cerebellum and hippocampus in PINK1 rats, similar to the cerebellar hyperconnectivity observed in PD patients.

3.3.7 New MRI sequences for PD

Recent studies have shown that neuromelanin, which is a dark pigment produced in dopaminergic neurons of the SN can be detected with high contrast using MRI (Sasaki et al. 2006). Indeed, Magnetization Transfer (MT) MRI has been shown to facilitate locus coeruleus (LC) and SN visualisation, and the observed contrast is assumed to be related to neuromelanin accumulation (Ogisu et al. 2013; Langley et al. 2015). They showed that the signal intensity of these cells was reduced in PD patients compared to controls (Sulzer et al. 2018). Other studies have shown that MRI-measured neuromelanin levels in the substantia nigra, correlate with disease severity and motor symptoms in PD patients (Schwarz et al. 2011). These findings suggest that neuromelanin imaging could be a useful tool for early diagnosis and monitoring of disease progression in PD (Priovoulous et al. 2020).

However, while neuromelanin is present in the human SNpc, it is absent in rodents' SNpc (Marsden, 1961; Barden and Levine, 1983), therefore preventing any investigation in those

animal models. The recent development of a rat model overexpressing human tyrosinase, has allowed the production of neuromelanin in the rats' nigral dopamine neurons (Carballo-Carbajal et al. 2019), which could open up the development of preclinical neuromelanin imaging strategies (Petiet et al. 2021).

Today, conventional MRI remains of little use in clinical practice in the context of PD, except for its differential diagnosis. However, the application and improvement of several MRI sequences in PD research, coupled with new analysis methods, have yielded interesting results. Indeed, by employing a multi-modal MR imaging approach that evaluates various facets of PD's pathophysiology, it could be possible to more comprehensively describe the disease's phenotypes while also offering a potential diagnostic and prognostic avenue to monitor its advancement.

Interestingly, most of these sequences have been applied preclinically on animal models of the disease, with similar results to the clinical application for the most part (Table 1). This indicates that the exploration of MRI in animal models, with the added value of easy histological analysis, has a great translational potential, to understand the significance of the images on a biological tissue level.

Method	Techniques	Information	Changes in PD	Changes in animal models of PD
Structural	T1w, T2w, IR, MT	Morphometry	SN: variable volume changes Cortex : mild reduction in volume thickness	Reduction of grey matter (Westphal et al. 2016)
Relaxometry	T2/T2* measurements	Brain iron	Reduced T2*; Increased R2*	Increased R2* (Olmedo et al. 2017; Virel et al. 2014; Cong et al. 2016)
Susceptibility-weighted	Phase images	Brain iron	Increased susceptibility to iron load	Increased QSM (Guan and Feng, 2018)
Neuromelanin	Spin echo T1-w	Presence of melanin-containing cells (mainly in SN)	Reduced signal intensity	Reduced in intensity in new model of Tyrosinase overexpression (Carballo-carbajal et al. 2019)
Diffusion	Diffusion Tensor Imaging (DTI)	Diffusion of water in biological tissues	Reduced Fractional anisotropy (FA), increased mean diffusivity (MD)	Reduced FA, increased MD (Monnot et al. 2017; Soria et al. 2011)
Tractography	DTI	Fiber tract-specific reconstruction	Reduced probability of connections	Abnormal fiber projections to the STN (Kim et al. 2020)
Functional	rs-fMRI (BOLD)	Functional connectivity (FC) within brain networks	Reduced FC in sensorimotor cortex Increased FC in associative cortex	Decreased FC cortices and striatum; Increased FC in sensorimotor cortex (Monnot et al. 2017; Perlberg et al. 2018; Westphal et al. 2017; Zhurakovskaya et al. 2019)
MR spectroscopy	1H MRS	NAA, Chi, Ins, GABA, Glx, GSH, lactate	Trend for metabolite reduction (mainly NAA)	Increased GABA (Coune et al. 2013), decreased NAA (Hou et al. 2010)

Table 1. MRI in clinical versus preclinical PD (Adapted from Pyatigorskaya et al. 2014). Similarities are observed in the results obtained from MRI sequences applied in humans and animals, notably for Relaxometry, QSM and DTI sequences, making MRI an adequate translational tool.

RATIONAL

The state of the art in Parkinson's disease (PD) research presented in the previous section has highlighted the limitations of the diagnosis and management of this disease. Currently, there is no treatment that can prevent or slow down its the progression. Although multiple attempts at neuroprotection have shown promise in preclinical studies, they have failed in patients in a clinical context. As hypothesised earlier, this could be due to the late diagnosis of PD, based on the late onset of motor symptoms. Therefore, earlier detection of PD is a major challenge for the development of new treatments, especially curative ones.

Furthermore, although patients may present with non-motor symptoms during the early stages of the disease, these symptoms are very different from one patient to the other, demonstrating the very heterogeneous aspect of the disease. These non-motor symptoms are also not always exclusive to PD, as they can also be found in other neurological conditions such as Huntington's disease, Alzheimer's disease, and depression, making it difficult to establish a specific non-motor phenotype associated with PD for an early diagnosis.

Structural and functional alterations in brain MRIs have been identified in PD patients, sometimes in the early phases of the disease. However, we still don't always know how to translate these imaging changes into a specific biological signature, and most importantly, how to identify and characterise them as specific imaging biomarkers for the early diagnosis and monitoring of the disease.

Therefore, the aim of my PhD project was to explore clinically relevant MRI sequences in animal models of PD, and correlate them with the behavioural phenotype and the histological changes observed in the animals' brain (figure).

This three-faceted project relies mainly on the explorations of improved methodologies to characterise the histological signature of fine imaging markers in different regions of the brain, without preconceptions or targeting a specific brain region. The challenge was to choose models that are not acute or severe, and could mimic the early stages of the disease. Additionally, the less severe the model is, especially on the motor front, the higher the chances it will exhibit examinable early non-motor symptoms.

Indeed, we proposed as a first step to examine the adeno-associated virus (AAV)-induced alpha-synuclein overexpression rat model, which as described in the introduction, recapitulates the major hallmarks of PD including the progressive loss of dopaminergic neurons and the accumulation of alpha-synuclein in the brain. This model has never been characterised on an MR imaging level, and its behavioural depiction is also lacking, especially on the cognitive and neuropsychiatric level. Therefore, the two major parts of this work will be first the behavioural characterization then the imaging characterization of this model, using histopathology both to correlate them and describe the underlying tissular changes in the brain. Additionally, a last part will describe the preliminary results obtained on complimentary animal models in order to prove the translational validity of the imaging markers.

Indeed, the ultimate objective is to use the obtained 3-facet characterization to deepen our understanding of the pathophysiology of PD and identify potential imaging biomarkers.

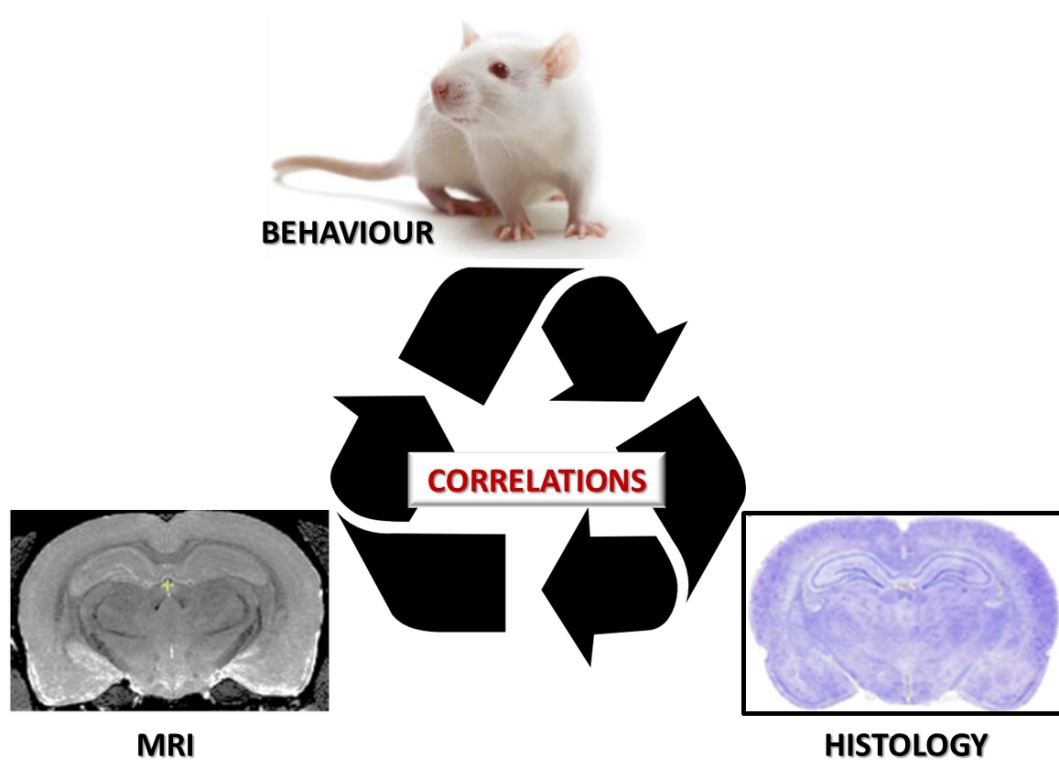


Figure 11. 3-facet methodology design and principal objective of this thesis project.

PART TWO

MATERIAL AND METHOD

1 ANIMAL MODELLING AND EXPERIMENTAL DESIGN

1.1 ANIMAL EXPERIMENTATION

All animal experiments were carried out in accordance with the national guidelines of the French Act Rural Code R.214-87 to R.214-126, and complied with the international Standards for Humane Care and Use of Laboratory Animals, as described by the Office of Laboratory Animal Welfare (OLAW – n°A5826-01) and the European Union (EU Directive 2010-63/EEC). They also received approval from the local ethical committee of Lille, Nord-Pas de-Calais (CEEA n°33933), and the French Ministry of Education and Research (APAFIS #33933-2021102916444252). All necessary measurements were taken to minimise animal suffering, and animal care was supervised by veterinarians and animal technicians skilled in rodent healthcare and housing.

All animals used in this PhD work were adult male Sprague Dawley (for AAV alpha-synuclein model) or Wistar (for toxin-based models) rats (JANVIER LABS; Le Genest Saint Isle, France), 5 to 6 weeks old at the time of their arrival, weighing approximately 180-200g, and acclimatised one week before the start of any experimental procedure. They were housed in a temperature-controlled room ($22\pm1^{\circ}\text{C}$, humidity 50%), paired in standard cages maintained on a 12-h light/12-h dark cycle, with the necessary enrichments. Access to food and water was provided *ad libitum* until experimental requirements. Daily care and weekly body weight evaluation accounted for the animals' well-being.

1.1.1 Stereotactic surgery – model creation

1.1.1.1 AAV *alpha-synuclein* model

Animals were randomly assigned to either the alpha synuclein (ASYN) group or control (CTRL) group.

Sprague Dawley male rats received two bilateral intranigral injections (Anteroposterior: -4.9 and -5.4; Mediolateral: ± 2.1 ; Dorsoventral: -7.8, in mm from bregma) (Figure 12A) of a recombinant AAV, encoding the human p.A53T alpha-synuclein protein or GFP degron protein for their control counterparts.

The Adeno-Associated Viral vector production was performed at the transcriptome core facility (Neurocentre Magendie, INSERM U862, Bordeaux, France). Recombinant AAV2/9-p.A53T-human- α -syn and AAV2/9-GFP was produced with the following titration:

- AAV9 CMVie/SynP/GFPdegren/WPRE (2×10^{13} gcp/ml)
- AAV9 CMVie/SynP/synA53T/WPRE (7×10^{12} gcp/ml)

The use AAV9 vector construct, as well as the Synapsin1 (SynP) promotor, which is neuron specific, enhanced by the CytoMegalovirus immediate early enhancer (CMVie) helped optimize the transduction efficiency.

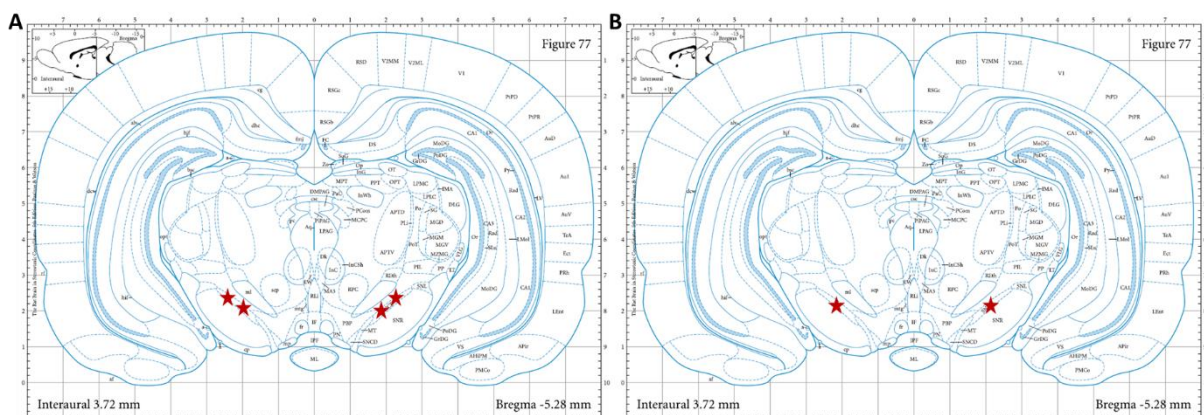


Figure 12. Coronal section of Rat brain atlas depicting the stereotactic coordinates of nigral injections (red stars) for the AAV alpha-synuclein model (A) and toxin-based models (B).

1.1.1.2 *Toxin-based models*

For these experiments, animals were randomly allocated to either the 6OHDA, MPTP or CTRL groups.

Wistar male rats received bilateral intranigral injections (Anteroposterior: -5.2; Mediolateral: \pm 2.2; Dorsoventral: -7.8, in mm from bregma) (Figure 12B) of:

- 6-hydroxydopamine (H4381, Sigma): 6 μ g/2 μ l in 0.2% ascorbic acid, for the 6OHDA group. A desipramine solution (25mg/Kg, D3900, Sigma) was injected intraperitoneally 30minutes prior to 6OHDA injection, to protect noradrenergic neurons.
- 1-methyl-4-phenyl-1,2,3,6-tetrahydropyridine (M0896, Sigma): 200 μ g/2 μ l, for the MPTP group.
- 2 μ l per injection of saline for the CTRL group.

1.1.1.3 *Detailed surgical procedures*

Surgical interventions were performed under full general anaesthesia with an intraperitoneal (i.p.) injection of a mixture of ketamine (100 mg/kg) and xylazine (5 mg/kg), for AAV-injected rats, and under a mix of oxygen/isoflurane (2%), for neurotoxin-injected rats.

Anaesthetized rats were placed in a stereotactic frame above a heating pad maintaining body temperature, and injected using 34-gauge blunt-tip canula linked to a 10 μ l Hamilton syringe (Hamilton; Reno, USA). After each injection the needle was kept in place for an additional 5 minutes and then slowly withdrawn. Both an antiseptic, betadine, and an analgesic cream, lidocaine, were administered prior to skin incision and post-sutures.

After surgery, rodents were kept in recovery at least a week (2 weeks in a level 2 biosafety animal facility for the AAV animals, to allow complete washout of the AAVs), before being transferred to a regular animal facility to conduct longitudinal behavioural and imaging testing.

1.1.2 Experimental design

1.1.2.1 AAV *alpha-synuclein* model

An 18-week longitudinal study was designed (figure), in which we conducted extensive behavioural analyses, evaluating motor, cognitive and emotional skills. Three MRI sessions were scheduled at 2, 10 and 18-weeks post-injection, in order to monitor visible changes in imaging. Finally, brains were retrieved to do a wide histological assessment of tissue lesions, at the end of the study (Figure 13A).

Three cohorts were evaluated, each consisting of a total of n=23 rats, divided to n=14 ASYN and n=9 CTRL. This number was decided upon, based on the limited housing and behavioural apparatus in our facility (mainly the Touchscreen apparatus).

-COGSYN 2020: January till June 2020, the behavioural and imaging evaluations were interrupted on March 17th, due to Covid19 pandemic quarantine, and only the histological evaluations of this cohort will be discussed in the following manuscript.

-COGSYN 2021: January till June 2021.

-COGSYN 2022: February till July 2022.

Tables in the following behavioural and imaging methodologies will detail the different behavioural tests and imaging sequences performed on each cohort.

1.1.2.2 Toxin-based models

Due to the acute nature of neurotoxic models and their propensity to compensate after lesion and recuperate (Deumens et al. 2002), we decided to reduce their evaluation to 8 weeks.

A study (**COGPARK-TOX2022**) of $n=12$ 6-OHDA, $n=14$ MPTP, and $n=10$ CTRL rats was performed with several behavioural analyses, evaluating motor, cognitive and emotional skills, as well as 2 MRI evaluations at 4 and 8-weeks post-injection (Figure 13B).

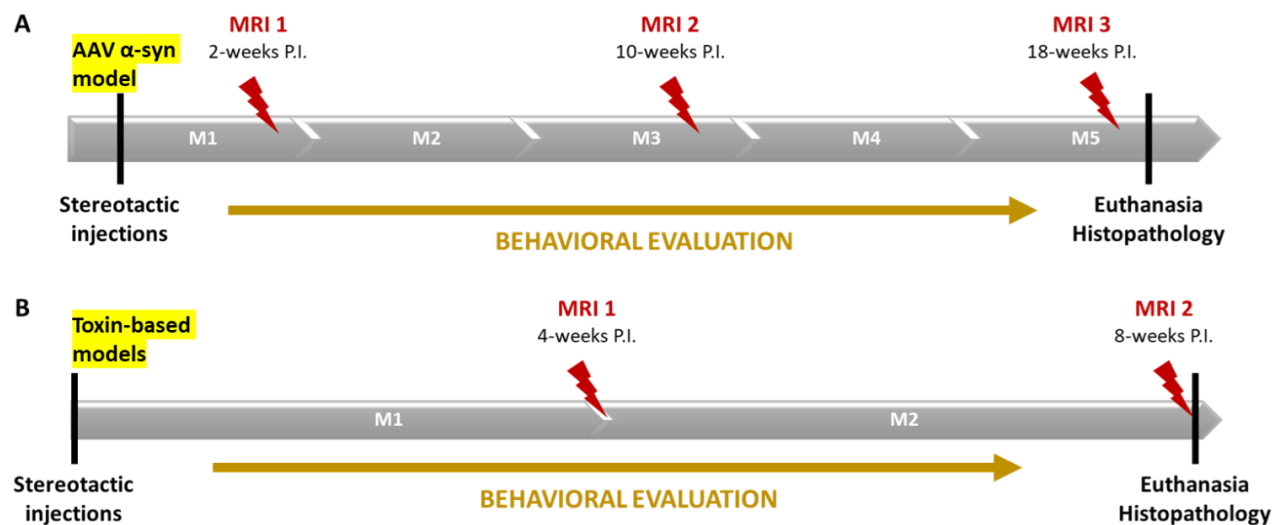


Figure 13. Experimental design for the AAV α -synuclein model (A) (18 weeks) and toxin-based models (B) (8 weeks).

2 BEHAVIOURAL EVALUATION

The cardinal symptoms of PD include akinesia, rigidity, and tremor which are the basis of behavioural testing in animal models of PD. Indeed, the validation of the most prominent PD models was based on their ability to recapitulate the features associated with motor impairments, using general locomotor activity tests, as well as sensorimotor, coordination and gait tests (Taylor et al. 2010).

Here, we have chosen to evaluate spontaneous locomotor activity using actimetry and openfield tests, while the stepping test was reserved for the evaluation of sensori-motricity and akinesia,

because it was shown to have a higher sensitivity compared to other sensorimotor tests, and therefore has the potential to identify mild motor deficits (Boix et al. 2015).

On the other hand, our aim is to use moderate and progressive models mimicking the early stages of the disease, before the onset of severe motor symptoms. So, the following work has concentrated its efforts on the evaluation of non-motor symptoms. Several cognitive functions are impaired in PD such as attention (Ballard et al. 2002), visual discrimination and procedural learning (Dujardin et al. 2003), which we will evaluate using the Touchscreen attentional and visual discrimination tasks. Visuospatial learning and memory (Levin 1990), as well as cognitive flexibility (Kourtidou et al. 2015), are also known to be affected in PD. We will use the Morris water maze and its reversal paradigm to assess it. As for the deficits in working memory observed in PD context (Kehagia et al. 2010), we will use the spontaneous alternation test to evaluate it. We also proposed to examine anxiety (Prediger et al. 2012) in our animals using the elevated plus maze, as well as apathy, anhedonia and depressive-like behaviour using sucrose test (Madiha & Haider 2019). Several well-being parameters are taken into account when performing these tests, and analysing the results, such as the weight of the animals and their level of performance and well-being (Faivre et al. 2018).

All behavioural tests were performed at the functional exploration platform **LIIFE** (*Lille In vivo Imaging and Functional Exploration - UMS2014-US41*).

2.1 STEPPING TEST - SENSORI-MOTRICITY, FORELIMB AKINESIA

Sensori-motricity and forelimb akinesia were assessed using the stepping test (Olsson et al. 1995; Laloux et al. 2017). The animals were gently held, while blocking left, then right forelimb (Figure 14A), and conducted over a 90 cm distance to allow forehand followed by backhand step count. Left and right limb performances were evaluated daily over 3 consecutive days. The number of left/right forehand steps was averaged over the three sessions per day, then over the three days. This test was performed monthly (Month 1, 2, 3 and 4) to assess the evolution of forelimb akinesia.

2.2 ACTIMETRY - SPONTANEOUS LOCOMOTRICITY

Spontaneous motor activity of rats was recorded over a 10- min period in an actimeter equipped with Actitrack analytical software (Panlab, Barcelona, Spain). The transparent Plexiglas open field was equipped with two frames of infrared beams for measuring horizontal motor activity (distance travelled and speed), as well as vertical motor activity (rearing) (Figure 14B). This test was also performed monthly (month 1, 2, 3 and 4).

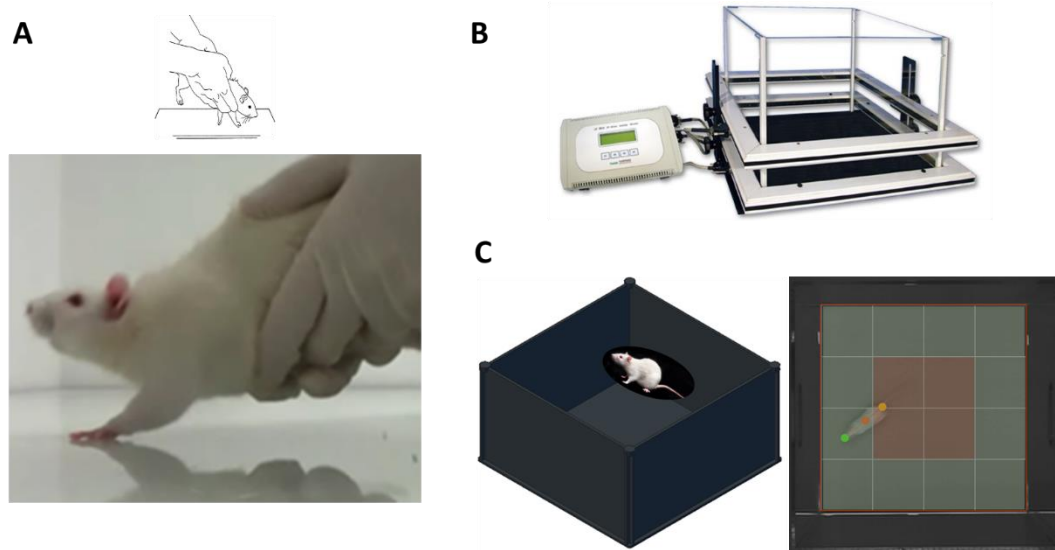


Figure 14. Illustration of the different tests used to evaluate motor activity in an animal model. A. Stepping test shows the blocking of one forelimb, to evaluate sensorimotoricity and forelimb akinesia. B. Actimeter with laser beams to evaluate both horizontal and vertical motor activity. C. Openfield arena used to evaluate general locomotion. Tracking the animal in the arena also helps assessing its anxiety level i.e. an animal staying in the periphery (green) is considered as displaying anxious-like behaviour.

2.3 OPENFIELD (OF) - SPONTANEOUS LOCOMOTRICITY & ANXIETY

The Openfield test was conducted in a 100cmx100cm square open arena, with 30 lux luminosity. The animals were gently placed in one corner of the open-field and were allowed to freely explore the area for 10 min. Average speed and distance travelled were measured using Ethovision recordings (Noldus et al. 2001). Time spent in the periphery versus the anxious -inducing center

of the arena was compared for anxious-like behaviour evaluation (Figure 14C). This test was performed monthly (month 1, 2, 3 and 4).

2.4 ELEVATED PLUS MAZE (EPM) - ANXIETY

To more specifically study anxiety in our rodent model, we used the elevated plus maze test which consists of two open arms and two closed arms of the same dimensions (50 cm long and 10 cm wide), arranged perpendicularly to form a plus shape. The closed arms have 40cm cm high walls. The entire apparatus was elevated 70cm above the floor. Illumination in the open arms didn't exceed 5 lux.

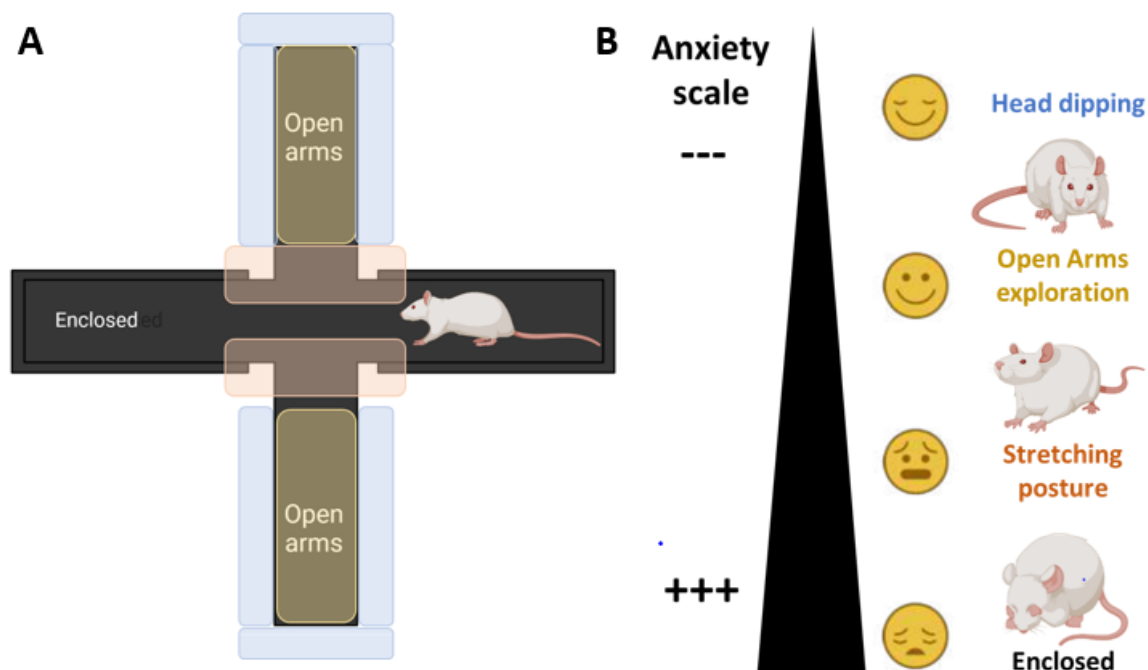


Figure 15. The Elevated Plus Maze test for Anxiety evaluation. A. Depiction of the Elevated Plus Maze Arena with open (yellow) and closed arms. B. Evaluation criteria based on detailed ethological parameters such as head-dipping and stretching postures. These were assessed to determine the subtleties of anxious-like behaviour in rats.

The animals were placed in the central area of the EPM, facing a closed arm, and allowed to explore the apparatus for 10 min. Before the next animal was tested, the maze was wiped clean

with water. Standard testing measures were recorded: the number of entries into and time spent on each of the closed and open arms (OA), as well as ethological parameters such as stretching and head dipping (Figure 15). This test was performed at month 1- and 3- post-injection.

2.5 Y-MAZE SPONTANEOUS ALTERNATION TEST - WORKING MEMORY

The y-maze consisted of three arms (50 cm x 15 cm) surrounded with walls (35 cm), with 30 lux illumination in the centre and 20 lux in the arms. The rat was placed at the end of one arm facing the back wall and recorded for 8 minutes during free exploration of all three arms. An arm entry was scored if all four paws of the rat entered the arm. Visiting all three arms consecutively was counted as one correct alternation (Figure 16). The maximum possible number of correct alternations was the total number of arm entries minus two. The alternation ratio was calculated as the number of correct alternations made normalised to the maximum number of possible alternations. This test was performed at month 1- and 3- post-injection.

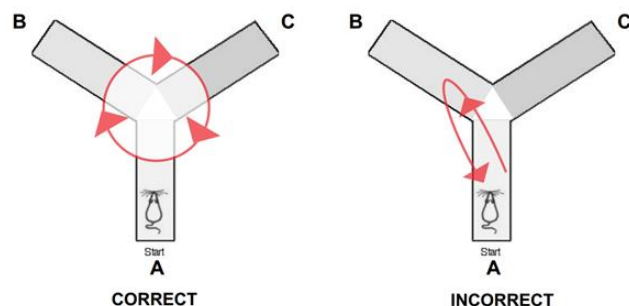


Figure 16. The spontaneous alternation test for working memory evaluation. Performed in a Y-maze, this test explores the order of explorations of each arm of the maze and quantifies the correct alternations (ABC, BCA, CAB).

2.6 MORRIS WATER MAZE (MWM) – VISUOSPATIAL LEARNING & MEMORY AND MENTAL FLEXIBILITY

The water maze consisted of a circular tank (diameter 180cm). It was filled with tepid water (23 °C) that was made opaque by the addition of an opacifier. An escape platform (height 40cm) was located 1 cm below the water surface near the center of one of the four quadrants of the maze.

The maze was surrounded by patterns affixed to provide a configuration of spatial cues. Data was analysed by a video tracking system and computer software (Ethovision; NOLDUS, Wageningen).

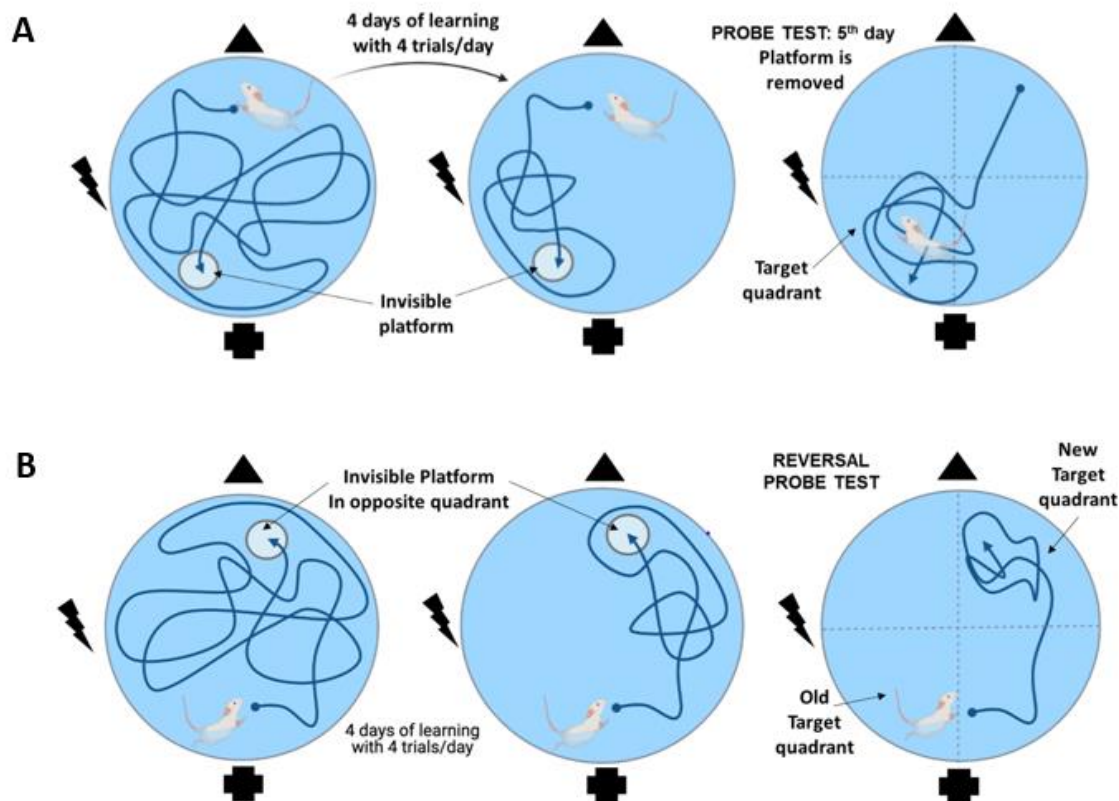


Figure 17. The Morris Water Maze test for Visuospatial learning and memory. A. The initial learning phase and probe test. B. The reversal learning phase and reversal probe test, for testing cognitive flexibility.

Rats received 4 trials per day for 4 consecutive days (Figure 17A). On each training trial, an animal was released in the maze from one of four equally spaced starting positions around the perimeter of the pool. The starting position varied from trial to trial to precluded the effective use of a response strategy (e.g., always turning left from the start location to locate the escape platform). If an animal did not locate the escape platform within 90s on any trial, the experimenter led the animal on the platform, where it remained for 30s. On the fifth day, a probe trial was administered where the platform was removed and the animal was left to swim around the maze for 90s (Figure 17A). For analysis of spatial learning, measures of path length and latency to

escape were analysed using average performance of 4 trials a day for 4 days. During probe trial data, the time spent in the target quadrant versus the other quadrants is calculated.

The reversal MWM trial was conducted the following week after the original test, with a 2-day weekend allowing the animal to rest. The platform was positioned in the opposite quadrant of the original test (Figure 17B). A similar 4-day training with the platform was performed. And on the fifth day, the platform was removed, and a reversal probe trial was conducted. This test was performed at month 2- and 4- post-injection.

2.7 TOUCHSCREEN TESTS

Several tasks can be applied to the use of touchscreen tests, with each task allowing the evaluation of a certain cognitive function based on a set of rules and parameters. Here, we have used 2 tasks:

- Paired visual discrimination task (PVD) to evaluate visual discrimination, learning, and cognitive flexibility during the reversal task (Figure 18A).
- 5-choice serial reaction time task (5CSRT) to evaluate attentional functions (Figure 18B).

2.7.1 Operant conditioning

The premise of the Touchscreen tasks relies on the operant conditioning paradigm in which the rat is rewarded by a 45mg sucrose pellet if his performance in a certain task is considered correct. To this end rats are trained over a period of time to interact with a touchscreen monitor, to perform various tasks, and to associate the reward with a correct answer (Bussey et al. 2008).

Preliminary training and behavioural testing were carried out in 8 automated touchscreen testing chambers (Campden Instruments Limited & Lafayette Instrument Company). The apparatus consists of a standard modular testing chamber with a houselight and tone generator. A pellet receptacle is attached to a pellet dispenser, where the rat receives the sucrose pellet whenever he has the right answer. It is illuminated by a light bulb and fitted with photocell head entry

detectors to detect the rat's presence in that area of the testing chamber. At the end of the box opposite the receptacle is a flatscreen monitor equipped with a touchscreen allowing the rat to nose-poke for the correct answer. A "mask" covers the screen with two or five response windows (PVD or 5CSRT respectively), through which the rat could make a nose-poke toward the screen. Attached to the PVD mask is a "shelf" forcing the rat to rear up, and stretch toward the stimuli head-on, hence facilitating the rat's attention to the stimuli.

After a 1-week acclimatisation period to their new home cages housed in the behavioural platform, rats were submitted to food restriction until reaching approximately 85% of their initial weight. This percentage was maintained all through the Touchscreen behavioural experiments, including training, PVD, PVD reversal and 5CSRT tasks. Food restriction helped maintain animals' motivation to respond for rewards.

The first few days of training allowed habituation to the new environment and learning where the food is presented. Rats were placed in the operant chamber for 15 minutes for acclimatisation. Four sucrose pellets are positioned in the receptacle for the animal to consume freely. Afterwards, a series of training paradigms were performed over the course of 2 weeks to prepare the rat for the PVD or 5CSRT tasks.

2.7.2 Paired visual discrimination task

The PVD training paradigm (Figure 18A) consisted of:

- Initial touch training: (1 day) if rat touches any image on the screen, it receives 3 pellets.
- Must touch training: (7 days): 1 touch = 1 pellet (criterion 100 trials in 60 min).
- Must initiate training (3 days): similar to must touch, with an initiation requirement.
- Punish incorrect (2 days): aversive tone + house light emitted when nose-poking the incorrect image.

Once the rats had completed training, they started the two-choice visual discrimination task in which a pair of images would appear on the screen; one image led to the correct response (a plane) and the other, to an incorrect one (a spider) (Figure 18A, left). A nose-poke to the correct

image resulted in a magazine light and a reward pellet. Incorrect responses resulted in a 5-sec time-out period followed by the correction procedure.

Both discriminative images were presented an equal number of times during a session, with a random left–right arrangement. The criteria for succeeding in the task was the successful completion of 75 trials, with at least 80% correct responses in a maximum of 45 minutes, during 2 consecutive days. If the rat did not meet the criteria, it was not included in the PVD reversal task.

2.7.3 Paired visual discrimination task - Reversal learning – Cognitive flexibility

To assess mental flexibility, a reversal of the PVD task was performed, in which the positive and negative stimuli were reversed: the plane becomes the S- and the spider becomes the S+ (Bussey et al. 2008) (Figure 18A, right). Experimental settings used were the same as previously described for PVD, with the same criteria for success (Kumar et al. 2015).

2.7.4 5 choice serial reaction time task - Attention

Sessions were conducted daily, Mondays through Fridays, over a period of approximately 35 days. One week of training (1 day of Must Touch and 4 days of Must Initiate) was necessary to accustom the rats to the new task. Each trial started with illumination of the house light and a sample stimulus light (initially for 60-s) behind one of the five apertures. A single response (nose poke) within the illuminated aperture was reinforced with a reward pellet, accompanied by illumination of the food-tray light. An inter-trial interval (ITI) followed food delivery, with the food-tray remaining illuminated for its duration, but without scheduled consequences for responses. If a response was not emitted within the illumination time of the sample stimulus (“limited hold” period, LH), or if a response was emitted in an incorrect aperture, the trial was

terminated and immediately followed by an ITI with the house light remaining illuminated, followed by the start of the next trial.

The session ended after the completion of 60 trials or 45 minutes, whichever occurred first.

The stimulus duration was gradually decreased over training sessions depending on the rats' performance (initially 60s, then 30s, 20s, 10s, 5s, and finally 2,5s), therefore increasing the task's difficulty, and mobilising more attentional resources. The stimulus decrease was set whenever the rat met two criteria during two consecutive days: at least 80% of correct responses (the rat touches the square that has lit up), and less than 20% of omissions (the rat does not touch any squares during the trial).

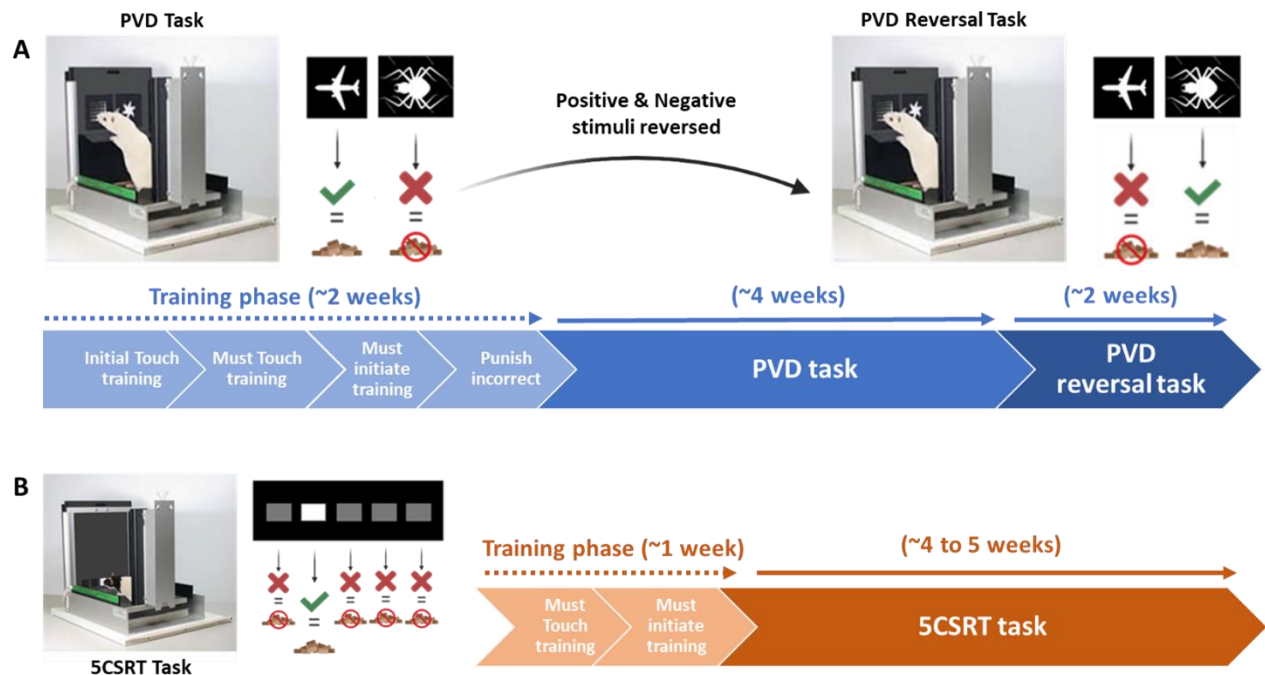


Figure 18. The Touchscreen visual discrimination, cognitive flexibility and attentional tasks. A. The Pairwise Visual Discrimination task contains a 2-choice mask: airplane is the correct stimulus, while spider is incorrect. The stimuli are reversed in the PVD Reversal task. B. The 5-choice serial reaction task contains a 5-choice mask: the correct stimulus is the illuminated square, which changes from one trial to the other. The illumination duration is decreased overtime (60s, 30s, 20s, 10s, 5s).

2.8 SUCROSE CONSUMPTION TEST

This test was carried out over a 2-day weekend period to assess the rats' preference to sucrose as well as their hedonic state right before the beginning of each task (PVD and 5CSRT).

The rats were housed in individual cages with complete food deprivation for 24h, and presented with 2 bottles: one with a 1% sucrose solution and one with water. The two bottles were weighed before and after the 24h to evaluate the percentage of sucrose consumption.

This panoply of motor, cognitive and neuropsychiatric tests offers a comprehensive look on the behavioural phenotype of the studied animal model, which can then be correlated, not only to the dopaminergic denervation but also other pathological features of PD, as well as the anatomical structures and functional networks affected in imaging.

The following table specifies the tests conducted for each of the cohorts evaluated in this PhD work.

A

	Motor evaluation		
COHORT	Actimetry	Openfield	Stepping test
COGSYN 2020	M1 - M2	M1 - M2	M1 - M2
COGSYN 2021	✓	✓	✓
COGSYN 2022	X	✓	✓

B

	Cognitive & neuropsychiatric evaluation						
COHORT	Y-maze Spontaneous alternation	Morris Water Maze	Reversal Morris Water Maze	Pairwise Visual Discrimination	5-Choice Serial Reaction Time	Elevated Plus Maze	Sucrose test
COGSYN 2020	M1	X	X	25 days	X	M1	✓
COGSYN 2021	✓	✓	✓	✓	✓	✓	✓
COGSYN 2022	X	✓	X	X	X	X	X

Table 2. The evaluation of behavioural phenotype in 3 cohorts of the AAV α -synuclein model. A. Motor function evaluation. B. Cognitive and neuropsychiatric evaluation. COGSYN2020 did not complete all the timepoints in the longitudinal study, so the behavioural results of this cohort will not be discussed. Working memory (SA test) and cognitive flexibility (MWM reversal) were not evaluated in COGSYN2022, as we had shown in 2 previous cohorts that there were no deficits in these functions. Touchscreen apparatus was under maintenance so COGSYN2022 did not have attentional or visual discrimination tests either. For the purpose of the *Results, Chapter 1*, only COGSYN2021 will be taken into consideration. (✓: test performed; X: test not performed; M1: test performed only in month 1)

3 MAGNETIC RESONANCE IMAGING EXPLORATIONS

All MRI proton imaging experiments were performed at 7 Teslas in a horizontal bore magnet (Bruker, Biospec, Ettlingen, Germany) located in the small animal imaging platform of **LIIFE** (UMS2014-US41).

Animals were anaesthetised with isoflurane (2%) in O₂ and scanned. Temperature and breathing rate were monitored during the course of the experiments.

We've chosen imaging sequences that are both frequently used in PD clinical sequences, and easily applicable to rodent brains. It includes a classical T2 weighted image to evaluate the structural changes, a T2* weighted image to evaluate iron inhomogeneities, Magnetic resonance spectroscopy to evaluate metabolite changes in the brain, and finally resting-state functional MRI to evaluate network connectivity.

3.1 STRUCTURAL T2-WEIGHTED (T2W) IMAGING

3.1.1 Acquisition

This sequence was acquired in TurboRARE (Rapid Acquisition with Relaxation Enhancement) mode, using a spin-echo sequence in axial orientation, with the following parameters:

- TR/TE= 3000/ 33 ms
- Field of view (FOV) = 4cm²
- Voxel size = 0,15x0,15x0,75mm³

3.1.2 T2w image analysis

The structural images were processed using two complementary methods: a whole-brain unbiased analysis using voxel-based morphometry and a region of interest (ROI)-based method using texture analysis.

3.1.3 Voxel based morphometry (VBM)

The VBM method was used for whole-brain unbiased analysis of the structural modifications of T2w MRIs of the different animal groups, as well as over the different MRI sessions.

This analysis was performed, using the Statistical Parametric Mapping (SPM12) toolbox (Wellcome Trust Center for NeuroImaging, London, UK) in MATLAB (MathWorks, Natick, MA, USA) as described in 2012 by Taki and colleagues, where the authors introduced a modified version of the human images procedure.

Briefly, the images were resized by a factor of 10 to account for the whole-brain volume difference between humans and rodents, then realigned and resliced to adjust for head motion (Suzuki et al. 2013). The obtained images were then averaged to produce mean images which were aligned with a rat brain template (Valdés-Hernández et al. 2011) (Figure 19a), and segmented into grey matter (GM), white matter (WM) and cerebrospinal fluid (CSF) (Figure 19b). This template is a 3D digital-brain atlas created based on an average T2 MR image of a Wistar rat brain, associated with labels and masks to define regions of interest (ROIs), thus facilitating the segmentation process. For this step the default settings in the SPM toolbox were used, except that human tissue priors were replaced by rat tissue priors.

After alignment of the tissue class images onto the stereotactic space, GM, WM and CSF images were used to create a customised, more population-specific template using diffeomorphic anatomical registration with exponentiated lie algebra (DARTEL) template-creation tool (Ashburner, 2007; Klein et al. 2009). Finally, the resulting tissue class (GM, WM and CSF) were warped and smoothed using a 10-mm FWHM Gaussian kernel (Figure 19c).

The statistical comparison was done voxel by voxel of grey matter, between the groups for each session, but also longitudinally between sessions for each rat.

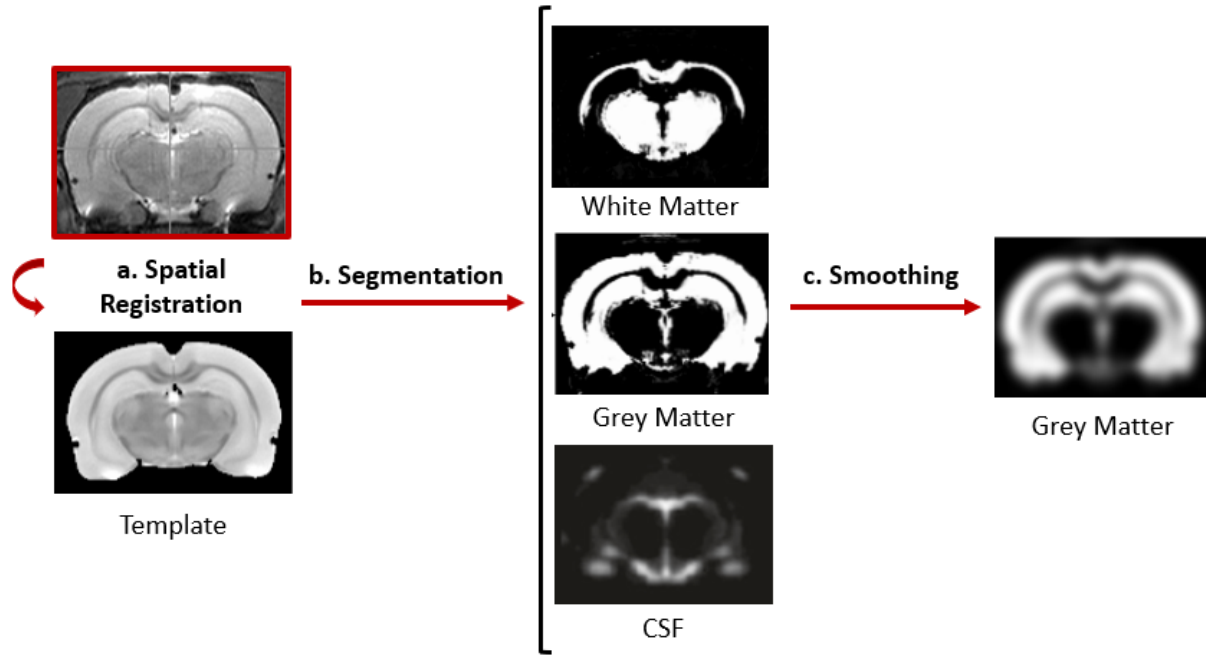


Figure 19. Rat brain MR images pre-processing pipeline. a. Native image is registered and adjusted to the rat brain template (Valdés-Hernández et al. 2011). b. Images are segmented into GM, WM and CSF. c. Images are warped and smoothed.

3.1.4 ROI-based analysis

3.1.4.1 Volumetric analysis

We assessed whether dynamic brain volume changes occurred over time, or between groups, by measuring the volume of several rat brain regions of interest such as the substantia nigra, the striatum, the hippocampus, the diencephalon and the amygdala. Delineation and segmentation were done as described previously.

3.1.4.2 Texture feature analysis

This method, which extracts different metrics (texture features) quantifying statistical signal distribution in an image region, was reported as more sensitive to detect early changes than other ROI-based approaches such as Volumetry.

The original T2w images were first corrected for intensity non-uniformity, caused by static field inhomogeneity, using the N3 algorithm (Sled et al. 1998) and then parcellation using the brain

template was applied after registration to automatically segment the SN and the striatum. Texture features were measured in these two regions.

Overall, and based on previous results (Betrouti et al. 2021), 10 texture features were considered and computed, using a home-made Matlab written script.

The first-order statistics are used to study the voxel value distribution without considering spatial relationships. Four of these features were chosen:

- 1- Mean gray level
- 2- Standard deviation (SD) of gray levels
- 3- Kurtosis, which is a measure of whether the data is heavy-tailed or light-tailed in relation to a normal distribution. Positive kurtosis indicates a peaked distribution, while negative kurtosis indicates a flat distribution.
- 4- Skewness, which also quantifies the asymmetry of signal values in relation to a normal distribution. It takes a null value for a symmetric distribution and negative values for left-skewed data.

The second-order statistics describe relationships between pairs of neighbouring voxels in the image, therefore quantifying the spatial relationships between the values. These are mainly computed through the gray level co-occurrence matrix (GLCM) introduced by Haralick and colleagues in 1973.

Second-order texture values were derived from the co-occurrence matrix whose entries represent the number of times that intensity levels i and j occur in two voxels separated by a distance (d) in a specific direction (a). To obtain a full neighbourhood interaction, a matrix was selected to cover 26 connected directions of neighbouring voxels in a 3D space. Seven parameters were considered:

- 1- Homogeneity (also called angular second moment), which represents uniformity of the texture intensity.

- 2- Contrast, representing the degree to which the texture intensity levels differ between voxels or local intensity variation.
- 3- Entropy, (aka. measure of randomness), which represents the degree of uncertainty.
- 4- Correlation, representing the degree of mutual dependency between voxels.
- 5- Variance (also called sum of squares), which gives high weights for elements different from the average value.
- 6- Sum average, measuring the relationship between occurrences of pairs with lower intensity values and occurrences of pairs with higher intensity values.
- 7- Inverse difference moment (InvDiff), which measures the difference between the highest and lowest values of a contiguous set of voxels.

3.2 T2* WEIGHTED IMAGING

3.2.1 Image acquisition

T2* weighted images were also acquired in TurboRARE mode with a 6-echo gradient sequence, using the following parameters:

- TR/TE= 100/4, 10, 16, 22, 28, 34ms
- isotropic voxel=0,15mm³

3.2.2 T2* image analysis

3.2.2.1 *Generation of R2* maps*

For each rat, the multi-echo images were processed to produce R2* maps using a home-made script in Matlab, implementing a voxel-by-voxel nonlinear least-squares fitting of the data acquired at the six echo times (Figure 20). This allowed us to obtain a monoexponential signal decay curve, with R2* values equalling $1/T2^*$, for each voxel, T2* being the effective transverse relaxation time.

We then compared the $R2^*$ values generated of each voxel in the same standard MNI (Montreal Neurological Institute)-space, between the different groups, and between the different sessions, as described previously. This protocol allows a very sensitive and reproducible analysis of the $R2^*$ maps while maintaining a high spatial resolution (Péran et al. 2007).

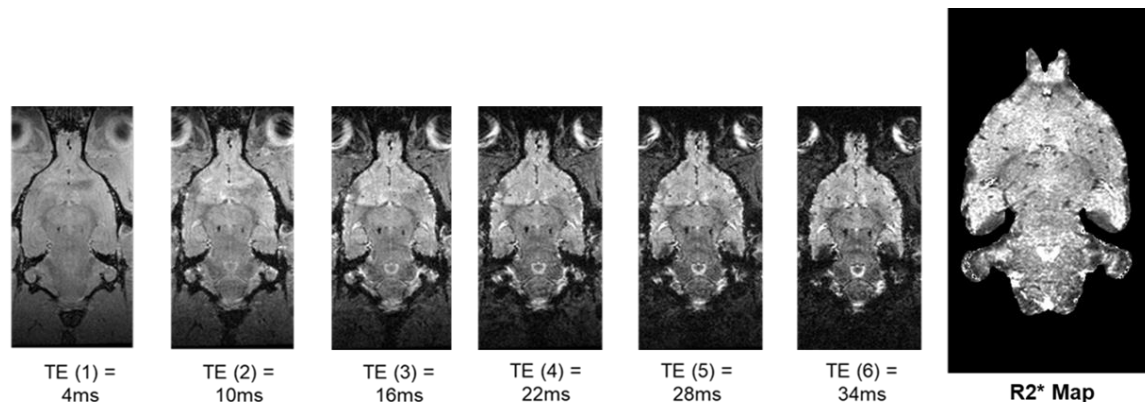


Figure 20. Generation of an $R2^*$ map from a multi-echo $T2^*$ sequence. Six $T2^*$ weighted images at TE= 4ms, 10ms, 16ms, 22ms, 28ms, and 34ms.

3.2.2.2 Voxel Based Relaxometry

Normalised $R2^*$ maps were averaged and filtered and smoothed as described above in the VBM protocol (Figure 19), to perform a whole-brain unbiased analysis of iron deposits in the brain, using the voxel based relaxometry (VBR) method (Pell et al. 2004).

3.2.2.3 ROI-based analysis

To study only specific regions of interest, a Matlab script was written to extract median values in 22 regions of interest (11 symmetrical regions in each hemisphere), using a Sprague-Dawley atlas (Papp et al. 2014) which has a delineated 76 major anatomical structures of the rat brain. The choice of these 22 ROIs was made according to the structures known to be involved in the behavioural and motor deficits in Parkinson's disease.

3.3 RESTING-STATE FUNCTIONAL IMAGING (RS-fMRI)

3.3.1 Image acquisition

For the rs-fMRI sequence, the rats were anaesthetized using IP injection of Medetomidine (0.3mg/Kg) instead of Isoflurane.

Indeed, according to several studies, medetomidine, which is a sympatholytic agent, was found to be the preferred anaesthetic for longitudinal fMRI studies in small animals, because it allows for adequate sedation while keeping the animal at the edge of consciousness. It also enables longitudinal fMRI studies with several administrations due to the molecule's non-toxicity, and most importantly, it does not directly affect the vascularization of the central nervous system or the neuronal activity, which is measured in rs-fMRI (Weber et al. 2006; Pawela et al. 2008; 2009). Rs-fMRI acquisition started 35minutes post- Medetomidine injection. Multi-slice echo-planar images (EPI) were acquired during 15minutes using the following parameters: TR/TE = 2000/17 msec - FOV 32x32 mm - Matrix 64x64 - Resolution 0,5 mm/pixel – slice thickness: 1mm; 20 slices - 450 repetitions. - Signal FID.

3.3.2 Rs-fMRI analysis

All fMRI Images were pre-processed by first, rescaling the voxel size of each image by a factor of ten for compatibility with the analysis software used for human scale images. The pre-processing also included standard steps of spatial and temporal alignment to correct for head motion and nuisance signal, including normalisation and smoothing, using the RestPlus toolbox (Jia et al. 2019). Next, the realigned images were co-registered to standard T2 images, and segmented.

After this parcellation into 150 ROIs regions (75 ROIs for each hemisphere) using an atlas, we extracted, for each region, a BOLD signal corresponding to the hemodynamic vascular influx linked to neuronal activity, which is considered an indirect measure of the region's activation.

These datasets were processed to produce functional connectivity maps (matrices) for each rat, by measuring the pairwise Pearson's correlation coefficients across ROIs from a pre-existing

template (Westphal et al. 2017). Indeed, the signals of all the regions were analysed two by two, and the correlation coefficient between the two corresponds to the synchronization of the two regions. We obtained a 150 by 150 matrix, corresponding to the 150 ROI parcellated, where each square represents the level of synchronization between the 2 regions, and red shows hyper-synchronized regions. This can also be graphically represented (Figure 21).

In a neurobiological framework, a graph consists of a collection of nodes, here represented by brain regions, and their connecting edges, here represented by the pair-wise functional connections between these brain regions defined by the correlation coefficients (Westphal et al. 2017).

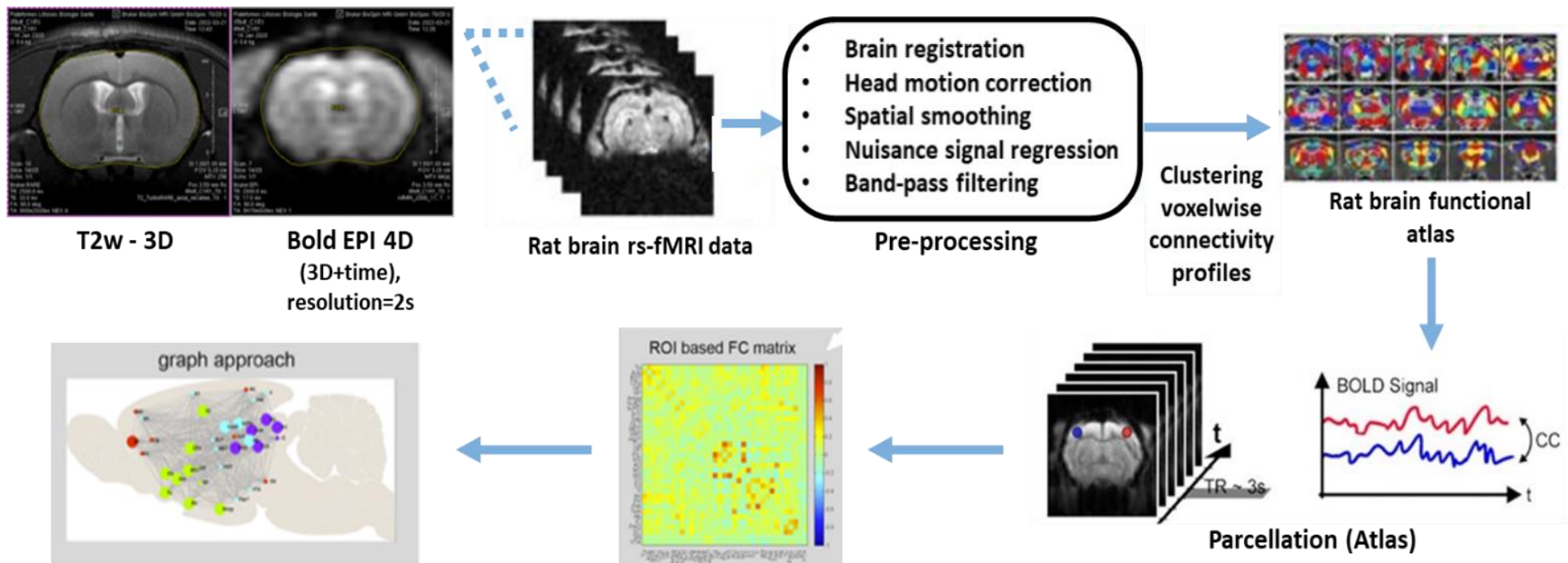


Figure 21. Schematic illustration of the data analysis pipeline used for rs-fMRI.

The preceding MRI sequences and state-of-the-art techniques used to analyse them offers a comprehensive multimodal exploration of anatomical structure and functional connectivity in our PD models. The fact that they were all adapted from what is used routinely in clinical research allows for better comparable parameters, and supports the translational validity of these explorations.

The following table specifies the imaging sequences explored for each of the cohorts evaluated in this PhD work.

COHORT	T2 weighted image	T2* weighted image	rs-fMRI
COGSYN 2020	W2 - W18	W2 - W18	X
COGSYN 2021	✓	✓	X
COGSYN 2022	✓	X	✓

Table 3. Multimodal MRI evaluation in 3 cohorts of the AAV α -synuclein model. A. COGSYN2020 only received 2 of the 3 MRI acquisition timepoints, and therefore was excluded from the longitudinal MRI analysis. COGSYN 2021 underwent a T2 and a T2* sequence for both morphological and quantitative MRI analyses. COGSYN 2022 underwent a T2wi and an rs-fMRI sequence for both morphological and functional MRI analyses. (✓ : test performed; X: test not performed; W1: test performed only in week 2)

4 HISTOPATHOLOGY

4.1 BRAIN TISSUE COLLECTION

At 18-weeks post injection for the COGSYN cohorts and 8-weeks post-injection for the toxin-based models, all animals were ultimately sacrificed for subsequent histological analyses.

After receiving a lethal dose of pentobarbital, rats were transcardially perfused with 4% paraformaldehyde at a rate of 14ml/min. Brains were extracted, fixed overnight in 4% PFA at 4°C, and then cryoprotected in a 30% sucrose solution (0.1 phosphate buffer, pH 7.4), before snap freezing in cooled isopentane then stored at -80°.

Forty micrometer-thick free-floating coronal sections of the entire brain were prepared using a cryostat (Leica, Nussloch, Germany). Serial sections of the entire brain, including the frontal region, striatal region, hippocampal region and SN region (Figure 23B) were then conserved in a cryoprotectant antifreeze solution (30% glycerol, 30% ethylene glycol in PBS) at -20°C, until use.

4.2 IMMUNOHISTOCHEMISTRY

4.2.1 Dopaminergic neurons

We assessed the dopaminergic denervation by tyrosine hydroxylase (TH) immunostaining of striatal and nigral sections from the fixed brains of lesioned animals.

Free-floating sections were thoroughly washed with PBS and incubated for 1 h in 0.3% Triton X-100 in PBS (PBST) and 10% normal goat serum (Chemicon). They were then incubated with primary antibody anti-TH 1:1000 (AB152 Sigma-Aldrich) diluted in PBST containing 10% normal goat serum overnight, with shaking, at 4°C. Then they were incubated in a secondary antibody (Goat Anti-Rabbit IgG Antibody (H+L), Biotinylated. BA-1000). Antibody binding was detected with the avidin–biotin–peroxidase conjugate (Vectastain ABC Elite; Vector Laboratories,

Burlingame, CA) using 3,3'-diaminobenzidine as chromogen. It was applied to the sections for 60 sec. Sections were dehydrated through graded ethanol solutions, cleared in xylene, mounted in DPX (DBH Laboratory Supplies, Poole, UK), and covered with a coverslip for microscopy.

4.2.2 Alpha-synuclein deposits

We assessed alpha-synuclein deposits in different brain regions, by immunolabeling using α -synuclein mouse mAb, clone LB509 (ref 180215 Invitrogen). This antibody solely recognises the human alpha-synuclein injected (h- α -syn). We also evaluated the phosphorylated form of α -synuclein at Serine129 using the Recombinant Anti- α -synuclein (phospho S129) antibody (ref ab51253 abcam), with the same protocol described above.

For some sections, a Nissl staining was performed with cresyl violet to observe the cellular distribution and general structure of the neuronal tissue.

4.2.3 Neuroinflammation markers

We also used neuroinflammatory markers' antibodies such as ionised calcium-binding adapter molecule 1 (IBA1; WAKO O1919741), to assess microglial activation, and glial fibrillary acidic protein (GFAP; ABCAM 53554), to assess astrogliosis.

4.3 IRON HISTOCHEMISTRY

Brain iron was determined by Perls' reaction without 3, 3' -diaminobenzidine (DAB) intensification. After inhibition of endogenous peroxidases using 1% H₂O₂ in 99% methanol. Sections were rinsed in PBS1X and incubated in Perls' solution (20% potassium ferrocyanide, 20% HCl) at room temperature for 4h, then rinsed in PBS1X for 30 min. Sections were dehydrated through graded ethanol solutions, cleared in xylene, mounted in DPX medium, and covered with a coverslip for microscopy.

4.4 HISTOLOGICAL QUANTIFICATION

Images were acquired using a Zeiss Axio Scan Z.1 slide scanner (20× objective) and Zen software, Blue edition (Zeiss, Oberkochen, Germany).

4.4.1 Stereology

For dopaminergic TH+ neurons in the SNpc, an unbiased stereological cell counting was performed using Mercator Software (Explora Nova, La Rochelle, France) (Laloux et al. 2017).

After a manual delimitation of the SNpc, TH+ cells were counted in randomly placed squares, over six serial 40µm-sections separated by 280µm each, encompassing the whole SNpc (anterior to posterior).

Then the optical fractionator principle was used to estimate the total number of dopaminergic TH+ neurons for the entire SNpc volume. Considering the bilateral nature of our models, we presented the separate values of left and right SNpc, as well as the sum of neurons counted for both SNpc (values used in the primary histological results).

4.4.2 Striatal TH quantification

For TH+ neurons in the striatum, we used the average optical density measurement at 4 points

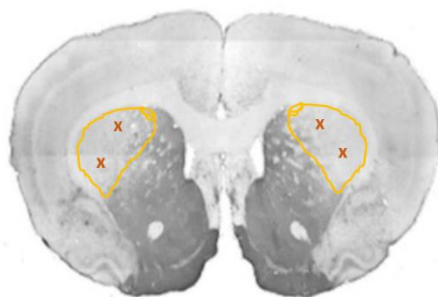


Figure 22. Illustration of the striatal tyrosine hydroxylase quantification. Segmentation of the dorso-lateral striatum (in yellow). Red X accounts for the location of optical density measurements.

of the right and left dorso-lateral striatum of each section (Figure 22), performed in Zen Software. This was done over six serial 40µm-sections separated by 440µm, encompassing the entire striatum (anterior to posterior).

4.4.3 Alpha-synuclein quantification

We explored a new method of synucleinopathy quantification, using state-of-the-art software QUICKNII (Puchades et al. 2019), allowing our brain images to be spatially registered with the same MR atlas that was used for our imaging analysis (Waxholm Space Atlas of the Sprague Dawley Rat Brain V4) (Figure 23B, C).

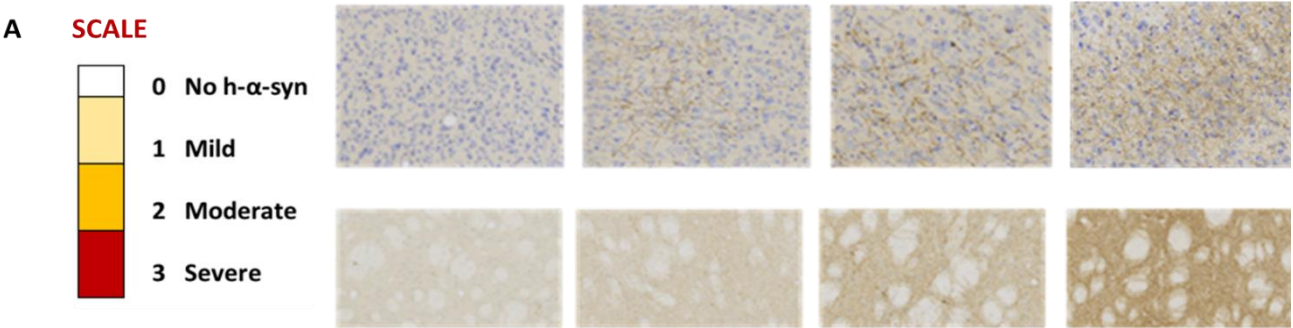


Figure 23 (part I). Adaptation of the QUINT workflow for histological analysis. A. The alpha-synuclein quantification 4-level scale used for analysis, defined for each region based on the number/density of α -syn strings.

An automatic histological quantification, using the Ilastik software (QUINT workflow) did not work due to low intensity staining with the human reactive monoclonal antibody. Therefore, alpha-synuclein deposits and propagation were assessed using a custom 4-point scale range from 0 to 3, 0 being the absence of α -synuclein, and 3 being diffuse α -synuclein (adapted from Joppe et al. 2021) (Figure 23A). 222 regions of interest from the atlas were scored. A distinction between left and right was later added for each region, based on the observation of asymmetrical evolution and propagation of the protein.

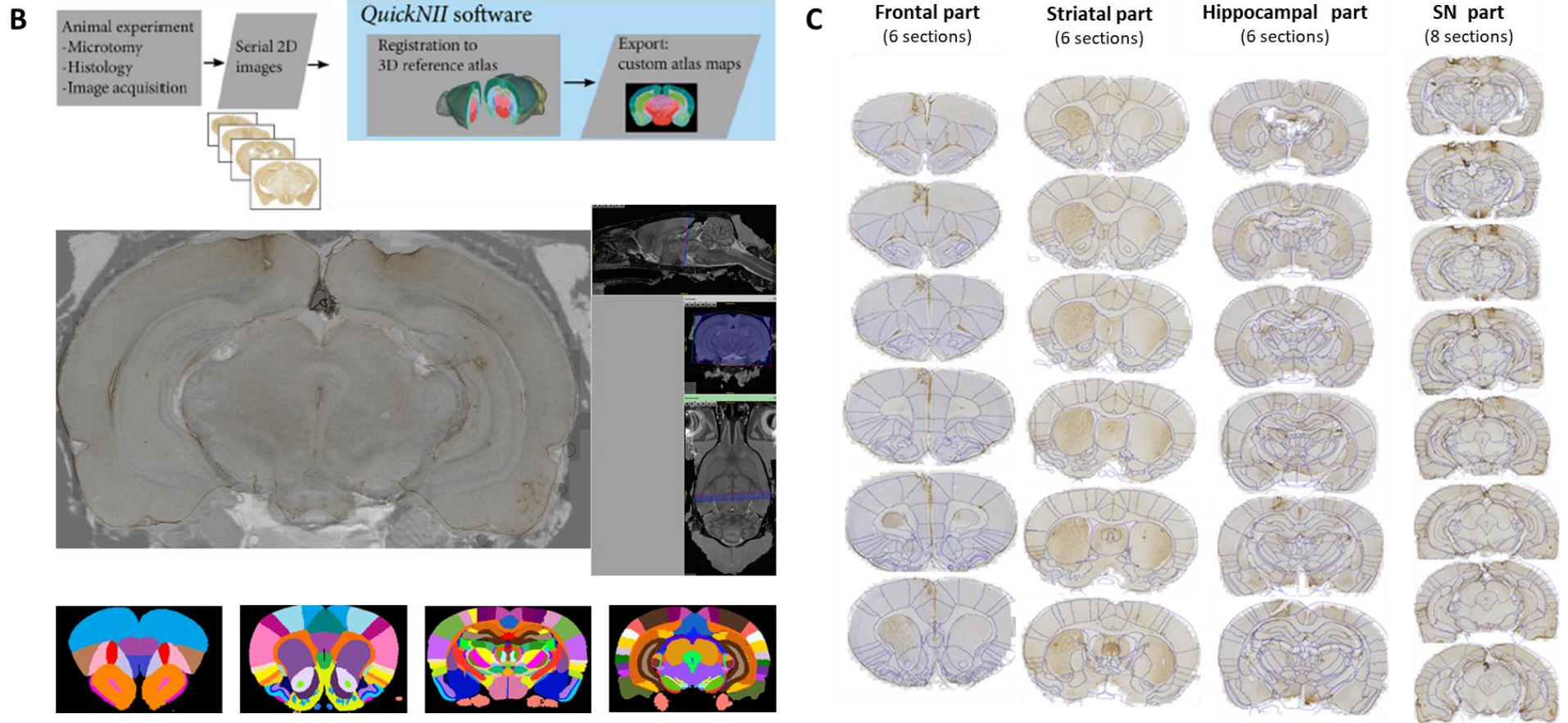


Figure 23 (part II). Adaptation of the QUINT workflow for histological analysis. B. Histological image registration to the WHS MRI atlas, and segmentation into 222 ROI, using QUICKNII software. C. Application on 26 sections per rat brain, with a mask representing the ROIs delineation.

Structural and functional clustering of the atlas's 222 regions allowed the extraction of 35 regions of interest, with an average score of alpha-synuclein deposit, and left-right distinction.

The advantage of this method is that it allows a whole-brain unbiased evaluation, similar to imaging analysis techniques such as VBM or VBR, without the need to focus on specific regions of interest prior to analysis, but rather the exploration of the entire brain *sans a priori*.

5 STATISTICAL ANALYSES

Statistical analyses for histological and behavioural data were performed using XLSTAT or JASP (v.0.14.1, University of Amsterdam), whereas SPM12 was used for imaging data.

Normal distribution was verified for each parameter using the Schapiro-Wilk test. Data following a normal distribution were analysed by comparing the two groups at different times with 2-way ANOVAs, followed by the Bonferroni post hoc test or paired Student's t test. For non-parametric paired t-tests, a Mann Whitney (MW) test was used.

For imaging methods (VBM and VBR), t tests were performed to identify whole brain differences between the two animal groups and in the same group between the MRI sessions. Clusters were considered significant with a fixed size threshold of 10 voxels and after controlling of familywise error rates using false discovery rate. The same comparison protocol (groups, sessions) was run for connectivity matrices, using the network-based statistics (NBS) method (Zalesky et al. 2010).

The relationships between the texture features and the non-imaging scores (from behavioural analysis and tissular quantifications) were examined using Spearman's correlation with FDR correction.

For all analyses, significance was set to $p < 0.05$. All data were expressed as mean \pm SEM or as percentage of the CTRL group. Graphs were created using the GraphPad Prism software (version 6.01), represented with mean and standard deviations.

PART THREE

RESULTS

1 CHAPTER ONE:

BEHAVIOURAL CHARACTERIZATION OF THE AAV ALPHA-SYNUCLEIN MODEL: A FOCUS ON THE COGNITIVE AND NEUROPSYCHIATRIC PHENOTYPE, AND THE UNDERLYING CHANGES IN BRAIN TISSUE.

1.1 BACKGROUND AND AIMS

1.1.1 Specifics of the model

As mentioned in the introduction, the use of viral vector-mediated alpha-synuclein overexpression in rodents has experienced a surge in the past decade, especially with the development of a new generation of AAV vectors that allowed an important and sustained delivery of alpha-synuclein with Lewy-like pathology (Visanji et al. 2016). Indeed, it has been considered one of the few models that replicates the extensive, and gradual alpha-synuclein related neuropathology in nigrostriatal neurons which develops overtime in PD patients (Dehay & Fernagut, 2016). In addition, it also replicates the significant dopaminergic degeneration which we do not observe in transgenic alpha-synuclein models, and, most interestingly, it exhibits a parkinsonian behavioural phenotype with a progressive and worsening motor impairment (Decressac et al. 2012).

Of course, the choice of the AAV, the animal and the site of injection have differed from one study to the other (Annexe Table 2). But it was mainly reported that the onset of the pathology, its severity and reproducibility was more adequate in rats compared to mice, making rats the better candidate for modelling the alpha-synuclein pathology via the AAV-based approach (Van

Der Perren et al. 2014). The bilateral injection in the SN was also proven to be the most effective in producing the desired phenotype, compared to unilateral models and those injected in the striatum (Gorbatyuk et al. 2008). As for the advantages of injecting either wild-type or mutant A53T alpha-synuclein at the same vector dose, there has been no consensus so far, with some studies showing that both WT and A53T alpha-synuclein induced a similar degree of dopaminergic denervation and alpha-synuclein accumulation (Oliveras-Salva et al. 2013), while others showing that the A53T alpha-synuclein overexpression had the more robust results (Roost, 2020).

Therefore, we have chosen in this work to explore the AAV alpha-synuclein rat model, characterized by a ***double bilateral injection*** of the ***AAV A53T-human-alpha-synuclein (h- α -syn)*** in the ***SN***, for a maximum transduction efficiency and transgene expression, as described by Bourdenx and colleagues in 2015, and detailed previously in the methodology section.

1.1.2 Beyond the motor symptomatology

As previously mentioned, many non-motor symptoms of PD including cognitive and neuropsychiatric dysfunctions, are not responsive to dopamine treatments, and therefore not necessarily linked to the dopaminergic denervation, which is the basis of most animal models of PD. Therefore, these symptoms were, for a long time, less evaluated in a preclinical context. However, the emerging importance of these debilitating non-motor features, has shifted research efforts towards more gradual and moderate models that allow for the analysis of the earlier stages of the disease (McDowell & Chesselet 2012). Indeed, less severe 6OHDA models have shown symptoms such as apathy, anxiety, and depression (Drui et al. 2014; Favier et al. 2017), as well as spatial and working memory impairments (De Leonibus et al. 2007; Campos et al. 2013). Bilateral MPTP rat models have shown learning and memory impairments, independently from any motor deficits (Da Cunha et al. 2001; Ferro et al. 2005; Hsieh et al. 2012). Additionally, some genetic models such as the A30P transgenic mouse (expressed under the Thy1 promoter), showed an age-dependent cognitive decline (Freichel et al. 2007).

However, this is but a foray into the exploration of non-motor symptoms, and there are many validated models of PD which have not yet been evaluated thoroughly for cognitive and neuropsychiatric symptoms (Lindgren & Dunnett, 2012).

1.1.3 Aims and study design

Although the motor aspect of the AAV alpha-synuclein model has been extensively evaluated in the literature (Decressac et al. 2012; Bourdenx et al. 2015), the psycho-cognitive phenotype has been widely lacking. Considering the relationship between alpha-synuclein pathology and non-motor symptoms, specifically the neuropsychiatric symptoms such as anxiety and depression, as well as the cognitive dysfunctions such as executive function and attention impairment (Jellinger, 2011; Goedert et al. 2013; Fan et al. 2022), we postulated that an extensive evaluation of these non-motor symptoms in an alpha-synuclein model is essential, especially to confirm its construct and predictive validity, in regards to the effects of the alpha-synuclein pathology on the phenotype.

Indeed, the aim of the first part of our work was to correlate the behavioural phenotype, not only with the dopaminergic degeneration, which is known to mainly affect the motor symptoms, but also with the spreading of alpha-synuclein which can be associated with non-motor symptoms.

To do so, we designed a longitudinal experiment over 5 months with motor, cognitive and neuropsychiatric evaluation of the ASYN animals compared to CTRL. Considering the progressive nature of the model, as described in the literature, we opted for performing these evaluations at different timepoints to observe and describe their evolution overtime (Table 4). Considering that only the COGSYN 2021 cohort underwent all the entirety of the tests at all timepoints, the following behavioural results will solely depict this cohort, while results from the other cohorts will be showed in **Annexe 4** and discussed.

TEST	FUNCTION	TIMEPOINTS
Actimetry & Openfield (OF)	Spontaneous locomotricity	M1, M2, M3, M4
Stepping	Sensori-motricity (forelimb akinesia)	M1, M2, M3, M4
Elevated plus maze (EPM) & OF	Anxiety	M1, M3
Y-maze Spontaneous alternation test (SA)	Working Memory	M1, M3
Morris water maze (MWM)	Visuospatial Learning & Memory	M2, M4
MWM reversal	Mental Flexibility	M2, M4
Pairwise visual discrimination (PVD)	Learning and Visual Discrimination	M1 & M2
5 choice serial reaction test (5CSRT)	Attention	M3 & M4

Table 4. Experimental design for the behavioural evaluation of the AAV alpha-synuclein model. List of the motor, sensorimotor, cognitive and neuropsychiatric tests and the behavioural function assessed over several timepoints along an 18-weeks longitudinal study.

1.2 MOTOR PHENOTYPE

1.2.1 Spontaneous locomotor activity

We used both the actimetry and Openfield tests at Month 1, 2, 3 and 4, to evaluate spontaneous locomotor activity in rats. We did not find any group differences between ASYN and CTRL animals, in any of the various motor activity parameters: mean speed, distance covered, rearing frequency, or resting time. We observed a significant increase in distance and speed at M2, 3 and 4 compared to M1 in both groups (Figure 24A, B). However, post-hoc tests confirmed that there was no difference between the two groups at any of these timepoints, indicating no deficits in spontaneous locomotor activity in ASYN rats. It is essential to note that the absence of these motor deficits was observed across all three cohorts (Results in Annex 4).

1.2.2 Sensori-motor activity

The longitudinal follow-up of basic sensori-motor function, using the stepping test, allowed us to observe a significant decrease in the number of adjusting steps, in ASYN animals compared to control (Figure 24C). The decrease reached 33% 16-weeks post-injection. This indicated the onset

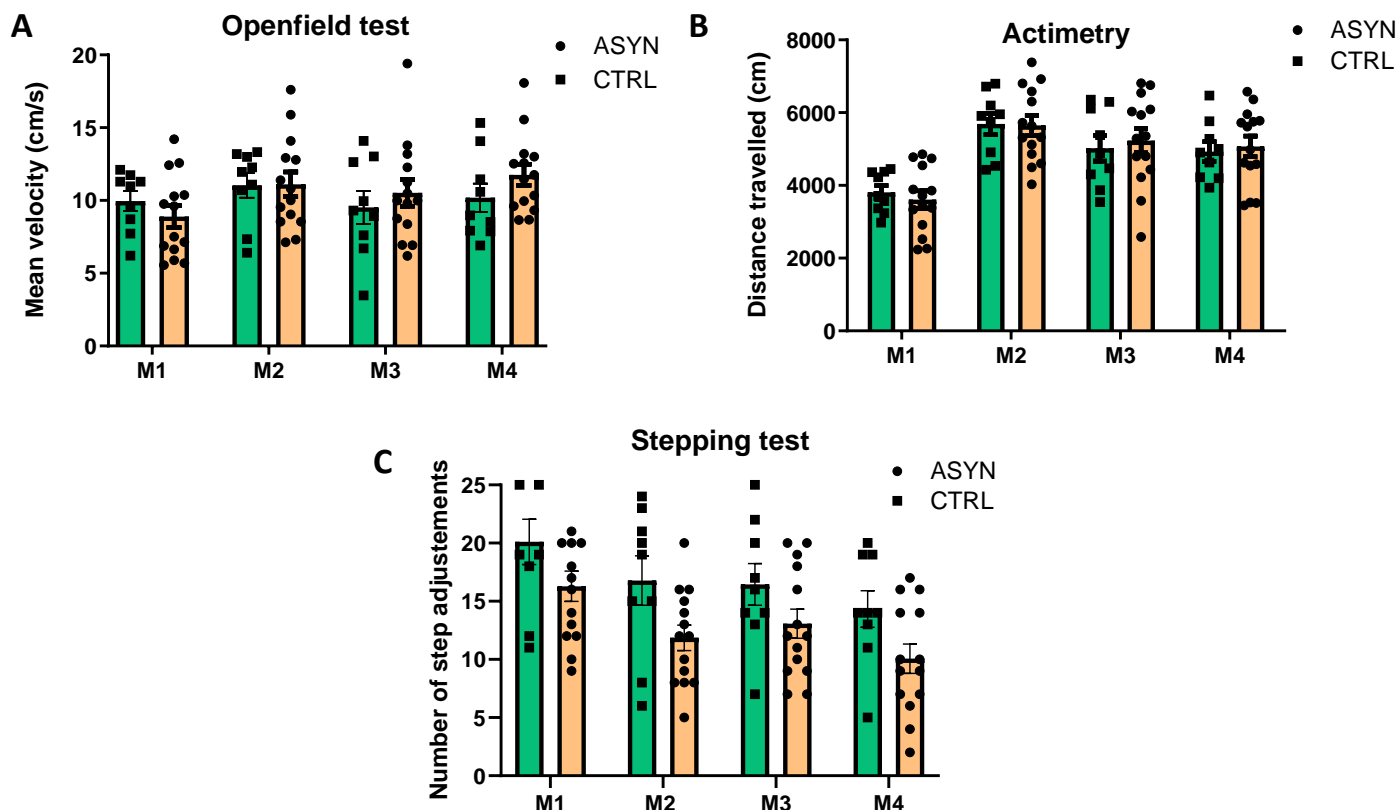


Figure 24. Spontaneous locomotor and sensorimotor activity evaluation in COGSYN 2021, at Months 1, 2, 3 and 4. A. Distance travelled in actimetry (cm). No significant changes overtime or between groups. B. Mean speed in Openfield arena (cm/s). No significant changes overtime or between groups. C. Average number of adjusting steps (Left + Right) in the stepping test. Significant group effect $F(1, 21) = 4.640$ ($p < 0.05$) and time effect $F(2.315, 48.62) = 19.28$ ($p < 0.001$). ($n=23$: 14 ASYN, 9 CTRL).

of forelimb akinesia. The left and right limb adjustments were analysed separately for all animals, and there were no significant differences in adjustments between the limbs.

1.3 COGNITIVE PHENOTYPE

1.3.1 Working memory

During the spontaneous alternation test that was performed at Months 1 and 3, we did not observe any significant differences in the percentage of alternations performed by the ASYN group compared to the control ($p > 0.05$; Figure not shown). This result is similar to what was obtained in COGSYN2020, therefore confirming the absence of deficits in working memory, up to the third month post-injection in this animal model.

1.3.2 Visuo-spatial learning and memory

The training trials of the MWM test allowed us to evaluate visuo-spatial learning at Month 2 and 4. We observed a significant increase in the latency to reach the escape platform in ASYN animals, on the fourth day of training in M2, and the third and fourth days of training in 4 (Figure 25A). This increase in latency showed trouble (a slowing down) in the spatial learning process in the ASYN animals. It is important to note that this increase was not due to any motor dysfunction related to the animals' swimming capabilities, as the mean velocity was the same across the 2 groups.

Spatial memory was evaluated on the probe test day of the MWM, when the platform is removed. There were no significant differences observed between the groups in the time spent in the target quadrant, indicating no deficits in spatial memory in ASYN animals (Figure 25B).

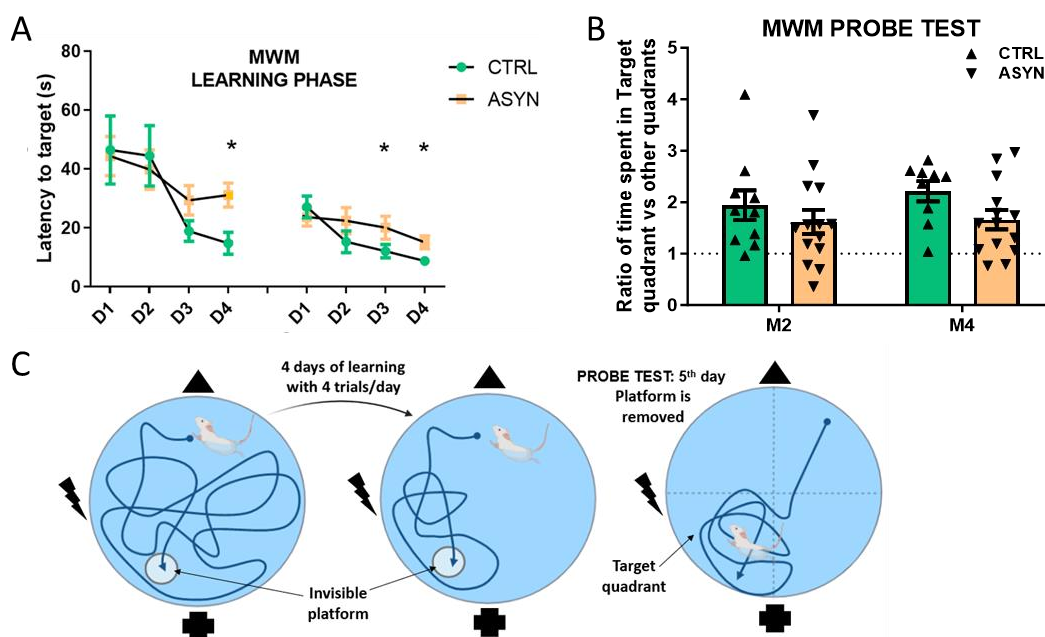


Figure 25. Visuo-spatial learning and memory evaluation in the Morris Water Maze test (MWM) at Months 2 & 4. A. Latency to target (platform) on 4 days of training at M2 & M4 for learning assessment. Significant differences are observed between ASYN & CTRL groups at day 4 of M2 and days 3&4 of M4 indicating a slowing down of the spatial learning process (* $p < 0.05$). B. Ratio of time spent in the Target quadrant (where the platform used to be) compared to time spent in the other 3 quadrants. No significant differences between the groups at M2 or M4. C. Depiction of the MWM paradigm. (n=23 : 14 ASYN, 9 CTRL).

1.3.3 Visual discrimination

Using the “Pairwise Visual Discrimination (PVD) task”, we generated a learning curve showing the daily evolution of the rats’ performances and their correct answer percentages. Although no significant differences were shown between the two groups in the percentage of correct answers (Figure 26A), we noticed that less alpha-synuclein animals were able to reach the criteria for completing the task and switching to the reversal PVD, compared to controls (80% correct answers in 75 trials in 45 minutes during 2 consecutive sessions). Indeed, only 42.9% of the ASYN reached the required criteria whereas over 70% of the controls did so after 15 days of learning (Figure 26B). This, like the MWM test, showed that although the ASYN animals did not have trouble discriminating the two images, they did indeed present learning impairments over the course of the training and needed more time to reach the required criteria.

1.3.4 Attention

The 5-choice serial reaction time task (5CSRT) uses the same touchscreen paradigm and apparatus, to evaluate attentional functions, with an overtime decrease in stimulus duration, thereby increasing the task’s difficulty (Figure 26C). Nose-poking the illuminated aperture was considered as the correct response, while an omission meant the lack of response or nose-poke (Figure 26C). The ASYN animals had no differences in omission percentages, but a significantly lower percentage of correct answers compared to CTRL animals ($p=0.01$) starting session 3 (20s stimulus), indicating a deficit in attentional function starting 12-weeks post-injection (Figure 26D).

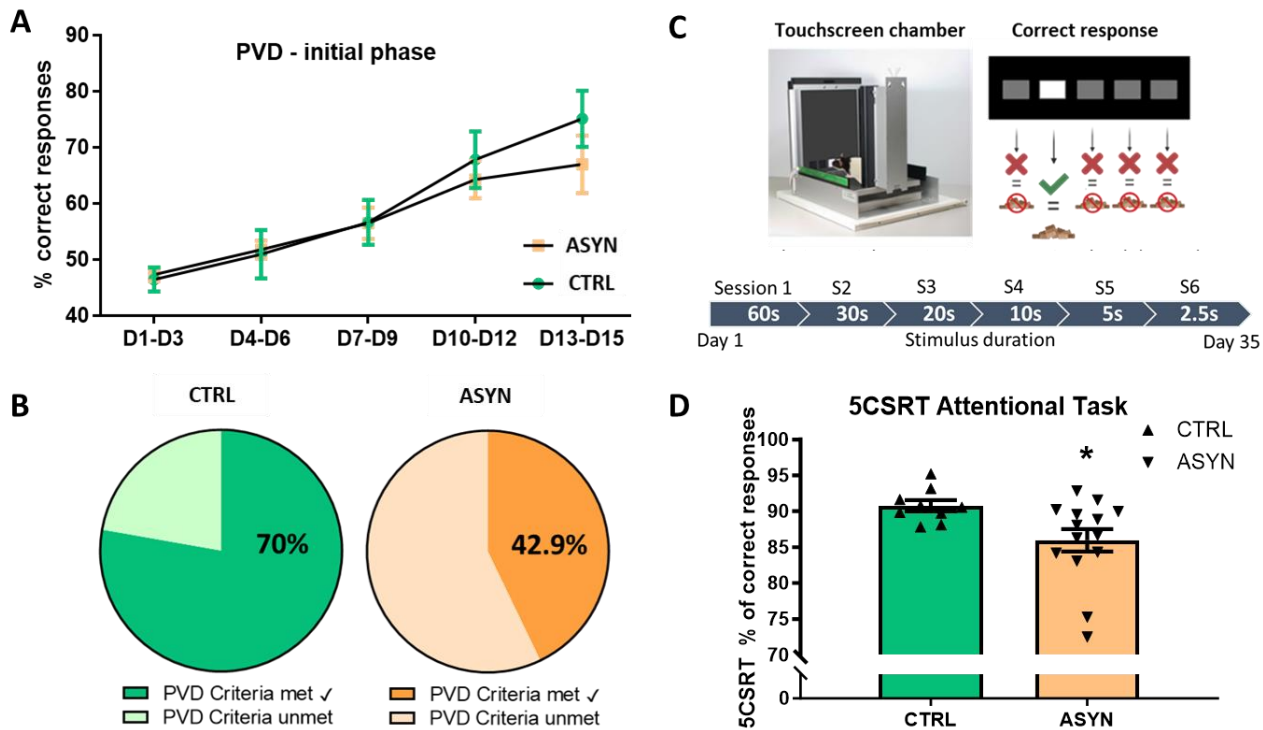


Figure 26. PVD and 5CSRT touchscreen tasks evaluated in ASYN (n=14) and CTRL (n=9) animals. A. Learning curve representing the evolution of the percentage of correct answers by a mean/average of 3 days, for the visual discrimination task over 15 days. B. Percentage of animals which completed the initial PVD criteria after 15days and were able to perform the PVD reversal test: ASYN (n=6/14) and CTRL (n=7/9). C. Depiction recall of the 5CSRT task paradigm. Stimulus duration equals the overall time the square is lit. Decreasing this duration over sessions increases the difficulty of the task. D. Attentional deficits are observed in ASYN animals with a significant decrease in the percentage of correct responses averaged over sessions 3 to 6, stimulus duration between 20s and 2.5s (* p=0.01).

1.3.5 Mental Flexibility

Both the MWM test and the PVD test allowed the evaluation of the animals' cognitive flexibility, thanks to the use of the reversal paradigm. For the MWM, the reversal test consists in placing the platform in the opposite quadrant et re-training the rats to the new location of the platform. There were no significant differences in the latency to reach the platform in its new location during the training sessions, between the two groups (Figures not shown). Similarly, during the probe test, both groups spent significantly more time in the new target quadrant, without any significant differences between both groups (Figure 27A).

In the PVD reversal task, where the positive and negative stimuli are reversed, we observed no significant differences in either the learning curve or the percentage of correct answers in the ASYN group compared to the CTRL group (Figure 27B).

Both of these results indicate the absence of deficits in cognitive flexibility over the course of our longitudinal evaluation in the ASYN animal model.

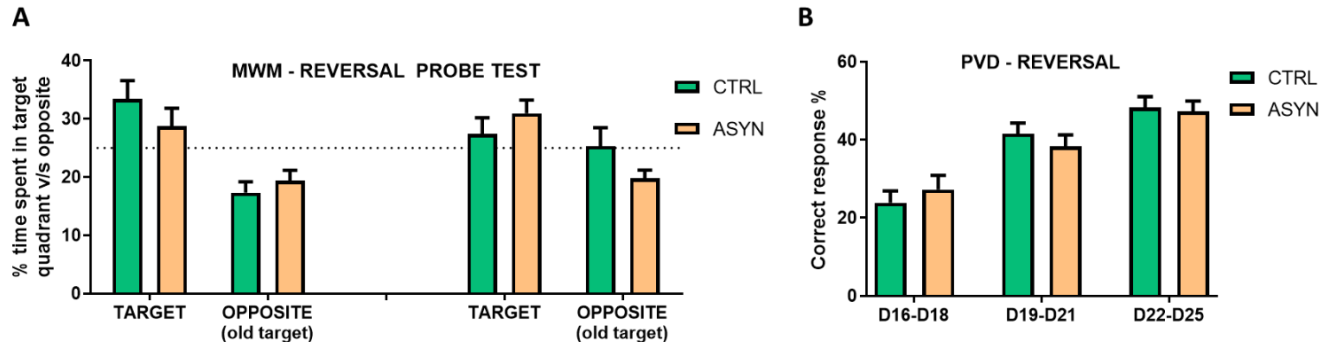


Figure 27. Analysis of the reversal paradigm accounting for mental flexibility. A. Reversal MWM probe test evaluated at Months 2 & 4 in ASYN (n=14) and CTRL (n=9). Time spent in target quadrant versus opposite quadrant did not differ between both groups. B. Reversal PVD evaluated only in animals which completed the initial PVD criteria at the end of M2: ASYN (n=6) and CTRL (n=7), with an average of 3-day correct response % ($p>0.05$).

1.4 NEUROPSYCHIATRIC PHENOTYPE

1.4.1 Anxiety in EPM

The animal's anxious behaviour was evaluated at Month 1 and 3 using the Elevated Plus Maze test. No significant differences in the time spent in the open arms at months 1 and 3 were shown between the two groups ($p>0.05$) (Figure 28A). However, ethological parameters evaluated, such as head dipping and number of entries in the open arms, allowed us to determine that the ASYN group performed significantly less open arm explorations compared to the control group, indicating an anxious-like behaviour (Figure 28B).

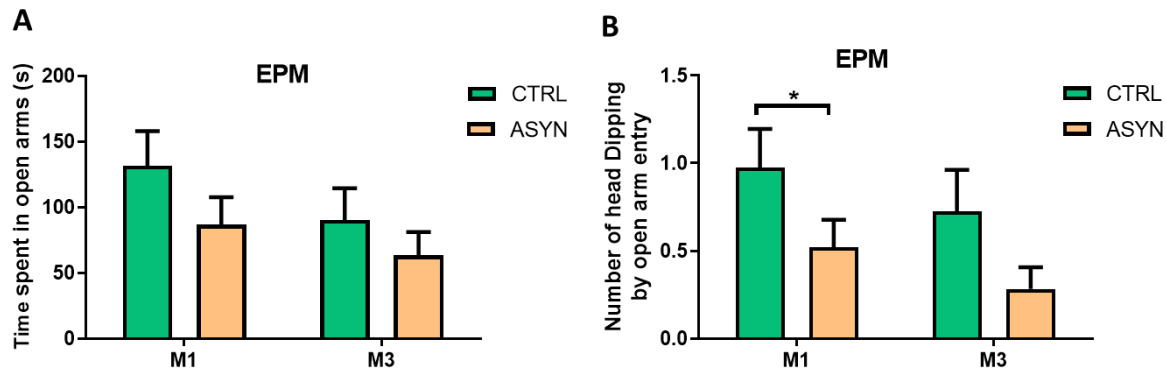


Figure 28. Assessment of anxious-like behaviour in the Elevated Plus Maze test. A. Evaluation of time spent in open arms (s) in EPM test at Month 1 & 2. No significant differences between groups. Time effect ($F(1, 17) = 11.99$; $p < 0.03$) B. Evaluation of average number of head dipping per open arm entry in EPM test. Significantly lower head dipping in ASYN group compared to CTRL ($*p < 0.05$). (n=19: 11 ASYN, 8 CTRL).

1.4.2 Depressive-like behaviour

Anhedonia was assessed using the sucrose preference test, and we found no significant differences in the percentage of sucrose intake between ASYN and CTRL animals, indicating that the former did not display any depressive-like behaviour.

1.5 HISTOPATHOLOGY

1.5.1 Dopaminergic Neurodegeneration: assessment of the lesion's extent

Neurodegeneration in the Substantia Nigra pars compacta (SNpc) projecting to the dorsal striatum was evaluated in all 3 cohorts, by assessing the tyrosine hydroxylase (TH) immunoreactivity in the nigrostriatal pathway. Intranigral injection of AAV-h α -syn resulted in a significant reduction of dopaminergic fibers, evidenced by a reduction of TH+ neurons in both striatum and SNpc, 4-month post injections. The progressive dopamine neuron death percentage was evaluated at an average of 30% in the striatum and 45% in the SNpc, compared to CTRL animals (Figure 29A, B).

We did see an overall intra-group variability, with dopaminergic loss in the AAV alpha-synuclein (ASYN) group ranging from 21% to 68% in the SNpc. However, the 3 cohorts which were injected one year apart, showed remarkable reproducibility despite this intra-group variability, with the same average of loss in both nigrostriatal structures. Additionally, we observed a significantly higher level of dopaminergic cell loss in the right SNpc compared to the left, indicating an asymmetrical degeneration (Figure 31A, B).

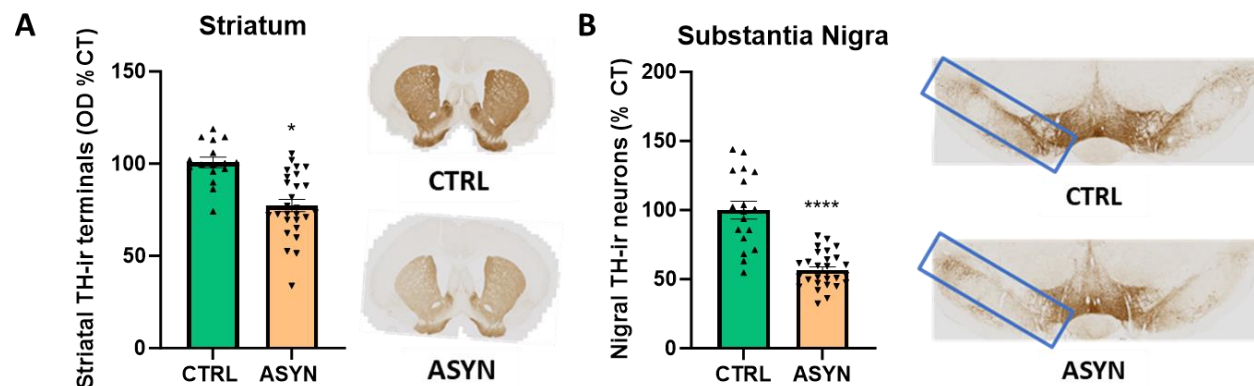


Figure 29. Evaluation of dopaminergic neurons in the dorsal striatum (A) and Substantia nigra pars compacta (B) of ASYN and CTRL rats. The percentage of TH+ neurons (mean \pm SEM) is shown compared to the mean value of CTRL. A. Images and optical density measurements of TH-ir terminals in the dorsal striatum, (* $p=0.01$). B. Images and stereological evaluation of TH-ir neurons in the substantia nigra, (**** $p<0.0001$). (ASYN: $n=42$; CTRL: $n=27$; pooled 3 cohorts).

1.5.2 Alpha-synuclein propagation

The propagation of alpha-synuclein was assessed in the entire brain, with 222 regions of interest that were defined thanks to the QUICKNII software, using the WHS atlas. We observed alpha-synuclein strings (Figure 30A) in both anterior and posterior regions from the injection site, with the protein reaching the olfactory bulb on one side and the brainstem on the other (Figure 30B, C).

The main regions with moderate to severe alpha-synuclein pathology included key regions of the nigrostriatal pathway such as caudate, putamen and substantia nigra pars compacta, in addition

to other regions of the midbrain such as the ventral tegmental area, the periaqueductal grey, the colliculus and the pretectal region. Several cortical regions also presented with moderate to severe alpha-synuclein scores, such as the cingulate, insular, association, entorhinal and perirhinal cortices. The primary and secondary motor and visual cortices also presented with alpha-synuclein strings. Additionally, we observed high alpha-synuclein scores in the hypothalamus, the amygdala and the basal forebrain region. As for the hippocampus and the fimbria, some ASYN rats scored 3 with a severe pattern of alpha-synuclein while others scored 0 with an absence of alpha-synuclein immunopositivity (Annexe Table 3).

Finally, the alpha-synuclein pattern spreading was more prominent on the right side (Figure 31D), with certain structures scoring more severely in the right hemisphere compared to the left such as the striatum, the secondary motor area, the insular and cingulate cortices and the basal forebrain region ($p=0.03$) (Figure 31C).

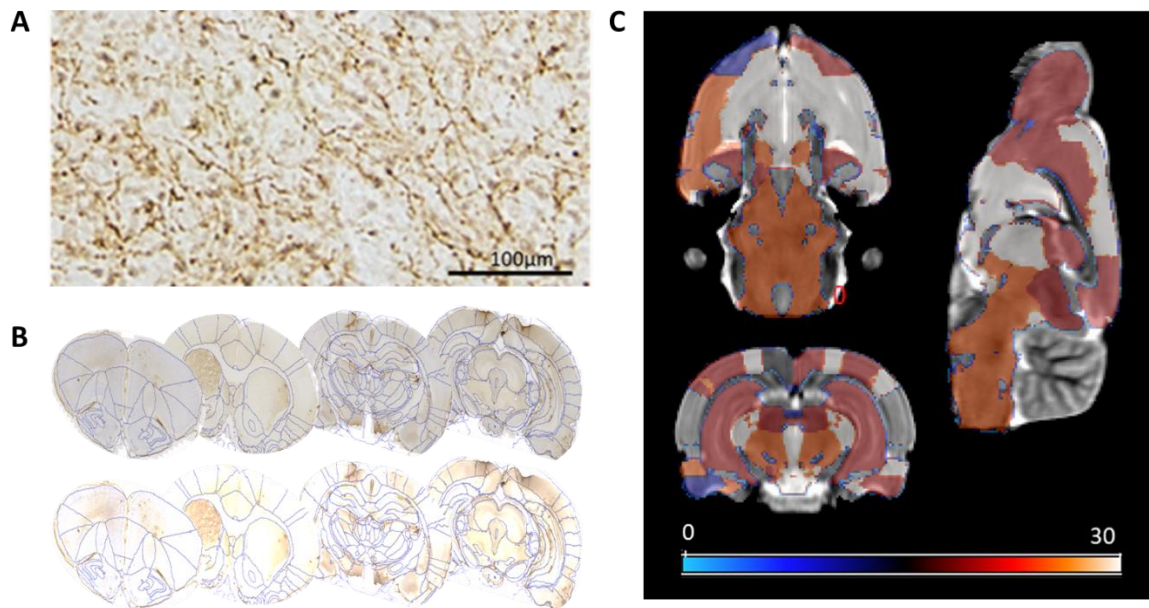


Figure 30. The evaluation of human alpha-synuclein (h- α -syn) propagation in ASYN group. A. α -synuclein strings observed in the striatum (x20). B. Representation of 4 out of 26 sections of a rat's brain, segmented into 222 ROIs, for h- α -syn quantification. C. 2D representation of α -synuclein spreading (average for ASYN: $n=13$).

1.5.3 Preliminary results: phospho-alpha-synuclein, aggregates and inflammation markers.

Staining of S219-phosphorylated alpha-synuclein, which is a marker for pathological α -syn was observed specifically in the ASYN rats' SNpc, but not the CTRL (Figure 32A). Alpha-synuclein aggregates were mainly observed in the olfactory bulb, the association cortex, the amygdala, the hypothalamus and the basal forebrain region (results to be confirmed by proteinase K treatment).

We assessed microglial activation using IBA1 marker and astrogliosis using GFAP marker, and found no differences between ASYN and CTRL rats, in any specific region of the brain, indicating that there were no neuroinflammatory processes detected in our model, 18 weeks p.i..

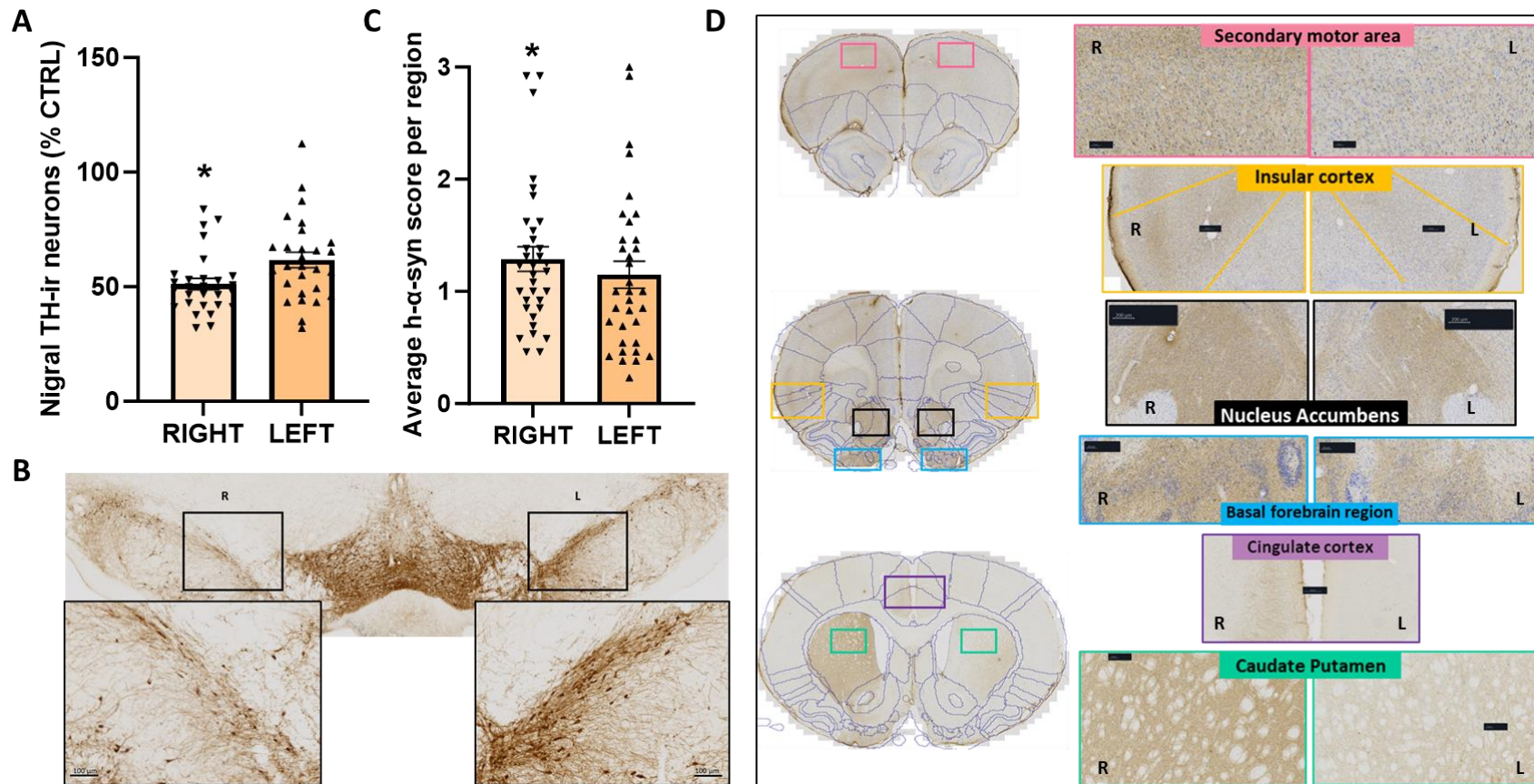


Figure 31. Assessment of asymmetrical neurodegeneration and alpha-synuclein accumulation in ASYN animals. A.B. Left and right comparison of TH immunoreactive cells in Substantia nigra pars compacta (* $p < 0.05$). C. Global h- α -syn score in left versus right hemisphere (* $p < 0.05$). D. Photos of 3 sections from 3 different ASYN brains, showing the asymmetrical spreading of alpha-synuclein in the secondary motor area, the insular and cingulate cortices, the striatum (caudate putamen), the nucleus accumbens and the basal forebrain region.

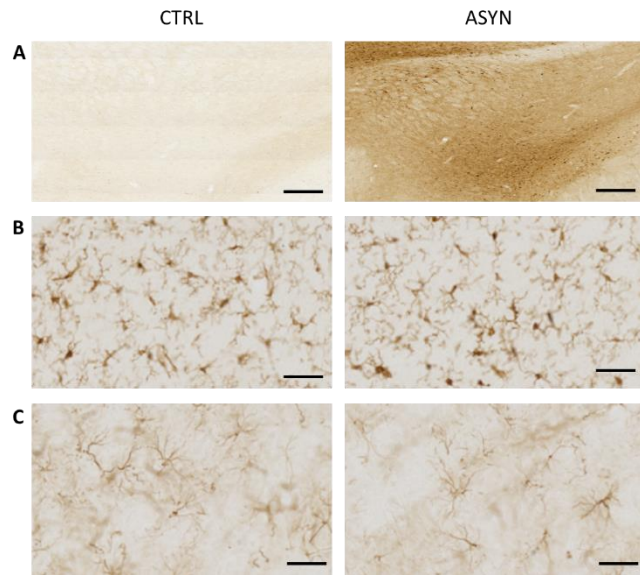


Figure 32. Assessment of alpha-synuclein phosphorylation and markers of neuroinflammation in the AAV alpha-synuclein model. A. Staining of S219-phosphorylated alpha-synuclein in the SNpc (scale bars: 200 μ m). B. IBA1 staining for microglia activation in the midbrain. C. GFAP staining for astrogliosis in the midbrain. (scale bars: 50 μ m).

1.6 DISCUSSION

In the present work, we have established that our AAV-mediated A53T human α -syn rat model induced moderate nigrostriatal dopaminergic neurodegeneration 18-weeks post-injection, evaluated at 30% in the striatum and 45% in the SNpc. These results diverged from other studies done on this model, where dopaminergic degeneration was evaluated between 60% and 80% (Bourdenx et al. 2015). It is worth noting that this variability was observed across several studies using the AAV model (Annexe Table 2), which can be due to the AAV type, the titer, the promoter... However, the reproducibility of the % of dopaminergic denervation over the 3 cohorts for which we used the same AAV preparation, shows a high degree of reliability in our model, despite observed intra-group variability. Interestingly, the variation in histological denervation profiles matched compellingly with the behavioural performance, which will be discussed further down.

We also noted an asymmetrical neurodegeneration with a significantly higher percentage of dopaminergic cell loss in the right Substantia Nigra compared to the left in ASYN rats. Consistently, a hemispheric asymmetry in nigrostriatal neurodegeneration has been described clinically, in early phases of PD (Djaldetti 2006).

As for alpha-synuclein immunopositivity, our unbiased whole-brain analysis confirmed the propagation of alpha-synuclein beyond the main transduction and tropism road. Indeed, we found alpha-synuclein in very distal regions to the injection site confirming the spreading nature of the protein in this synucleinopathy model. Interestingly, the asymmetry observed in neurodegeneration is also revealed in alpha-synuclein spreading which is more prevalent in the right hemisphere, where we observe the higher dopaminergic loss.

This asymmetry was evident in all three cohorts and was not due to any experimental bias, as we had two independent experimenters performing the stereotactic surgeries, alternating between the order of injection sites, with automatic volume injection, and later, blinded histological analyses. Many hypotheses have attributed this asymmetry to either a compensatory mechanism, or a lateralization of neuropathological changes (Blesa et al. 2011; Claassen et al. 2016).

The characterization of the AAV alpha-synuclein rat model on a behavioural level showed no spontaneous locomotor deficits across all three cohorts. This result is coherent with the percentage of dopaminergic neuronal loss observed in our animals which did not exceed 40%.

However, the evaluation of sensori-motor function revealed the onset of forelimb akinesia at M2 post-injection, similar to what was observed in the literature (Bourdenx et al. 2015). Remarkably, studies have shown that a functional reorganisation of the sensorimotor cortex is observed in early Parkinson disease, preceding the severe clinical motor dysfunction (Kojovic et al. 2012), which could explain the impairment in sensori-motor, but not locomotor activity.

The moderate loss of dopaminergic neurons and the lack of major motor deficits attributed to it, played in favour of our experimental design which involves a comprehensive cognitive evaluation of the rats during four months, with extensive behavioural tasks. Indeed, we could attribute any dysfunctions observed in these tasks to the cognitive function evaluated, without any motor impairment bias.

Working and spatial memory impairments are part of the non-motor symptoms observed in PD, amongst other executive function deficits (Simioni et al. 2007). In this model however, they were not impaired, as opposed to toxic PD models, in which working memory dysfunctions were

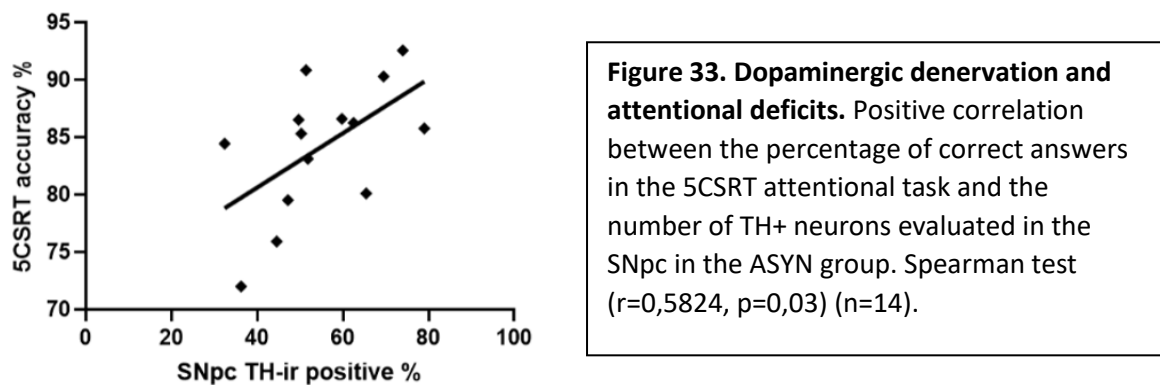
reported (Ferro et al. 2005). It is noteworthy to mention that these deficits emerge, and subsequently progress, according to a defined sequence, according to the disease's severity (Owen et al. 1997). We hypothesise that their evolution may be linked to the spatiotemporal progression of dopamine depletion within the striatum that projects to cortical afferents, in which case, our model's moderate dopaminergic death could explain the lack of dysfunction.

Although both working and spatial memory were not altered in our model, visuo-spatial learning was clearly impaired as evaluated in both the MWM test and the PVD test. Coincidentally, structures involved in the visuo-spatial function such as the fimbria and the visual cortex presented with high levels of alpha-synuclein strings. Additionally, a study by Schneider and colleagues in 2017 reported spatial learning deficits in PD patients, that could be attributed to very early signs of dopamine (DA) depletion independent of the presence of mild cognitive impairment in the patients, indicating that learning deficits precede memory deficits in the evolution of PD cognitive impairment.

On the other hand, little is known about the contribution of DA in cognitive flexibility (Klanker et al. 2013; Lhost et al. 2021), but our results showing no deficits in mental flexibility suggest that the frontostriatal network related to this function (Kimchi & laubach 2009), was not highly affected during the first few months post-injection in AS animals.

Attention dysfunction is another major part of cognitive decline in PD (Lawson et al. 2016; Ballard et al. 2002). In our model, we confirmed the presence of attentional deficits in ASYN animals compared to CTRL, in the touchscreen attentional task. This test, which includes assays of various neuropsychological constructs, and utilises appetitive rather than aversive motivation, offers a high translational potential, as it is similar to human CANTAB (Cambridge Neuropsychological Test Automated Battery) tests. Attentional impairments and fluctuations have been associated with lesions in the frontal lobe of the animal (Solari et al. 2013). Interestingly, we observed high levels of alpha-synuclein strings in the frontal cortex.

Additionally, the dopaminergic loss in the substantia nigra pars compacta positively correlated with attentional deficits evaluated by the percentage of correct answers in the Touchscreen's 5 Choice serial reaction test at 4-month pi. (Figure 33).



On the other hand, we noted the lack of strong parameters revealing anxiety, which are usually observed in other PD rodent models such as the MPTP mouse model (Da Cunha et al. 2017), and the 6OHDA rat model (Sun et al. 2015). However, studying ethological parameters of the EPM test revealed anxious-like behaviour in the ASYN model, which strongly supports the inclusion of such refined parameters when evaluating the wide spectrum of anxiety in animal models (Carobrez & Bertoglio 2005; Walf & Frye 2007). Alterations of the mesolimbic dopaminergic network in PD, as well as a smaller amygdala in PD patients' MRI, have been associated with anxiety (Thobois et al. 2017; Vriend et al. 2015). It should be noted that the amygdaloid area was amongst the regions with the most alpha-synuclein deposits.

All in all, these results show that alpha-synuclein deposits were found in most of the regions related to the functional deficits observed, supporting the link between the presence of alpha-synuclein and the appearance of cognitive and neuropsychiatric dysfunctions. However, we do not know the exact mechanisms by which the presence of the alpha-synuclein protein affected the neuronal network functioning in our model, nor the contribution of alpha-synuclein protein-protein interaction and cell-to-cell propagation.

1.7 CONCLUSION

Taken together, the moderate levels of dopaminergic neuronal loss and the level of motor and cognitive deficits observed, which are associated with early symptoms of PD allow us to conclude that this model is both a progressive and moderate model of PD, which simulates a rather early phase of the disease, making it advantageous for longitudinal therapeutic testing (Tagushi et al. 2020).

Furthermore, this model could also be interesting in testing pharmacological approaches targeting alpha-synucleinopathy, since the alterations in the behavioural phenotype, especially some of the non-motor symptoms, suggest that the deficits are not only linked to dopaminergic denervation, but to alpha-synuclein propagation and accumulation. Indeed, the specific topographical and chronological spread of alpha-synuclein lesions may have contributed to the appearance of these symptoms, and it would be interesting to evaluate the consequences of the removal of the toxic proteins in this model (Shahaduzzaman et al. 2015), by assessing whether or not it can rescue the behavioural deficits.

2 CHAPTER TWO:

IMAGING CHARACTERIZATION OF THE AAV ALPHA-SYNUCLEIN MODEL: STRUCTURAL AND FUNCTIONAL ALTERATIONS LINKED TO BEHAVIOURAL PHENOTYPE AND HISTOPATHOLOGY.

2.1 BACKGROUND AND AIMS

2.1.1 Neuroimaging in preclinical PD

In a Parkinson's disease context, the majority of the preclinical neuroimaging studies have been performed on toxin-based and transgenic models. In fact, the most used model has been the unilateral 6-OHDA rat, which was evaluated using DTI, MRS and rs-fMRI (Petiet et al. 2021). In DTI, it has shown decreased fractional anisotropy and axial diffusivity in the SN, as well as increased mean diffusivity in the SN and striatum, similar to what is observed in PD context compared to CTRL rats (Soria et al. 2011; Monnot et al. 2017). This DTI pattern is similarly observed in PD patients, as mentioned in the introduction (Chapter 3.3.3). In MRS, it has shown a decrease in NAA and an increase in GABA in the striatum, also similar to a clinical context (Coune et al. 2013). In rs-fMRI, studies have been more variable and mitigated, with some showing a decrease in functional connectivity in corticostriatal networks, which could be interpreted as a direct effect of the unilateral injection lesion done in the striatum (Zhurakovskaya et al. 2019). While other studies showed an increased FC in striatal networks, also in animals injected unilaterally in the striatum (Perlberg et al. 2018). Transgenic mice models have also shown unreliable results. For example, the PINK1 model exhibited a general decrease of functions in both quantitative and functional MRI (Cai et al. 2019), but these changes occurred in the absence

of any motor or cognitive deficits, making it difficult to understand the significance of such data in relation to disease progression.

Ultimately, these preclinical neuroimaging studies have been hampered by the limitations of the chosen animal model. It is also noteworthy to mention the lack of imaging in bilateral models of PD, especially in functional MRI, which as we know, evaluates the brain as a whole network, and for which unilateral models supplement a large bias, including compensatory mechanisms between the left and right hemispheres.

On the other hand, and most interestingly, very few preclinical studies evaluated iron accumulation in these models, with one team from Umea University using T2* acquisitions in a unilateral 6OHDA rat model (Virel et al. 2014; Olmeda-Diaz et al. 2017), and another showing decreased T2* in the MitoPark mouse model (Cong et al. 2016). Finally, to our knowledge, only one team has explored the brain's structural modification in a preclinical context, again, in a unilateral 6OHDA rat model, and observed grey matter volume modifications (Westphal et al. 2016).

Taken together, these information particulars encourage the exploration of routinely used clinical MRI sequences and analyses such T2-wi, T2*-wi, and rs-fMRI on a bilateral PD model with a good construct and face validity, with the aim of better translational frame in understanding imaging markers.

2.1.2 The AAV alpha-synuclein model's validated characteristics: what is left?

Based on the molecular pathology of both genetic and sporadic PD, the AAV alpha-synuclein model presents a high construct validity (Koprach et al. 2017). Also, as demonstrated repeatedly in the literature and in our work, it models the main hallmarks of PD, including the progressive dopaminergic degeneration, alpha-synuclein accumulation, phosphorylation and aggregation, and PD-like motor deficits. Additionally, as shown in the precedent chapter, it exhibits some early-phase non-motor symptoms, thereby showcasing a strong face validity.

However, its predictive validity is still immensely lacking. Some studies have used it to assess therapeutic candidates such as autophagy enhancement (He et al. 2016), inhibitors of Janus kinase (JAK)–signal transducer and activator of transcription signalling (Qin et al. 2016), glucocerebrosidase (Rocha et al. 2015), and calcineurin inhibitor FK506 (Van der Perren et al. 2015). Considering that the main assessment of their therapeutic efficacy has been conducted post-mortem, the use of neuroimaging could be an interesting approach for efficacy validation, and the amelioration of the model's predictive validity. But to do so, our model has to be first characterized on an imaging level, and at different timepoints, considering its progressive nature and its slow-developing phenotype.

In 2015, Van der Perren and colleagues were able to show that DAT binding significantly decreased in the ipsilateral caudate putamen of the A53T α -synuclein unilaterally injected rats compared to the eGFP CTRL rats, using DAT PET (Van der Perren et al. 2015). They also showed a decreased level of N-acetyl aspartate concentrations, in the ASYN rats' SN, using MRS. To our knowledge, this has been the only study where neuroimaging was used to evaluate the AAV α -synuclein model. In fact, despite its interest in the study of Parkinson's disease-associated synucleinopathy, our model has not yet been investigated in terms of MR structural and functional imaging.

2.1.3 Aims and study design

The aim of this part of the project is therefore to offer a comprehensive and multimodal MR imaging characterization of the AAV α -synuclein model. To do so, using our previous longitudinal experimental design, we implemented 3 MRI acquisition timepoints at 2-, 10- and 18-weeks post-injection (p.i.), with the COGSYN2021 cohort receiving a T2 structural acquisition and a T2* quantitative acquisition, and the COGSYN2022 cohort receiving a T2 structural acquisition and a rs-fMRI evaluation (Table 3).

2.2 STRUCTURAL CHANGES

2.2.1 Voxel based morphometry (VBM)

The morphological changes in each group were investigated using the T2w sequences. No significant differences between the two groups could be identified by VBM analysis, at any of the imaging timepoints. Nevertheless, the intra-group comparison between the different sessions showed morphological changes between each session only in the ASYN group (Figure XX A and B). Indeed, between the first and the second imaging sessions at 2- and 10-weeks p.i. respectively, we observed a signal decrease in different anterior and posterior regions of the brain, predominantly in the midbrain, with the substantia nigra in particular, as well as the fimbria, the primary somatosensory, motor, cingulate, insular, association, parietal and retrosplenial cortices (Figure 34; Table 5). At 18-weeks p.i. additional changes were observed in the diencephalon, the striatum, the hypothalamus, the hippocampus, the amygdala, and the entorhinal cortex, amongst other regions (Figure 34; Table 5).

2.2.2 ROI-based volumetry

We additionally performed an ROI-based study to assess possible volume changes in five chosen regions divided into left and right: The substantia nigra, the striatum, the amygdala, the diencephalon (thalamus, hypothalamus and subthalamic nucleus), and the hippocampus. We observed no significant changes in volumetry measures in ASYN rats compared to CTRL, nor overtime across the 3 MRI sessions (Table).

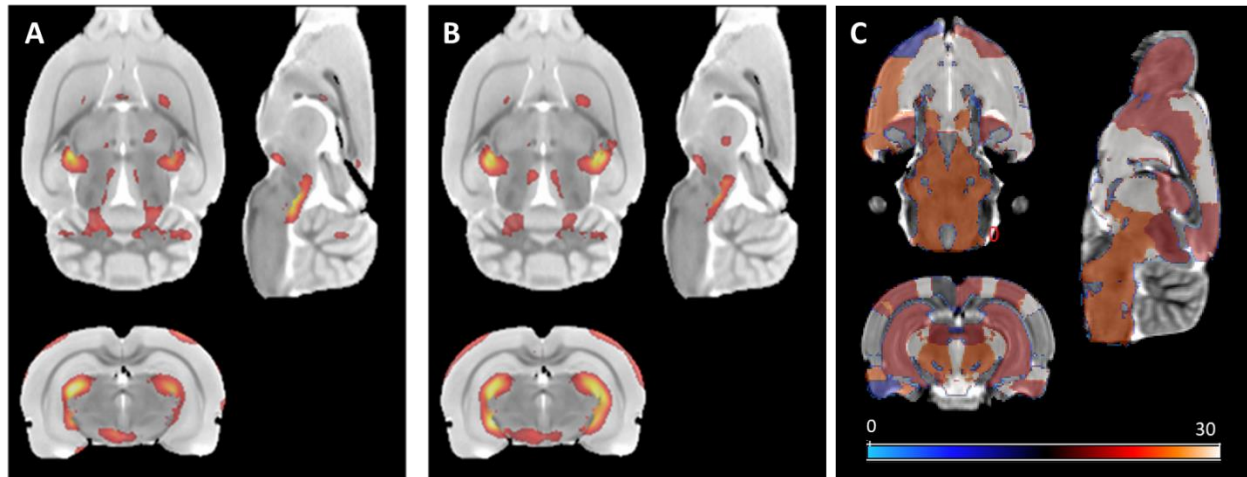


Figure 34. MRI structural changes and alpha-synuclein spreading in ASYN model. A. Voxel-wise differences in local grey matter in the ASYN group between 2 and 10 weeks p.i. assessed via VBM. B. between 2 and 18 weeks p.i. C. 2D representation of alpha-synuclein spreading in the brain of AAV-mediated alpha-synuclein overexpression rat model, 18 weeks after surgery (average of n=13 ASYN rats).

	MRI session 1		MRI session 2		MRI session 3	
	ASYN	CTRL	ASYN	CTRL	ASYN	CTRL
ICV	1482569.62	1484350.65	1487955.64	1482959.01	1489941.00	1498181.15
SN Left	2.80	2.79	2.85	2.84	2.81	2.77
SN Right	2.56	2.57	2.62	2.56	2.62	2.62
Striatum Left	41.67	41.44	41.55	41.72	41.52	41.85
Striatum Right	40.86	40.99	40.93	40.93	40.86	40.84
Amygdala Left	20.30	20.18	20.18	20.22	20.28	20.02
Amygdala Right	20.98	20.98	21.01	21.09	21.00	21.13
Diencephalon Left	49.52	49.66	49.57	49.50	49.63	49.51
Diencephalon Right	48.50	48.50	48.35	48.29	48.45	48.18
Hippocampus Left	44.66	44.71	44.74	44.75	44.79	44.75
Hippocampus Right	46.26	46.16	46.51	46.22	46.24	46.04

Table 4. Volumetric measures of selected ROIs in ASYN versus CTRL groups overtime. No significant changes between groups or overtime. Volume expressed in mm3. ICV= intracranial volume. (n=14 ASYN, n=6 CTRL).

2.3 IRON ACCUMULATION

Voxel based relaxometry (VBR) analysis did not reveal any differences in $R2^*$ mapping between the ASYN and CTRL groups for each MRI session, nor between each session for either groups.

$R2^*$ ROI-based analyses were then performed in 11 selected regions of interest. Only the right associative cortex displayed significantly higher values of $R2^*$ in the ASYN group compared to the CTRL during the first MRI session (t-test $p < 0.05$). In contrast, there were no significant differences in SN $R2^*$ values between both groups, as usually observed in a clinical context (Figure 35A).

Similarly, Perls' iron histochemistry evaluation revealed no specific iron accumulation in the ASYN brain, except along the syringe's line made during injection (Figure 35B).

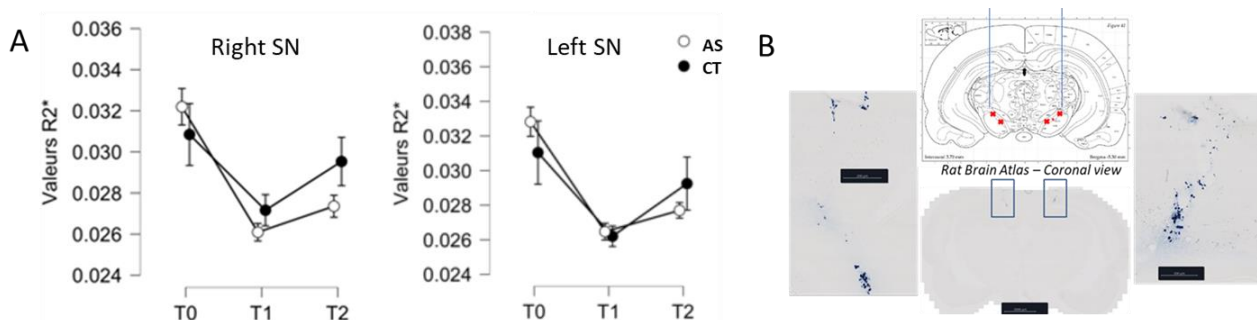


Figure 35. Evaluation of Iron accumulation in ASYN model. A. ROI-based analysis of $R2^*$ values in the SN both groups from the COGSYN2021 cohort: ASYN ($n=14$) & CTRL ($n=6$), over 3 MRI sessions: T0 at 2 weeks p.i., T1 at 10 weeks p.i. and T2 at 18 weeks p.i. B. Iron histochemistry in ASYN rat brain 18-weeks p.i. Perls staining only shows iron accumulation along the injection line.

2.4 FUNCTIONAL CONNECTIVITY

NBS analyses of the connectivity matrices between the ASYN and CTRL groups showed a hyperconnectivity pattern between many regions in the ASYN group at 18 weeks p.i. (Figure 36B, C). Several networks were modified, with regions such as the midbrain making $N=15$ abnormal connections, the primary and secondary visual cortex: $N=15$, the retrosplenial cortex: $N=23$, the cingulate cortex: $N=8$, the somatosensory cortex: $N=8$, the posterior parietal cortex: $N=7$, the fimbria: $N=5$, and the substantia nigra: $N=3$ abnormal connections.

In a neuroimaging framework, these brain regions are called nodes and constitute the edges of brain networks. The synchronization levels between the regions translate into abnormal connections, in this case an increased functional connectivity in their networks. These nodes have been represented graphically in figure 36D; the size of the line connecting the nodes correlates with the number of abnormal connections registered.

The graph demonstrates that the neuronal networks subject to this hyperconnectivity pattern include the basal ganglia network's connection with widespread frontal, temporal, parietal cortical as well as striatal and brainstem regions. Other networks involved are the corticostriatal–thalamic pathway and the fronto-parietal network. We also observe an asymmetrical pattern in the functional hyperconnectivity, with the left basal ganglia and cortico-cortical nodes being more prevalent than the right ones (Figure 36D).

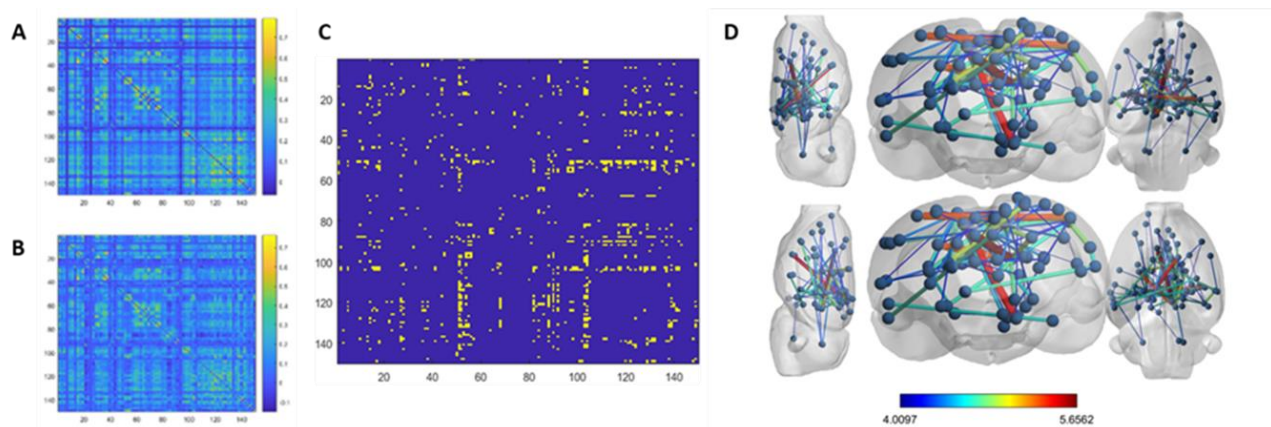


Figure 36. Functional connectivity between brain regions in ASYN animals compared to CTRL at 18-weeks p.i. A. Mean connectivity matrix in ASYN animals. B. Mean connectivity matrix in CTRL animals. C. The difference between the first two panels. Yellow pixels denote statistically significant differences between groups ($p > 0.05$, FDR-corrected for multiple comparisons). D. Glass brain depicting significantly increased functional connectivity between different regions in ASYN rats compared to CTRL rats.

2.5 DISCUSSION

2.5.1 Imaging and behavioural phenotype

The VBM structural study displayed an evolution of significant morphological differences in the ASYN brain, which were not detected by traditional ROI volumetry. These signal differences could be interpreted in mild reduced grey matter, which has not yet reached the critical point of atrophy, as to be detected by volumetry (Voormolen et al. 2010).

The alterations observed in the nigrostriatal pathway structures (SN and striatum) and the basal ganglia of the ASYN group, as well as the primary and secondary motor cortex, are coherent with the sensori-motor deficit observed in these animals, and can reflect the dopaminergic neurodegeneration described in these regions.

Other signal differences involved the prefrontal, cingulate and insular cortices, as well as the limbic structures, the diencephalon, the hippocampus and the fimbria. These regions play various roles in visuospatial learning and attention (Delgado-Alvarado et al. 2016; Almaguer-Melian et al. 2015), also impaired during ASYN rat behavioural evaluation.

The functional networks affected by the hyperconnectivity patterns are also associated with behavioural phenotypes. For example, visuo-spatial learning impairment which was observed in PD patients, has been mostly attributed to dysfunctions of the cortico-striatal circuits that include prefrontal and posterior parietal cortices (Galtier et al. 2009), highlighted here in the rs-fMRI analysis. Therefore, this abnormal functional connectivity can reflect the learning and attentional impairments observed in the ASYN animals.

Other major nodes include the visual and cingulate cortices, via their abnormal connections to structures of the basal ganglia. These regions are known to be involved in the directed and executive control of attention, one of the earliest dysfunctions to occur in early-phase PD (Botha & Carr 2012), a behavioural impairment observed in our model.

Last but not least, the parahippocampal-retrosplenial network exhibiting the most abnormal connections (N=23) in ASYN rats, is part of the larger limbic network, known to regulate functions like memory, emotional control, tactile feedback, and movement (Zeng et al. 2022). We postulate

that these alterations could be responsible for the deficits displayed in the Touchscreen paradigm, as it involves several of these functions.

2.5.2 Imaging and histopathology

2.5.2.1 *Alpha-synuclein*

The progressive MRI structural changes were observed in regions of interest which had the most severe alpha-synuclein scores. Indeed, insular, cingulate and entorhinal cortices, as well as the fimbria and the diencephalon (thalamus and hypothalamus) scored between 1.5 and 3 on the alpha-synuclein scale, and were all subject to signal changes between MRI sessions in ASYN animals. These ROIs are distal from the injection site and separate from the main nigrostriatal pathway, highlighting the potential of non-biased fine automated image analysis in revealing new and unexpected sites of neurodegeneration and tissue alteration beyond the primary lesioned pathway. In fact, these VBM analyses may not only reflect atrophy and neuronal degeneration but probably a general loss of tissue integrity due to toxic protein accumulation and aggregation.

On the other hand, it is hypothesized that certain brain regions are more permissible (sensitive) to synuclein pathology than others, and the spreading of the protein along specific connectome topologies can alter the functional connectivity of certain networks (Carli et al. 2020; Rahayel et al. 2022). This could be the case of the nigro-striato-cortical cholinergic network, whose functional connectivity was altered in ASYN animals. Interestingly, the 2 main hubs of this network are the basal forebrain region and the brainstem, which presented with high levels of alpha-synuclein deposits in all ASYN animals. This highlights a possible bidirectional link between network functional changes and alpha-synuclein propagation.

2.5.2.2 *Absence of iron accumulation*

Relaxometry analysis revealed that the AAV alpha-synuclein model does not exhibit any iron accumulation in the SN, nor in other brain regions, as assessed by the lack of magnetic

inhomogeneities during the T2* acquisition. This was confirmed by Perls histochemistry done post-mortem.

We hypothesise that this is due to the use of young adult rats which may not be as susceptible to iron accumulation as 24 to 28-month old rats (Suh et al. 2013). Indeed, investigating age-related iron deposition has shown that the concurrence of age and neurodegenerative processes induces alteration of iron homeostasis leading to an increase in iron level in the brain (Ficiarà et al. 2022). Another explanation is the lack of neuromelanin in albino rats' substantia nigra, which is considered a major iron storage in SNpc neurons (Barden & Levine 1983; Zecca et al. 2001).

2.5.3 Asymmetry

One of the most interesting result in our study has been the asymmetrical neurodegeneration observed in our bilateral model, with a significantly higher percentage of dopaminergic cell loss in the right substantia nigra compared to the left (Figure 31A, B), and a significantly more prevalent alpha-synuclein spreading in the right hemisphere (Figure 31C, D). This asymmetry is also noted in both the structural and functional alterations observed in the ASYN brain (Table 5; Figure 36D).

2.6 CONCLUSION

In conclusion the use of clinical imaging sequences on the AAV alpha-synuclein model has yielded interesting results, mainly in regards to backing up the face validity of the model, as most structural changes occurring in the midbrain, diencephalon and cortical areas, as well as the functional alterations in basal ganglia and cortico-striatal networks observed in preclinical MRI, were similar to those observed in PD patients in the early phase of the disease (J. Wang et al. 2015; Summerfield et al. 2005; Wolters et al. 2019).

The added value of preclinical neuroimaging studies is the ensuing and readily available histopathological analysis which has provided insights into the biological significance of the brain

imaging alterations, especially in regards to alpha-synuclein pathology, and how it can be perceived in MR imaging.

The application of this neuroimaging multimodal framework in other models of Parkinson's disease, could allow for a more comprehensive characterization, hence enabling researchers to make an educated choice depending on their needs.

	ALPHASYNUCLEIN HISTOLOGY (A)		VBM of T2w images in ASYN MRI W2>W18 (B)		rs-fMRI Connectivity matrices comparisons (W18>W2) in ASYN compared to CTRL (C)		
Functional ROI	ROI	AVERAGE SCORE	ROI	T score	ROI 1	ROI2	T score
ST	Striatum = Caudate Putamen L	1.85	striatum L	12.42458	striatum L	secondary visual cortex, lateral area L	4.11
	Striatum = Caudate Putamen R	2.77	striatum R	11.47665			
SN	Substantia Nigra = (SNpc, R, L) L	1.46	substantia nigra L	14.75288	substantia nigra R	isocortex R	4.53
	Substantia Nigra = (SNpc, R, L) R	1.15	substantia nigra R	39.09948	substantia nigra R substantia nigra L	hindbrain L secondary visual cortex, mediolateral area L	4.15 4.11
PALLIDUM	Globus Pallidus (ext, int) L	0.46	pallidum L	12.37483	NO functional coonectivity CHANGES IN Pallidum		
	Globus Pallidus (ext, int) R	0.69	pallidum R	11.55522			
	Ventral Pallidum L	0.54					
	Ventral Pallidum R	0.85					
NUCLEUS ACCUMBENS	Nucleus Accumbens (Shell + Core) L	1.00	NO STRUCTURAL CHANGES IN Nacc		accumbens nucleus L	midbrain L	4.77
	Nucleus Accumbens (Shell + Core) R	1.23					
DIENCEPHALON	Subthalamic Nucleus L	1.25	diencephalon R	13.4412	diencephalon L	prelimbic infralimbic cortex L	4.15
	Subthalamic Nucleus R	1.25	diencephalon L	11.56524			
	Thalamic Nuclei L	1.00					
	Thalamic Nuclei R	1.08					
	Zona Incerta L	1.31					
	Zona Incerta R	1.62					
HYPOTHALAMUS	Hypothalamic area L	3.00	hypothalamus L	13.59101	hypothalamus L	retrosplenial dysgranular cortex R	4.11
	Hypothalamic area R	2.92	hypothalamus R	11.49234			
			preoptic area L	11.99504			
			preoptic area R	11.49239			
MIDBRAIN	Periaqueductal gray L	2.31	midbrain R	29.86144	midbrain L	corpus callosum R	5.35
	Periaqueductal gray R	2.00	midbrain L	12.97527	midbrain L	corpus callosum L	4.93
	Pretectal region L	1.46			midbrain L	cingulum L	4.13
	Pretectal region R	1.23			midbrain L	prelimbic infralimbic cortex L	4.24
	Colliculus (sup, inf) L	1.38			midbrain L	accumbens nucleus L	4.77
	Colliculus (sup, inf) R	1.31			midbrain R	septum L	4.27
	Ventral Tegmental Area (VTA) L	1.62			midbrain L	septum L	4.76
	Ventral Tegmental Area (VTA) R	1.54			midbrain L	fimbria R	4.54
					midbrain R	primary visual cortex L	4.65
					midbrain L	cingulate cortex, area 2 R	5.66
					midbrain L	cingulate cortex, area 2 L	4.03
					midbrain R	cingulate cortex, area 2 L	4.45
					midbrain R	cingulate cortex, area 1 L	4.1
					midbrain R	cingulate cortex, area 2 R	4.1
					midbrain R	medial Ventral lateral dorsolateral orbital cortex L	4.03

	ALPHASYNNUCLEIN HISTOLOGY (A)		VBM of T2w images in ASYN MRI W2>W18 (B)		rs-fMRI Connectivity matrices comparisons (W18>W2) in ASYN compared to CTRL (C)		
Functional ROI	ROI	AVERAGE SCORE	ROI	T score	ROI 1	ROI2	T score
HIPPOCAMPUS	Hippocampus = DG+CA1+CA2+CA3 L	1.08	hippocampal formation L	12.55708	hippocampal formation L	retrosplenial dysgranular cortex R	4.42
	Hippocampus = DG+CA1+CA2+CA3 R	1.00	hippocampal formation R	11.75813	hippocampal formation R	retrosplenial dysgranular cortex R	4.68
FIMBRIA	Fimbria L	0.85	fimbria L	13.32267	fimbria L	ectorhinal cortex R	4.21
	Fimbria R	0.85	fimbria R	11.97373	fimbria R	primary somatosensory cortex, hindlimb region L	4.92
PRE & INFRA LIMBIC	Prelimbic Area L	0.83	prelimbic infralimbic cortex L	12.28411	prelimbic infralimbic cortex L	retrosplenial dysgranular cortex R	4.76
	Prelimbic Area R	0.92	prelimbic infralimbic cortex R	11.38235	prelimbic infralimbic cortex L	midbrain L	4.54
	Infralimbic Area L	0.42			prelimbic infralimbic cortex L	primary visual cortex L	4.21
	Infralimbic Area R	0.58			prelimbic infralimbic cortex R		
AMYGDALA	Amygdaloid Area L	1.69	amygdala L	12.78413	amygdala L	isocortex L	4.25
	Amygdaloid Area R	0.92	amygdala R	23.664		midbrain L	4.24
OLFACTORY	Olfactory bulb L	0.73	olfactory structures L	12.06113	olfactory structures R	diencephalon L	4.15
	Olfactory bulb R	1.00	olfactory structures R	12.03226		retrosplenial dysgranular cortex R	4.01
HINDBRAIN	Brainstem L	1.69	hindbrain R	12.96055	hindbrain L	dorsolateral entorhinal cortex R	4.62
	Brainstem R	1.38	hindbrain L	11.58605	cerebellum L		
			cerebellum R	11.41023	cerebellum R	substantia nigra R	4.15
BF CHOLINERGIC SYSTEM			cerebellum L	11.62313	cerebellum R	cingulate cortex, area 2 L	4.4
	Basal forebrain region L	1.38	diagonal domain L	14.0068	diagonal domain L	isocortex R	4.22
INSULAR CORTEX	Basal forebrain region R	1.85			diagonal domain L	secondary auditory cortex, ventral area R	4.36
	Insular cortex (granular, dysg, ag) L	0.85	agranular insular cortex, dorsal part L	23.6874	agranular insular cortex, ventral part R	secondary visual cortex, mediolateral area L	4.17
	Insular cortex (granular, dysg, ag) R	1.46	agranular insular cortex, dorsal part R	11.87243	granular insular cortex L	retrosplenial dysgranular cortex R	5.44
			agranular insular cortex, ventral part R	11.63345		retrosplenial granular cortex, b region R	4.37
						secondary auditory cortex, ventral area L	4.33

	ALPHASYNUCLEIN HISTOLOGY (A)		VBM of T2w images in ASYN MRI W2>W18 (B)		rs-fMRI Connectivity matrices comparisons (W18>W2) in ASYN compared to CTRL (C)		
Functional ROI	ROI	AVERAGE SCORE	ROI	T score	ROI 1	ROI2	T score
RETROSPLENIAL CORTEX	Retrosplenial cortex (granular, dysgranular) L	0.23	retrosplenial dysgranular cortex L	14.57744	retrosplenial dysgranular cortex R	diagonal domain L	5.44
		0.46	retrosplenial dysgranular cortex R	13.70656	retrosplenial dysgranular cortex R	corpus callosum L	4.88
	Retrosplenial cortex (granular, dysgranular) R		retrosplenial granular cortex, c region R	12.72883	retrosplenial dysgranular cortex R	fimbria R	4.76
			retrosplenial granular cortex, b region R	11.65025	retrosplenial dysgranular cortex L	isocortex R	4.71
			retrosplenial granular cortex, c region L	11.56918	retrosplenial dysgranular cortex R	hippocampal formation R	4.68
			retrosplenial granular cortex, b region L	11.53214	retrosplenial dysgranular cortex R	internal capsule L	4.56
					retrosplenial dysgranular cortex R	preoptic area L	4.52
					retrosplenial dysgranular cortex R	corpus callosum R	4.43
					retrosplenial dysgranular cortex R	hippocampal formation L	4.42
					retrosplenial dysgranular cortex R	primary somatosensory cortex R	4.41
					retrosplenial granular cortex, b region R	agranular insular cortex, ventral part R	4.37
					retrosplenial granular cortex, c region R	primary visual cortex L	4.35
					retrosplenial granular cortex, b region L	parietal cortex, posterior area, rostral part L	4.26
					retrosplenial dysgranular cortex R	isocortex R	4.24
					retrosplenial dysgranular cortex R	olfactory structures R	4.24
					retrosplenial granular cortex, b region L	corpus callosum R	4.24
					retrosplenial granular cortex, b region L	cingulum L	4.23
					retrosplenial dysgranular cortex R	parietal cortex, posterior area, dorsal part L	4.22
					retrosplenial granular cortex, c region R	frontal assocn cortex L	4.19
					retrosplenial dysgranular cortex R	secondary auditory cortex, ventral area R	4.13
					retrosplenial dysgranular cortex R	hypothalamus L	4.11
					retrosplenial granular cortex, b region L	corpus callosum L	4.06
					retrosplenial dysgranular cortex R	prelimbic infralimbic cortex R	4.01
CINGULATE CORTEX	Cingulate cortex (area 1,2) L	0.54	cingulate cortex, area 1 L	13.65496	cingulate cortex, area 2 R	midbrain L	5.66
	Cingulate cortex (area 1,2) R	1.31	cingulate cortex, area 1 R	20.1164	cingulate cortex, area 2 L	dorsal intermediate entorhinal cortex R	4.71
			cingulate cortex, area 2 R	17.46389	cingulate cortex, area 2 L	midbrain R	4.45
			cingulate cortex, area 2 L	11.38416	cingulate cortex, area 2 L	cerebellum L	4.4
					cingulate cortex, area 1 L	midbrain R	4.1
					cingulate cortex, area 2 R	midbrain R	4.1
					cingulate cortex, area 2 L	perirhinal cortex L	4.03
					cingulate cortex, area 2 L	midbrain L	4.03
VISUAL CORTEX	Primary visual area L	0.92	primary visual cortex L	11.42267	primary visual cortex R	parietal cortex, posterior area, rostral part L	5.33
	Primary visual area R	0.62	primary visual cortex R	16.45123	primary visual cortex L	midbrain R	4.65
	Secondary visual area medial part L	2.92	secondary visual cortex, lateral area L	13.77167	primary visual cortex L	fimbria R	4.21
	Secondary visual area medial part R	2.92	secondary visual cortex, lateral area R	15.57221	primary visual cortex L	retrosplenial granular cortex, c region R	4.35
			primary visual cortex, binocular area L	11.52233	primary visual cortex, monocular area R	primary somatosensory cortex, oral dysgranular zo L	4.31
			primary visual cortex, binocular area R	11.36746	primary visual cortex, monocular area L	primary somatosensory cortex, oral dysgranular zo L	4.16
			primary visual cortex, monocular area L	11.34175	secondary visual cortex, lateral area L	corpus callosum L	4.23
					secondary visual cortex, lateral area L	striatum L	4.11
					secondary visual cortex, lateral area L	internal capsule R	4.68
					secondary visual cortex, lateral area L	primary auditory cortex L	4.85
					secondary visual cortex, lateral area L	primary somatosensory cortex, barrel field R	4.22
					secondary visual cortex, lateral area L	isocortex R	4.17
					secondary visual cortex, mediolateral area L	septum L	4.39
					secondary visual cortex, mediolateral area L	diagonal domain L	4.17
					secondary visual cortex, mediolateral area L	substantia nigra L	4.11

	ALPHASYNNUCLEIN HISTOLOGY (A)		VBM of T2w images in ASYN MRI W2>W18 (B)		rs-fMRI Connectivity matrices comparisons (W18>W2) in ASYN compared to CTRL (C)		
Functional ROI	ROI	AVERAGE SCORE	ROI	T score	ROI 1	ROI2	T score
ENTORRHINAL CORTEX	Entorhinal cortex L	0.73	medial entorhinal cortex L	12.99886	dorsal intermediate entorhinal cortex R	cingulate cortex, area 2 L	4.71
	Entorhinal cortex R	1.18	medial entorhinal cortex R	13.30852	dorsolateral entorhinal cortex R	amygdala L	4.62
			dorsolateral entorhinal cortex R	11.51425			
ASSOCIATION CORTEX	Association cortex (frontal, parietal, temporal) L	1.00	lateral parietal association cortex R	25.19616	NO functional coonectivity CHANGES		
		1.62	lateral parietal association cortex L	12.96581			
PERIRHINAL CORTEX	Perirhinal cortex (35,36) L	2.23	NO STRUCTURAL CHANGES IN PERIRHINAL CX		perirhinal cortex L	parietal cortex, posterior area, dorsal part L	4.04
	Perirhinal cortex (35,36) R	1.92			perirhinal cortex L	cingulate cortex, area 2 L	4.03
MOTOR CORTEX	Primary motor cortex L	0.46	primary motor cortex L	11.65533	secondary motor cortex L	internal capsule L	4.27
	Primary motor cortex R	1.00	primary motor cortex R	11.66815			
	Secondary motor cortex L	0.69	secondary motor cortex L	11.41012			
	Secondary motor cortex R	1.38	secondary motor cortex R	11.94441			
SOMATOSENSORY CORTEX	Primary somatosensory cortex (forelimb, hindlimb, barrel, trunk, dysgranular, facerep) L	0.38	primary somatosensory cortex, shoulder region R	27.2218	primary somatosensory cortex, hindlimb region R	cingulum R	4.17
		0.77	primary somatosensory cortex, dysgranular zone R	23.90065	primary somatosensory cortex, hindlimb region L	fimbria R	4.92
	Primary somatosensory cortex (forelimb, hindlimb, barrel, trunk, dysgranular, facerep) R		primary somatosensory cortex, forelimb region R	22.47878	primary somatosensory cortex R	retrosplenial dysgranular cortex R	4.41
			primary somatosensory cortex, oral dysgranular R	17.94628	primary somatosensory cortex R	parietal cortex, posterior area, caudal part R	4.31
			primary somatosensory cortex, hindlimb region R	15.83684	primary somatosensory cortex, oral dysgranular zo L	primary visual cortex, monocular area L	4.16
					primary somatosensory cortex, oral dysgranular zo L	primary visual cortex, monocular area R	4.31
			primary somatosensory cortex, trunk region R	15.50901	primary somatosensory cortex, barrel field R	secondary visual cortex, lateral area L	4.22
			primary somatosensory cortex, jaw region R	12.72488	primary somatosensory cortex, hindlimb region L	corpus callosum R	4.09
			primary somatosensory cortex, upper lip region R	12.25981			
			primary somatosensory cortex, barrel field R	12.2017			
			primary somatosensory cortex R	11.98039			
			primary somatosensory cortex L	13.09267			
			primary somatosensory cortex, jaw region L	13.08271			
			primary somatosensory cortex, hindlimb region L	12.5678			
			primary somatosensory cortex, forelimb region L	12.52363			
			primary somatosensory cortex, trunk region L	12.24115			
			primary somatosensory cortex, upper lip region L	11.581			
			primary somatosensory cortex, barrel field L	11.55798			
			primary somatosensory cortex, shoulder region L	11.51304			
			primary somatosensory cortex, oral dysgranular zo L	11.39746			
			primary somatosensory cortex, dysgranular zone L	11.38795			

	ALPHASYNNUCLEIN HISTOLOGY (A)		VBM of T2w images in ASYN MRI W2>W18 (B)		rs-fMRI Connectivity matrices comparisons (W18>W2) in ASYN compared to CTRL (C)		
Functional ROI	ROI	AVERAGE SCORE	ROI	T score	ROI 1	ROI2	T score
AUDITORY CORTEX			primary auditory cortex R	11.72805	primary auditory cortex L	secondary visual cortex, lateral area L	4.85
			secondary auditory cortex, dorsal area L	12.13995	primary auditory cortex L	secondary auditory cortex, ventral area L	4.68
			secondary auditory cortex, dorsal area R	11.58427	secondary auditory cortex, ventral area L	bed nucleus of the stria terminalis R	4.72
			primary auditory cortex L	11.4214	secondary auditory cortex, ventral area L	granular insular cortex L	4.33
					secondary auditory cortex, ventral area R	cerebellum R	4.36
PARIETAL CORTEX					secondary auditory cortex, ventral area R	retrosplenial dysgranular cortex R	4.13
			parietal cortex, posterior area, dorsal part R	18.67093	parietal cortex, posterior area, caudal part R	parietal cortex, posterior area, rostral part L	4.73
			parietal cortex, posterior area, rostral part R	17.52633	parietal cortex, posterior area, caudal part R	primary somatosensory cortex R	4.31
			parietal cortex, posterior area, caudal part R	14.9858	parietal cortex, posterior area, dorsal part L	retrosplenial dysgranular cortex R	4.22
			parietal cortex, posterior area, dorsal part L	11.79073	parietal cortex, posterior area, rostral part L	primary visual cortex R	5.33
			parietal cortex, posterior area, caudal part L	11.43439	parietal cortex, posterior area, rostral part L	pituitary L	4.27
			parietal cortex, posterior area, rostral part L	11.41745	parietal cortex, posterior area, rostral part L	retrosplenial granular cortex, b region L	4.26
					parietal cortex, posterior area, dorsal part L	perirhinal cortex L	4.04

Table 5. Functionally grouped regions used for VBM, fMRI and h- α -syn histological analyses.

(A) Average alpha-synuclein score in 34 regions (left and right) in ASYN brains. * **Score using the semi-quantitative scale**

(B) Detailed VBM ROI with T scores corresponding to significative differences between 2 and 18 weeks p.i. in ASYN group.

**** Score from the t-tests using SPM**

(C) Detailed rs-fMRI ROI with T scores corresponding to the ASYN/CTRL group comparison of 2 paired ROI, at 18 weeks p.i. using NBS method. (n=13 ASYN n=9 CTRL). ***** Score from the NBS analysis**

3 CHAPTER THREE:

BEYOND CONVENTIONAL IMAGING ANALYSES: EXPLORATION OF TEXTURE FEATURES AS FINER IMAGING MARKERS TO SPATIALLY CORRELATE WITH THE HISTOPATHOLOGICAL SIGNATURE.

3.1 BACKGROUND AND AIMS

3.1.1 Radiomics in Neurodegenerative diseases

Over the past decade, we have witnessed an exponential growth in the field of medical image analysis, benefitting from the AI revolution, and the development of new tools such as machine learning which facilitated pattern recognition, as well as the ability to analyse large data sets (Coppola et al. 2021). As a result of these advances, radiomics has emerged as a practice involving the high-throughput extraction of quantitative features from medical images, and their conversion into mineable data, identifying patterns and associations between image features and clinical outcomes, to aid in diagnosis and prognosis strategies (Lambin et al. 2017).

Although it has been used in cancer research since the late 1990s, the application of Radiomics in the context of neurodegenerative diseases is in its relative infancy (Salvatore et al. 2019). It was first explored in the context of Alzheimer's disease (AD) by Sørensen and colleagues in 2016. They worked on the hypothesis that although cognitive impairment is known to be associated with hippocampal volume reduction, perhaps finer hippocampal texture alteration preceding the volume decrease could inform on earlier stages of the disease with mild cognitive impairment (MCI). They were able to correlate hippocampal texture abnormalities with MCI and postulated

that texture features could serve as a prognostic neuroimaging marker of early cognitive impairment (Sørensen et al. 2016). They also proposed a texture working hypothesis, in which the texture features they extracted could reflect the presence of neurofibrillary tangles and amyloid-beta plaques between neurons in the hippocampus. A study by Colgan and colleagues managed to correlate histological measures of tau burden with the MRI texture feature kurtosis, in an AD mouse model (Colgan et al. 2017). To our knowledge, this is the only study combining texture feature analysis with post-mortem brain histopathology, in AD, and so Sørensen's hypothesis is yet to be confirmed.

Bearing that in mind, a recent study in our laboratory, used texture features in a combination of clinical and preclinical settings to explore the underlying tissular changes of textures in a stroke brain. First, they demonstrated that texture features in the hippocampus and the entorhinal cortex were strongly correlated with stroke patients' cognitive scores, and these features could be used to predict post-stroke cognitive impairment with 88% accuracy. Then they applied the same first order texture feature measurements on the hippocampus of an animal model of ischemic stroke (the middle cerebral artery occlusion model), and were able to correlate them with neuronal density (Betrouni et al. 2019). We therefore decided to use this top-down framework in a PD context.

3.1.2 MRI Texture features in PD: from clinical findings to preclinical investigations

In Parkinson's disease, the application of Radiomics and texture feature analysis is also at its very beginning. It has been explored for FDG PET (Y Wu et al. 2019) and DAT SPECT (Rahmim et al. 2016), but most studies have used it on functional and structural MRI acquisitions.

In structural T1 and T2 images, one of the earliest studies found significant textural differences in the dentate nucleus, basilar pons, and SN pars compacta of PD patients compared to healthy controls (HC) (Sikio et al. 2015). Later, studies were conducted using texture based-models to evaluate their diagnostic abilities by distinguishing PD from HC, with some reaching 80% accuracy (Guan et al. 2022) and 98% accuracy (Cui et al. 2022). One study even differentiated subjects

based on sex and found 96% accuracy in women and 99% in men (Solana-Lavalle & Rosas-Romero 2022).

Others have explored texture features' ability to distinguish idiopathic Parkinson's from other parkinsonian syndromes such as Multiple System Atrophy (MSA) or Progressive Supranuclear Palsy (PSP). They showed a 92% accuracy in the differential diagnosis, especially between PD and PSP (Tupe-Waghmare et al. 2022). By combining texture features in the putamen and UPDRSIII scores, they were also able to distinguish PD and MSA (Pang et al. 2020).

It should be noted that each team employed a different model with different choices of ROIs and different feature selection techniques.

Some performed texture-based analysis on QSM and $R2^*$ maps in the substantia nigra specifically, and were able to distinguish PD from HC (Cheng et al. 2019; Li et al. 2019). The QSM texture analysis outperformed that of $R2^*$.

One study performed radiomics analysis on rs-fMRI data, distinguishing PD from HC with up to 81% accuracy. They found that the discriminative features were mainly located in brain regions of the sensorimotor network and the lateral parietal cortex (Shi et al. 2022).

All of these studies focus on the differential diagnostic potential of texture features, but none of them actually investigates their correlation to the appearance of motor or non-motor symptoms, nor the underlying pathological changes that could possibly be reflected by these markers.

3.1.3 Aims: Top-down exploration in our model

In our laboratory, as mentioned in the introduction, the application of radiomics has shown that texture features in the hippocampus, amygdala and thalamus, correlated with slight cognitive changes in PD patients with different cognitive phenotypes (Betrouti et al. 2020). Texture features measured in the Substantia Nigra, the Putamen, the Caudate nucleus and the thalamus, were significantly associated with clinical scores for motor handicap as well (Betrouti et al. 2021).

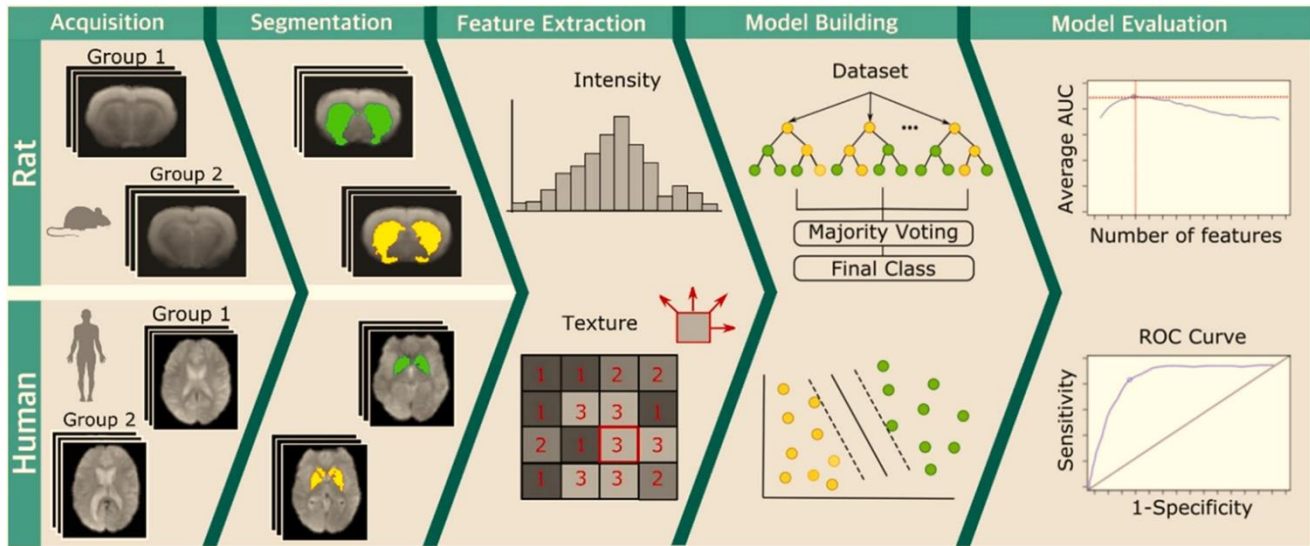


Figure 37. Major steps of radiomics pipeline: image acquisition, region of interest definition (segmentation) and pre-processing, feature extraction, feature selection, and classification. The model building and evaluation were only performed in clinical context as shown in Betrouni et al. 2020;2021. Part of this thesis project was to apply this pipeline on the AAV animal model of PD. (From Ruiz-España et al. 2023).

Feature	Description	Equation
First-order statistics		
Mean	Mean image grey level values	
SD	Standard deviation of grey level values	
Kurtosis (Kurt)	Kurtosis is a measure of whether the data are heavy-tailed or light-tailed, relative to a normal distribution. Positive kurtosis indicates a peaked distribution, while negative kurtosis indicates a flat distribution	$Kurt = E \left[\left(\frac{X - \text{Mean}}{SD} \right)^4 \right]$
Skewness (Skew)	Skewness quantifies the lack of symmetry: it is zero for a symmetric distribution and negative for left-skewed data	$Skew = E \left[\left(\frac{X - \text{Mean}}{SD} \right)^3 \right]$
Second-order statistics		
Homogeneity contrast (Cont)	Uniformity of texture intensity (a measure of the closeness of the distribution of elements in the co-occurrence matrix) Contrast represents the degree to which the texture intensity levels differ between voxels (i.e. local intensity variations). It will favour contributions from $p(i,j)$ away from the diagonal	$\text{Homogeneity} = \sum_{i=0}^{G-1} \sum_{j=0}^{G-1} \frac{P(i,j)}{(i-j)^2}$ $\text{Contrast} = \sum_{i=0}^{G-1} \sum_{j=0}^{G-1} (i-j)^2 \cdot P(i,j)$
Entropy (Ent)	Entropy represents the degree of uncertainty (a measure of randomness)	$\text{Entropy} = - \sum_{i=0}^{G-1} \sum_{j=0}^{G-1} P(i,j) \cdot \log(P(i,j))$
Correlation (Corr)	Correlation represents the degree of mutual dependency between pixels	$\text{Correlation} = \frac{\sum_{i=0}^{G-1} \sum_{j=0}^{G-1} \{i \cdot j\} \cdot P(i,j) - [\mu_x \mu_y]}{\sigma_x \sigma_y}$
Sum of squares (SumSqr)	Sum of squares also called variance gives a high weighting to elements that differ from the average value	$\text{SumSQR} = \sum_{i=0}^{G-1} \sum_{j=1}^{G-1} (i - \mu)^2 P(i,j)$
Sum average (SumA) Sum variation (SumV)	Sum average measures the relationship between occurrences of pairs with lower intensity values and occurrences of pairs with higher intensity values. Quantifies brightness Sum variation represents the global variation in the sum of the grey-levels of voxel-pairs distribution	$\text{SumAvg} = \sum_{l=1}^{2G} l \cdot P_{x+y}(j)$ $\text{SumV} = \sum_{l=1}^{2G} (l - \text{SumAvg})^2 \cdot P_{x+y}(i)$
Inverse difference moment (IDM)	The IDM corresponds to small contributions from in-homogeneous areas ($i \neq j$). The value is low for in-homogeneous images and relatively high for homogeneous images	$\text{IDM} = \sum_{i=0}^{G-1} \sum_{j=1}^{G-1} \frac{P(i,j)}{1 + (i-j)^2}$

Table 6. List of Texture features computed, together with a description of their significance, equations and models. G number of grey levels used, I intensity value of a neighbour voxel, j intensity value of a reference pixel, $P(i,j)$ probability of the appearance of the (i,j) pair in the co-occurrence matrix, μ mean value of P, P_x and P_y marginal probabilities, σ_x , σ_y SD of P_x and P_y , respectively. (From Betrouni et al. 2021).

We therefore proposed to use the same texture-based analysis, with the selection of the same features used in Betrouni et al. 2021 (Table 6), to be computed and analysed in the structural T2wi that were acquired in our AAV alpha-synuclein model (Figure 37).

The goal was to correlate the texture feature data with both the behavioural scores of the animals and the histological results we obtained. The latter would rely on precise spatial correlation which can be achieved thanks to the precise segmentation performed in histology analysis.

3.2 RESULTS AND CORRELATIONS

We analysed 10 texture features in several chosen regions of interest, including the substantia nigra, the striatum and the hippocampus. The texture features included first order statistics, that do not take into consideration voxel neighbourhood: Mean gray level, Standard deviation (SD) of gray levels, Kurtosis, Skewness; as well as second order statistics, computed from the occurrence matrix which is built by considering the neighbouring voxels. These features included: homogeneity (aka. angular second moment), Contrast, Entropy, (aka. measure of randomness), Correlation, Variance (aka sum of squares), Sum average, and Inverse difference moment (InvDiff).

The analysis revealed differences between the ASYN and CTRL groups, mainly a significant increase in both kurtosis and energy parameters in the right Substantia Nigra, in the ASYN rat compared to the CTRL, at 18-weeks pi. (Figure 38).

We plotted the texture feature data extracted from the images against the different behavioural scores obtained during the at different timepoints in our longitudinal study, as well as the histological data acquired post-mortem. We obtained the following correlations:

3.2.1 Texture features and behavioural parameters

First and second order texture features computed in the substantia nigra, in images acquired at 10-weeks p.i., positively correlated with the number of adjusting steps in the stepping test evaluated at month 3 and 4 of the longitudinal study (Spearman's coefficient $r > 0.5$, $p < 0.001$).

Texture features computed in the striatum 2-weeks p.i. also correlated with both the distance travelled and the speed level in the spontaneous locomotor actimetry test evaluated in the first month (Spearman's coefficient $r>0.5$, $p<0.001$).

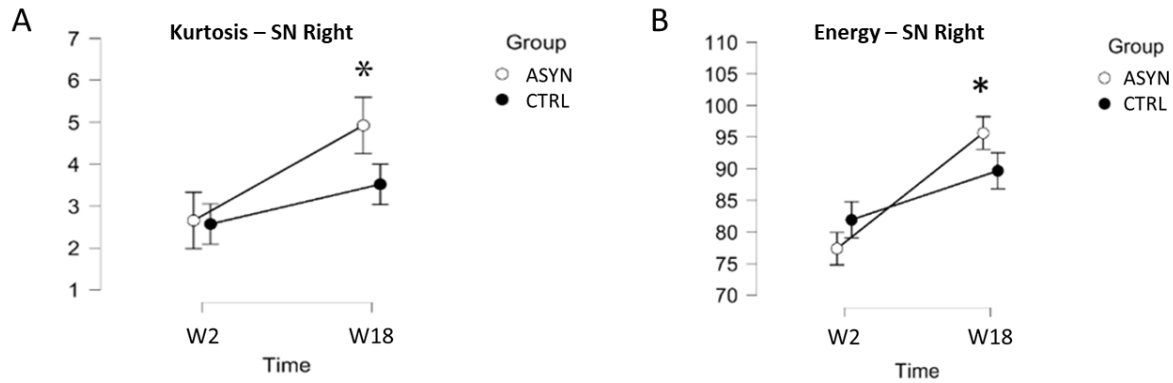


Figure 38. Texture features comparison of the Substantia Nigra in ASYN versus CTRL animals, between MRI sessions 1 and 3, at 2- and 18-weeks p.i. respectively. (* $p<0.05$)

3.2.2 Texture features and neurodegeneration

We also observed positive correlations between different first and second order texture features computed in the substantia nigra and the striatum, measured using the images at 18-weeks p.i., with the dopaminergic neuronal density quantified post-mortem (Spearman's coefficient $r>0.5$, $p<0.001$).

3.2.3 Texture feature and alpha-synuclein deposits

First and second order texture features computed in the Substantia Nigra, the Striatum and the Hippocampus, using the images acquired at 18-weeks p.i., revealed correlations with the scores of alpha-synuclein deposits in the SN, the striatum and the hippocampus, respectively, in the ASYN group (Spearman's coefficient $r>0.5$, $p<0.001$).

3.3 DISCUSSION

The preliminary results reported herein constitute the first steps towards the application of texture analysis for the extraction of additional knowledge from images. This application in the AAV animal model has added valuable input to our imaging characterization study. First, it proved the texture-based analysis feasibility in small cohorts of animal models. The large data set made from computing selected features in all animals at different timepoints in their pathological progression and in several regions of interest, accounts for the intra-group variability that could be observed in the ASYN model. These finer analyses allowed us to make correlations with both behavioural and histopathological scores, hence suggesting that the imaging features reflect both the underlying tissue changes occurring in the brain, as well as the changes in the behavioural phenotype, progressing overtime.

In fact, texture features in the nigrostriatal pathway mirrored the dopaminergic degeneration which was observed in both the striatum and SN, as shown in the histology study, even though the actual volume of these structures in the ROI-based studies did not significantly differ over the three MRI sessions. This confirms that ROI-based texture analysis is a more sensitive image analysis technique that could detect very subtle changes in the signal, in this case, when the neurodegeneration was valued at 30 to 40 %, and therefore has not yet reached a critical point leading to major morphological changes in the structure.

Additionally, texture feature scores in these two main structures of the nigrostriatal pathway also correlated with the sensori-motor scores evaluated in the stepping test at month 3 and 4, thereby showing that these subtle image alterations can also reflect the evolution of akinesia overtime in the animals.

Notably, both first and second order texture features also correlated with the alpha-synuclein scores, not only in the SN and striatum, but also in the hippocampus, which in some ASYN rats presented with a high level of alpha-synuclein strings while in others, had no alpha-synuclein deposits at all. This suggests that the features can also reflect the different spreading patterns of

the protein, and could eventually be used as a marker of synucleinopathy, and its cell damage consequences.

It would be interesting to apply this texture-based analysis on the entire list of regions of interest that were found to be altered in the VBM study but showed no differences in volumetric measures, and see if they also quantitatively correlate with the alpha-synuclein deposit scores in these same regions.

Ultimately, using this analysis framework in different models of PD, or even other neurodegenerative diseases, and studying correlations with the cellular signature by different biochemical and histological techniques, could potentially establish texture features as an early imaging biomarker of Parkinson's disease's neurodegeneration and proteinopathy. The use of other models which have neuroinflammation or iron accumulation can widen the spectrum of the possible underlying biological changes reflected by texture features.

To this end, we proposed a working hypothesis supporting the idea that texture features may be sensitive to earlier stages of the disease process as illustrated in Figure 39.

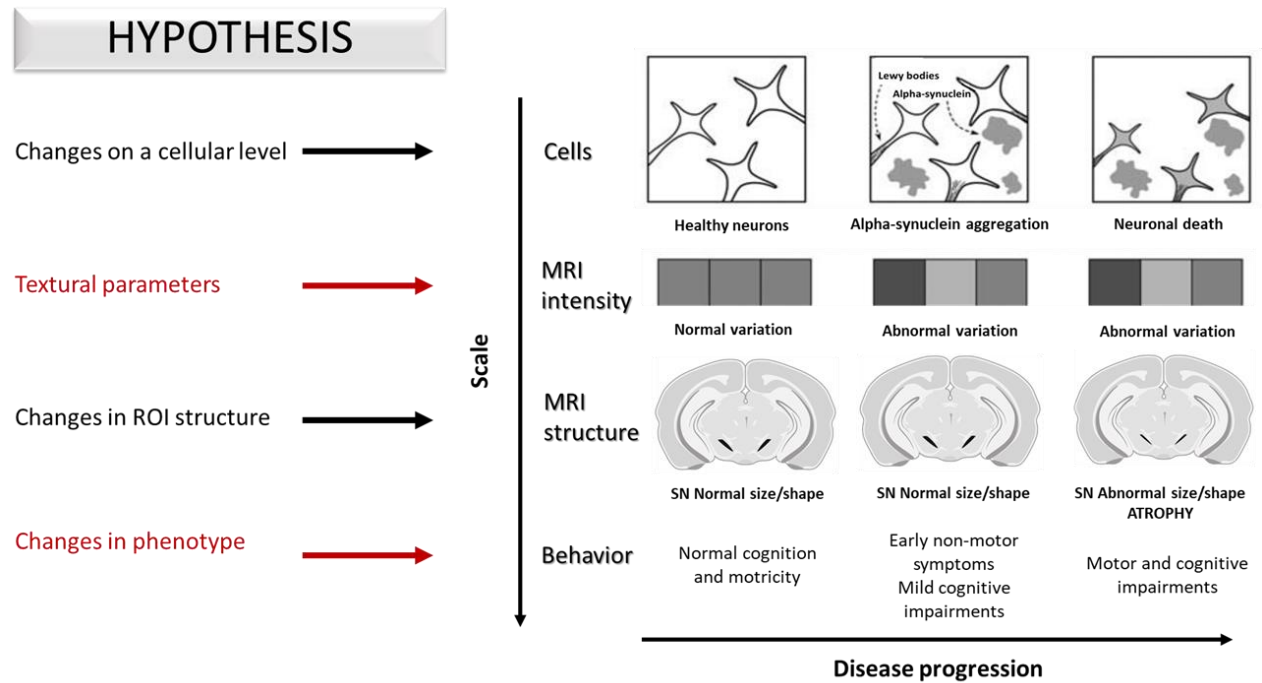


Figure 39. Schematic view of the proposed texture working hypothesis in animal models of PD. Top row: Alpha-synuclein and Lewy bodies pathology in the brain, as well as neuronal loss (Neuroinflammation and oxidative stress could also be evaluated depending on the model). Second row: changes in the statistical properties of the image intensities due to the synucleinopathy and early stage of neurodegeneration, may be reflected as certain textural patterns prior to atrophy. Third row: atrophy manifests as the shrinkage and possible morphological and volumetric change of the brain structures. Fourth row: progression of the behavioural phenotype from normal to early to advanced motor and non-motor impairments.

3.4 CONCLUSION

In 2016, Robert Gillies wrote: “Images Are More than Pictures, They Are Data”. But they can only become data, and to a certain extent, possible biomarkers, when we find a way to interpret the underlying anatomical, cellular and molecular changes that are reflected in images. This process remains a challenge, especially in neurology, because unlike the oncology field, where we can readily have biopsies of the tissue, the brain’s histological signature remains a mystery and only the association of clinical cohorts with brain biobanks could afford the kind of analysis at the human level.

Nevertheless, the analysis framework we propose here, with application of advanced texture-based analysis used in clinical research on animal models of the disease has allowed us to add the histopathology facet to the global analysis blueprint, and has yielded interesting results.

Radiomics has also been called “the bridge between medical imaging and personalised medicine” (Lambin et al. 2017). As we know, PD is a multisystem heterogenous disease that can widely benefit from the advances in precision medicine, and radiomics studies will undoubtedly propel these advances, and support an earlier diagnosis and a better clinical monitoring of the disease.

4 CHAPTER FOUR:

APPLICATION OF THE 3-FACET METHODOLOGY IN TOXIN-BASED MODELS OF PD. PRELIMINARY RESULTS AND PROOF OF CONCEPT.

4.1 BACKGROUND AND AIMS

This last part of our project will concentrate on the application of the methodological framework combining multimodal imaging evaluation, histopathological assessment and description of behavioural phenotype progression, on different and complementary animal models of PD.

This will allow us to validate the imaging representation of certain common histological features such as dopaminergic denervation, but also other parameters which were lacking in our alpha-synuclein genetic model, such as iron accumulation and inflammatory mechanisms in the brain.

To that end, we chose the more established toxin-based models, which are known to exhibit many signs of oxidative stress and neuroinflammation.

4.1.1 Description of the selected toxin-based models

The 6-OHDA rat model is the most widely used and studied model of nigrostriatal lesions, with a highly reproducible dopaminergic degeneration. It is however dependent on the amount of 6-OHDA injected and the injection site (Betarbet et al. 2002). As described in the introduction, this neurotoxin is most commonly injected unilaterally in the substantia nigra, medial forebrain bundle, or striatum. It induces a significant dopaminergic loss, ranging from 50% (striatum-injected) to 95% (MFB-injected) (Blandini et al. 2008), as well as an important inflammatory response with microglial activation (Cicchetti et al. 2002). The unilateral form of the model also exhibits gross and significant motor disturbances such as rotation behaviour in response to

dopamine agonists, and spontaneous limb asymmetries (Meredith & Kang 2006). However, the fact that disease in humans affects the brain bilaterally limits the face validity of the unilateral 6OHDA model. Moreover, compensation mechanisms resulting from the intact site, such as dopaminergic fiber sprouting, alleviate the PD-related deficits, making the evaluation of complex functional behaviour somewhat unreliable (Deumans et al. 2002).

Therefore, for the purpose of this study which includes a comprehensive behavioural evaluation, and for comparative purposes with the AAV alpha-synuclein model, the first neurotoxic model we chose is the bilateral intranigral 6OHDA rat model. Studies have shown that it exhibits both motor and cognitive deficits, accompanied by anxious-like and depressive behaviours (Campos et al. 2013; Ferro et al. 2005; Santiago et al. 2010). On the other hand, 6-OHDA rats might have been the most characterized PD models in MR imaging, but only in their unilateral form, as detailed earlier (Results: Chapter 2/ background). To our knowledge, no study has focused on MRI in bilateral models of 6-OHDA.

The second chosen neurotoxic model is the bilateral intranigral MPTP rat. This model is much less studied in literature. Da Cunha and colleagues have suggested that it is a good representative of the early phase of PD, particularly for the study of non-motor symptoms. Indeed, they have shown that MPTP-lesioned rats had reduced dopamine denervation compared to other MPTP and 6OHDA models (less than 60% loss), which translated in only mild motor impairments. This allowed the evaluation of cognitive tasks without the risk of confounding interpretations that can happen in the context of severe motor dysfunction (Ferro et al. 2005). Bilateral MPTP-injected animals exhibited specific learning and memory impairments (Da Cunha et al. 2001), as well as depressive-like behaviour (Santiago et al. 2010). They have been used for studying neuroprotective and cognition improving treatments (Huang et al. 2015). This MPTP rat model also has never been studied on an imaging level.

It is important to note that both of our chosen models can be identified as moderate bilateral neurotoxic PD models, due to the low doses of neurotoxins injected in the SN. We therefore postulate that bilateral intranigral 6-OHDA and MPTP rat models make interesting candidates for the 3-facet methodology application.

4.1.2 Study design & aims:

Due to the acute nature of neurotoxic models and their propensity to compensate and recuperate after lesion, especially the 6-OHDA model (Deumens et al. 2002), we decided to reduce their evaluation to 8 weeks. 6OHDA, MPTP and CTRL animals underwent several behavioural examinations, to assess motor, cognitive and emotional skills, as well as 2 MRI evaluations at Month 1 and 2 post-injection, which included a structural T2-wi and a T2*-wi (Figure 40). Histological studies to evaluate dopaminergic degeneration were done post-mortem.

The first objective was to explore imaging parameters in these different models and their possible correlations with both the behavioural phenotype and histological features. The second objective was to assess both similarities and differences between these toxin-based moderate models and the AAV alpha-synuclein model, keeping in mind that our entire project has focused on the modelling of early-phase PD. The comparisons between these different preclinical models could add a translational value to our methodological framework. For instance, similarities in the interpretation of imaging results on a histological level, in specific ROIs, between 2 or 3 complimentary models can validate them as markers of specific biological processes. The same logic could be applied if 2 models had similar imaging alterations in regions involved in a specific functional impairment.

Toxin-based Models Experimental Design

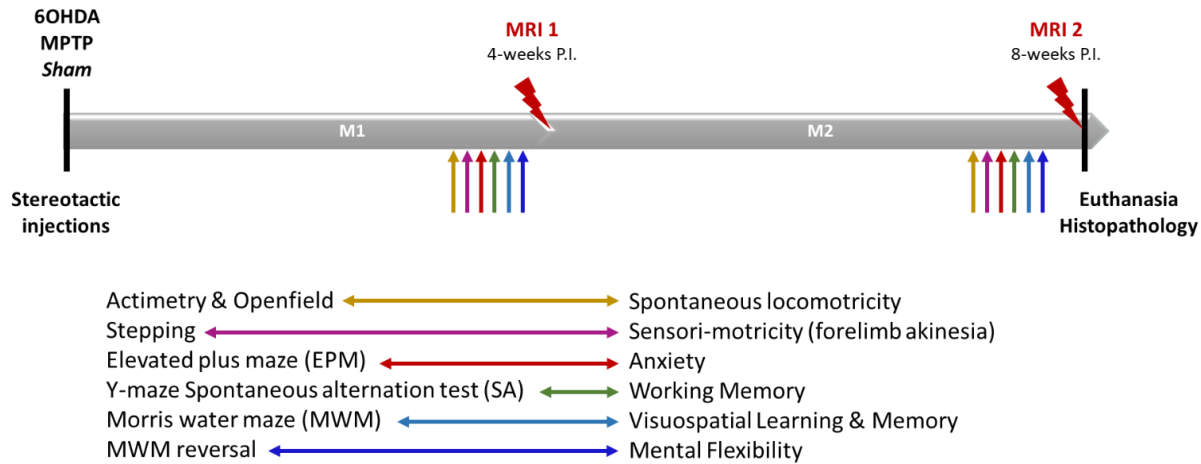


Figure 40. Toxin-based model experimental design. 6-OHDA (n=12), MPTP (n=14), and CTRL (n=10) rats underwent several behavioral analyses, evaluating motor, cognitive and emotional skills, as well as 2 MRI evaluations (T2-wi and T2*-wi) at month 1 (M1) and month 2 (M2) post-injection.

4.2 BEHAVIOURAL EVALUATION

4.2.1 Motor and sensorimotor evaluations

4.2.1.1 Spontaneous locomotor activity

Spontaneous locomotor activity was evaluated in MPTP, 6OHDA and CTRL sham rats at M1 and M2 p.i.. Both the travelled distance (cm) and the rearing number significantly decreased between M1 and M2 for all three groups ($p < 0.05$) (Figure 41A, B). This could be due to a motivational decrease because the actitrack arena is no longer a novel environment that the rats want to explore.

MPTP animals showed no differences in any of the parameters evaluated in actimetry, compared to CTRL animals, implying that this group had no dysfunction in spontaneous locomotor activity. 6OHDA animals performed significantly lower number of rearing in M2, compared to CTRL ($p < 0.05$) (Figure 41B), suggesting a vertical motor impairment in this group.

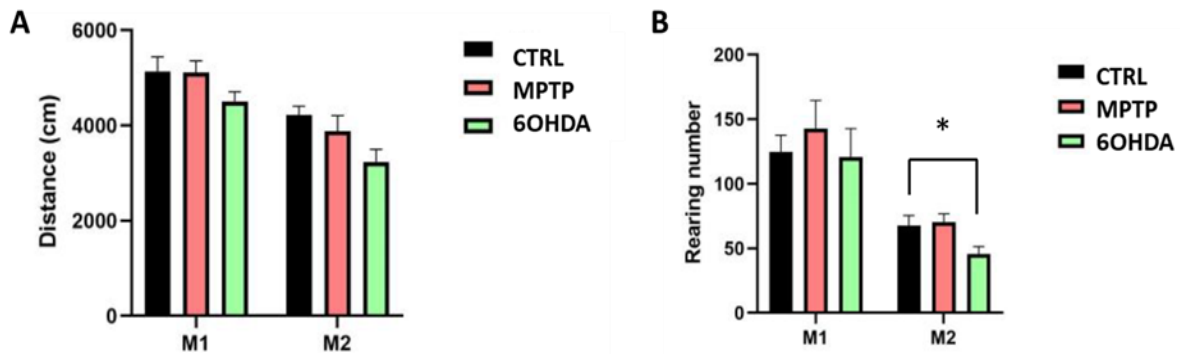


Figure 41. Spontaneous locomotor evaluation of toxin-based models. A. Analysis of travelled distance (cm) in an actimeter. Significant group effect ($F_{2, 32} = 3.404$; $p < 0.05$) and time effect ($F_{1, 32} = 46.32$; $p < 0.01$). Significant decrease in distance travelled between M1 and M2 for all three groups ($p < 0.05$). B. Analysis of the rearing number (vertical motor activity) in an actimeter. Significant decrease in the rearing number between M1 and M2 for all three groups ($p < 0.05$), and significant difference in rearing number at M2 between 6-OHDA and CTRL groups (* $p < 0.05$). ($n=12$ 6-OHDA, $n=14$ MPTP, and $n=10$ CTRL)

1.7.1.1 Sensori-motor activity

As for sensori-motricity, we performed the stepping test to evaluate forelimb akinesia, also at M1 and M2 p.i.. We observed a significant decrease in postural adjustments in the 6OHDA group between M1 and M2, indicating the progressive onset of forelimb akinesia (Figure 42A). At M2,

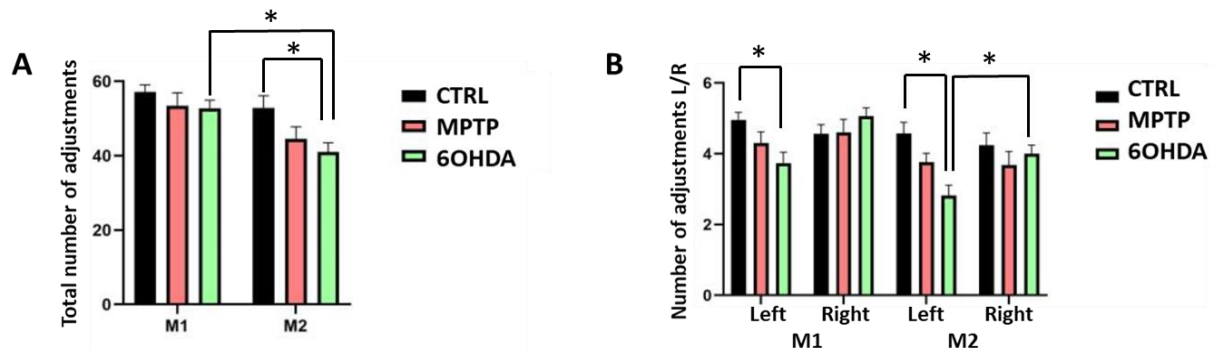


Figure 42. Sensorimotricity and Forelimb akinesia evaluation of toxin-based models. A. Analysis of the sum of left and right adjustment steps during the stepping test. Time effect ($F_{1, 32} = 18.91$; $p < 0.01$) and group effect ($F_{2, 32} = 3.311$; $p < 0.05$). Significant difference at M2 between 6OHDA and CTRL groups ($p < 0.05$). Significant decrease of total step adjustments in 6OHDA rats between M1 and M2 ($p < 0.01$). B. Differential analysis of left and right step adjustments. For the left forelimb, a time effect ($F_{1, 32} = 18.64$; $p < 0.01$) and a group effect ($F_{2, 32} = 7.965$; $p < 0.01$) are observed. For the right forelimb, only a time effect was observed ($F_{1, 32} = 33.76$; $p < 0.01$). Significant difference between the left and right paw for the 6OHDA group at M1 and M2 ($p < 0.01$). Significant difference in the left paw between 6OHDA and CTRL groups at M1 ($p < 0.05$) and M2 ($p < 0.01$). ($n=12$ 6-OHDA, $n=14$ MPTP, and $n=10$ CTRL).

the number of adjustments performed by the 6OHDA group is significantly lower than that of the control group (Figure 42A). We also noted a significant decrease in adjustments in the left forelimb compared to the right in 6OHDA rats, at both M1 and M2, indicating a lateralized impairment in sensori-motricity in this group (Figure 42B).

As for the MPTP group, no significant differences were observed in the number of adjustments compared to the CTRL group at either timepoints, nor any significant progression between M1 and M2 (Figure 42A, B).

4.2.2 Cognitive evaluation

4.2.2.1 Working memory

Next, we compared the performances of the three groups in the Y-maze spontaneous alternation test, to assess working memory. We observed no significant differences between any of the groups in the number of alternations performed by rats (Figure 43), indicating that animals alternated correctly between the different arms at M1 and M2 p.i.. We can conclude that neither

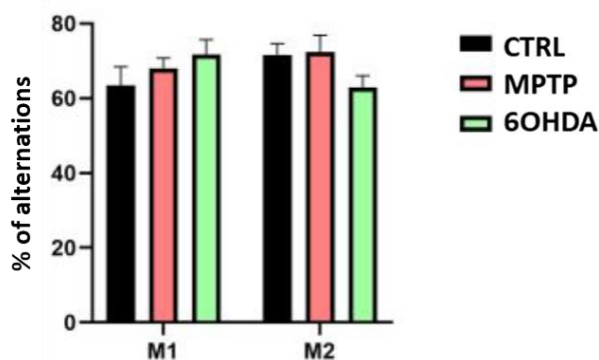


Figure 43. Analysis of the alternation score in the Y-maze spontaneous alternation test in toxin-based models. No significant differences were found between the groups or at any time points. ($n=12$ 6-OHDA, $n=14$ MPTP, and $n=10$ CTRL)

MPTP nor 6OHDA rats displayed a working memory impairment.

1.7.1.2 Visuospatial learning and memory

We performed the Morris Water maze test to assess spatial reference learning and memory in rats at M1 and M2. Using the same MWM evaluation paradigm described earlier, we first

evaluated the initial learning over four consecutive dates. We observed a significant decrease in latency to find the platform between Day 1 and Day 2, in all three groups (Figure 44A), indicating a successful learning process. Additionally, on probe test day, when we removed the platform, all three groups spent significantly more time in the target quadrant (Figure 44B), showing spatial memory consolidation. Therefore, neither MPTP, nor 6OHDA rats exhibited any impairment in spatial learning or memory.

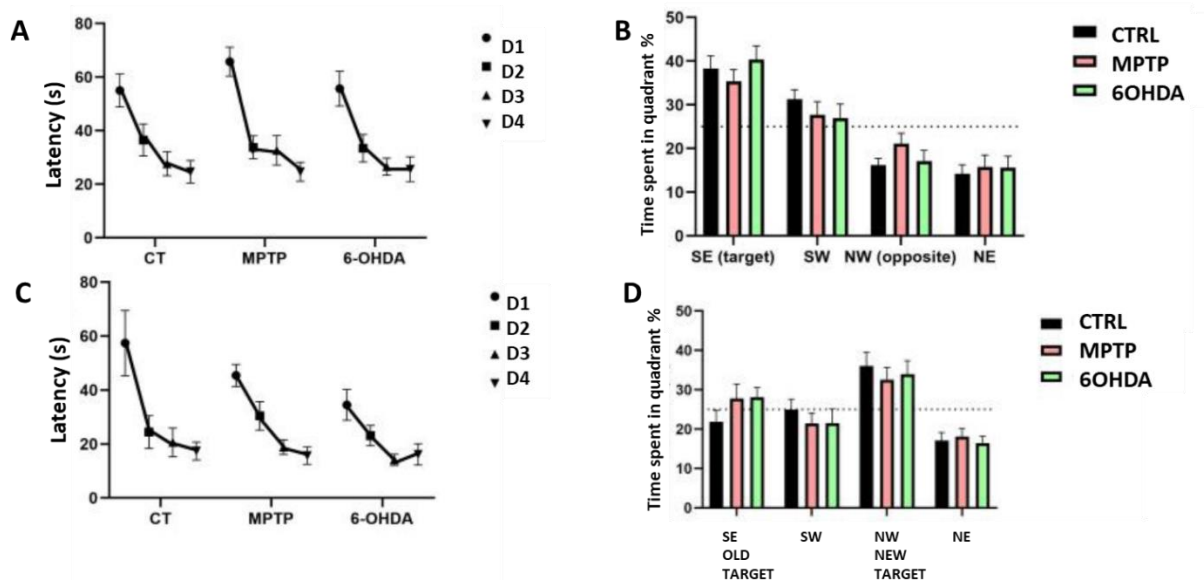


Figure 44. Visuospatial learning, memory and cognitive flexibility evaluation of toxin-based models in the MWM test. A. Initial phase of learning. Significant differences between day 1 and 2 for all three groups ($p < 0.01$). B. Probe test: Analysis of the time spent in the four quadrants when the platform is removed. Effect of the quadrants ($F_{2.4, 77} = 18.64$; $p < 0.0001$). All three groups spend significantly more time in the target quadrant than in the other quadrants ($p < 0.01$). C. Reversal learning phase, when platform is switch from old to new target quadrant. Analysis of latency to reach the new platform location shows time or group effects. D. Reversal probe test: Analysis of time spent in the quadrants. Effect of quadrant ($F_{2.5, 80} = 13.28$; $p < 0.0001$). All 3 groups spend significantly more time in the new target quadrant than in the other quadrants ($p < 0.01$). ($n = 12$ 6-OHDA, $n = 14$ MPTP, and $n = 10$ CTRL).

4.2.2.2 Mental flexibility

We then performed MWM reversal to assess cognitive flexibility in the neurotoxic models. During the reversal learning phase, the learning curves for the new location of the platform were similar

between the 3 groups (Figure 44C). On reversal probe test day, in the platform's absence, all 3 groups spent significantly more time in the new target quadrant compared to the other 3 quadrants (Figure 44D), indicating that both MPTP and 6OHDA rats were able to consolidate the new memory, therefore showing aptitudes for mental flexibility.

4.2.3 Neuropsychiatric evaluation

We assessed anxiety parameters using both the EPM and OF tests. We did not see any significant differences between the groups in the time spent in open arms in the EPM test or the frequency in which rats explored the open arms (Figure 45A, B). We made the same observations in the OF arena, with neither the time spent in the center of the arena nor the frequency differed significantly between the groups, or over time (Figure 45C, D).

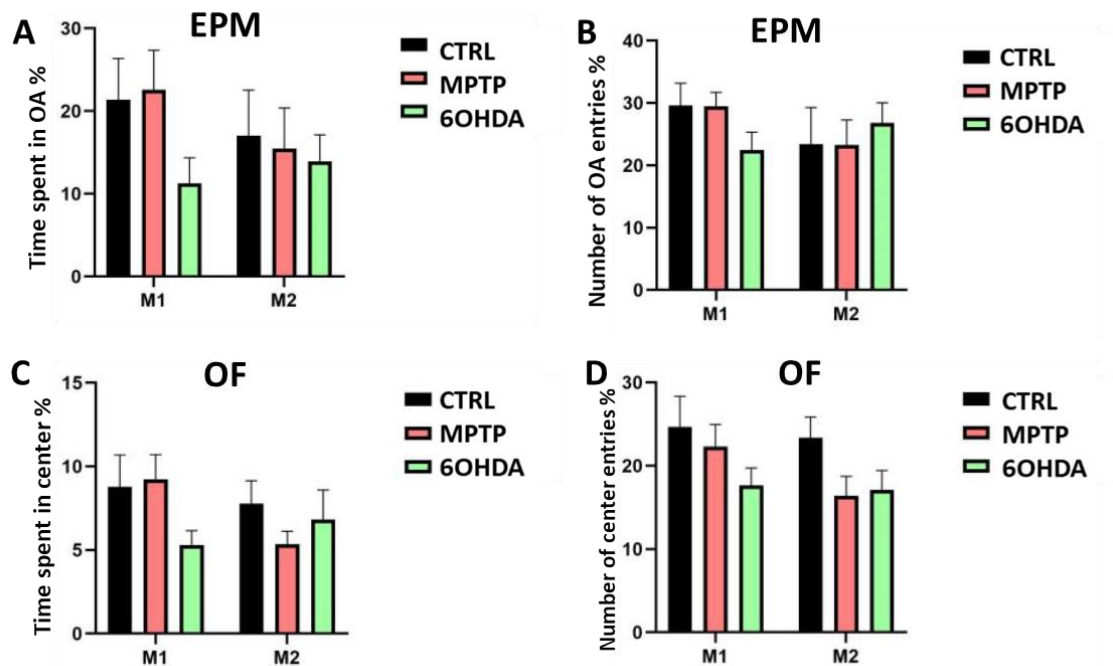


Figure 45. Evaluation of anxiety in MPTP and 6OHDA rats. Analysis of time spent (A) and frequency (B) in the open arms (OA) of the Elevated Plus Maze (EPM)). No significant differences were observed between the groups and at different time points. Analysis of time spent (C) and frequency (D) in the center of the Openfield (OF). No significant differences were found between groups and at different time points. ($n=12$ 6-OHDA, $n=14$ MPTP, and $n=10$ CTRL).

4.3 IMAGING EVALUATION

4.3.1 Structural MR imaging

The examination of T2w images using both VBM and ROI-based analysis techniques, did not yield any significant results. Indeed, we did not observe any structural changes in terms of overall volume or grey matter volume in any structures or regions of interest, for any of the neurotoxic groups at any of the timepoints.

4.3.2 R2* Iron accumulation

ROI-based analysis of R2* maps were conducted to examine iron inhomogeneities in the neurotoxic models' brains.

First, we evaluated the **Substantia Nigra**, being the most pertinent region in regards to iron accumulation in PD context. We observed a significant increase in R2* values in the **right SN**, in the 6OHDA group compared to the CTRL group at M1, and compared to the MPTP and CTRL groups at M2 (Figure 46A). We also noted a significant increase in R2* values in the **left SN** of the 6OHDA group at M1 and M2 compared to the CTRL and MPTP groups (Figure 46A). Therefore, the 6OHDA model is the only group showing an accumulation of iron in both the left and right SN, accentuated between M1 and M2.

As the second major structure of the nigrostriatal pathway, we then evaluated R2* values in the **Striatum**. We did not observe any significant differences between the groups or overtime, in the left or right striatum. Nevertheless, the 6OHDA group showed a tendency for iron accumulation between M1 and M2 (Figure 46B).

Next, we evaluated iron inhomogeneities in the **Subthalamic Nucleus**, a critical structure in PD, known for its propensity to accumulate iron (DeBarros et al. 2019). We observed a significant

increase in $R2^*$ values in the right subthalamic nucleus, between M1 and M2, in the 6OHDA model (Figure 46C), indicating a progression in the iron pathology in this structure. In the left subthalamic nucleus however, we only observed a non-significant trend towards an increase ($p=0.625$) in $R2^*$ values overtime for the 6OHDA group (Figure 46C).

The 6OHDA group also displayed significantly increased $R2^*$ values in the left and right **hypothalamic regions**, between M1 and M2 (Figure 46D), thereby showing an evolution of the iron pathology in this region.

In the **hippocampal area**, CA1-CA2 and CA3 regions did not present with any notable iron inhomogeneities. However, we observed a tendency for iron accumulation in the left and right gyri, but no significant differences were noted between groups or overtime (Figure 46E).

The analysis of $R2^*$ values did not yield significant results or trends in the thalamus, nor the frontal and cingulate cortices.

Interestingly, all three groups showed a significant decrease in $R2^*$ value in the left and right entorhinal cortex between M1 and M2 (Figure 46F).

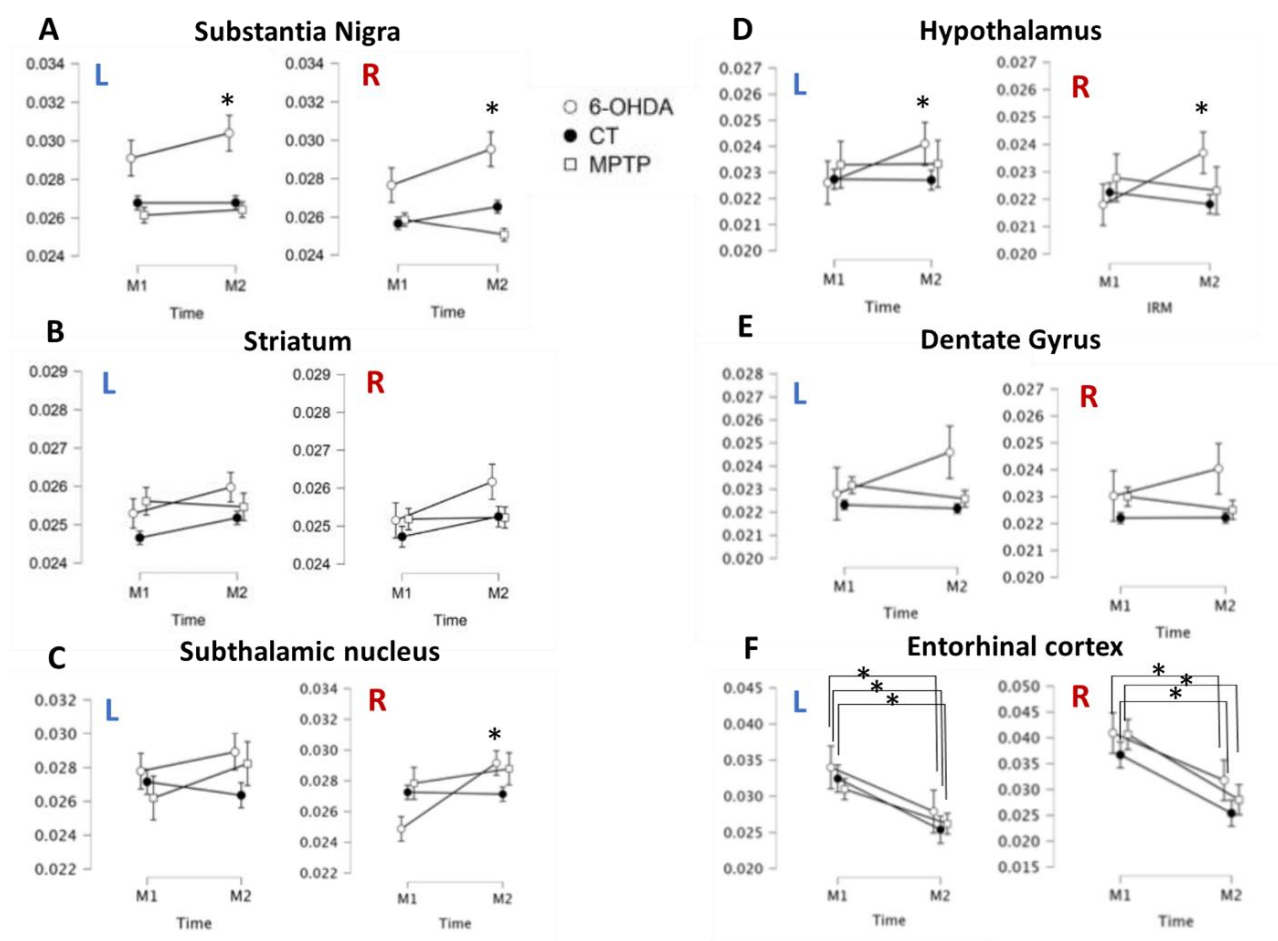


Figure 46. Variation of $R2^*$ values per ROI in MRI sessions 1 (M1) and 2 (M2). 12 ROI were evaluated, with a Left/Right distinction. * ($p < 0.05$) ($n=12$ 6-OHDA, $n=14$ MPTP, and $n=10$ CTRL).

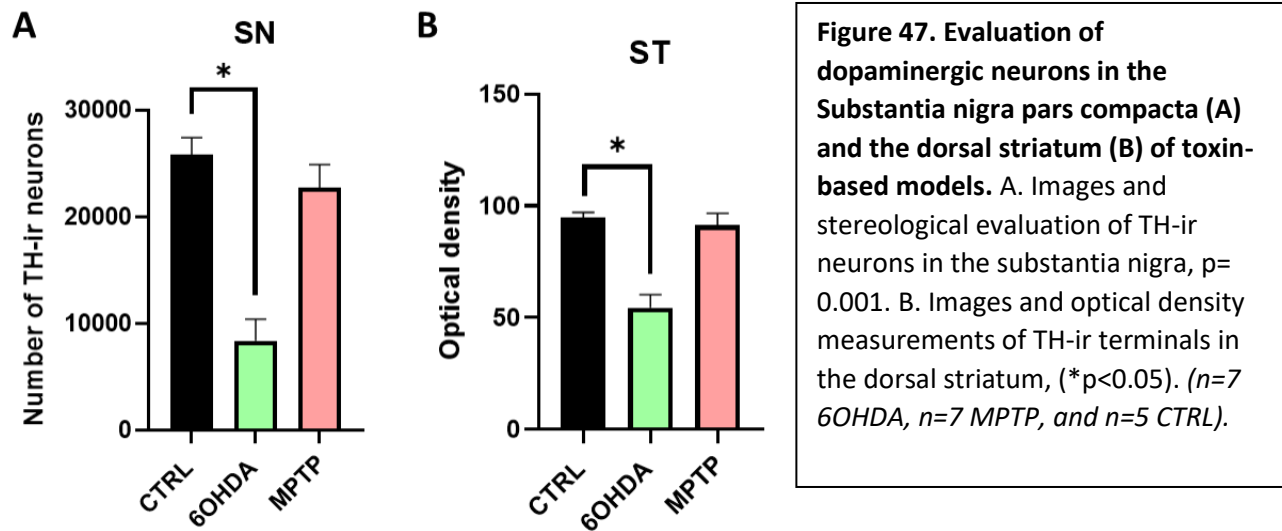
4.4 HISTOPATHOLOGY

4.4.1 Dopaminergic degeneration

The evaluation of dopaminergic degeneration in the SN revealed a significant decrease in the number of TH+ cells in the 6OHDA group compared to the CTRL group (Figure 47A).

We also observed a significant decrease in optical density measured in the striatum of 6OHDA rats compared to controls (Figure 47B).

The MPTP model however, did not show any significant dopaminergic denervation in either the SN or the striatum at 2 months p.i..



4.4.2 Iron accumulation and inflammation?

We are in the process of quantifying iron accumulation in the 6OHDA rat brain, especially in the ROIs which revealed R2* iron inhomogeneities in the MRI study.

Since neurotoxin models are known for displaying neuroinflammatory mechanisms in response to neurodegeneration and iron accumulation, we will also evaluate histological markers such as IBA1 for microglial activation, mainly in regions with neurodegenerative and iron pathologies.

4.5 DISCUSSION

This last part of the project examined the three-facet evaluation of 2 toxin-based bilateral intranigral models: MPTP and 6OHDA.

4.5.1 MPTP model

We did not observe any significant motor or sensori-motor deficits in the MPTP model. This was confirmed by the lack of dopaminergic degeneration in both the striatum and the SN, as well as the lack of any structural changes or iron inhomogeneities in these regions of the nigrostriatal

tract. Additionally, we did not observe any deficits in working or visuo-spatial memory, nor any prominent anxious-like behaviour in the MPTP group. This is not the case in the literature, where studies have shown such cognitive and neuropsychiatric impairments (Da Cunha et al. 2001; Santiago et al. 2010). We could attribute the lack of distinguishable dopaminergic lesions, and the resulting behavioural phenotype, to a possible low dose, or a less potent batch of MPTP that did not trigger the expected response. Indeed, a less potent dose could require a longer time to start the degenerative process, especially because the MPTP lesion is not very acute/severe, and compensation mechanisms may be in play (Perry et al. 2005).

Fortunately, even these negative results serve to support the 3-facet evaluation method, because the analyses in behaviour, imaging and histology, are perfectly coherent.

4.5.2 6OHDA model

In the 6OHDA model, we did not observe general locomotor deficits, but we did see a significant vertical motor impairment, as well as a pronounced forelimb akinesia developing progressively over time. These results matched with the level of dopaminergic degeneration observed in the SN and striatum, as well as the iron inhomogeneities in the SN and the subthalamic nucleus. Interestingly, we also noted a lateralization of the akinesia to the left, while the STN iron inhomogeneities were significant in the right hemisphere.

The 6OHDA model did not display anxious-like behaviour that could be accounted for via significant parameters in the EPM & OF tests. It would be interesting to evaluate more ethological parameters that could better detect slight tendencies towards an anxious-like behaviour.

Additionally, none of the cognitive functions evaluated in our study was impaired in the 6OHDA model, and regions related to learning, memory and mental flexibility such as the frontal and cingulate cortices and the hippocampus (Kehagia et al. 2010), did not display any alterations in structural T2 or T2*w images. It is important to note that these functions have been impaired in other more traditional models of the 6OHDA rat (Z Wang et al. 2020). The fact that this model is not cognitively impacted, coupled with the percentage of dopaminergic denervation, which is significant but also lower than usual, and the milder motor and sensorimotor impairments, supports the idea that this bilateral intranigral 6OHDA model is indeed moderate, and could

represent an earlier phase of PD. This observation is consistent with our plan to use early-phase models, to help find subtle imaging markers that could reflect the subtle change during this phase.

4.5.3 Toxin-based versus AAV alpha-synuclein animal model?

Furthermore, the absence of morphological image changes in the 6OHDA and MPTP brains at 2-months p.i. is interesting when compared to the AAV alpha-synuclein model. The latter did show several structural alterations in VBM as early as 10-weeks p.i.. This can validate the fact that the alterations are not direct consequences of the lesion's effect (Westphal et al. 2016), as we do not see it in either 6OHDA or MPTP, who were injected bilaterally at the same stereotactic coordinates in the SN.

We can also postulate that these VBM changes were not necessarily a reflection of dopaminergic degeneration, as we have seen a high level of neuronal loss in the SN of 6OHDA animals, and yet did not display any structural alterations in VBM or ROI-based structural analysis.

Alternatively, the 6-OHDA group revealed significant variations in $R2^*$ maps in different regions of the brain, suggesting an iron accumulation which we did not see in the AAV animal model. It is noteworthy to mention that this iron accumulation is not due to any ageing effects, as the 6OHDA, and both the AAV alpha synuclein and the MPTP models were injected and evaluated at the same age.

Ultimately, the bilateral intranigral 6OHDA model emerges as an interesting tool to evaluate anti-ferroptotic treatments, as it seems to develop iron pathology in several regions of the brain.

4.6 CONCLUSION

To conclude, these preliminary results establish the pertinence of combining imaging, behavioural and histological evaluations in one study, in order to explore possible correlations between the different settings, and eventually propose possible imaging markers of the early-phase of the disease.

Under this perspective, the bilateral intranigral 6OHDA rat model can bring new insights into the iron pathology in the context of PD. But there are still many evaluations to be made, mainly the histological perls coloration to confirm the $R2^*$ evaluation, but also checking for inflammation and oxidative stress markers, using a whole-brain analysis, as was done for alpha-synuclein. This could help extract ROIs that would be pertinent to push forward our imaging study, towards the exploration of texture features in the model.

A new cohort with both MPTP and 6OHDA animals has been under investigation since March 2023, with the same framework, but adding rs-fMRI to the imaging sequence and the touchscreen attentional task. A comprehensive texture feature and histological analysis exploration is planned using the methodology developed for the AAV alpha-synuclein model. This could also be a push in the right direction for the characterization of both these models.

PART FOUR

DISCUSSION & CONCLUSION

GENERAL DISCUSSION

FROM PRECLINICAL STUDIES...

AAV alpha-synuclein model: 3-facet characterization and model limitations

The main work of this PhD project (detailed in Results: Chapters 1 to 3) was to characterise the bilateral intranigral AAV A53T alpha-synuclein overexpression mode:

- On an MR imaging level, which to our knowledge, has never been done before.
- On a behavioural level with a focus on the cognitive and neuropsychiatric aspects that have been lacking in the literature.
- On a finer histopathological level, to study the alpha-synuclein pathology and propagation.

The aim was to explore the links and correlations between these three aspects, and how they could be employed to characterise imaging markers, by delving into both their underlying biological mechanisms as well as their symptomatologic reflection.

The functional exploration showed that the AAV alpha-synuclein model exhibited a mild sensorimotor dysfunction but no general locomotor impairment. It also presented with visuospatial learning and attentional impairment, but no deficits in working memory or mental flexibility. When taking this together with the level of dopaminergic loss evaluated between 30 and 40% at 18-weeks p.i., we postulated that this model is a progressive and moderate one that rather mimics the early phase of Parkinson's disease. Interestingly, the structural and functional imaging exploration showed morphological changes in regions related to the behavioural deficits observed, as well as a hyperconnectivity pattern in functional networks also involved in the sensorimotor and cognitive impairments. The structures that were modified morphologically and made abnormal connections, also presented with a significant score of alpha-synuclein deposits.

Finally, we selected regions of interest to perform a texture-based analysis which revealed correlations between texture features and behavioural scores, as well as alpha-synuclein deposits' scores.

The AAV alpha-synuclein model was therefore a good tool to test our 3-facet methodology. But it remains just one model of Parkinson's disease, with its limitations like any other animal model. For example, we showed both in MR imaging and histochemistry that ASYN brains did not have any form of iron accumulation, which is found in PD context (Mochizuki & Yasuda 2012), and considered a good differential marker in MRI, especially in the substantia nigra (Péran et al. 2010). This absence could be due to several factors, one of which is the age of our animals (6 months at the time of sacrifice). Indeed, several studies have noted that older animals have a higher susceptibility to specific neuropathological patterns such as iron accumulation, and the age-dependent effects should be considered when choosing the preclinical model (Potashkin et al. 2011). However, despite ageing being the main risk factor for developing idiopathic PD, most research studies do not use aged animals because it complexifies the experimental design (Barata-Antunes et al. 2020). In the case of our model for example, effects of stereotactic surgery, multiple anaesthesia for MRI acquisitions, food restriction for Touchscreen tests, and a longitudinal follow-up, can significantly increase the risk of complications and death rates in aged animals.

Moreover, this AAV model did not show any proteinopathy-related neuroinflammation, unlike the new exogenous preformed toxic species models (Balzano et al. 2023). Indeed, one of the more recent approaches to modelling synucleinopathy has been the direct inoculation of rodents with pre-formed fibrils (PFF) or oligomers of alpha-synuclein, or even human brain tissue homogenate containing Lewy bodies (LB) (Recasens et al. 2014; Thakur et al 2017). These models have exhibited neuroinflammation on top of alpha-synuclein pathology and motor dysfunction. However, not all oligomeric/PFFs species have the same toxicity patterns, and the mechanisms behind their seeding and spreading properties is still largely unclear. So, while these recent models hold a great promise, further investigations are required to establish them as valid and standardised models of PD, compared to the viral vector models (Carta et al. 2020).

Experimental design: methodological limitations and improvement strategies

Our study has faced several limitations, most of them due to research framework constraints. Mainly, the limited number of rats used significantly hindered the quantitative correlation results. We could not follow-up more than 24 rats at a time, because of material constraints (animal housing, number of behavioural test chambers), and the need to respect timelines (imaging all animals around the same timepoint). This led us to evaluate three different cohorts, over three years, taking into account the induced variability and bias risks. Ultimately, this played in our favour, because although the AAV alpha-synuclein model is known to show major intra-group variability, our evaluation of the dopaminergic degeneration was similar in the 3 cohorts, confirming its overall reproducibility. Additionally, even though we tried to respect the same timeline for each cohort, they did not always undergo the same behavioural tests, nor the same imaging sequences.

On the other hand, our study also suffers from the lack of biological and biochemical evaluations other than histology, which could provide additional information on the neurobiological processes occurring in our preclinical model. One reason for choosing to focus on histology was that we wanted to spatially correlate the cellular changes with what is observed in imaging, because our main goal was to define the significance of specific imaging markers on a biological level. And although techniques such as Western blot and PCR can provide more robust quantitative information about protein expression levels and gene expression changes in the brain tissue, they cannot provide valuable information about the distribution and density of protein aggregates and cell loss, that we wanted to evaluate.

We explored the possibility of adding metabolomics or proteomics evaluation to our model's characterization, in order to complement imaging features. Indeed, integrating genotypic and phenotypic information, such as RNA expression levels or protein abundances, to an MR imaging profile can increase our chances in establishing imaging features as relevant biomarkers (Antonelli et al. 2019). Recent studies have used metabolomic technology on cerebrospinal fluid and blood of animal models of PD, to better characterise them (Y. Wang et al. 2018; Kumari et

al. 2020). Correlations between metabolic perturbations and imaging alterations could provide valuable information in the search of early biomarkers of PD.

MR Imaging versus Histology: Originalities and challenges

The main objective of our project was to better understand histopathological signature of imaging features, in order to establish them as relevant biomarkers. To do so, we explored a novel method that allows a whole-brain unbiased analysis of histological markers, which can then be correlated to MR imaging analyses. This method relies on the use of QUINT, a workflow for the quantification and spatial analysis of features in histological images from rodent brains (Yates et al. 2019). It allowed the segmentation of 26 coronal sections per rat brain, into 222 regions of interest, based on the WHS rat brain atlas (Puchades et al. 2019), much like the segmentation we do in imaging. The next step in this workflow is to use Ilastik, which is a machine learning software, to quantify a histological marker, in every one of these 222 regions. The aim is to then correlate fine histological scores acquired from QUINT in a specific region, to the texture features acquired from MR imaging in the same anatomical region. This would give a comprehensive look on the tissue modification reflected by imaging features. We used this workflow on our alpha-synuclein stained histological sections, but due to the low intensity of the staining, we were not able to use Ilastik to automatically quantify each region. To address this problem, we created a 4-level scale range from 0 to 3 (adapted from Joppe et al. 2021), and manually scored the segmented regions.

This analysis gave us an overview of the alpha-synuclein spreading in the whole brain of the AAV alpha-synuclein expression. The spreading pattern was not the same between all ASYN animals, which is a good reflection on the heterogeneity of PD, however the alpha-synuclein score correlated with first and second order texture features in regions such as the SN, the striatum and the hippocampus. We postulated that these features could reflect on the presence of alpha-synuclein deposits in the brain. We are now executing the integral QUINT workflow (including Ilastik's automatic quantification) on a different alpha-synuclein staining to get a more accurate

score per region, which will be followed by an all-inclusive correlative evaluation of texture features vs alpha-synuclein deposit (Figure).

This workflow will also be used in the evaluation of neuroinflammation markers and iron accumulation in the 6OHDA toxin-based model.

The serial histological analysis is a succession of tedious manual interventions, which are incredibly time-consuming, so quantification of histological markers and staining is classically performed on a few tissue sections, which restricts the analysis to limited portions of the brain (Vandenberghe et al. 2016). In our study, we analysed 26 sections per brain and per staining, to encompass all the rostro-causal regions from the olfactory bulb to the brainstem.

However, recently, the evaluation of whole-brain histology has benefitted from new state-of-the-art tissue-clearing methods, which, when combined with light-sheet microscopy and automated image analysis techniques, can allow whole-brain antibody labelling, without loss of tissue (Ueda et al. 2020). The high-resolution 3D image that can be obtained from such techniques, allows a detailed look at the brain's entire architectural structure, as well as the functional cellular and subcellular changes that can occur in a pathological context. Such a 3D image could also be correlated with 3D images obtained in structural and functional MRI. Indeed, a team from Duke recently managed to combine MRI and lightsheet approaches to create the highest-resolution image ever obtained of the mouse brain (Johnson et al. 2023). This could revolutionise our understanding of imaging features and their biological significance. However, although this technique has been perfected for the mouse brain, tissue-clearing an entire rat brain has proved more difficult, and hasn't always yielded reproducible results. One of the several impediments to which researchers have been confronted, is mainly the fact that the rat brain is much more lipidic than the mouse's, making antibody penetration very variable and unreliable. A new optimised method for rat brain clearing, including an additional delipidation step, could help address this problem. The continuation of this project could largely benefit from using tissue clearing to better characterise the whole-brain histopathology and how it is reflected in MR imaging. It could be especially interesting when studying the propagation of alpha-synuclein, or networks' functional connectivity (Parra-Damas & Sora 2020).

Translational validity of preclinical observations

It is now clear that preclinical studies on animal models have the potential to elucidate the underlying histopathological changes that can be associated with MR images' alterations in disease context. The improvement of many techniques to visualise the brain's structure and networks, at the cellular and molecular level, can help translate the radiological observations into biological ones.

Additionally, this work has shown that reproducing the same imaging sequences done in clinical research, on a rodent's brain, has been successful, and yielded similar imaging features to those observed in humans, with the added bonus of being able to study the brains' histopathology.

However, choosing the right model for specific imaging investigations remains a challenge as not all models have the same phenotype, histopathology or progression mechanisms. Our work showed that functional MRI was adequate for the evaluation of the moderate AAV alpha-synuclein model, which is characterised by the propagation of alpha-synuclein along different connectomes and brain networks. Conversely, R2* mapping was more adequate for the 6OHDA model, which features a prominent iron pathology pattern. We proposed that the validation of these observations and correlations in multiple animal models of PD, can strengthen their translational value.

Alternatively, researchers have also tried to answer the same question of the histological significance of MR images, using human brain tissues. Indeed, some studies have tried to match post-mortem ex-vivo MR images of human brain sections, to histopathological changes. They were able to match MRI signal contrast in cerebral microinfarcts to loss of nissl-stained neurons and lipofuscin pigment accumulation on a histological level (Yilmazer-Hanke et al. 2019). Doing these evaluations on the human scale allows researchers to overcome the translational validity question. However, the differences between in vivo and ex-vivo MRI creates some uncertainties regarding the interpretation of such results.

... TO CLINICAL REPERCUSSIONS

DIAGNOSTIC, PROGNOSTIC AND IMAGING BIOMARKERS OF PD

Alpha synuclein and PD.

Finding biomarkers for the early diagnosis of Parkinson's disease is considered a major challenge today. This early phase is characterised by many non-motor symptoms which aren't necessarily PD-specific, such as anxiety and mild cognitive impairments. Such overlapping clinical signs make differential diagnosis of PD very challenging, leading to a high rate of misclassification, especially in those early stages of the disease.

Moreover, it has been hypothesised that the phenotype seen in early PD patients is primarily influenced by a functional alpha-synuclein pathology that disrupts normal cell functioning, rather than by obvious degeneration (Koprach et al 2017).

Strategies to establish the presence of alpha-synuclein in the blood, tissue, or cerebrospinal fluid (CSF), as an early biomarker have been booming. So far, CSF alpha-synuclein levels appear to be the most consistent marker (Atik et al. 2016). However due to the invasive nature of the procedure for obtaining CSF, it is not considered an ideal biomarker.

Despite a lot of efforts to develop a PET radiotracer for imaging alpha-synuclein aggregates, many challenges have arisen, especially in relation to binding site affinities and selectivity of the tracer (Kotzbauer et al. 2016).

But what if a simple non-invasive structural MRI can provide information on the presence and spreading of alpha-synuclein in the brain?

The use of texture-based analysis on structural T2 images in our preclinical animal model has shown that several first and second order texture features correlated with the alpha-synuclein deposits in specific regions of the brain. This allowed us to hypothesize that these subtle markers,

accounting for very subtle changes in the brain, sometimes before neuronal loss and grey matter atrophy occurs, could reflect the pathological presence of alpha-synuclein. Also, the association between specific behavioural deficits, and the presence of alpha-synuclein in a specific region related to the behavioural function, could add to the specificity of such biomarkers.

Additional and more extensive studies are obviously needed to confirm such a possibility, perhaps using other animal models of synucleinopathy such as the PFF model, or even using post-mortem ex-vivo MRIs of human brains, and performing texture-based analysis followed by histopathology analysis. If validated, the idea that texture features represent a proteinopathy phenomenon, which occurs early on in the disease, could be applied on the clinical scale, for an early diagnosis.

It is however important to note that the role of proteinopathy in Neurodegenerative diseases, remains a debatable subject. Indeed, after the failure of more than 40 anti-amyloid randomized clinical trials, 2 anti-synuclein trials, and 4 anti-tau trials, researchers have started to question the toxic proteinopathy hypothesis, noting that the causality it has been attributed is largely misguided (Espay et al. 2023). Some have even proposed that protein oligomerization and aggregation can be the consequence of brain pathological processes, a mere byproduct of other pathogenic pathways, and not the cause of it (Espay et al. 2019). So, while biomarkers targeting these proteins are essential, they will not in the long run, be sufficient, as long as we don't understand the pathophysiology and molecular pathways underlying the disease.

The promise of Multimodal imaging in PD.

Interestingly, while biofluid markers of PD have focused essentially on the presence of alpha-synuclein in the CSF or blood, non-invasive neuroimaging with different scan sequences and analytical techniques can provide several information regarding the entire brain's function.

As related throughout this dissertation, MRI has introduced numerous promising measures to identify alterations within the nigrostriatal system, implicated in the cardinal motor symptoms of

the disease, and detect broader dysfunction involved in the appearance of non-motor symptoms, such as cognitive impairment (Ryman & Poston 2019; Betrouni et al. 2020, 2021).

For example, imaging studies have shown that one early sign of PD is axonal damage, which appears long before any symptoms of the disease, and therefore goes unnoticed. It was detected by assessing structural brain white matter, using Diffusion Tensor Imaging, which could potentially turn specific DTI metrics into early markers of PD (Bergamino et al. 2020).

PD-associated changes in the SN and basal ganglia such as increased iron load can be detected by various iron-sensitive MR imaging techniques and analysis such as R2* and QSM maps, but also neuromelanin sequences. For example, the loss of nigrosome-1, which is a region of the SN that undergoes the greatest and earliest dopaminergic neuron loss in PD, has been assessed using T2*wi and has emerged as a new marker for idiopathic PD (Cheng et al. 2019).

Last but not least, rs-fMRI has been largely utilized for diagnosis (Heim et al. 2017; Shi et al. 2021), monitoring of treatment effects (Morgan et al. 2017; Ge et al. 2020), and clinical score prediction of PD (Hou et al. 2016). It gives information about the entire brain's network functioning, and therefore is not limited to specific structures, or specific pathological or degenerative processes. It is therefore very interesting in the correlation to specific motor and non-motor symptoms, which are the product of global network dysfunctions made by degenerative and inflammatory processes.

Overall, it seems that a multimodal imaging approach combining structural, quantitative and functional neuroimaging seems to be the answer to diagnostic, prognostic and disease monitoring criteria, because it can provide complimentary information on the brain's state, from degeneration and atrophy, to white matter connectivity changes, to iron accumulation, to brain network disruptions

And with the advent of Machine learning methods and the use of computer-aided diagnosis (CAD) and follow-up, combining large cohorts and mining Big Data could eventually provide useful information to identify specific signatures of brain abnormalities (Zhang 2022).

Integrating all this information using a Radiomics-based approach could offer alternatives in diagnosis and treatment. It has the potential to identify new subgroups of this widely heterogeneous disease, enhance the precision medicine scope, and, why not, offer new therapeutic targets, while waiting for fundamental research to breach the mystery of the underlying biological processes of neurodegenerative diseases.

CONCLUSION

The entirety of my thesis work is part of the bidirectional translational research approach carried out within my research team: “Degenerative and vascular cognitive disorders”.

Indeed, the majority of our team’s projects aim to transpose experimental data obtained in rodents to humans, to evaluate new therapeutic strategies. On the other hand, clinical observations and data from human trials conducted by colleagues have proven interesting to inform novel characterization and refinement of animal models to better mimic human disease.

This is specifically the case of Magnetic Resonance imaging, which is routinely used in clinical research, despite the fact that we don’t know the exact underlying cellular and molecular changes that it represents. The absence of readily available brain biobanks, and the inability to perform brain biopsies as one would do for tumours for example, has inspired our clinical researchers to implement the MRI sequences and analyses performed in a clinical context, on animal models of PD, with the aim of using routine histological and behavioural evaluations to explain the changes observed in MRI on an imaging level.

Therefore, we devised a 3-facet approach relying on the evaluation and correlation of MR imaging sequences with the behavioural phenotype and the histological changes. Our results show that certain imaging markers, like texture features, correlate with alpha-synucleinopathy, in addition to neuronal loss. Texture features had already managed to discriminate cognitive and motor symptoms in a clinical context, making them a reliable imaging marker. With the addition of this potential underlying biological significance (reflection of the accumulation of a toxic protein), this work suggests that it could, in the future, be an interesting **biomarker** for the early diagnosis of PD.

Although the specificity of these imaging markers for PD compared to other neurodegenerative diseases remains to be evaluated, our translational approach provides a proof of concept for the development of MRI texture feature markers identifying synucleinopathy in PD, and confirms the potential of imaging biomarkers in clinical settings.

In conclusion, although the road to early diagnosis of PD using imaging biomarker and offering curative therapies is still long, this doctoral work, reinforces the relevance of using a bidirectional translational approach to address the diagnostic and therapeutic challenges of PD.

REFERENCES

1. Samii A, Nutt JG, Ransom BR. Parkinson's disease. *The Lancet*. 2004 May 29;363(9423):1783–93.
2. Pringsheim T, Jette N, Frolkis A, Steeves TDL. The prevalence of Parkinson's disease: a systematic review and meta-analysis. *Mov Disord Off J Mov Disord Soc*. 2014 Nov;29(13):1583–90.
3. Kalia LV, Lang AE. Parkinson's disease. *The Lancet*. 2015 Aug 29;386(9996):896–912.
4. Bernheimer H, Birkmayer W, Hornykiewicz O, Jellinger K, Seitelberger F. Brain dopamine and the syndromes of Parkinson and Huntington. Clinical, morphological and neurochemical correlations. *J Neurol Sci*. 1973 Dec;20(4):415–55.
5. Greffard S, Verny M, Bonnet AM, Beinis JY, Gallinari C, Meaume S, et al. Motor score of the Unified Parkinson Disease Rating Scale as a good predictor of Lewy body-associated neuronal loss in the substantia nigra. *Arch Neurol*. 2006 Apr;63(4):584–8.
6. Braak H, Del Tredici K, Rüb U, de Vos RAI, Jansen Steur ENH, Braak E. Staging of brain pathology related to sporadic Parkinson's disease. *Neurobiol Aging*. 2003;24(2):197–211.
7. Kim S, Kwon SH, Kam TI, Panicker N, Karuppagounder SS, Lee S, et al. Transneuronal Propagation of Pathologic α -Synuclein from the Gut to the Brain Models Parkinson's Disease. *Neuron*. 2019 Aug 21;103(4):627–641.e7.
8. Herting B, Schulze S, Reichmann H, Haehner A, Hummel T. A longitudinal study of olfactory function in patients with idiopathic Parkinson's disease. *J Neurol*. 2008 Mar 1;255(3):367–70.
9. Dickson DW, Fujishiro H, Orr C, DelleDonne A, Josephs KA, Frigerio R, et al. Neuropathology of non-motor features of Parkinson disease. *Parkinsonism Relat Disord*. 2009 Dec 1;15:S1–5.
10. Pfeiffer RF. Gastrointestinal dysfunction in Parkinson's disease. *Parkinsonism Relat Disord*. 2011 Jan 1;17(1):10–5.
11. Zarow C, Lyness SA, Mortimer JA, Chui HC. Neuronal Loss Is Greater in the Locus Coeruleus Than Nucleus Basalis and Substantia Nigra in Alzheimer and Parkinson Diseases. *Arch Neurol*. 2003 Mar 1;60(3):337–41.
12. Adler CH, Hentz JG, Shill HA, Sabbagh MN, Driver-Dunckley E, Evidente VGH, et al. Probable RBD is increased in Parkinson's disease but not in essential tremor or restless legs syndrome. *Parkinsonism Relat Disord*. 2011 Jul 1;17(6):456–8.
13. Zhang W, Zhang L, Liu L, Wang X. Time course study of fractional anisotropy in the substantia nigra of a parkinsonian rat model induced by 6-OHDA. *Behav Brain Res*. 2017 Jun;328:130–7.
14. Aarsland D, Pålhlagen S, Ballard CG, Ehrt U, Svenningsson P. Depression in Parkinson disease—epidemiology, mechanisms and management. *Nat Rev Neurol*. 2012 Jan;8(1):35–47.

15. Poewe W, Seppi K. Treatment options for depression and psychosis in Parkinson's disease. *J Neurol*. 2001 Sep 1;248(3):12–21.
16. Reijnders JSAM, Ehrt U, Weber WEJ, Aarsland D, Leentjens AFG. A systematic review of prevalence studies of depression in Parkinson's disease. *Mov Disord*. 2008;23(2):183–9.
17. Chaudhuri KR, Healy DG, Schapira AH. Non-motor symptoms of Parkinson's disease: diagnosis and management. *Lancet Neurol*. 2006 Mar 1;5(3):235–45.
18. Ehrt U, Brønnick K, Leentjens AFG, Larsen JP, Aarsland D. Depressive symptom profile in Parkinson's disease: a comparison with depression in elderly patients without Parkinson's disease. *Int J Geriatr Psychiatry*. 2006;21(3):252–8.
19. Leentjens AFG. Depression in Parkinson's disease: conceptual issues and clinical challenges. *J Geriatr Psychiatry Neurol*. 2004 Sep;17(3):120–6.
20. Chaudhuri KR, Schapira AH. Non-motor symptoms of Parkinson's disease: dopaminergic pathophysiology and treatment. *Lancet Neurol*. 2009 May 1;8(5):464–74.
21. Menza MA, Robertson-Hoffman DE, Bonapace AS. Parkinson's disease and anxiety: Comorbidity with depression. *Biol Psychiatry*. 1993 Oct 1;34(7):465–70.
22. Thobois S, Ardouin C, Lhommée E, Klinger H, Lagrange C, Xie J, et al. Non-motor dopamine withdrawal syndrome after surgery for Parkinson's disease: predictors and underlying mesolimbic denervation. *Brain*. 2010 Apr 1;133(4):1111–27.
23. Prospective study of phobic anxiety and risk of Parkinson's disease - Weisskopf - 2003 - Movement Disorders - Wiley Online Library [Internet]. [cited 2023 May 9]. Available from: https://movementdisorders.onlinelibrary.wiley.com/doi/full/10.1002/mds.10425?casa_token=Fn4wW_O4_cOAAAAA%3AZlpZVj6tA7FELnAql4bZ6UTzf6_5xnzRNCp7Eh1qWzWJBM3gJ6TKVTOGCSSV9V3skgABLpeScx8awgZI8g
24. Pontone GM, Dissanayaka N, Apostolova L, Brown RG, Dobkin R, Dujardin K, et al. Report from a multidisciplinary meeting on anxiety as a non-motor manifestation of Parkinson's disease. *Npj Park Dis*. 2019 Dec 11;5(1):1–9.
25. Lee DJ, Milosevic L, Gramer R, Sasikumar S, Al-Ozzi TM, Vloo PD, et al. Nucleus basalis of Meynert neuronal activity in Parkinson's disease. *J Neurosurg*. 2019 Feb 22;132(2):574–82.
26. Bolam JP, Hanley JJ, Booth P a. C, Bevan MD. Synaptic organisation of the basal ganglia. *J Anat*. 2000 May;196(4):527–42.
27. Park J, Coddington LT, Dudman JT. Basal Ganglia Circuits for Action Specification. *Annu Rev Neurosci*. 2020;43(1):485–507.
28. David Smith A, Paul Bolam J. The neural network of the basal ganglia as revealed by the study of synaptic connections of identified neurones. *Trends Neurosci*. 1990 Jul 1;13(7):259–65.
29. Parent A, Cicchetti F. The current model of basal ganglia organization under scrutiny. *Mov Disord*. 1998;13(2):199–202.

30. Prange S, Pagonabarraga J, Krack P, Kulisevsky J, Sgambato V, Tremblay L, et al. Historical crossroads in the conceptual delineation of apathy in Parkinson's disease. *Brain*. 2018 Feb 1;141(2):613–9.
31. Marin RS. Apathy: A neuropsychiatric syndrome. *J Neuropsychiatry Clin Neurosci*. 1991;3:243–54.
32. Starkstein SE, Brockman S, Hayhow BD. Psychiatric syndromes in Parkinson's disease. *Curr Opin Psychiatry*. 2012 Nov;25(6):468.
33. Benito-León J, Cubo E, Coronell C, Group on behalf of the AS. Impact of apathy on health-related quality of life in recently diagnosed Parkinson's disease: The ANIMO study. *Mov Disord*. 2012;27(2):211–8.
34. Williams DR, Litvan I. Parkinsonian Syndromes. *Contin Lifelong Learn Neurol*. 2013 Oct;19(5 Movement Disorders):1189–212.
35. Miller-Patterson C, Buesa R, McLaughlin N, Jones R, Akbar U, Friedman JH. Motor asymmetry over time in Parkinson's disease. *J Neurol Sci*. 2018 Oct 15;393:14–7.
36. Sterling NW, Cusumano JP, Shaham N, Piazza SJ, Liu G, Kong L, et al. Dopaminergic Modulation of Arm Swing During Gait Among Parkinson's Disease Patients. *J Park Dis*. 2015 Jan 1;5(1):141–50.
37. Helmich RC, Hallett M, Deuschl G, Toni I, Bloem BR. Cerebral causes and consequences of parkinsonian resting tremor: a tale of two circuits? *Brain*. 2012 Nov 1;135(11):3206–26.
38. Xia R, Mao ZH. Progression of motor symptoms in Parkinson's disease. *Neurosci Bull*. 2012 Feb 1;28(1):39–48.
39. Jankovic J. Parkinson's disease: clinical features and diagnosis. *J Neurol Neurosurg Psychiatry*. 2008 Apr 1;79(4):368–76.
40. Pavese N. PET studies in Parkinson's disease motor and cognitive dysfunction. *Parkinsonism Relat Disord*. 2012 Jan 1;18:S96–9.
41. Braak H, Del Tredici K. Cortico-basal ganglia-cortical circuitry in Parkinson's disease reconsidered. *Exp Neurol*. 2008 Jul 1;212(1):226–9.
42. Aarsland D, Beyer MK, Kurz MW. Dementia in Parkinson's disease. *Curr Opin Neurol*. 2008 Dec;21(6):676.
43. Goetz CG, Emre M, Dubois B. Parkinson's disease dementia: Definitions, guidelines, and research perspectives in diagnosis. *Ann Neurol*. 2008;64(S2):S81–92.
44. Diederich NJ, Surmeier DJ, Uchihara T, Grillner S, Goetz CG. Parkinson's disease: Is it a consequence of human brain evolution? *Mov Disord*. 2019 Apr;34(4):453–9.
45. Diederich NJ, Fénelon G, Stebbins G, Goetz CG. Hallucinations in Parkinson disease. *Nat Rev Neurol*. 2009 Jun;5(6):331–42.

46. Kosaka K. Lewy bodies in cerebral cortex. Report of three cases. *Acta Neuropathol (Berl)*. 1978 Jan 1;42(2):127–34.
47. Braak H, Rüb U, Steur ENHJ, Tredici KD, Vos RAI de. Cognitive status correlates with neuropathologic stage in Parkinson disease. *Neurology*. 2005 Apr 26;64(8):1404–10.
48. Kingsbury AE, Bandopadhyay R, Silveira-Moriyama L, Ayling H, Kallis C, Sterlacci W, et al. Brain stem pathology in Parkinson's disease: An evaluation of the Braak staging model. *Mov Disord*. 2010;25(15):2508–15.
49. Dijkstra AA, Voorn P, Berendse HW, Groenewegen HJ, Bank NB, Rozemuller AJM, et al. Stage-dependent nigral neuronal loss in incidental Lewy body and Parkinson's disease. *Mov Disord*. 2014;29(10):1244–51.
50. Attems J, Jellinger KA. The dorsal motor nucleus of the vagus is not an obligatory trigger site of Parkinson's disease. *Neuropathol Appl Neurobiol*. 2008 Aug 1;34(4):466–7.
51. Kalaitzakis ME, Graeber MB, Gentleman SM, Pearce RKB. Striatal β -Amyloid Deposition in Parkinson Disease With Dementia. *J Neuropathol Exp Neurol*. 2008 Feb 1;67(2):155–61.
52. Zaccai J, Brayne C, McKeith I, Matthews F, Ince PG. Patterns and stages of α -synucleinopathy: Relevance in a population-based cohort. *Neurology*. 2008 Mar 25;70(13):1042–8.
53. Parkkinen L, Pirttilä T, Alafuzoff I. Applicability of current staging/categorization of α -synuclein pathology and their clinical relevance. *Acta Neuropathol (Berl)*. 2008 Apr 1;115(4):399–407.
54. Blesa J, Trigo-Damas I, del Rey NLG, Obeso JA. The use of nonhuman primate models to understand processes in Parkinson's disease. *J Neural Transm*. 2018 Mar 1;125(3):325–35.
55. Surmeier DJ, Obeso JA, Halliday GM. Selective neuronal vulnerability in Parkinson disease. *Nat Rev Neurosci*. 2017 Feb;18(2):101–13.
56. Burke RE, Dauer WT, Vonsattel JPG. A critical evaluation of the Braak staging scheme for Parkinson's disease. *Ann Neurol*. 2008 Nov;64(5):485–91.
57. Jellinger KA. Critical evaluation of the Braak staging scheme for Parkinson's disease. *Ann Neurol*. 2010 Apr;67(4):550.
58. Djaldetti R, Ziv I, Melamed E. The mystery of motor asymmetry in Parkinson's disease. *Lancet Neurol*. 2006 Sep 1;5(9):796–802.
59. Kempster PA, Gibb WR, Stern GM, Lees AJ. Asymmetry of substantia nigra neuronal loss in Parkinson's disease and its relevance to the mechanism of levodopa related motor fluctuations. *J Neurol Neurosurg Psychiatry*. 1989 Jan 1;52(1):72–6.
60. Wang J, Yang QX, Sun X, Vesek J, Mosher Z, Vasavada M, et al. MRI evaluation of asymmetry of nigrostriatal damage in the early stage of early-onset Parkinson's disease. *Parkinsonism Relat Disord*. 2015 Jun 1;21(6):590–6.
61. Claassen DO, McDonnell KE, Donahue M, Rawal S, Wylie SA, Neimat JS, et al. Cortical asymmetry in Parkinson's disease: early susceptibility of the left hemisphere. *Brain Behav*. 2016;6(12):e00573.

62. van der Hoorn A, Burger H, Leenders KL, de Jong BM. Handedness correlates with the dominant Parkinson side: A systematic review and meta-analysis. *Mov Disord.* 2012;27(2):206–10.
63. de la Fuente-Fernández R, Kishore A, Calne DB, Ruth TJ, Stoessl AJ. Nigrostriatal dopamine system and motor lateralization. *Behav Brain Res.* 2000 Jul 1;112(1):63–8.
64. Morgan JC, Fox SH. Treating the Motor Symptoms of Parkinson Disease. *Contin Lifelong Learn Neurol.* 2016 Aug;22(4):1064.
65. Vijayakumar D, Jankovic J. Drug-Induced Dyskinesia, Part 1: Treatment of Levodopa-Induced Dyskinesia. *Drugs.* 2016 May 1;76(7):759–77.
66. Albarrán-Bravo S, Ávalos-Fuentes JA, Cortés H, Rodríguez-Sánchez M, Leyva-García N, Rangel-Barajas C, et al. Severity of Dyskinesia and D3R Signaling Changes Induced by L-DOPA Treatment of Hemiparkinsonian Rats Are Features Inherent to the Treated Subjects. *Biomolecules.* 2019 Sep;9(9):431.
67. Antonini A, Bondiolotti G, Natuzzi F, Bareggi SR. Levodopa and 3-OMD levels in Parkinson patients treated with Duodopa. *Eur Neuropsychopharmacol.* 2010 Oct 1;20(10):683–7.
68. Iravani MM, McCreary AC, Jenner P. Striatal plasticity in Parkinson's disease and L-DOPA induced dyskinesia. *Parkinsonism Relat Disord.* 2012 Jan 1;18:S123–5.
69. Chung SJ, Yoo HS, Lee HS, Oh JS, Kim JS, Sohn YH, et al. The Pattern of Striatal Dopamine Depletion as a Prognostic Marker in De Novo Parkinson Disease. *Clin Nucl Med.* 2018 Nov;43(11):787.
70. Borovac JA. Side effects of a dopamine agonist therapy for Parkinson's disease: a mini-review of clinical pharmacology. *Yale J Biol Med.* 2016 Mar 24;89(1):37–47.
71. Carbone F, Djamshidian A, Seppi K, Poewe W. Apomorphine for Parkinson's Disease: Efficacy and Safety of Current and New Formulations. *CNS Drugs.* 2019;33(9):905–18.
72. Reichmann H, Odin P, Brecht HM, Köster J, Kraus PH. Changing dopamine agonist treatment in Parkinson's disease: experiences with switching to pramipexole. In: Parvez H, Riederer P, editors. *Oxidative Stress and Neuroprotection* [Internet]. Vienna: Springer; 2006 [cited 2023 May 9]. p. 17–25. (Journal of Neural Transmission. Supplementa). Available from: https://doi.org/10.1007/978-3-211-33328-0_2
73. Dapier S, Eusebio A, Degos B, Vérin M, Durif F, Azulay JP, et al. Quality of life in Parkinson's disease improved by apomorphine pump: the OPTIPUMP cohort study. *J Neurol.* 2016 Jun;263(6):1111–9.
74. Rascol O, Brooks DJ, Korczyn AD, De Deyn PP, Clarke CE, Lang AE. A Five-Year Study of the Incidence of Dyskinesia in Patients with Early Parkinson's Disease Who Were Treated with Ropinirole or Levodopa. *N Engl J Med.* 2000 May 18;342(20):1484–91.
75. Stocchi F, Jenner P, Obeso JA. When Do Levodopa Motor Fluctuations First Appear in Parkinson's Disease? *Eur Neurol.* 2010 Mar 24;63(5):257–66.
76. Goldenberg MM. Medical Management of Parkinson's Disease. *Pharm Ther.* 2008 Oct;33(10):590–606.

77. Laloux C, Gouel F, Lachaud C, Timmerman K, Do Van B, Jonneaux A, et al. Continuous cerebroventricular administration of dopamine: A new treatment for severe dyskinesia in Parkinson's disease? *Neurobiol Dis.* 2017 Jul;103:24–31.
78. Atmaca M. Drug-Induced Impulse Control Disorders: A Review. *Curr Clin Pharmacol.* 2014 Feb 1;9(1):70–4.
79. Moreau C, Rolland AS, Pioli E, Li Q, Odou P, Barthelemy C, et al. Intraventricular dopamine infusion alleviates motor symptoms in a primate model of Parkinson's disease. *Neurobiol Dis.* 2020 Jun 1;139:104846.
80. Devos D, Devedjian JC, Moreau C. Intracerebroventricular dopamine for Parkinson's disease. *Oncotarget.* 2017 May 3;8(28):45034–5.
81. Fox SH. Non-dopaminergic Treatments for Motor Control in Parkinson's Disease. *Drugs.* 2013 Sep 1;73(13):1405–15.
82. Jankovic J, Poewe W. Therapies in Parkinson's disease. *Curr Opin Neurol.* 2012 Aug;25(4):433.
83. Turner RS, Desmurget M. Basal ganglia contributions to motor control: a vigorous tutor. *Curr Opin Neurobiol.* 2010 Dec 1;20(6):704–16.
84. Parent A, Hazrati LN. Functional anatomy of the basal ganglia. II. The place of subthalamic nucleus and external pallidum in basal ganglia circuitry. *Brain Res Rev.* 1995 Jan 1;20(1):128–54.
85. Bergman H, Wichmann T, DeLong MR. Reversal of Experimental Parkinsonism by Lesions of the Subthalamic Nucleus. *Science.* 1990 Sep 21;249(4975):1436–8.
86. Benazzouz A, Boraud T, Féger J, Burbaud P, Bioulac B, Gross C. Alleviation of experimental hemiparkinsonism by high-frequency stimulation of the subthalamic nucleus in primates: A comparison with L-dopa treatment. *Mov Disord.* 1996;11(6):627–32.
87. Benabid AL, Koudsié A, Benazzouz A, Fraix V, Ashraf A, Le Bas JF, et al. Subthalamic stimulation for Parkinson's disease. *Arch Med Res.* 2000 Jun;31(3):282–9.
88. Krack P, Batir A, Van Blercom N, Chabardes S, Fraix V, Ardouin C, et al. Five-Year Follow-up of Bilateral Stimulation of the Subthalamic Nucleus in Advanced Parkinson's Disease. *N Engl J Med.* 2003 Nov 13;349(20):1925–34.
89. Limousin P, Krack P, Pollak P, Benazzouz A, Ardouin C, Hoffmann D, et al. Electrical Stimulation of the Subthalamic Nucleus in Advanced Parkinson's Disease. *N Engl J Med.* 1998 Oct 15;339(16):1105–11.
90. Artusi CA, Lopiano L, Morgante F. Deep Brain Stimulation Selection Criteria for Parkinson's Disease: Time to Go beyond CAPSIT-PD. *J Clin Med.* 2020 Dec 4;9(12):3931.
91. Castrioto A, Lhommée E, Moro E, Krack P. Mood and behavioural effects of subthalamic stimulation in Parkinson's disease. *Lancet Neurol.* 2014 Mar 1;13(3):287–305.

92. Lhommée E, Klinger H, Thobois S, Schmitt E, Ardouin C, Bichon A, et al. Subthalamic stimulation in Parkinson's disease: restoring the balance of motivated behaviours. *Brain*. 2012 May 1;135(5):1463–77.
93. Vachez Y, Carcenac C, Magnard R, Kerkerian-Le Goff L, Salin P, Savasta M, et al. Subthalamic Nucleus Stimulation Impairs Motivation: Implication for Apathy in Parkinson's Disease. *Mov Disord*. 2020;35(4):616–28.
94. Bjorklund A, Stenevi U. Regeneration of monoaminergic and cholinergic neurons in the mammalian central nervous system. *Physiol Rev*. 1979 Jan;59(1):62–100.
95. Yang JR, Lin YT, Liao CH. Application of Embryonic Stem Cells on Parkinson's Disease Therapy. *Genomic Med Biomark Health Sci*. 2011 Mar 1;3(1):17–26.
96. Freed CR, Zhou W, Breeze RE. Dopamine Cell Transplantation for Parkinson's Disease: The Importance of Controlled Clinical Trials. *Neurotherapeutics*. 2011 Oct 1;8(4):549–61.
97. Kordower JH, Chu Y, Hauser RA, Freeman TB, Olanow CW. Lewy body-like pathology in long-term embryonic nigral transplants in Parkinson's disease. *Nat Med*. 2008 May;14(5):504–6.
98. Jang SE, Qiu L, Chan LL, Tan EK, Zeng L. Current Status of Stem Cell-Derived Therapies for Parkinson's Disease: From Cell Assessment and Imaging Modalities to Clinical Trials. *Front Neurosci* [Internet]. 2020 [cited 2023 May 9];14. Available from: <https://www.frontiersin.org/articles/10.3389/fnins.2020.558532>
99. Barker RA, Parmar M, Studer L, Takahashi J. Human Trials of Stem Cell-Derived Dopamine Neurons for Parkinson's Disease: Dawn of a New Era. *Cell Stem Cell*. 2017 Nov 2;21(5):569–73.
100. Kikuchi T, Morizane A, Doi D, Onoe H, Hayashi T, Kawasaki T, et al. Survival of Human Induced Pluripotent Stem Cell-Derived Midbrain Dopaminergic Neurons in the Brain of a Primate Model of Parkinson's Disease. *J Park Dis*. 2011 Jan 1;1(4):395–412.
101. Schweitzer JS, Song B, Herrington TM, Park TY, Lee N, Ko S, et al. Personalized iPSC-Derived Dopamine Progenitor Cells for Parkinson's Disease. *N Engl J Med*. 2020 May 14;382(20):1926–32.
102. Doi D, Magotani H, Kikuchi T, Ikeda M, Hiramatsu S, Yoshida K, et al. Pre-clinical study of induced pluripotent stem cell-derived dopaminergic progenitor cells for Parkinson's disease. *Nat Commun*. 2020 Jul 6;11(1):3369.
103. Kirik D, Rosenblad C, Björklund A, Mandel RJ. Long-Term rAAV-Mediated Gene Transfer of GDNF in the Rat Parkinson's Model: Intrastratial But Not Intranigral Transduction Promotes Functional Regeneration in the Lesioned Nigrostriatal System. *J Neurosci*. 2000 Jun 15;20(12):4686–700.
104. Rosenblad C, Kirik D, Devaux B, Moffat B, Phillips HS, Björklund A. Protection and regeneration of nigral dopaminergic neurons by neurturin or GDNF in a partial lesion model of Parkinson's disease after administration into the striatum or the lateral ventricle. *Eur J Neurosci*. 1999;11(5):1554–66.
105. Rosenblad C, Martinez-Serrano A, Björklund A. Intrastratial glial cell line-derived neurotrophic factor promotes sprouting of spared nigrostriatal dopaminergic afferents and induces recovery of function in a rat model of Parkinson's disease. *Neuroscience*. 1997 Sep 25;82(1):129–37.

106. Sullivan AM, O'Keeffe GW. Neurotrophic factor therapy for Parkinson's disease: past, present and future. *Neural Regen Res*. 2016 Feb;11(2):205–7.
107. Marks WJ, Bartus RT, Siffert J, Davis CS, Lozano A, Boulis N, et al. Gene delivery of AAV2-neurturin for Parkinson's disease: a double-blind, randomised, controlled trial. *Lancet Neurol*. 2010 Dec 1;9(12):1164–72.
108. Chu Y, Bartus RT, Manfredsson FP, Olanow CW, Kordower JH. Long-term post-mortem studies following neurturin gene therapy in patients with advanced Parkinson's disease. *Brain*. 2020 Mar 1;143(3):960–75.
109. Kaplitt MG, Feigin A, Tang C, Fitzsimons HL, Mattis P, Lawlor PA, et al. Safety and tolerability of gene therapy with an adeno-associated virus (AAV) borne GAD gene for Parkinson's disease: an open label, phase I trial. *The Lancet*. 2007 Jun 23;369(9579):2097–105.
110. LeWitt PA, Rezai AR, Leehey MA, Ojemann SG, Flaherty AW, Eskandar EN, et al. AAV2-GAD gene therapy for advanced Parkinson's disease: a double-blind, sham-surgery controlled, randomised trial. *Lancet Neurol*. 2011 Apr 1;10(4):309–19.
111. Palfi S, Gurruchaga JM, Ralph GS, Lepetit H, Lavisse S, Buttery PC, et al. Long-term safety and tolerability of ProSavin, a lentiviral vector-based gene therapy for Parkinson's disease: a dose escalation, open-label, phase 1/2 trial. *The Lancet*. 2014 Mar 29;383(9923):1138–46.
112. Palfi S, Gurruchaga JM, Lepetit H, Howard K, Ralph GS, Mason S, et al. Long-Term Follow-Up of a Phase I/II Study of ProSavin, a Lentiviral Vector Gene Therapy for Parkinson's Disease. *Hum Gene Ther Clin Dev*. 2018 Sep;29(3):148–55.
113. Meissner WG. Stratégies thérapeutiques ciblant l'alpha-synucléine pour le traitement de la maladie de Parkinson et des autres synucléinopathies. *Prat Neurol - FMC*. 2018 Apr 1;9(2):156–61.
114. Jankovic J, Goodman I, Safirstein B, Marmon TK, Schenk DB, Koller M, et al. Safety and Tolerability of Multiple Ascending Doses of PRX002/RG7935, an Anti- α -Synuclein Monoclonal Antibody, in Patients With Parkinson Disease: A Randomized Clinical Trial. *JAMA Neurol*. 2018 Oct 1;75(10):1206–14.
115. Schwab AD, Thurston MJ, Machhi J, Olson KE, Namminga KL, Gendelman HE, et al. Immunotherapy for Parkinson's disease. *Neurobiol Dis*. 2020 Apr 1;137:104760.
116. Brauer R, Wei L, Ma T, Athauda D, Girges C, Vijjaratnam N, et al. Diabetes medications and risk of Parkinson's disease: a cohort study of patients with diabetes. *Brain*. 2020 Oct 1;143(10):3067–76.
117. Peelaerts W, Bergkvist L, George S, Johnson M, Meyerdirk L, Schulz E, et al. Inhibiting the mitochondrial pyruvate carrier does not ameliorate synucleinopathy in the absence of inflammation or metabolic deficits. *Free Neuropathol*. 2020;1:33.
118. Mochizuki H, Yasuda T. Iron accumulation in Parkinson's disease. *J Neural Transm*. 2012 Dec 1;119(12):1511–4.
119. Devos D, Labreuche J, Rascol O, Corvol JC, Duhamel A, Guyon Delannoy P, et al. Trial of Deferiprone in Parkinson's Disease. *N Engl J Med*. 2022 Dec 1;387(22):2045–55.

120. Stocchi F. Therapy for Parkinson's Disease: What is in the Pipeline? *Neurotherapeutics*. 2014 Jan 1;11(1):24–33.
121. Kilzheimer A, Hentrich T, Burkhardt S, Schulze-Hentrich JM. The Challenge and Opportunity to Diagnose Parkinson's Disease in Midlife. *Front Neurol* [Internet]. 2019 [cited 2023 May 9];10. Available from: <https://www.frontiersin.org/articles/10.3389/fneur.2019.01328>
122. Mou L, Ding W, Fernandez-Funez P. Open questions on the nature of Parkinson's disease: from triggers to spreading pathology. *J Med Genet*. 2020 Feb 1;57(2):73–81.
123. Perlmuter JS. Assessment of Parkinson Disease Manifestations. *Curr Protoc Neurosci*. 2009;49(1):10.1.1-10.1.14.
124. Marsili L, Rizzo G, Colosimo C. Diagnostic Criteria for Parkinson's Disease: From James Parkinson to the Concept of Prodromal Disease. *Front Neurol* [Internet]. 2018 [cited 2023 May 9];9. Available from: <https://www.frontiersin.org/articles/10.3389/fneur.2018.00156>
125. Hughes AJ, Ben-Shlomo Y, Daniel SE, Lees AJ. What features improve the accuracy of clinical diagnosis in Parkinson's disease: A clinicopathologic study. *Neurology*. 1992 Jun 1;42(6):1142–1142.
126. Postuma RB, Berg D, Stern M, Poewe W, Olanow CW, Oertel W, et al. MDS clinical diagnostic criteria for Parkinson's disease. *Mov Disord*. 2015;30(12):1591–601.
127. Postuma RB, Poewe W, Litvan I, Lewis S, Lang AE, Halliday G, et al. Validation of the MDS clinical diagnostic criteria for Parkinson's disease. *Mov Disord*. 2018;33(10):1601–8.
128. Adler CH, Beach TG, Hentz JG, Shill HA, Caviness JN, Driver-Dunckley E, et al. Low clinical diagnostic accuracy of early vs advanced Parkinson disease: Clinicopathologic study. *Neurology*. 2014 Jul 29;83(5):406–12.
129. Tolosa E, Garrido A, Scholz SW, Poewe W. Challenges in the diagnosis of Parkinson's disease. *Lancet Neurol*. 2021 May 1;20(5):385–97.
130. Blauwendraat C, Nalls MA, Singleton AB. The genetic architecture of Parkinson's disease. *Lancet Neurol*. 2020 Feb 1;19(2):170–8.
131. Fereshtehnejad SM, Zeighami Y, Dagher A, Postuma RB. Clinical criteria for subtyping Parkinson's disease: biomarkers and longitudinal progression. *Brain*. 2017 Jul 1;140(7):1959–76.
132. Bandres-Ciga S, Saez-Atienzar S, Kim JJ, Makarious MB, Faghri F, Diez-Fairen M, et al. Large-scale pathway specific polygenic risk and transcriptomic community network analysis identifies novel functional pathways in Parkinson disease. *Acta Neuropathol (Berl)*. 2020 Sep 1;140(3):341–58.
133. Nalls MA, McLean CY, Rick J, Eberly S, Hutten SJ, Gwinn K, et al. Diagnosis of Parkinson's disease on the basis of clinical and genetic classification: a population-based modelling study. *Lancet Neurol*. 2015 Oct 1;14(10):1002–9.
134. Tolosa E, Vila M, Klein C, Rascol O. LRRK2 in Parkinson disease: challenges of clinical trials. *Nat Rev Neurol*. 2020 Feb;16(2):97–107.

135. Parnetti L, Gaetani L, Eusebi P, Paciotti S, Hansson O, El-Agnaf O, et al. CSF and blood biomarkers for Parkinson's disease. *Lancet Neurol*. 2019 Jun 1;18(6):573–86.
136. Gao L, Tang H, Nie K, Wang L, Zhao J, Gan R, et al. Cerebrospinal fluid alpha-synuclein as a biomarker for Parkinson's disease diagnosis: a systematic review and meta-analysis. *Int J Neurosci*. 2015 Sep 2;125(9):645–54.
137. Mollenhauer B, Caspell-Garcia CJ, Coffey CS, Taylor P, Singleton A, Shaw LM, et al. Longitudinal analyses of cerebrospinal fluid α -Synuclein in prodromal and early Parkinson's disease. *Mov Disord*. 2019;34(9):1354–64.
138. Öhman A, Forsgren L. NMR metabonomics of cerebrospinal fluid distinguishes between Parkinson's disease and controls. *Neurosci Lett*. 2015 May 6;594:36–9.
139. Trezzi JP, Galozzi S, Jaeger C, Barkovits K, Brockmann K, Maetzler W, et al. Distinct metabolomic signature in cerebrospinal fluid in early parkinson's disease. *Mov Disord*. 2017;32(10):1401–8.
140. Trupp M, Jonsson P, Öhrfelt A, Zetterberg H, Obudulu O, Malm L, et al. Metabolite and Peptide Levels in Plasma and CSF Differentiating Healthy Controls from Patients with Newly Diagnosed Parkinson's Disease. *J Park Dis*. 2014 Jan 1;4(3):549–60.
141. Willkommen D, Lucio M, Moritz F, Forcisi S, Kanawati B, Smirnov KS, et al. Metabolomic investigations in cerebrospinal fluid of Parkinson's disease. *PLOS ONE*. 2018 déc;13(12):e0208752.
142. Plewa S, Poplawska-Domaszewicz K, Florczał-Wyspińska J, Klupczynska-Gabryszak A, Sokol B, Milyk W, et al. The Metabolomic Approach Reveals the Alteration in Human Serum and Cerebrospinal Fluid Composition in Parkinson's Disease Patients. *Pharmaceuticals*. 2021 Sep;14(9):935.
143. Stoessel D, Schulte C, Teixeira dos Santos MC, Scheller D, Rebollo-Mesa I, Deuschle C, et al. Promising Metabolite Profiles in the Plasma and CSF of Early Clinical Parkinson's Disease. *Front Aging Neurosci* [Internet]. 2018 [cited 2023 May 9];10. Available from: <https://www.frontiersin.org/articles/10.3389/fnagi.2018.00051>
144. Burté F, Houghton D, Lowes H, Pyle A, Nesbitt S, Yarnall A, et al. metabolic profiling of Parkinson's disease and mild cognitive impairment. *Mov Disord*. 2017;32(6):927–32.
145. Zhao A, Qi L, Li J, Dong J, Yu H. A hybrid spatio-temporal model for detection and severity rating of Parkinson's disease from gait data. *Neurocomputing*. 2018 Nov 13;315:1–8.
146. Quinones MP, Kaddurah-Daouk R. Metabolomics tools for identifying biomarkers for neuropsychiatric diseases. *Neurobiol Dis*. 2009 Aug 1;35(2):165–76.
147. Gayed I, Joseph U, Fanous M, Wan D, Schiess M, Ondo W, et al. The Impact of DaTscan in the Diagnosis of Parkinson Disease. *Clin Nucl Med*. 2015 May;40(5):390.
148. de la Fuente-Fernández R. Frontostriatal Cognitive Staging in Parkinson's Disease. *Park Dis*. 2011 Dec 6;2012:e561046.
149. Bega D, Kuo PH, Chalkidou A, Grzeda MT, Macmillan T, Brand C, et al. Clinical utility of DaTscan in patients with suspected Parkinsonian syndrome: a systematic review and meta-analysis. *NPJ Park Dis*. 2021 May 24;7(1):43.

150. Jennings DL, Seibyl JP, Oakes D, Eberly S, Murphy J, Marek K. (123I) β -CIT and Single-Photon Emission Computed Tomographic Imaging vs Clinical Evaluation in Parkinsonian Syndrome: Unmasking an Early Diagnosis. *Arch Neurol*. 2004 Aug 1;61(8):1224–9.
151. Meles SK, Teune LK, Jong BM de, Dierckx RA, Leenders KL. Metabolic Imaging in Parkinson Disease. *J Nucl Med*. 2017 Jan 1;58(1):23–8.
152. Meles SK, Renken RJ, Pagani M, Teune LK, Arnaldi D, Morbelli S, et al. Abnormal pattern of brain glucose metabolism in Parkinson's disease: replication in three European cohorts. *Eur J Nucl Med Mol Imaging*. 2020 Feb 1;47(2):437–50.
153. Holtbernd F, Ma Y, Peng S, Schwartz F, Timmermann L, Kracht L, et al. Dopaminergic correlates of metabolic network activity in Parkinson's disease. *Hum Brain Mapp*. 2015;36(9):3575–85.
154. Akamatsu G, Ohnishi A, Aita K, Nishida H, Ikari Y, Sasaki M, et al. A revisit to quantitative PET with 18F-FDOPA of high specific activity using a high-resolution condition in view of application to regenerative therapy. *Ann Nucl Med*. 2017 Feb 1;31(2):163–71.
155. Maillet A, Krack P, Lhommée E, Météreau E, Klinger H, Favre E, et al. The prominent role of serotonergic degeneration in apathy, anxiety and depression in de novo Parkinson's disease. *Brain*. 2016 Sep 1;139(9):2486–502.
156. Rizzo G, Copetti M, Arcuti S, Martino D, Fontana A, Logroscino G. Accuracy of clinical diagnosis of Parkinson disease: A systematic review and meta-analysis. *Neurology*. 2016 Feb 9;86(6):566–76.
157. Berry C, La Vecchia C, Nicotera P. Paraquat and Parkinson's disease. *Cell Death Differ*. 2010 Jul;17(7):1115–25.
158. Bonne-Barkay D, Langston WJ, Di Monte DA. Toxicity of Redox Cycling Pesticides in Primary Mesencephalic Cultures. *Antioxid Redox Signal*. 2005 May;7(5–6):649–53.
159. Kamel F, Goldman SM, Umbach DM, Chen H, Richardson G, Barber MR, et al. Dietary fat intake, pesticide use, and Parkinson's disease. *Parkinsonism Relat Disord*. 2014 Jan 1;20(1):82–7.
160. Xiong N, Long X, Xiong J, Jia M, Chen C, Huang J, et al. Mitochondrial complex I inhibitor rotenone-induced toxicity and its potential mechanisms in Parkinson's disease models. *Crit Rev Toxicol*. 2012 Aug 1;42(7):613–32.
161. Ungerstedt U. Adipsia and Aphagia after 6-Hydroxydopamine Induced Degeneration of the Nigro-striatal Dopamine System. *Acta Physiol Scand*. 1971;82(S367):95–122.
162. Bové J, Prou D, Perier C, Przedborski S. Toxin-induced models of Parkinson's disease. *NeuroRX*. 2005 Jul;2(3):484–94.
163. Drui G, Carnicella S, Carcenac C, Favier M, Bertrand A, Boulet S, et al. Loss of dopaminergic nigrostriatal neurons accounts for the motivational and affective deficits in Parkinson's disease. *Mol Psychiatry*. 2014 Mar;19(3):358–67.
164. Rodriguez-Pallares J, Parga JA, Muñoz A, Rey P, Guerra MJ, Labandeira-Garcia JL. Mechanism of 6-hydroxydopamine neurotoxicity: the role of NADPH oxidase and microglial activation in 6-hydroxydopamine-induced degeneration of dopaminergic neurons. *J Neurochem*. 2007;103(1):145–56.

165. Schober A. Classic toxin-induced animal models of Parkinson's disease: 6-OHDA and MPTP. *Cell Tissue Res.* 2004 Oct 1;318(1):215–24.
166. Campos FL, Carvalho MM, Cristovão AC, Je G, Baltazar G, Salgado AJ, et al. Rodent models of Parkinson's disease: beyond the motor symptomatology. *Front Behav Neurosci* [Internet]. 2013 [cited 2021 Feb 11];7. Available from: <http://journal.frontiersin.org/article/10.3389/fnbeh.2013.00175/abstract>
167. Erwan Bezard, Christelle Imbert, Christian E. Gross. Experimental Models of Parkinson's Disease: From the Static to the Dynamic. *Rev Neurosci.* 1998 Apr 1;9(2):71–90.
168. Tieu K. A Guide to Neurotoxic Animal Models of Parkinson's Disease. *Cold Spring Harb Perspect Med.* 2011 Sep 1;1(1):a009316.
169. Masini D, Plewnia C, Bertho M, Scalbert N, Caggiano V, Fisone G. A Guide to the Generation of a 6-Hydroxydopamine Mouse Model of Parkinson's Disease for the Study of Non-Motor Symptoms. *Biomedicines.* 2021 Jun;9(6):598.
170. Favier M, Carcenac C, Drui G, Vachez Y, Boulet S, Savasta M, et al. Implication of dorsostriatal D3 receptors in motivational processes: a potential target for neuropsychiatric symptoms in Parkinson's disease. *Sci Rep.* 2017 Jan 30;7(1):41589.
171. Favier M, Duran T, Carcenac C, Drui G, Savasta M, Carnicella S. Pramipexole reverses Parkinson's disease-related motivational deficits in rats. *Mov Disord.* 2014;29(7):912–20.
172. Decressac M, Mattsson B, Björklund A. Comparison of the behavioural and histological characteristics of the 6-OHDA and α -synuclein rat models of Parkinson's disease. *Exp Neurol.* 2012 May;235(1):306–15.
173. Langston JW, Ballard P, Tetrud JW, Irwin I. Chronic Parkinsonism in Humans Due to a Product of Meperidine-Analog Synthesis. *Science.* 1983 Feb 25;219(4587):979–80.
174. Langston JW, Irwin I, Langston EB, Forno LS. 1-Methyl-4-phenylpyridinium ion (MPP⁺): Identification of a metabolite of MPTP, a toxin selective to the substantia nigra. *Neurosci Lett.* 1984 Jul 13;48(1):87–92.
175. Chiba K, Trevor A, Castagnoli N. Metabolism of the neurotoxic tertiary amine, MPTP, by brain monoamine oxidase. *Biochem Biophys Res Commun.* 1984 Apr 30;120(2):574–8.
176. Markey SP, Johannessen JN, Chiueh CC, Burns RS, Herkenham MA. Intraneuronal generation of a pyridinium metabolite may cause drug-induced parkinsonism. *Nature.* 1984 Oct;311(5985):464–7.
177. Castagnoli N, Chiba K, Trevor AJ. V. Potential bioactivation pathways for the neurotoxin 1-methyl-4-phenyl-1,2,3,6-tetrahydropyridine (MPTP). *Life Sci.* 1985 Jan 21;36(3):225–30.
178. Ballanger B, Beaudoin-Gobert M, Neumane S, Epinat J, Metereau E, Duperrier S, et al. Imaging Dopamine and Serotonin Systems on MPTP Monkeys: A Longitudinal PET Investigation of Compensatory Mechanisms. *J Neurosci.* 2016 Feb 3;36(5):1577–89.
179. Bezard E, Przedborski S. A tale on animal models of Parkinson's disease. *Mov Disord.* 2011;26(6):993–1002.

180. Veyres N, Hamadjida A, Huot P. Predictive Value of Parkinsonian Primates in Pharmacologic Studies: A Comparison between the Macaque, Marmoset, and Squirrel Monkey. *J Pharmacol Exp Ther*. 2018 May 1;365(2):379–97.
181. Giovanni A, Sieber BA, Heikkila RE, Sonsalla PK. Studies on species sensitivity to the dopaminergic neurotoxin 1-methyl-4-phenyl-1,2,3,6-tetrahydropyridine. Part 1: Systemic administration. *J Pharmacol Exp Ther*. 1994 Sep 1;270(3):1000–7.
182. Schmidt N, Ferger B. Neurochemical findings in the MPTP model of Parkinson's disease. *J Neural Transm*. 2001 Nov 1;108(11):1263–82.
183. Da Cunha C, Gevaerd MS, Vital MABF, Miyoshi E, Andreatini R, Silveira R, et al. Memory disruption in rats with nigral lesions induced by MPTP: a model for early Parkinson's disease amnesia. *Behav Brain Res*. 2001 Sep 28;124(1):9–18.
184. Ferro MM, Bellissimo MI, Anselmo-Franci JA, Angellucci MEM, Canteras NS, Da Cunha C. Comparison of bilaterally 6-OHDA- and MPTP-lesioned rats as models of the early phase of Parkinson's disease: Histological, neurochemical, motor and memory alterations. *J Neurosci Methods*. 2005 Oct;148(1):78–87.
185. Polymeropoulos MH, Lavedan C, Leroy E, Ide SE, Dehejia A, Dutra A, et al. Mutation in the α -Synuclein Gene Identified in Families with Parkinson's Disease. *Science*. 1997 Jun 27;276(5321):2045–7.
186. Chesselet MF, Richter F, Zhu C, Magen I, Watson MB, Subramaniam SR. A Progressive Mouse Model of Parkinson's Disease: The Thy1-aSyn ("Line 61") Mice. *Neurotherapeutics*. 2012 Apr 1;9(2):297–314.
187. Chia SJ, Tan EK, Chao YX. Historical Perspective: Models of Parkinson's Disease. *Int J Mol Sci*. 2020 Jan;21(7):2464.
188. Cookson MR. Parkinsonism Due to Mutations in PINK1, Parkin, and DJ-1 and Oxidative Stress and Mitochondrial Pathways. *Cold Spring Harb Perspect Med*. 2012 Sep 1;2(9):a009415.
189. Selvaraj S, Piramanayagam S. Impact of gene mutation in the development of Parkinson's disease. *Genes Dis*. 2019 Jun 1;6(2):120–8.
190. Kitada T, Pisani A, Porter DR, Yamaguchi H, Tscherter A, Martella G, et al. Impaired dopamine release and synaptic plasticity in the striatum of PINK1-deficient mice. *Proc Natl Acad Sci*. 2007 Jul 3;104(27):11441–6.
191. Sanchez G, Varaschin RK, Büeler H, Marcogliese PC, Park DS, Trudeau LE. Unaltered Striatal Dopamine Release Levels in Young Parkin Knockout, Pink1 Knockout, DJ-1 Knockout and LRRK2 R1441G Transgenic Mice. *PLOS ONE*. 2014 Apr 9;9(4):e94826.
192. Creed RB, Goldberg MS. New Developments in Genetic rat models of Parkinson's Disease. *Mov Disord Off J Mov Disord Soc*. 2018 May;33(5):717–29.
193. Maroteaux L, Campanelli JT, Scheller RH. Synuclein: a neuron-specific protein localized to the nucleus and presynaptic nerve terminal. *J Neurosci*. 1988 Aug 1;8(8):2804–15.

194. Jakes R, Spillantini MG, Goedert M. Identification of two distinct synucleins from human brain. *FEBS Lett.* 1994 May 23;345(1):27–32.
195. Chen X, Silva HAR de, Pettenati MJ. The human NACP/{alpha}-synuclein gene: Chromosome assignment to 4q21.3-q22 and TaqI RFLP analysis. *Genomics* [Internet]. 1995 Mar 20 [cited 2023 May 9];26(2). Available from: <https://www.osti.gov/biblio/219914>
196. Weinreb PH, Zhen W, Poon AW, Conway KA, Lansbury PT. NACP, A Protein Implicated in Alzheimer's Disease and Learning, Is Natively Unfolded. *Biochemistry.* 1996 Jan 1;35(43):13709–15.
197. Davidson WS, Jonas A, Clayton DF, George JM. Stabilization of α -Synuclein Secondary Structure upon Binding to Synthetic Membranes *. *J Biol Chem.* 1998 Apr 17;273(16):9443–9.
198. Jensen PH, Nielsen MS, Jakes R, Dotti CG, Goedert M. Binding of α -Synuclein to Brain Vesicles Is Abolished by Familial Parkinson's Disease Mutation *. *J Biol Chem.* 1998 Oct 9;273(41):26292–4.
199. Rodriguez JA, Ivanova MI, Sawaya MR, Cascio D, Reyes FE, Shi D, et al. Structure of the toxic core of α -synuclein from invisible crystals. *Nature.* 2015 Sep;525(7570):486–90.
200. Binolfi A, Rasia RM, Bertoncini CW, Ceolin M, Zweckstetter M, Griesinger C, et al. Interaction of α -Synuclein with Divalent Metal Ions Reveals Key Differences: A Link between Structure, Binding Specificity and Fibrillation Enhancement. *J Am Chem Soc.* 2006 Aug 1;128(30):9893–901.
201. Gallardo J, Escalona-Noguero C, Sot B. Role of α -Synuclein Regions in Nucleation and Elongation of Amyloid Fiber Assembly. *ACS Chem Neurosci.* 2020 Mar 18;11(6):872–9.
202. Dehay B, Vila M, Bezard E, Brundin P, Kordower JH. Alpha-synuclein propagation: New insights from animal models. *Mov Disord.* 2016;31(2):161–8.
203. Villar-Piqué A, Lopes da Fonseca T, Outeiro TF. Structure, function and toxicity of alpha-synuclein: the Bermuda triangle in synucleinopathies. *J Neurochem.* 2016;139(S1):240–55.
204. Burré J, Sharma M, Tsetsenis T, Buchman V, Etherton MR, Südhof TC. α -Synuclein Promotes SNARE-Complex Assembly in Vivo and in Vitro. *Science.* 2010 Sep 24;329(5999):1663–7.
205. Burré J, Sharma M, Südhof TC. Definition of a Molecular Pathway Mediating α -Synuclein Neurotoxicity. *J Neurosci.* 2015 Apr 1;35(13):5221–32.
206. Perez RG, Waymire JC, Lin E, Liu JJ, Guo F, Zigmond MJ. A Role for α -Synuclein in the Regulation of Dopamine Biosynthesis. *J Neurosci.* 2002 Apr 15;22(8):3090–9.
207. Lou H, Montoya SE, Alerte TNM, Wang J, Wu J, Peng X, et al. Serine 129 Phosphorylation Reduces the Ability of α -Synuclein to Regulate Tyrosine Hydroxylase and Protein Phosphatase 2A in Vitro and in Vivo*. *J Biol Chem.* 2010 Jun 4;285(23):17648–61.
208. Wersinger C, Sidhu A. Attenuation of dopamine transporter activity by α -synuclein. *Neurosci Lett.* 2003 Apr 17;340(3):189–92.
209. Ostrerova N, Petrucelli L, Farrer M, Mehta N, Choi P, Hardy J, et al. α -Synuclein Shares Physical and Functional Homology with 14-3-3 Proteins. *J Neurosci.* 1999 Jul 15;19(14):5782–91.

210. Souza JM, Giasson BI, Lee VMY, Ischiropoulos H. Chaperone-like activity of synucleins. *FEBS Lett.* 2000 May 26;474(1):116–9.
211. Perez RG. Editorial: The Protein Alpha-Synuclein: Its Normal Role (in Neurons) and Its Role in Disease. *Front Neurosci* [Internet]. 2020 [cited 2023 May 9];14. Available from: <https://www.frontiersin.org/articles/10.3389/fnins.2020.00116>
212. Pinho R, Paiva I, Jerčić KG, Fonseca-Ornelas L, Gerhardt E, Fahlbusch C, et al. Nuclear localization and phosphorylation modulate pathological effects of alpha-synuclein. *Hum Mol Genet.* 2019 Jan 1;28(1):31–50.
213. Jin H, Kanthasamy A, Ghosh A, Yang Y, Anantharam V, Kanthasamy AG. α -Synuclein Negatively Regulates Protein Kinase C δ Expression to Suppress Apoptosis in Dopaminergic Neurons by Reducing p300 Histone Acetyltransferase Activity. *J Neurosci.* 2011 Feb 9;31(6):2035–51.
214. Greten-Harrison B, Polydoro M, Morimoto-Tomita M, Diao L, Williams AM, Nie EH, et al. $\alpha\beta\gamma$ -Synuclein triple knockout mice reveal age-dependent neuronal dysfunction. *Proc Natl Acad Sci.* 2010 Nov 9;107(45):19573–8.
215. De Mattos EP, Wentink A, Nussbaum-Krammer C, Hansen C, Bergink S, Melki R, et al. Protein Quality Control Pathways at the Crossroad of Synucleinopathies. *J Park Dis.* 2020 Jan 1;10(2):369–82.
216. Brundin P, Melki R, Kopito R. Prion-like transmission of protein aggregates in neurodegenerative diseases. *Nat Rev Mol Cell Biol.* 2010 Apr;11(4):301–7.
217. Alam P, Bousset L, Melki R, Otzen DE. α -synuclein oligomers and fibrils: a spectrum of species, a spectrum of toxicities. *J Neurochem.* 2019;150(5):522–34.
218. Flavin WP, Bousset L, Green ZC, Chu Y, Skarpathiotis S, Chaney MJ, et al. Endocytic vesicle rupture is a conserved mechanism of cellular invasion by amyloid proteins. *Acta Neuropathol (Berl).* 2017 Oct 1;134(4):629–53.
219. Gustot A, Gallea JI, Sarroukh R, Celej MS, Ruyschaert JM, Raussens V. Amyloid fibrils are the molecular trigger of inflammation in Parkinson's disease. *Biochem J.* 2015 Oct 16;471(3):323–33.
220. Gasser T. Mendelian forms of Parkinson's disease. *Biochim Biophys Acta BBA - Mol Basis Dis.* 2009 Jul 1;1792(7):587–96.
221. Lees AJ, Hardy J, Revesz T. Parkinson's disease. *The Lancet.* 2009 Jun 13;373(9680):2055–66.
222. Dawson TM, Ko HS, Dawson VL. Genetic Animal Models of Parkinson's Disease. *Neuron.* 2010 Jun 10;66(5):646–61.
223. Thiruchelvam MJ, Powers JM, Cory-Slechta DA, Richfield EK. Risk factors for dopaminergic neuron loss in human α -synuclein transgenic mice. *Eur J Neurosci.* 2004;19(4):845–54.
224. Giasson BI, Duda JE, Quinn SM, Zhang B, Trojanowski JQ, Lee VMY. Neuronal α -Synucleinopathy with Severe Movement Disorder in Mice Expressing A53T Human α -Synuclein. *Neuron.* 2002 May 16;34(4):521–33.

225. Masliah E, Rockenstein E, Veinbergs I, Mallory M, Hashimoto M, Takeda A, et al. Dopaminergic Loss and Inclusion Body Formation in α -Synuclein Mice: Implications for Neurodegenerative Disorders. *Science*. 2000 Feb 18;287(5456):1265–9.
226. Fernagut PO, Chesselet MF. Alpha-synuclein and transgenic mouse models. *Neurobiol Dis*. 2004 Nov 1;17(2):123–30.
227. Jagmag SA, Tripathi N, Shukla SD, Maiti S, Khurana S. Evaluation of Models of Parkinson's Disease. *Front Neurosci* [Internet]. 2016 [cited 2023 May 10];9. Available from: <https://www.frontiersin.org/articles/10.3389/fnins.2015.00503>
228. Bourdenx M, Dovero S, Engeln M, Bido S, Bastide MF, Dutheil N, et al. Lack of additive role of ageing in nigrostriatal neurodegeneration triggered by α -synuclein overexpression. *Acta Neuropathol Commun*. 2015 Dec;3(1):46.
229. Kirik D, Rosenblad C, Burger C, Lundberg C, Johansen TE, Muzyczka N, et al. Parkinson-like neurodegeneration induced by targeted overexpression of alpha-synuclein in the nigrostriatal system. *J Neurosci Off J Soc Neurosci*. 2002 Apr 1;22(7):2780–91.
230. Caudal D, Alvarsson A, Björklund A, Svenningsson P. Depressive-like phenotype induced by AAV-mediated overexpression of human α -synuclein in midbrain dopaminergic neurons. *Exp Neurol*. 2015 Nov 1;273:243–52.
231. Oliveras-Salvá M, Van der Perren A, Casadei N, Stroobants S, Nuber S, D'Hooge R, et al. rAAV2/7 vector-mediated overexpression of alpha-synuclein in mouse substantia nigra induces protein aggregation and progressive dose-dependent neurodegeneration. *Mol Neurodegener*. 2013 Nov 25;8(1):44.
232. Ip CW, Klaus LC, Karikari AA, Visanji NP, Brotchie JM, Lang AE, et al. AAV1/2-induced overexpression of A53T- α -synuclein in the substantia nigra results in degeneration of the nigrostriatal system with Lewy-like pathology and motor impairment: a new mouse model for Parkinson's disease. *Acta Neuropathol Commun*. 2017 Feb 1;5(1):11.
233. Petiet A. Current and Emerging MR Methods and Outcome in Rodent Models of Parkinson's Disease: A Review. *Front Neurosci* [Internet]. 2021 [cited 2023 Apr 1];15. Available from: <https://www.frontiersin.org/articles/10.3389/fnins.2021.583678>
234. Patterson JR, Duffy MF, Kemp CJ, Howe JW, Collier TJ, Stoll AC, et al. Time course and magnitude of alpha-synuclein inclusion formation and nigrostriatal degeneration in the rat model of synucleinopathy triggered by intrastriatal α -synuclein preformed fibrils. *Neurobiol Dis*. 2019 Oct 1;130:104525.
235. Paumier KL, Luk KC, Manfredsson FP, Kanaan NM, Lipton JW, Collier TJ, et al. Intrastriatal injection of pre-formed mouse α -synuclein fibrils into rats triggers α -synuclein pathology and bilateral nigrostriatal degeneration. *Neurobiol Dis*. 2015 Oct 1;82:185–99.
236. Shimozawa A, Ono M, Takahara D, Tarutani A, Imura S, Masuda-Suzukake M, et al. Propagation of pathological α -synuclein in marmoset brain. *Acta Neuropathol Commun*. 2017 Feb 2;5(1):12.

237. Lama J, Buhidma Y, Fletcher EJR, Duty S. Animal models of Parkinson's disease: a guide to selecting the optimal model for your research. *Neuronal Signal*. 2021 Dec 8;5(4):NS20210026.
238. Polinski NK. A Summary of Phenotypes Observed in the In Vivo Rodent Alpha-Synuclein Preformed Fibril Model. *J Park Dis*. 2021 Jan 1;11(4):1555–67.
239. Lauterbur PC. Image Formation by Induced Local Interactions: Examples Employing Nuclear Magnetic Resonance. *Nature*. 1973 Mar;242(5394):190–1.
240. Stehling MK, Turner R, Mansfield P. Echo-Planar Imaging: Magnetic Resonance Imaging in a Fraction of a Second. *Science*. 1991 Oct 4;254(5028):43–50.
241. Balafar MA, Ramli AR, Saripan MI, Mashohor S. Review of brain MRI image segmentation methods. *Artif Intell Rev*. 2010 Mar 1;33(3):261–74.
242. Kawahara D, Nagata Y. T1-weighted and T2-weighted MRI image synthesis with convolutional generative adversarial networks. *Rep Pract Oncol Radiother*. 2021 Feb 25;26(1):35–42.
243. Kennedy DN, Makris N, Herbert MR, Takahashi T, Caviness Jr. VS. Basic principles of MRI and morphometry studies of human brain development. *Dev Sci*. 2002;5(3):268–78.
244. Frank LR, Rowe TB, Boyer DM, Witmer LM, Galinsky VL. Unveiling the third dimension in morphometry with automated quantitative volumetric computations. *Sci Rep*. 2021 Jul 14;11(1):14438.
245. Glasser MF, Essen DCV. Mapping Human Cortical Areas In Vivo Based on Myelin Content as Revealed by T1- and T2-Weighted MRI. *J Neurosci*. 2011 Aug 10;31(32):11597–616.
246. Haacke EM, Cheng NYC, House MJ, Liu Q, Neelavalli J, Ogg RJ, et al. Imaging iron stores in the brain using magnetic resonance imaging. *Magn Reson Imaging*. 2005 Jan;23(1):1–25.
247. Bagnato F, Hametner S, Boyd E, Endmayr V, Shi Y, Ikonomidou V, et al. Untangling the R2* contrast in multiple sclerosis: A combined MRI-histology study at 7.0 Tesla. *PLOS ONE*. 2018 Mar 21;13(3):e0193839.
248. Bassler PJ, Mattiello J, Lebihan D. Estimation of the Effective Self-Diffusion Tensor from the NMR Spin Echo. *J Magn Reson B*. 1994 Mar 1;103(3):247–54.
249. Le Bihan D, Johansen-Berg H. Diffusion MRI at 25: Exploring brain tissue structure and function. *NeuroImage*. 2012 Jun 1;61(2):324–41.
250. Assaf Y, Pasternak O. Diffusion Tensor Imaging (DTI)-based White Matter Mapping in Brain Research: A Review. *J Mol Neurosci*. 2008 Jan 1;34(1):51–61.
251. Öz G, Alger JR, Barker PB, Bartha R, Bizzi A, Boesch C, et al. Clinical Proton MR Spectroscopy in Central Nervous System Disorders. *Radiology*. 2014 Mar;270(3):658–79.
252. Soares DP, Law M. Magnetic resonance spectroscopy of the brain: review of metabolites and clinical applications. *Clin Radiol*. 2009 Jan 1;64(1):12–21.
253. Buxton RB. Introduction to Functional Magnetic Resonance Imaging: Principles and Techniques. Cambridge University Press; 2009. 479 p.

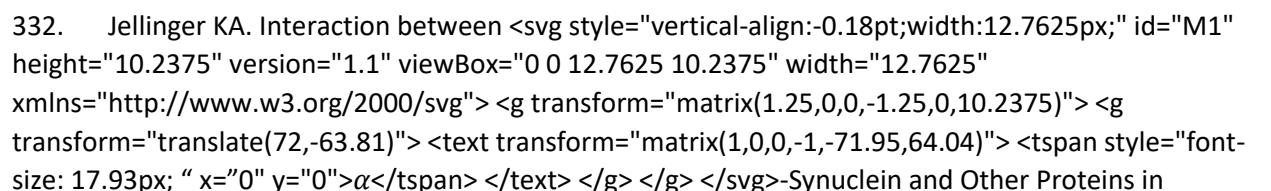
254. Logothetis NK. What we can do and what we cannot do with fMRI. *Nature*. 2008 Jun;453(7197):869–78.
255. Ashburner J, Friston KJ. Voxel-based morphometry--the methods. *NeuroImage*. 2000 Jun;11(6 Pt 1):805–21.
256. Good CD, Johnsrude IS, Ashburner J, Henson RN, Friston KJ, Frackowiak RS. A voxel-based morphometric study of ageing in 465 normal adult human brains. *NeuroImage*. 2001 Jul;14(1 Pt 1):21–36.
257. Mechelli A, Price C, Friston K, Ashburner J. Voxel-Based Morphometry of the Human Brain: Methods and Applications. *Curr Med Imaging Rev*. 2005 Jun 1;1(2):105–13.
258. Fenchel M, Thesen S, Schilling A. Automatic Labeling of Anatomical Structures in MR FastView Images Using a Statistical Atlas. In: Metaxas D, Axel L, Fichtinger G, Székely G, editors. *Medical Image Computing and Computer-Assisted Intervention – MICCAI 2008*. Berlin, Heidelberg: Springer; 2008. p. 576–84. (Lecture Notes in Computer Science).
259. Giorgio A, De Stefano N. Clinical use of brain volumetry. *J Magn Reson Imaging*. 2013;37(1):1–14.
260. Dahnke R, Yotter RA, Gaser C. Cortical thickness and central surface estimation. *NeuroImage*. 2013 Jan 15;65:336–48.
261. Davatzikos C. Machine learning in neuroimaging: Progress and challenges. *NeuroImage*. 2019 Aug 15;197:652–6.
262. Aerts HJWL, Velazquez ER, Leijenaar RTH, Parmar C, Grossmann P, Carvalho S, et al. Decoding tumour phenotype by noninvasive imaging using a quantitative radiomics approach. *Nat Commun*. 2014 Jun 3;5(1):4006.
263. Gillies RJ, Kinahan PE, Hricak H. Radiomics: Images Are More than Pictures, They Are Data. *Radiology*. 2016 Feb;278(2):563–77.
264. Liu ZY, Liu FT, Zuo CT, Koprach JB, Wang J. Update on Molecular Imaging in Parkinson's Disease. *Neurosci Bull*. 2018 Apr 1;34(2):330–40.
265. Heim B, Krismer F, De Marzi R, Seppi K. Magnetic resonance imaging for the diagnosis of Parkinson's disease. *J Neural Transm*. 2017;124(8):915–64.
266. Summerfield C, Junqué C, Tolosa E, Salgado-Pineda P, Gómez-Ansón B, Martí MJ, et al. Structural Brain Changes in Parkinson Disease With Dementia: A Voxel-Based Morphometry Study. *Arch Neurol*. 2005 Feb 1;62(2):281–5.
267. Gao Y, Nie K, Huang B, Mei M, Guo M, Xie S, et al. Changes of brain structure in Parkinson's disease patients with mild cognitive impairment analyzed via VBM technology. *Neurosci Lett*. 2017 Sep;658:121–32.
268. Tinaz S, Courtney MG, Stern CE. Focal cortical and subcortical atrophy in early Parkinson's disease. *Mov Disord*. 2011;26(3):436–41.

269. Jubault T, Gagnon JF, Karama S, Ptito A, Lafontaine AL, Evans AC, et al. Patterns of cortical thickness and surface area in early Parkinson's disease. *NeuroImage*. 2011 Mar 15;55(2):462–7.
270. Chaudhary S, Kumaran SS, Goyal V, Kalaivani M, Kaloiya GS, Sagar R, et al. Frontal lobe metabolic alterations characterizing Parkinson's disease cognitive impairment. *Neurol Sci Off J Ital Neurol Soc Ital Soc Clin Neurophysiol*. 2021 Mar;42(3):1053–64.
271. Kwon DH, Kim JM, Oh SH, Jeong HJ, Park SY, Oh ES, et al. Seven-Tesla magnetic resonance images of the substantia nigra in Parkinson disease. *Ann Neurol*. 2012 Feb;71(2):267–77.
272. Minati L, Grisoli M, Carella F, De Simone T, Bruzzone MG, Savoirdo M. Imaging degeneration of the substantia nigra in Parkinson disease with inversion-recovery MR imaging. *AJNR Am J Neuroradiol*. 2007 Feb;28(2):309–13.
273. Péran P, Cherubini A, Assogna F, Piras F, Quattrocchi C, Peppe A, et al. Magnetic resonance imaging markers of Parkinson's disease nigrostriatal signature. *Brain J Neurol*. 2010 Nov;133(11):3423–33.
274. Westphal R, Sumiyoshi A, Simmons C, Mesquita M, Wood TC, Williams SCR, et al. Characterization of gray matter atrophy following 6-hydroxydopamine lesion of the nigrostriatal system. *Neuroscience*. 2016 Oct 15;334:166–79.
275. Ulla M, Bonny JM, Ouchchane L, Rieu I, Claise B, Durif F. Is R2* a new MRI biomarker for the progression of Parkinson's disease? A longitudinal follow-up. *PloS One*. 2013;8(3):e57904.
276. Wieler M, Gee M, Camicioli R, Martin WRW. Freezing of gait in early Parkinson's disease: Nigral iron content estimated from magnetic resonance imaging. *J Neurol Sci*. 2016 Feb 15;361:87–91.
277. Murakami Y, Kakeda S, Watanabe K, Ueda I, Ogasawara A, Moriya J, et al. Usefulness of Quantitative Susceptibility Mapping for the Diagnosis of Parkinson Disease. *AJNR Am J Neuroradiol*. 2015 Jun;36(6):1102–8.
278. Guan XJ, Guo T, Zhou C, Gao T, Wu JJ, Han V, et al. A multiple-tissue-specific magnetic resonance imaging model for diagnosing Parkinson's disease: a brain radiomics study. *Neural Regen Res*. 2022 Apr 29;17(12):2743–9.
279. Cochrane CJ, Ebmeier KP. Diffusion tensor imaging in parkinsonian syndromes: A systematic review and meta-analysis. *Neurology*. 2013 Feb 26;80(9):857–64.
280. Vaillancourt DE, Spraker MB, Prodoehl J, Abraham I, Corcos DM, Zhou XJ, et al. High-resolution diffusion tensor imaging in the substantia nigra of de novo Parkinson disease. *Neurology*. 2009 Apr 21;72(16):1378–84.
281. Scherfler C, Schocke MF, Seppi K, Esterhammer R, Brenneis C, Jaschke W, et al. Voxel-wise analysis of diffusion weighted imaging reveals disruption of the olfactory tract in Parkinson's disease. *Brain J Neurol*. 2006 Feb;129(Pt 2):538–42.
282. Rolheiser TM, Fulton HG, Good KP, Fisk JD, McKelvey JR, Scherfler C, et al. Diffusion tensor imaging and olfactory identification testing in early-stage Parkinson's disease. *J Neurol*. 2011 Jul;258(7):1254–60.

283. Soria G, Aguilar E, Tudela R, Mullol J, Planas AM, Marin C. In vivo magnetic resonance imaging characterization of bilateral structural changes in experimental Parkinson's disease: a T2 relaxometry study combined with longitudinal diffusion tensor imaging and manganese-enhanced magnetic resonance imaging in the 6-: Bilateral structural changes in a PD model. *Eur J Neurosci*. 2011 Apr;33(8):1551–60.
284. Van Camp N, Vreys R, Van Laere K, Lauwers E, Beque D, Verhoye M, et al. Morphologic and functional changes in the unilateral 6-hydroxydopamine lesion rat model for Parkinson's disease discerned with μ SPECT and quantitative MRI. *Magn Reson Mater Phys Biol Med*. 2010 Apr;23(2):65–75.
285. Monnot C, Zhang X, Nikkhou-Aski S, Damberg P, Svenningsson P. Asymmetric dopaminergic degeneration and levodopa alter functional corticostriatal connectivity bilaterally in experimental parkinsonism. *Exp Neurol*. 2017 Jun 1;292:11–20.
286. Guan X, Xuan M, Gu Q, Huang P, Liu C, Wang N, et al. Regionally progressive accumulation of iron in Parkinson's disease as measured by quantitative susceptibility mapping. *NMR Biomed*. 2017;30(4):e3489.
287. Cao H, Shi J, Cao B, Kang B, Zhang M, Qu Q. Evaluation of the Braak staging of brain pathology with 1H-MRS in patients with Parkinson's disease. *Neurosci Lett*. 2017 Nov 1;660:57–62.
288. Firbank MJ, Harrison RM, O'Brien JT. A Comprehensive Review of Proton Magnetic Resonance Spectroscopy Studies in Dementia and Parkinson's Disease. *Dement Geriatr Cogn Disord*. 2002;14(2):64–76.
289. Gröger A, Bender B, Wurster I, Chadzynski GL, Klose U, Berg D. Differentiation between idiopathic and atypical parkinsonian syndromes using three-dimensional magnetic resonance spectroscopic imaging. *J Neurol Neurosurg Psychiatry*. 2013 Jun 1;84(6):644–9.
290. Coune PG, Craveiro M, Gaugler MN, Mlynárik V, Schneider BL, Aebischer P, et al. An in vivo ultrahigh field 14.1 T (1) H-MRS study on 6-OHDA and α -synuclein-based rat models of Parkinson's disease: GABA as an early disease marker. *NMR Biomed*. 2013 Jan;26(1):43–50.
291. Betrouni N, Yasmina M, Bombois S, Pétrault M, Dondaine T, Lachaud C, et al. Texture Features of Magnetic Resonance Images: an Early Marker of Post-stroke Cognitive Impairment. *Transl Stroke Res*. 2020 Aug;11(4):643–52.
292. Betrouni N, Moreau C, Rolland AS, Carrière N, Chupin M, Kuchcinski G, et al. Texture-based markers from structural imaging correlate with motor handicap in Parkinson's disease. *Sci Rep*. 2021 Feb 1;11(1):2724.
293. Prodoehl J, Burciu RG, Vaillancourt DE. Resting State Functional Magnetic Resonance Imaging in Parkinson's Disease. *Curr Neurol Neurosci Rep*. 2014 Apr 18;14(6):448.
294. Helmich RC, Derikx LC, Bakker M, Scheeringa R, Bloem BR, Toni I. Spatial Remapping of Corticostriatal Connectivity in Parkinson's Disease. *Cereb Cortex*. 2010 May 1;20(5):1175–86.
295. Cerasa A, Novellino F, Quattrone A. Connectivity Changes in Parkinson's Disease. *Curr Neurol Neurosci Rep*. 2016 Oct;16(10):91.

296. Tuovinen N, Seppi K, de Pasquale F, Müller C, Nocker M, Schocke M, et al. The reorganization of functional architecture in the early-stages of Parkinson's disease. *Parkinsonism Relat Disord*. 2018 May 1;50:61–8.
297. Perlberg V, Lambert J, Butler B, Felfli M, Valabrègue R, Privat AL, et al. Alterations of the nigrostriatal pathway in a 6-OHDA rat model of Parkinson's disease evaluated with multimodal MRI. Ariga H, editor. *PLOS ONE*. 2018 Sep 6;13(9):e0202597.
298. Westphal R, Simmons C, Mesquita MB, Wood TC, Williams SCR, Vernon AC, et al. Characterization of the resting-state brain network topology in the 6-hydroxydopamine rat model of Parkinson's disease. *PLOS ONE*. 2017 Mar 1;12(3):e0172394.
299. Zhurakovskaya E, Leikas J, Pirttimäki T, Casas Mon F, Gynther M, Aliev R, et al. Sleep-State Dependent Alterations in Brain Functional Connectivity under Urethane Anesthesia in a Rat Model of Early-Stage Parkinson's Disease. *eNeuro*. 2019 Feb 26;6(1):ENEURO.0456-18.2019.
300. Sasaki M, Shibata E, Tohyama K, Takahashi J, Otsuka K, Tsuchiya K, et al. Neuromelanin magnetic resonance imaging of locus ceruleus and substantia nigra in Parkinson's disease. *NeuroReport*. 2006 Jul 31;17(11):1215.
301. Sulzer D, Cassidy C, Horga G, Kang UJ, Fahn S, Casella L, et al. Neuromelanin detection by magnetic resonance imaging (MRI) and its promise as a biomarker for Parkinson's disease. *Npj Park Dis*. 2018 Apr 10;4(1):1–13.
302. Schwarz ST, Rittman T, Gontu V, Morgan PS, Bajaj N, Auer DP. T1-Weighted MRI shows stage-dependent substantia nigra signal loss in Parkinson's disease. *Mov Disord*. 2011;26(9):1633–8.
303. Barden H, Levine S. Histochemical observations on rodent brain melanin. *Brain Res Bull*. 1983 Jun 1;10(6):847–51.
304. Carballo-Carbajal I, Laguna A, Romero-Giménez J, Cuadros T, Bové J, Martínez-Vicente M, et al. Brain tyrosinase overexpression implicates age-dependent neuromelanin production in Parkinson's disease pathogenesis. *Nat Commun*. 2019 Mar 7;10(1):973.
305. Deumens R, Blokland A, Prickaerts J. Modeling Parkinson's Disease in Rats: An Evaluation of 6-OHDA Lesions of the Nigrostriatal Pathway. *Exp Neurol*. 2002 Jun 1;175(2):303–17.
306. Taylor TN, Greene JG, Miller GW. Behavioral phenotyping of mouse models of Parkinson's disease. *Behav Brain Res*. 2010 Jul 29;211(1):1–10.
307. Boix J, Padel T, Paul G. A partial lesion model of Parkinson's disease in mice – Characterization of a 6-OHDA-induced medial forebrain bundle lesion. *Behav Brain Res*. 2015 May 1;284:196–206.
308. Ballard CG, Aarsland D, McKeith I, O'Brien J, Gray A, Cormack F, et al. Fluctuations in attention: PD dementia vs DLB with parkinsonism. *Neurology*. 2002 Dec 10;59(11):1714–20.
309. Kourtidou P, Kasselimis D, Potagas C, Zalonis I, Evdokimidis I. Effects of Mental Flexibility and Motor Dysfunction on Cognitive Performance in Patients With Parkinson's Disease. *Arch Neurosci* [Internet]. 2015 Jul 1 [cited 2021 Feb 22];2(3). Available from: <https://sites.kowsarpub.com/ans/articles/20536.html>

310. Kehagia AA, Barker RA, Robbins TW. Neuropsychological and clinical heterogeneity of cognitive impairment and dementia in patients with Parkinson's disease. *Lancet Neurol*. 2010 Dec 1;9(12):1200–13.
311. Madiha S, Haider S. Curcumin restores rotenone induced depressive-like symptoms in animal model of neurotoxicity: assessment by social interaction test and sucrose preference test. *Metab Brain Dis*. 2019 Feb 1;34(1):297–308.
312. Faivre F, Joshi A, Bezard E, Barrot M. The hidden side of Parkinson's disease: Studying pain, anxiety and depression in animal models. *Neurosci Biobehav Rev*. 2019 Jan 1;96:335–52.
313. Olsson M, Nikkhah G, Bentlage C, Bjorklund A. Forelimb akinesia in the rat Parkinson model: differential effects of dopamine agonists and nigral transplants as assessed by a new stepping test. *J Neurosci*. 1995 May 1;15(5):3863–75.
314. Bussey TJ, Padain TL, Skillings EA, Winters BD, Morton AJ, Saksida LM. The touchscreen cognitive testing method for rodents: How to get the best out of your rat. *Learn Mem*. 2008 Jul 1;15(7):516–23.
315. Suzuki H, Sumiyoshi A, Taki Y, Matsumoto Y, Fukumoto Y, Kawashima R, et al. Voxel-based morphometry and histological analysis for evaluating hippocampal damage in a rat model of cardiopulmonary resuscitation. *NeuroImage*. 2013 Aug 15;77:215–21.
316. Valdes Hernandez P, Sumiyoshi A, Nonaka H, Haga R, Aubert Vasquez E, Ogawa T, et al. An in vivo MRI Template Set for Morphometry, Tissue Segmentation, and fMRI Localization in Rats. *Front Neuroinformatics* [Internet]. 2011 [cited 2023 May 10];5. Available from: <https://www.frontiersin.org/articles/10.3389/fninf.2011.00026>
317. Pell GS, Briellmann RS, Waites AB, Abbott DF, Jackson GD. Voxel-based relaxometry: a new approach for analysis of T2 relaxometry changes in epilepsy. *NeuroImage*. 2004 Feb 1;21(2):707–13.
318. Papp EA, Leergaard TB, Calabrese E, Johnson GA, Bjaalie JG. Waxholm Space atlas of the Sprague Dawley rat brain. *NeuroImage*. 2014 Aug 15;97:374–86.
319. Pawela CP, Biswal BB, Cho YR, Kao DS, Li R, Jones SR, et al. Resting-state functional connectivity of the rat brain. *Magn Reson Med*. 2008;59(5):1021–9.
320. Puchades MA, Csucs G, Ledergerber D, Leergaard TB, Bjaalie JG. Spatial registration of serial microscopic brain images to three-dimensional reference atlases with the QuickNII tool. *PLOS ONE*. 2019 mai;14(5):e0216796.
321. Yates SC, Groeneboom NE, Coello C, Lichtenthaler SF, Kuhn PH, Demuth HU, et al. QUINT: Workflow for Quantification and Spatial Analysis of Features in Histological Images From Rodent Brain. *Front Neuroinformatics* [Internet]. 2019 [cited 2023 May 5];13. Available from: <https://www.frontiersin.org/articles/10.3389/fninf.2019.00075>
322. Dauer née Joppe K, Tatenhorst L, Caldi Gomes L, Zhang S, Parvaz M, Carboni E, et al. Brain iron enrichment attenuates α -synuclein spreading after injection of preformed fibrils. *J Neurochem*. 2021;159(3):554–73.

323. Zalesky A, Fornito A, Bullmore ET. Network-based statistic: identifying differences in brain networks. *NeuroImage*. 2010 Dec;53(4):1197–207.
324. Visanji NP, Brotchie JM, Kalia LV, Koprich JB, Tandon A, Watts JC, et al. α -Synuclein-Based Animal Models of Parkinson's Disease: Challenges and Opportunities in a New Era. *Trends Neurosci*. 2016 Nov 1;39(11):750–62.
325. Dehay B, Fernagut PO. Alpha-synuclein-based models of Parkinson's disease. *Rev Neurol (Paris)*. 2016 Jun;172(6–7):371–8.
326. Van der Perren A, Toelen J, Casteels C, Macchi F, Van Rompuy AS, Sarre S, et al. Longitudinal follow-up and characterization of a robust rat model for Parkinson's disease based on overexpression of alpha-synuclein with adeno-associated viral vectors. *Neurobiol Aging*. 2015 Mar;36(3):1543–58.
327. Van der Perren A, Van den Haute C, Baekelandt V. Viral Vector-Based Models of Parkinson's Disease. In: Nguyen HHP, Cenci MA, editors. *Behavioral Neurobiology of Huntington's Disease and Parkinson's Disease* [Internet]. Berlin, Heidelberg: Springer; 2015 [cited 2023 Apr 27]. p. 271–301. (Current Topics in Behavioral Neurosciences). Available from: https://doi.org/10.1007/7854_2014_310
328. McDowell K, Chesselet MF. Animal models of the non-motor features of Parkinson's disease. *Neurobiol Dis*. 2012 Jun 1;46(3):597–606.
329. De Leonibus E, Pascucci T, Lopez S, Oliverio A, Amalric M, Mele A. Spatial deficits in a mouse model of Parkinson disease. *Psychopharmacology (Berl)*. 2007 Nov;194(4):517–25.
330. Freichel C, Neumann M, Ballard T, Müller V, Woolley M, Ozmen L, et al. Age-dependent cognitive decline and amygdala pathology in alpha-synuclein transgenic mice. *Neurobiol Aging*. 2007 Sep;28(9):1421–35.
331. Lindgren HS, Dunnett SB. Cognitive dysfunction and depression in Parkinson's disease: what can be learned from rodent models? *Eur J Neurosci*. 2012;35(12):1894–907.
332. Jellinger KA. Interaction between  α -Synuclein and Other Proteins in Neurodegenerative Disorders. *Sci World J*. 2011 Oct 24;11:1893–907.
333. Fan TS, Liu SCH, Wu RM. Alpha-Synuclein and Cognitive Decline in Parkinson Disease. *Life*. 2021 Nov 16;11(11):1239.
334. Jellinger KA. Synuclein deposition and non-motor symptoms in Parkinson disease. *J Neurol Sci*. 2011 Nov 15;310(1):107–11.
335. Blesa J, Juri C, García-Cabezas MÁ, Adánez R, Sánchez-González MÁ, Cavada C, et al. Inter-hemispheric asymmetry of nigrostriatal dopaminergic lesion: a possible compensatory mechanism in Parkinson's disease. *Front Syst Neurosci* [Internet]. 2011 [cited 2021 Apr 30];5. Available from: <https://www.frontiersin.org/articles/10.3389/fnsys.2011.00092/full>

336. Kojovic M, Bologna M, Kassavetis P, Murase N, Palomar FJ, Berardelli A, et al. Functional reorganization of sensorimotor cortex in early Parkinson disease. *Neurology*. 2012 May 1;78(18):1441–8.
337. Simioni AC, Dagher A, Fellows LK. Effects of levodopa on corticostriatal circuits supporting working memory in Parkinson's disease. *Cortex*. 2017 Aug 1;93:193–205.
338. Owen AM, Iddon JL, Hodges JR, Summers BA, Robbins TW. Spatial and non-spatial working memory at different stages of Parkinson's disease. *Neuropsychologia*. 1997 Apr;35(4):519–32.
339. Schneider CB, Linse K, Schönfeld R, Brown S, Koch R, Reichmann H, et al. Spatial learning deficits in Parkinson's disease with and without mild cognitive impairment. *Parkinsonism Relat Disord*. 2017 Mar 1;36:83–8.
340. Klanker M, Feenstra M, Denys D. Dopaminergic control of cognitive flexibility in humans and animals. *Front Neurosci*. 2013;7:201.
341. Kimchi EY, Laubach M. The Dorsomedial Striatum Reflects Response Bias during Learning. *J Neurosci*. 2009 Nov 25;29(47):14891–902.
342. Lawson RA, Yarnall AJ, Duncan GW, Breen DP, Khoo TK, Williams-Gray CH, et al. Cognitive decline and quality of life in incident Parkinson's disease: The role of attention. *Parkinsonism Relat Disord*. 2016 Jun 1;27:47–53.
343. Solari N, Bonito-Oliva A, Fisone G, Brambilla R. Understanding cognitive deficits in Parkinson's disease: lessons from preclinical animal models. *Learn Mem*. 2013 Oct 1;20(10):592–600.
344. Cunha MP, Pazini FL, Lieberknecht V, Budni J, Oliveira Á, Rosa JM, et al. MPP+-Lesioned Mice: an Experimental Model of Motor, Emotional, Memory/Learning, and Striatal Neurochemical Dysfunctions. *Mol Neurobiol*. 2017 Oct 1;54(8):6356–77.
345. Carobrez AP, Bertoglio LJ. Ethological and temporal analyses of anxiety-like behavior: The elevated plus-maze model 20 years on. *Neurosci Biobehav Rev*. 2005 Jan 1;29(8):1193–205.
346. Walf AA, Frye CA. The use of the elevated plus maze as an assay of anxiety-related behavior in rodents. *Nat Protoc*. 2007 Feb;2(2):322–8.
347. Thobois S, Prange S, Sgambato-Faure V, Tremblay L, Broussolle E. Imaging the Etiology of Apathy, Anxiety, and Depression in Parkinson's Disease: Implication for Treatment. *Curr Neurol Neurosci Rep*. 2017 Aug 18;17(10):76.
348. Vriend C, Boedhoe PS, Rutten S, Berendse HW, Werf YD van der, Heuvel OA van den. A smaller amygdala is associated with anxiety in Parkinson's disease: a combined FreeSurfer—VBM study. *J Neurol Neurosurg Psychiatry*. 2016 May 1;87(5):493–500.
349. Shahaduzzaman M, Nash K, Hudson C, Sharif M, Grimmig B, Lin X, et al. Anti-human α -synuclein N-terminal peptide antibody protects against dopaminergic cell death and ameliorates behavioral deficits in an AAV- α -synuclein rat model of Parkinson's disease. *PLoS One*. 2015;10(2):e0116841.
350. Virel A, Faergemann E, Orädd G, Strömberg I. Magnetic Resonance Imaging (MRI) to Study Striatal Iron Accumulation in a Rat Model of Parkinson's Disease. Wang Y, editor. *PLoS ONE*. 2014 Nov 14;9(11):e112941.

351. Olmedo-Díaz S, Estévez-Silva H, Orädd G, Af Bjerkén S, Marcellino D, Virel A. An altered blood-brain barrier contributes to brain iron accumulation and neuroinflammation in the 6-OHDA rat model of Parkinson's disease. *Neuroscience*. 2017 Oct 24;362:141–51.
352. Koprach JB, Kalia LV, Brotchie JM. Animal models of α -synucleinopathy for Parkinson disease drug development. *Nat Rev Neurosci*. 2017 Sep;18(9):515–29.
353. Voormolen EHJ, Wei C, Chow EWC, Bassett AS, Mikulis DJ, Crawley AP. Voxel-based morphometry and automated lobar volumetry: The trade-off between spatial scale and statistical correction. *NeuroImage*. 2010 Jan 1;49(1):587–96.
354. Delgado-Alvarado M, Gago B, Navalpotro-Gomez I, Jiménez-Urbieto H, Rodríguez-Oroz MC. Biomarkers for dementia and mild cognitive impairment in Parkinson's disease: Biomarkers and Cognition in Parkinson's Disease. *Mov Disord*. 2016 Jun;31(6):861–81.
355. Galtier I, Nieto A, Barroso J, Norelis Lorenzo J. [Visuospatial learning impairment in Parkinson Disease]. *Psicothema*. 2009 Feb 1;21(1):21–6.
356. Botha H, Carr J. Attention and visual dysfunction in Parkinson's disease. *Parkinsonism Relat Disord*. 2012 Jul 1;18(6):742–7.
357. Carli G, Caminiti SP, Sala A, Galbiati A, Pilotto A, Ferini-Strambi L, et al. Impaired metabolic brain networks associated with neurotransmission systems in the α -synuclein spectrum. *Parkinsonism Relat Disord*. 2020 Dec 1;81:113–22.
358. Wolters AF, van de Weijer SCF, Leentjens AFG, Duits AA, Jacobs HIL, Kuijf ML. Resting-state fMRI in Parkinson's disease patients with cognitive impairment: A meta-analysis. *Parkinsonism Relat Disord*. 2019 May 1;62:16–27.
359. Lambin P, Leijenaar RTH, Deist TM, Peerlings J, de Jong EEC, van Timmeren J, et al. Radiomics: the bridge between medical imaging and personalized medicine. *Nat Rev Clin Oncol*. 2017 Dec;14(12):749–62.
360. Sørensen L, Igel C, Liv Hansen N, Osler M, Lauritzen M, Rostrup E, et al. Early detection of Alzheimer's disease using MRI hippocampal texture. *Hum Brain Mapp*. 2016;37(3):1148–61.
361. Colgan N, Ganeshan B, Harrison IF, Ismail O, Holmes HE, Wells JA, et al. In Vivo Imaging of Tau Pathology Using Magnetic Resonance Imaging Textural Analysis. *Front Neurosci*. 2017 Nov 6;11:599.
362. Betrouni N, Lopes R, Defebvre L, Leentjens AFG, Dujardin K. Texture Features of Magnetic Resonance Images: A Marker of Slight Cognitive Deficits in Parkinson's Disease. *Mov Disord*. 2020 Mar;35(3):486–94.
363. Sikiö M, Holli-Helenius KK, Harrison LC, Ryymin P, Ruottinen H, Saunamäki T, et al. MR image texture in Parkinson's disease: a longitudinal study. *Acta Radiol*. 2015 Jan;56(1):97–104.
364. Cui X, Xu Y, Lou Y, Sheng Q, Cai M, Zhuang L, et al. Diagnosis of Parkinson's disease based on feature fusion on T2 MRI images. *Int J Intell Syst*. 2022;37(12):11362–81.

365. Tupe-Waghmare P, Rajan A, Prasad S, Saini J, Pal PK, Ingalhalikar M. Radiomics on routine T1-weighted MRI can delineate Parkinson's disease from multiple system atrophy and progressive supranuclear palsy. *Eur Radiol*. 2021 Nov 1;31(11):8218–27.
366. Pang H, Yu Z, Li R, Yang H, Fan G. MRI-Based Radiomics of Basal Nuclei in Differentiating Idiopathic Parkinson's Disease From Parkinsonian Variants of Multiple System Atrophy: A Susceptibility-Weighted Imaging Study. *Front Aging Neurosci* [Internet]. 2020 [cited 2023 May 2];12. Available from: <https://www.frontiersin.org/articles/10.3389/fnagi.2020.587250>
367. Cheng Z, Zhang J, He N, Li Y, Wen Y, Xu H, et al. Radiomic Features of the Nigrosome-1 Region of the Substantia Nigra: Using Quantitative Susceptibility Mapping to Assist the Diagnosis of Idiopathic Parkinson's Disease. *Front Aging Neurosci*. 2019 Jul 16;11:167.
368. Shi D, Zhang H, Wang G, Wang S, Yao X, Li Y, et al. Machine Learning for Detecting Parkinson's Disease by Resting-State Functional Magnetic Resonance Imaging: A Multicenter Radiomics Analysis. *Front Aging Neurosci* [Internet]. 2022 [cited 2023 May 7];14. Available from: <https://www.frontiersin.org/articles/10.3389/fnagi.2022.806828>
369. Ruiz-España S, Ortiz-Ramón R, Pérez-Ramírez Ú, Díaz-Parra A, Ciccocioppo R, Bach P, et al. MRI texture-based radiomics analysis for the identification of altered functional networks in alcoholic patients and animal models. *Comput Med Imaging Graph*. 2023 Mar 1;104:102187.
370. Betarbet R, Sherer TB, Greenamyre JT. Animal models of Parkinson's disease. *BioEssays*. 2002;24(4):308–18.
371. Blandini F, Armentero MT, Martignoni E. The 6-hydroxydopamine model: News from the past. *Parkinsonism Relat Disord*. 2008 Jul 1;14:S124–9.
372. Meredith GE, Kang UJ. Behavioral models of Parkinson's disease in rodents: A new look at an old problem. *Mov Disord*. 2006;21(10):1595–606.
373. Santiago RM, Barbiero J, Lima MMS, Dombrowski PA, Andreatini R, Vital MABF. Depressive-like behaviors alterations induced by intranigral MPTP, 6-OHDA, LPS and rotenone models of Parkinson's disease are predominantly associated with serotonin and dopamine. *Prog Neuropsychopharmacol Biol Psychiatry*. 2010 Aug;34(6):1104–14.
374. Perry JC, Hipólido DC, Tufik S, Martins RD, Da Cunha C, Andreatini R, et al. Intra-nigral MPTP lesion in rats: Behavioral and autoradiography studies. *Exp Neurol*. 2005 Oct 1;195(2):322–9.
375. Potashkin JA, Blume SR, Runkle NK. Limitations of Animal Models of Parkinson's Disease. *Park Dis*. 2010 Dec 20;2011:e658083.
376. Balzano T, Esteban-García N, Blesa J. Neuroinflammation, immune response and α -synuclein pathology: how animal models are helping us to connect dots. *Expert Opin Drug Discov*. 2023 Jan 2;18(1):13–23.
377. Recasens A, Dehay B. Alpha-synuclein spreading in Parkinson's disease. *Front Neuroanat* [Internet]. 2014 Dec 18 [cited 2021 Mar 17];8. Available from: <http://journal.frontiersin.org/article/10.3389/fnana.2014.00159/abstract>

378. Thakur P, Breger LS, Lundblad M, Wan OW, Mattsson B, Luk KC, et al. Modeling Parkinson's disease pathology by combination of fibril seeds and α -synuclein overexpression in the rat brain. *Proc Natl Acad Sci*. 2017 Sep 26;114(39):E8284–93.
379. Carta AR, Boi L, Pisanu A, Palmas MF, Carboni E, De Simone A. Advances in modelling alpha-synuclein-induced Parkinson's diseases in rodents: Virus-based models versus inoculation of exogenous preformed toxic species. *J Neurosci Methods*. 2020 May 15;338:108685.
380. Antonelli L, Guarracino MR, Maddalena L, Sangiovanni M. Integrating imaging and omics data: A review. *Biomed Signal Process Control*. 2019 Jul 1;52:264–80.
381. Wang Y, Zhang GJ, Sun YN, Yao L, Wang HS, Du CX, et al. Identification of metabolite biomarkers for L-DOPA-induced dyskinesia in a rat model of Parkinson's disease by metabolomic technology. *Behav Brain Res*. 2018 Jul 16;347:175–83.
382. Kumari S, Kumaran SS, Goyal V, Bose S, Jain S, Dwivedi SN, et al. Metabolomic analysis of serum using proton NMR in 6-OHDA experimental PD model and patients with PD. *Neurochem Int*. 2020 Mar 1;134:104670.
383. Vandenberghe ME, Hérard AS, Souedet N, Sadouni E, Santin MD, Briet D, et al. High-throughput 3D whole-brain quantitative histopathology in rodents. *Sci Rep*. 2016 Aug;6(1):20958.
384. Ueda HR, Ertürk A, Chung K, Gradinaru V, Chédotal A, Tomancak P, et al. Tissue clearing and its applications in neuroscience. *Nat Rev Neurosci*. 2020 Feb;21(2):61–79.
385. Johnson GA, Tian Y, Ashbrook DG, Cofer GP, Cook JJ, Gee JC, et al. Merged magnetic resonance and light sheet microscopy of the whole mouse brain. *Proc Natl Acad Sci U S A*. 2023 Apr 25;120(17):e2218617120.
386. Parra-Damas A, Saura CA. Tissue Clearing and Expansion Methods for Imaging Brain Pathology in Neurodegeneration: From Circuits to Synapses and Beyond. *Front Neurosci* [Internet]. 2020 [cited 2023 May 5];14. Available from: <https://www.frontiersin.org/articles/10.3389/fnins.2020.00914>
387. Yilmazer-Hanke D, Mayer T, Müller HP, Neugebauer H, Abaei A, Scheuerle A, et al. Histological correlates of postmortem ultra-high-resolution single-section MRI in cortical cerebral microinfarcts. *Acta Neuropathol Commun*. 2020 Dec;8(1):33.
388. Atik A, Stewart T, Zhang J. Alpha-Synuclein as a Biomarker for Parkinson's Disease: Alpha-Synuclein as a Biomarker for PD. *Brain Pathol*. 2016 May;26(3):410–8.
389. Kotzbauer PT, Tu Z, Mach RH. Current status of the development of PET radiotracers for imaging alpha synuclein aggregates in Lewy bodies and Lewy neurites. *Clin Transl Imaging*. 2017 Feb 1;5(1):3–14.
390. Walusinski O. Jean-Martin Charcot and Parkinson's disease: Teaching and teaching materials. *Rev Neurol (Paris)*. 2018;174(7–8):491–505.
391. Bergamino M, Keeling EG, Mishra VR, Stokes AM, Walsh RR. Assessing White Matter Pathology in Early-Stage Parkinson Disease Using Diffusion MRI: A Systematic Review. *Front Neurol*. 2020 May 14;11:314.

392. Espay AJ, Lang AE. Parkinson Diseases in the 2020s and Beyond: Replacing Clinico-Pathologic Convergence With Systems Biology Divergence. *J Park Dis*. 2018 Jan 1;8(s1):S59–64.
393. Espay AJ, Vizcarra JA, Marsili L, Lang AE, Simon DK, Merola A, et al. Revisiting protein aggregation as pathogenic in sporadic Parkinson and Alzheimer diseases. *Neurology*. 2019 Feb 12;92(7):329–37.
394. Espay AJ, Herrup K, Daly T. Chapter 10 - Finding the falsification threshold of the toxic proteinopathy hypothesis in neurodegeneration. In: Espay AJ, editor. *Handbook of Clinical Neurology* [Internet]. Elsevier; 2023 [cited 2023 May 10]. p. 143–54. (Precision Medicine in Neurodegenerative Disorders, Part I; vol. 192). Available from: <https://www.sciencedirect.com/science/article/pii/B9780323855389000080>
395. Péran P, Hagberg G, Luccichenti G, Cherubini A, Brainovich V, Celsis P, et al. Voxel-based analysis of R2* maps in the healthy human brain. *J Magn Reson Imaging JMRI*. 2007 Dec;26(6):1413–20.
396. Ryman SG, Poston KL. MRI biomarkers of motor and non-motor symptoms in Parkinson's disease. *Parkinsonism Relat Disord*. 2020 Apr 1;73:85–93.
397. Fénelon G, Parant J, Cleret de Langavant L. Victor Parant (1848–1924) and the first report of psychosis in the course of Parkinson's disease with dementia. *Rev Neurol (Paris)*. 2021 Dec 1;177(10):1221–7.
398. Hawkes CH, Del Tredici K, Braak H. Parkinson's disease: a dual-hit hypothesis. *Neuropathol Appl Neurobiol*. 2007;33(6):599–614.
399. Lhost J, More S, Watabe I, Louber D, Ouagazzal AM, Liberge M, Amalric M. Interplay Between Inhibitory Control and Behavioural Flexibility: Impact of Dorsomedial Striatal Dopamine Denervation in Mice. *Neuroscience*. 2021 Nov 21;477:25–39.

ANNEXES

Table 1. Treatment of nonmotor symptoms	
Nonmotor symptoms	Possible treatments
Cognitive impairment, dementia	Rivastigmine, donepezil, galantamine, memantine
Psychosis	Quetiapine, clozapine
Depression	SSRIs, SNRIs, tricyclics
Apathy, anhedonia, fatigue	Armodafinil, modafinil, CNS stimulants
Orthostatic hypotension	Fludrocortisone, midodrine, etilefrine, droxidopa
Constipation	Polyethylene glycol, lubiprostone, macrogol, prucalopride, neostigmine
Urinary dysfunction (overactive bladder)	Oxybutinin, tolterodine, trospium chloride, BoNT, sacral nerve stimulation
Sexual dysfunction	Solifenacin, darifenacin, sildenafil
Hyperhidrosis	Anticholinergics, intracutaneous BoNT injections
Seborrhea	Topical steroids, intracutaneous BoNT injections
Weight loss	Nutritional management
Daytime drowsiness	Armodafinil, modafinil, CNS stimulants
RBD, vivid dreams	Clonazepam, melatonin, quetiapine
Insomnia, sleep fragmentation	Nighttime levodopa, dopamine agonists, trazodone, tricyclics (doxepin), zolpidem, eszopiclon, melatonin
Pain (e.g. shoulder), paresthesias	Levodopa, gabapentin, pregabalin, duloxetine

BoNT, botulinum toxin; CNS, central nervous system; RBD, rapid eye movement (REM) and behavioral disorder; SNRI, serotonin and norepinephrine reuptake inhibitor; SSRI, selective serotonin reuptake inhibitor.

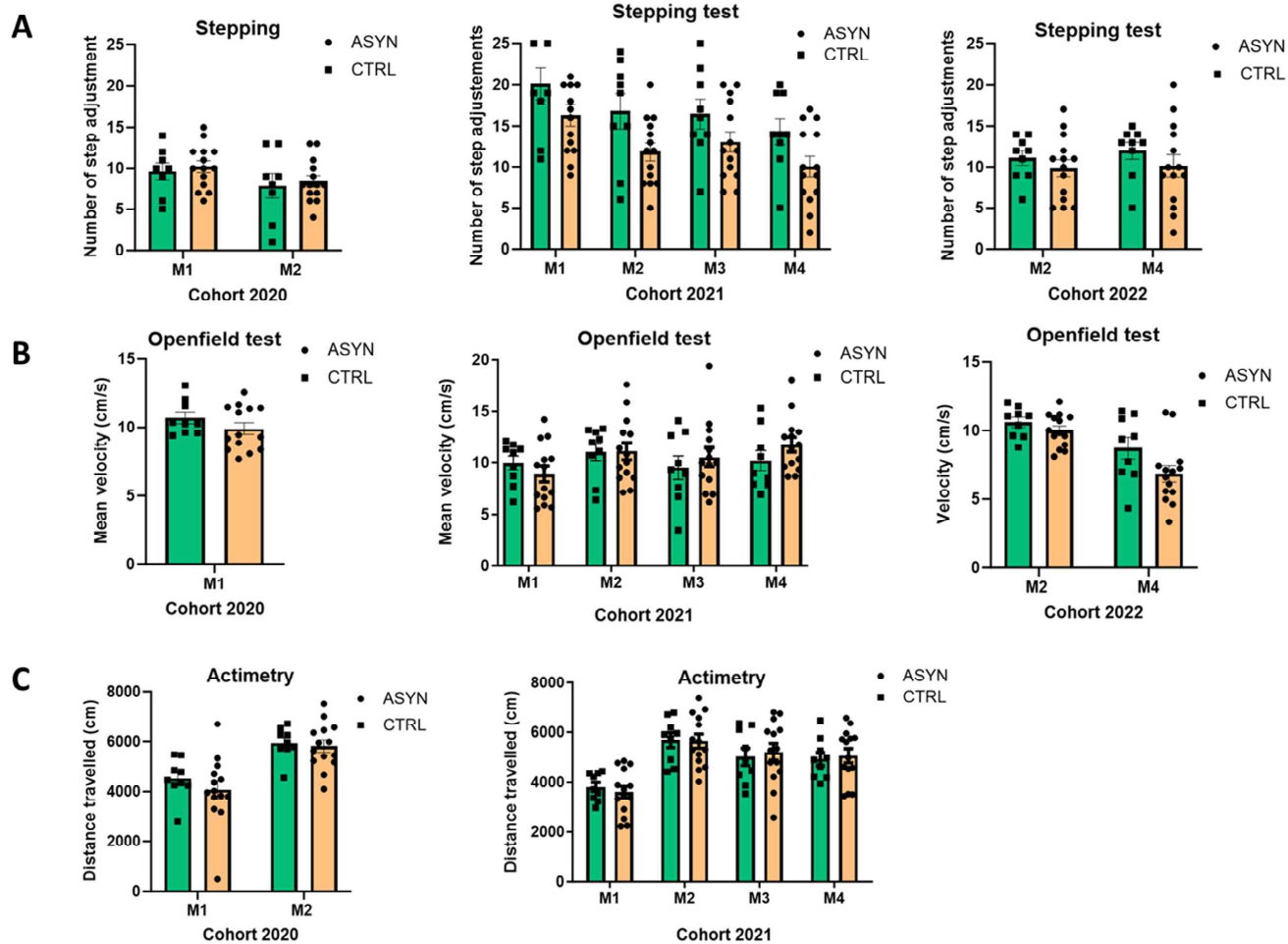
Annexe. Table 1. Therapeutic Options for Treating Non-Motor Symptoms of Parkinson's Disease. From Jancovik & Poewe 2012

Alpha-synuclein	Vector system	Promoter	Species	Dopaminergic neurodegeneration %	Time course (weeks)	Synucleinopathy	Motor phenotype	Reference
WT, A53T	rAAV2/2	CBA	Rattus norvegicus	30–80	8–16	a-syn-positive inclusions	Mild	Kirik et al. 2002
WT	rAAV2/2	CMV	Rattus norvegicus	50	13	a-syn- and pS129-positive inclusions	Mild	Yamada et al. 2004
WT	rAAV2/2	CBA	Mus musculus	25	24	-	-	St Martin et al. 2007; Theodore et al. 2008
WT	rAAV2/5	CBA	Rattus norvegicus	60	26	a-syn-positive inclusions	-	Gorbatyuk et al. 2008
WT, A30P	rAAV2/6	CMV	Rattus norvegicus	11 to 22	8	a-syn-, pS129-, PK-resistant and positive inclusions	-	Azeredo da Silveira et al. 2009
WT	rAAV2/6	Syn-1	Rattus norvegicus	80	16	a-syn-, pS129-, PK-resistant and positive inclusions	Good	Decressac et al. 2012
WT	rAAV2/5	CBA/CMV hybrid	Rattus norvegicus	60	8	-	Good	Gombash et al. 2013
WT, A53T	rAAV2/7	CMV/Syn-1	Mus musculus	82	8	a-syn- and pS129-positive inclusions	-	Oliveras-salva et al. 2013
A53T	rAAV2/7	CMV/Syn-1	Rattus norvegicus	80-90	4	a-syn- and ubiquitin-positive inclusions	Good	Van der Perren et al. 2015
A53T	rAAV2/9	CMV/Syn-1	Rattus norvegicus	80	16	a-syn- and pS129-positive inclusions	Good	Bourdenx et al. 2015
WT	rAAV2/6	Syn-1	Rattus norvegicus	50 - 70	12	a-syn-, pS129-, PK-resistant and positive inclusions	Mild	Thakur et al. 2017
WT	rAAV2/9	Syn-1	Rattus norvegicus	57 - 60	1 and 4	a-syn- and pS129-positive inclusions	Good	Rodriguez Perez et al. 2018
A53T	rAAV2/9	CBA/CAG	Rattus norvegicus	55	10	a-syn-positive inclusions	Good	Yang et al. 2020

Annexe. Table 2. AAV-based alpha-synuclein overexpression rodent models. Adapted from Dehay & Fernagut 2016

Functional ROIs	Alpha-synuclein average score (L+R)
Hypothalamic area	2.96
Secondary visual area medial part (injection)	2.92
Striatum = Caudate Putamen	2.31
Periaqueductal gray	2.15
Perirhinal cortex (35,36)	2.08
Diencephalon	1.79
Basal forebrain region	1.62
Ventral Tegmental Area (VTA)	1.58
Brainstem	1.54
Zona Incerta	1.46
Subthalamic Nucleus	1.38
Pretectal region	1.35
Colliculus (sup, inf)	1.35
Association cortex (frontal, parietal, temporal)	1.31
Amygdaloid Area	1.31
Substantia Nigra = (SNpc, R, L)	1.31
Insular cortex (granular, dysg, ag)	1.17
Nucleus Accumbens (Shell + Core)	1.12
Secondary motor cortex	1.04
Hippocampus = DG+CA1+CA2+CA3	1.04
Thalamic Nuclei	1.04
Entorhinal cortex	0.95
Cingulate cortex (area 1,2)	0.92
Prelimbic Area	0.88
Olfactory bulb	0.86
Fimbria	0.85
Primary visual area	0.77
Primary motor cortex	0.73
Ventral Pallidum	0.69
Primary somatosensory cortex (forelimb, hindlimb, barrel, trunk, dysgranular, facerep)	0.58
Globus Pallidus (ext, int)	0.58
Orbital area	0.50
Infralimbic Area	0.50
Piriform cortex	0.42
Retrosplenial cortex (granular, dysgranular)	0.35

Annexe. Table 3. Alpha-synuclein deposit scores. Based on the 4-level scale: 0, absence of alpha-synuclein, 1, mild deposits, 2, moderate deposits, 3 severe deposits. 222 regions were scored, then clustered into the present 35 spatio-functional regions of interest (ROI) relevant in PD pathology, and involved in the symptoms observed in our animal model. These scored were average between the left and right scores of subregions making each ROI.



Annex 4. Overview of behavioural results of cohorts 2020, 2021, 2022.

A. Average number of adjusting steps (Left + Right) in the Stepping test in cohorts 2020, 2021 and 2022;

In **2020** (ASYN n=14 ; CTRL n=9) no significant differences between ASYN and CTRL groups at month 1 nor 2; no significant overtime changes in either group. In **2021**: (n=23: 14 ASYN, 9 CTRL) significant group effect $F(1, 21) = 4.640$ ($p < 0.05$) and time effect $F(2.315, 48.62) = 19.28$ ($p < 0.001$). In **2022**: (ASYN n=14 ; CTRL n=9) no significant differences between ASYN and CTRL groups at month 2 nor 4; no significant overtime changes in either group.

B. Mean speed in Openfield arena (cm/s). No significant changes overtime or between groups, in all cohorts.

C. Distance travelled in actimetry (cm). No significant changes overtime or between groups, in all cohorts.

MRI Evaluation of AAV α -Synuclein Model of Parkinson's Disease is associated with α -Synuclein propagation

Journal:	<i>Brain</i>
Manuscript ID	Draft
Manuscript Type:	Original Article
Date Submitted by the Author:	n/a
Complete List of Authors:	<p>KATRIB, Chirine; Lille Neuroscience & Cognition Research Centre, Department of Medical Pharmacology, INSERM UMRS_1772, Lille University Hospital</p> <p>Hladky, Hector; Lille Neuroscience & Cognition Research Centre, Department of Medical Pharmacology, INSERM UMRS_1772, Lille University Hospital</p> <p>Timmerman, Kelly; Lille Neuroscience & Cognition Research Centre, Department of Medical Pharmacology, INSERM UMRS_1772, Lille University Hospital</p> <p>Durieux, Nicolas; University of Lille, US41-UAR2014 PLBS, Lille In vivo imaging and functional exploration platform, CNRS, Inserm, CHU Lille, Institut Pasteur de Lille</p> <p>DUTHEIL, Nathalie; University of Bordeaux, CNRS, Institut des Maladies Neurodégénératives, UMR 5293</p> <p>Bezard, Erwan; University of Bordeaux, CNRS, Institut des Maladies Neurodégénératives, UMR 5293</p> <p>Devos, David; Lille Neuroscience & Cognition Research Centre, Department of Medical Pharmacology, INSERM UMRS_1772, Lille University Hospital</p> <p>Laloux, Charlotte; Lille Neuroscience & Cognition Research Centre, Department of Medical Pharmacology, INSERM UMRS_1772, Lille University Hospital; University of Lille, US41-UAR2014 PLBS, Lille In vivo imaging and functional exploration platform, CNRS, Inserm, CHU Lille, Institut Pasteur de Lille</p> <p>Betrouni, Nacim; Lille Neuroscience & Cognition Research Centre, Department of Medical Pharmacology, INSERM UMRS_1772, Lille University Hospital</p>
Methodology:	NEUROBIOLOGY OF DISEASE
Subject area:	MOVEMENT DISORDERS, OTHER

MRI Evaluation of AAV α -Synuclein Model of Parkinson's Disease is associated with α -Synuclein propagation.

Chirine KATRIB^{1*}, Hector HLADKY¹, Kelly TIMMERMAN¹, Nicolas DURIEUX², Nathalie DUTHEIL^{3,4}, Erwan BEZARD^{3,4}, David DEVOS¹, Charlotte LALOUX^{1,2}, and Nacim BETROUNI¹.

¹Department of Medical Pharmacology, Lille University, INSERM UMRS_1772, LiNCog – Lille Neuroscience & Cognition, Lille University Hospital, 59000 Lille, France.

²US41-UAR2014 PLBS, Lille In vivo imaging and functional exploration platform, Univ. Lille, CNRS, Inserm, CHU Lille, Institut Pasteur de Lille, F-59000 Lille, France.

³Univ. de Bordeaux, Institut des Maladies Neurodégénératives, UMR 5293, F-33000 Bordeaux, France.

⁴CNRS, Institut des Maladies Neurodégénératives, UMR 5293, F-33000 Bordeaux, France.

*Correspondence to: Chirine KATRIB Université de Lille, INSERM, U1172, CHU-Lille, Lille Neuroscience & Cognition Research Centre, 1 place de Verdun, 59045 Lille, France; E-mail: chirinekatrib@gmail.com

Short running title: **MRI AND α -SYNUCLEIN SIGNATURE IN RAT PD MODEL**

ABSTRACT

Advanced methods in Magnetic Resonance Imaging (MRI) analysis is providing new insights into the mechanisms underlying Parkinson's Disease (PD), notably assessments of both dopaminergic cell death and iron accumulation. Still, no imaging method has yet been able to represent the α -synuclein presence. The AAV α -synuclein rat model allows the investigation of MRI sequences and their significance on a behavioural and histopathological level.

The aim is therefore to determine a radiological signature from several MRI sequences related to histological and behavioural characteristics of the AAV α -synuclein rat model.

Rats underwent exploration of motor and cognitive functions over 4 months. Three MRI acquisitions were held at 2-, 10- and 18-weeks post-injection, including a whole-brain morphological T2-weighted image, a T2*-weighted image for iron presence, and a resting-state functional MRI assessment. Histological studies evaluated dopaminergic degeneration, iron accumulation and human α -synuclein propagation in the brain.

The progressive dopaminergic neurodegeneration and spreading of human α -synuclein corresponds to the level of sensorimotor, attentional and learning deficits observed in this PD model. MRI analyses show progressive structural abnormalities in the midbrain, the diencephalon and several cortical structures, and a hyperconnectivity pattern in basal ganglia and cortical networks. The regions affected in imaging present the highest load of human α -synuclein.

Morphological MRI alterations in regions unaffected by the dopaminergic denervation and large hyperconnectivity patterns across several networks prove that a whole-brain imaging approach is necessary to evaluate animal models beyond the primary lesioned pathway. This model's structural and functional MRI changes could indirectly reflect α -synuclein presence related to impaired non-motor functions.

Key Words: Parkinson's disease; α -synuclein; Magnetic Resonance Imaging (MRI); Rodent model; Histopathology.

INTRODUCTION

Parkinson's disease (PD) is a multisystem progressive neurodegenerative disorder with pathological hallmarks, including dopaminergic neuronal degeneration, α -synuclein accumulation forming Lewy body inclusions, neuroinflammation and iron accumulation^{1,2}. Over the last few decades, structural, functional and molecular neuroimaging studies have provided invaluable insights into the mechanisms underlying PD³. Amongst these techniques, Magnetic resonance Imaging (MRI) has been widely explored to enhance diagnostic accuracy and monitor the disease's progression⁴. Indeed, many MR sequences have been used to reflect some of PD's main hallmarks. T1-weighted (w) sequence with advanced analysis techniques, such as morphometry and volumetry, have allowed the detection of voxel-to-voxel differences in the local density of different brain tissue types revealing grey matter atrophy⁵. T2* relaxometry sequence has shown increased R2* values in the substantia nigra, indicating iron accumulation⁶⁻⁸. On the other hand, the alterations in basal ganglia processing and cortico-striatal connections have been unravelled using a network approach through functional MRI sequences. Such analysis is fundamental for understanding PD pathophysiology⁹. Indeed, resting-state functional (rs-f)MRI has helped distinguish PD patients from control subjects¹⁰ and revealed abnormal resting state spontaneous brain activity associated with early PD¹¹. Still, these sequences are used in clinical practice mainly for differential diagnosis to rule out atypical Parkinsonian syndromes and not for diagnosing PD based on imaging alterations. The need for earlier diagnosis to maximize the chances of neuroprotective treatments has proved a significant challenge, and imaging markers are potential candidates. However, there is a need to understand the underlying tissue changes reflected by these imaging alterations in conjunction with motor and non-motor symptomatology.

Animal models are ideal for defining these relationships between histological and radiological abnormalities. New spatial registration and 3D mapping techniques such as the QUINT workflow^{12,13}, allows the assignment of precise anatomical locations of over 222 regions of interest in histological images, which can then be correlated with MRI image analysis. Such correlations performed in animal models, could help define imaging markers as reliable cross-species biomarkers for the non-invasive detection and longitudinal monitoring of neuropathological changes in PD. Amongst animal models recapitulating PD features, the adeno-associated virus (AAV)-induced α -synuclein overexpression rat model, which consists of two bilateral intranigral injections of the AAV human p.A53T α -synuclein mutant, has shown reliable dopaminergic degeneration, correlating in time with α -synuclein accumulation in the brain, as well as parkinsonian-like deficits such as akinesia, bradykinesia, and abnormal gait¹⁴. Although it has been characterised using small animal PET imaging^{15,16}, which showed that nigral overexpression of α -synuclein impaired the striatal dopamine release, this model has never been investigated in MR imaging, neither structurally nor functionally. Such a characterisation could help fill the knowledge gap, especially considering that human α -synuclein presence and possible pathology has yet to be distinguished on an imaging level.

The present work is a multimodal characterisation of the AAV α -synuclein rat model, with in vivo behavioural, morphological and functional imaging explorations established at different time points and histological characterisation, focusing mainly on dopaminergic neurons and human- α -synuclein staining (h- α -synuclein), done at the end. Links between the various endpoints are explored for decoding underlying tissular abnormalities. The aim is to determine a radiological signature from several MRI sequences related to the behavioural and histological characteristics, which could then be transposed to PD patients.

METHODS

Animal model and experimental design

Experiments were carried out following institutional and national guidelines for the care and use of laboratory animals. They were approved by the regional and French ethical committees (Authorization number 6281-20 16072517437766).

Sprague Dawley (SD) adult male rats ($n = 46$, 6 weeks old, 180–200 g) were randomly assigned to either the α -synuclein group (ASYN) or the control group (CTRL). Rats received two bilateral intranigral injections (Anteroposterior: -4.9 and -5.4 , mediolateral: ± 2.1 , dorsoventral: -7.8 , in mm from bregma) of a recombinant AAV2/9-synapsin-p.A53T-human- α -syn-WPRE or AAV2/9-synapsin-GFPdegron-WPRE ($2\mu\text{l} - 7.0 \times 10^{12}$ vg/ml; Institut des Maladies Neurodegeneratives UMR 5293, Bordeaux, France), encoding respectively the human p.A53T α -synuclein protein or green fluorescent protein. All the interventions were performed under complete general anaesthesia with ketamine (100 mg/kg) and xylazine (5 mg/kg).

Two cohorts consisting of 23 rats, each divided into an ASYN group ($n=14$) and a CTRL group ($n=9$), were used for two separate experiments with a similar experimental design, including a behavioural assessment over 4 months, 3 MRI sessions at 2-, 10- and 18-weeks post-injection (p.i.), and a histological evaluation of tissue modifications in the end. Animals in the first cohort underwent extensive motor and psycho-cognitive behavioural evaluation, and their MRI sequences consisted of a morphological T2w to evaluate structural changes such as grey matter atrophy, corresponding to the T1w sequence used clinically, and a quantitative T2* weighted image

sequence to evaluate iron accumulation. The second cohort had standard motor and sensorimotor testing and a resting-state functional MRI (rs-fMRI) sequence to assess functional connectivity.

In vivo imaging

MRI proton imaging experiments were performed at 7 Tesla in a horizontal bore magnet (Bruker, Biospec, Ettlingen, Germany). Animals were anaesthetized with isoflurane (2%) or DOMITOR (0.05mg/kg, specifically for rs-fMRI), and their temperature and breathing rate were monitored during the experiments. Two of the most used MR sequences in PD were acquired in Turbo RARE (Rapid Acquisition with Relaxation Enhancement) mode: morphological T2w images (spin-echo sequence: TR/TE= 3000/ 33 ms, field of view (FOV) = 4 cm², voxel size = 0.15x0.15x0.75mm³), and T2*w images with a 6-echo gradient (TR = 100 ms, TE= (4, 10, 16, 22, 28, 34 ms) and isotropic voxel with size=0.15 mm³). For rs-fMRI, multi-slice echo-planar images (EPI) were acquired using the following parameters: TR/TE = 2000/17 msec - FOV 32x32 mm - Matrix 64x64 - Resolution 0,5 mm/pixel – slice thickness: 1mm; 20 slices - 450 repetitions. - Signal FID. A specific protocol of Medetomidine anaesthesia (DOMITOR) was used for rs-fMRI acquisition because it provides a stable, high-quality connectivity data acquisition while preserving brain network function^{17–23}.

Image processing

T2-weighted images

Structural images were processed using the voxel-based morphometry (VBM) method (SPM12 DARTEL toolbox (Wellcome Trust Centre for NeuroImaging, London, UK) to study the grey matter variations between groups and sessions. Adaptations to rat images were implemented

similarly to Suzuki and colleagues' description²⁴. The rat brain atlas described by Valdés-Hernández and colleagues²⁵ was used to align the images.

Relaxometry and R2* mapping of Multi-echo T2* weighted images

Magnetic resonance relaxometry allows to quantify iron loading in the tissue. It is based on processing T2* images to produce R2* maps. We have used the method described in Peran et al. 2007. In our study, the multi-echo protocol consisted of 6 echos times, TE= 4, 10, 16, 22, 28 and 34 ms (Supp. Fig.1 A to F). First, for each rat, the morphological image (T2w) was registered using an affined transformation to the T2 image of a rat brain template (a volumetric Atlas of the Sprague Dawley Rat Brain)²⁶, then the obtained transformation was applied to the six echo images to map them into this common space.

For the creation of the R2* maps for each rat, a voxel by voxel nonlinear least-squares fitting of the data acquired at the 6 echo times was applied to obtain a mono-exponential signal decay curve as $S(t) = S_0 e^{-\frac{t}{T2^*}}$ where t = echo time, S = measured data, S0= multiplicative constant, T2* = effective transverse relaxation time (Supp. Fig.1G). Then from the T2* values, the R2* values were obtained as $R2^* = \frac{1}{T2^*}$. The individual maps were registered to the common space of the rat brain template to conduct whole-brain analysis using the voxel-based relaxometry (VBR) method²⁷, hence allowing direct comparison between rats.

rs-fMRI analysis

All fMRI Images were pre-processed by first, rescaling the voxel size of each image by a factor of ten for compatibility with the analysis software used for human scale images. The pre-processing

also included standard steps of spatial and temporal alignment to correct for head motion and nuisance signal, including normalization and smoothing, using the RestPlus toolbox²⁸. Next, the realigned images were co-registered to standard T2 images, and segmented (Supp. Fig.2).

After this parcellation into 150 ROIs regions (75 ROIs for each hemisphere) using an atlas, we extracted, for each region, a BOLD signal corresponding to the hemodynamic vascular influx linked to neuronal activity, which is considered an indirect measure of the region's activation (Supp. Fig.2).

These datasets were processed to produce functional connectivity maps (matrices) for each rat, by measuring the pairwise Pearson's correlation coefficients across regions of interest from a pre-existing template²⁹. Indeed, the signals of all the regions were analysed two by two, and the correlation coefficient between the two corresponds to the synchronization of the two regions. We obtained a 150 by 150 matrix, corresponding to the 150 ROI parcellated, where each square represents the level of synchronization between the 2 regions, and red shows hyper-synchronized regions (Supp. Fig.2). This can also be graphically represented.

In a neurobiological framework, a graph consists of a collection of nodes, here represented by brain regions, and their connecting edges, here represented by the pair-wise functional connections between these brain regions defined by the correlation coefficients.

Histological assessment

Rats were transcardially perfused with 4% paraformaldehyde (PFA) at 18 weeks p.i. Brains were fixed overnight in 4% PFA and then cryoprotected in 30% sucrose solution before snap freezing in isopentane and then stored at -80°C. Forty micrometre-thick free-floating coronal sections of the entire brain were prepared using a cryostat (Leica, Nussloch, Germany).

Dopaminergic degeneration

We assessed the dopaminergic denervation by tyrosine hydroxylase (TH) immunostaining of striatal and nigral sections. The sections were first incubated with 0.3% hydrogen peroxide in a 0.1 phosphate buffer, pH 7.4 (PBS), to quench endogenous peroxidase activity. Then they were incubated in a 0.3% Triton X-100 PBS blocking solution with 10% normal serum. A primary antibody: anti-TH 1:1000 (AB152 Sigma-Aldrich), then a biotinylated secondary antibody goat anti-rabbit (BA1000, VectorLabs) were used. Antibody binding was detected with the avidin–biotin–peroxidase conjugate (Vectastain ABC Elite; VectorLabs) using 3,3'-diaminobenzidine as the chromogen. Sections were dehydrated through graded ethanol solutions, cleared in xylene, and mounted in DPX (DBH Laboratory Supplies).

Images were acquired using a Zeiss Axio Scan Z.1 slide scanner with a 20× objective (Zeiss, Oberkochen, Germany). Using Zen Software, Blue edition, we assessed the optical density (OD) of TH-ir terminals in the striatum, by measuring the OD bilaterally in 6 different striatal sections per brain, where we manually delimit the striatal zone, and subtract background noise localized in the striosomes. The number of TH-ir neurons in the substantia nigra pars compacta (SNpc) was counted by unbiased stereology using Mercator Explora Nova Software, with an optical fractionator method to allow an accurate and efficient estimate of labelled neuron number as previously described³⁰.

H- α -synuclein spreading

The same immunohistochemistry protocol described above was used for h- α -synuclein staining, with primary antibody α -synuclein mouse mAb, clone LB509 (180215 Invitrogen) for human α -synuclein (h- α -syn), and secondary antibody horse anti-mouse (BA-2000, Vectorlabs).

After axioscan acquisition, α -synuclein deposits and propagation were assessed using a custom 4-point scale range from 0 to 3, quantifying the presence and amount of h- α -synuclein staining (Fig.2A) (0: absence of h- α -synuclein burden; 1: few h- α -synuclein strings; 2: moderate presence of h- α -synuclein strings; 3: Dense h- α -synuclein strings), adapted from Joppe and colleagues³¹. Using the QuickNII registration software¹², each region of interest in the Waxholm Space Atlas of the Sprague Dawley Rat Brain (SCR_017124)²⁶ was scored. Structural and functional clustering of the atlas's 222 regions allowed the extraction of 34 regions of interest, with an average score of h- α -synuclein deposit and left-right distinction (Fig.2B).

Iron histochemistry

Perls' reaction determined brain iron presence. After inhibition of endogenous peroxidases using 1% H₂O₂ in 99% methanol, sections were incubated in Perls' solution (20% potassium ferrocyanide, 20% HCl) and dehydrated as described earlier.

Behavioural phenotype assessment

The selected behavioural tests considered the main motor and psycho-cognitive dysfunctions observed in PD symptomatology.

Motor and sensorimotor evaluation

Spontaneous motor activity was recorded over a 10-min period in an actimeter equipped with Actitrack analytical software (Panlab, Barcelona, Spain) to evaluate distance travelled, speed, and rearing behaviour as previously described³⁰. Sensori-motricity was assessed using the stepping test, which accounts for the number of left/right forehand adjusting steps during a sliding movement while the other forehand is blocked. Nine trials were conducted over 3 days³². These tests were performed monthly to follow the evolution of spontaneous locomotion and forelimb akinesia.

Attention and visuospatial learning and memory evaluation

Attention performances were assessed using the 5-choice serial reaction time task (5CSRT), conducted in automated touchscreen-based testing chambers over 40 days starting 13 weeks p.i. (Campden Instruments Limited & Lafayette Instrument Company). This task is based on the operant conditioning paradigm whereby the animal receives a reward when its nose pokes the correct lit square (Fig. 4C). The light duration gradually decreases over training sessions, increasing the task's difficulty and mobilising more attentional resources³³.

Visuospatial learning and memory assessment was done using the Morris Water Maze test as previously described³⁴. It includes a 4-day training period evaluating spatial learning, with 4 trials/day measures of the rat's ability to find a hidden platform in a pool using external spatial cues. The learning phase is followed by a probe test on the fifth day when the platform is removed.

Spatial memory encoding is thus evaluated by calculating the time spent in the target quadrant where the platform used to be (Fig 4F).

Statistical analysis

All data are expressed as mean \pm SEM or as a percentage of the CTRL group. We used the Mann-Whitney test to compare ASYN & CTRL groups at each time point for behavioural analyses. T-tests were applied to histological findings to evaluate the differences between the 2 groups.

For imaging methods (VBM and VBR), t-tests were performed to identify whole-brain differences between the two animal groups and the same group between the MRI sessions (Table1). Clusters were considered significant with a fixed size threshold of 10 voxels after controlling familywise error rates using a false discovery rate^{35,36}.

The same comparison protocol (groups, sessions) was run for connectivity matrices using the network-based statistics (NBS) method³⁷, which is a robust approach for neuroimaging data that is modelled as a network because it translates conventional cluster statistics to a graph, dispensing the need for a topological property interpretation, and thereby reducing family-wise error rate. The robustness of NBS increases when the number of nodes and links is increased, which is important in a complex neural network, and yields a greater accuracy in the detection of pathologically valuable connections in a disease context.

For all analyses, the significance was set to $p < 0.05$.

RESULTS

Intranigral AAV-h- α -synuclein injection induces dopaminergic degeneration and h- α -synuclein spreading.

Assessment of TH immunoreactivity in the nigrostriatal pathway revealed a significant reduction of dopaminergic TH-ir neurons in the substantia nigra pars compacta (SNpc) and of dopaminergic terminals in the striatum, 4-month post injections in the ASYN group. The progressive percentage of dopamine TH-ir neuron loss was evaluated at an average of 30% in the striatum and 43% in the SNpc, compared to CTRL animals (Fig.1A,B) ($p < 0.001$). Additionally, we observed a significantly higher level of dopaminergic cell loss in the right SNpc compared to the left in the ASYN group ($p = 0.0101$) (Fig.3A,B).

The propagation of h- α -synuclein was observed both anterior and posterior to the injection site, with the protein reaching the olfactory bulb on one side and the mesencephalon on the other (Fig.2B,D). The main regions with moderate to severe h- α -synuclein load include the caudate-putamen (Fig.2C) and substantia nigra pars compacta, in addition to the midbrain, hypothalamus, hippocampus, fimbria and basal forebrain regions. Several cortical areas also presented with moderate to severe h- α -synuclein scores, such as the cingulate, insular, association, entorhinal and perirhinal cortices (Table1; Fig. 5C). The h- α -synuclein pattern spreading was more prominent on

the right side (Fig.3C), with specific structures scoring more severely in the right hemisphere compared to the left such as the striatum, the secondary motor area, the insular and cingulate cortices and the basal forebrain region ($p=0.03$) (Fig.3D).

H- α -synuclein AAV-mediated overexpression induces progressive sensorimotor, attentional and visuospatial learning deficits

Behavioural analysis over 4 months revealed no spontaneous locomotor deficits (not shown), but a significant decrease in the number of adjusting steps in the stepping test in ASYN animals compared to CTRL at month 4 (Fig.4A), indicating the onset of forelimb akinesia.

A decline in the 5-CSRT task performance was observed in ASYN animals starting 3 months p.i., with a significantly lower percentage of correct answers than CTRL (Fig.4B), indicating an early attentional deficit.

In the Morris Water Maze task, ASYN rats exhibited a slower learning curve than their CTRL counterparts, starting 2 months p.i., exacerbated at 4 months p.i., as shown by a longer latency to join the target platform (Fig.4D). However, probe day revealed that spatial memory was unaffected as there were no significant differences between ASYN and CTRL animals regarding the time spent in the target quadrant at month 2 or 4 (Fig.4E). This slowing down is not due to an alteration of the ability to move since the swimming speed was not different between the 2 groups (not shown). This indicates that ASYN rats had a visuospatial learning impairment but not a deficit in spatial reference memory.

Intranigral h- α -synuclein AAV-mediated overexpression induces progressive structural changes in the rat brain

No significant differences between the two groups could be identified by VBM analysis at any of the imaging time points. Nevertheless, the intra-group comparison between the different sessions showed morphological changes between each session only in the ASYN group. Indeed, between the first and the second imaging session at 2- and 10-weeks p.i., respectively, we observed a signal decrease in different anterior and posterior regions of the brain, predominantly in the midbrain, particularly the substantia nigra, as well as the fimbria, the primary somatosensory, motor, cingulate, insular, association, parietal and retrosplenial cortices (Fig.5A; Table1). At 18-weeks p.i., additional changes were observed in the diencephalon, the striatum, the hypothalamus, the hippocampus, the amygdala, and the entorhinal cortex, amongst other regions (Fig.5B; Table1). Interestingly, all regions above, which exhibited a significantly decreased signal, scored between 1 and 3 on the α -synuclein scale, highlighting a possible link between structural changes and h- α -synuclein propagation (Table1; Fig. 5C).

Intranigral h- α -synuclein AAV-mediated overexpression does not induce iron accumulation in the rat brain

VBR analysis did not reveal any difference in R2* mapping between the ASYN and CTRL groups for each MRI time point nor between each time point for either group (not shown). Similarly, Perls' iron histochemistry evaluation revealed no specific iron accumulation in the brain except along the injection track (not shown).

Intranigral h- α -synuclein AAV-mediated overexpression instigates a hyperconnectivity pattern in several brain networks

NBS analyses of the connectivity matrices between the groups showed a hyperconnectivity pattern between several regions in the ASYN group at 18 weeks p.i. (Fig.6). Several networks were modified with areas such as the midbrain making N=15 abnormal connections, the primary and secondary visual cortex: N=15, the retrosplenial cortex: N=23, the cingulate cortex: N=8, the somatosensory cortex: N=8, the posterior parietal cortex: N=7, the fimbria: N=5, and the substantia nigra: N=3 abnormal connections (Table1). In a neuroimaging framework, these brain regions are called nodes and constitute the edges of brain networks. The synchronization levels between the regions translate into abnormal connections. These nodes have been represented graphically in figure 6D, demonstrating that the ASYN neuronal networks subject to this hyperconnectivity pattern include the basal ganglia network's connection with widespread frontal, temporal, and parietal cortices as well as striatal and brainstem regions. Other networks involved were the corticostriatal–thalamic pathway and the frontoparietal network. The size of the line connecting the nodes correlates with the number of abnormal connections registered. We also observed an asymmetrical pattern in the functional hyperconnectivity, with the left basal ganglia and cortico-cortical nodes being more prevalent than the right ones (Fig.6D).

DISCUSSION

In this study, the AAV α -synuclein animal model has shown both moderate dopaminergic degeneration in the nigrostriatal pathway and widespread h- α -synuclein accumulation in the brain,

recapitulating the two main pathological hallmarks of PD³⁸. The spatial registration of an average of 26 h- α -synuclein stained sections per rat brain, allowed us to score the level of h- α -synuclein burden in over 222 regions of the entire brain¹², and therefore to map the specific spreading pattern of the protein. Despite its lack of Lewy-like pathology and limited aggregates³⁹, the pattern of h- α -synuclein burden in this model goes beyond the documented transduction efficiency and tropism of the AAV used^{40,41}. This has been confirmed by GFP expression evaluation from AAV2/9-synapsin-GFP injected rats which was limited to the substantia nigra (Supp.Fig.3), unlike the h- α -synuclein propagation pattern. This suggests a possible cell-to-cell transfer mechanism of α -synuclein, which has been recently described as a generalised phenomenon due to the structural and functional characteristics of the synuclein protein, and not its increased expression⁴².

Interestingly, progressive MRI structural changes were observed in regions of interest with the most severe h- α -synuclein scores. Indeed, insular, cingulate and entorhinal cortices, as well as the fimbria, thalamus and hypothalamus, scored between 1.5 and 3 on the α -synuclein scale and were all subject to signal changes between MRI sessions in ASYN animals. This indicates that VBM analyses not only reflect atrophy and neuronal degeneration but probably a general loss of tissue integrity due to toxic protein accumulation. Altogether, this MRI structural analysis highlights the potential of refined automated image analysis in revealing new and unexpected sites of neurodegeneration and tissue alteration beyond the primary lesioned pathway.

The model has also shown sensorimotor but not global motor deficits and non-motor dysfunctions such as attentional impairment and slowing of visuospatial learning, also described in clinical PD symptomatology⁴³. The imaging morphological analysis shows overtime signal differences that can be interpreted in reduced grey matter, involving the same regions affected in clinical PD MRIs^{44,45}, and known to be involved in both motor and non-motor dysfunctions. Indeed, signal

differences were observed in the basal ganglia and motor cortex, which are known to be involved in sensorimotor function, here impaired, and resulting in akinesia observed in PD⁴⁶. Other signal differences involved the prefrontal, cingulate and insular cortices, the limbic system, the diencephalon, the hippocampus and the fimbria. These regions play various roles in visuospatial learning and attention^{47,48}, also impaired during ASYN rat behavioural evaluation.

Additionally, the hyperconnectivity patterns observed in ASYN animals are similar to ones described in PD patients⁴⁹, notably regarding the functional connectivity (FC) alterations in the motor and frontoparietal networks. These marked disturbances of connectivity in cortical and basal ganglia areas are associated with early to moderately advanced stages of PD, with some studies suggesting the involvement of recovery and compensatory mechanisms for affected functions⁵⁰. These similarities between human and rat data confirms once again that rs-fMRI can be used as a translational tool especially in bilateral animal models¹⁹.

On the other hand, this model shows no iron accumulation in the rat brain, as revealed by relaxometry analysis and Perl's histochemistry. We hypothesize that this is due to the use of young adult rats, which may not be susceptible to iron accumulation. Indeed, investigating age-related iron deposition has shown that the concurrence of age and neurodegenerative processes induce alteration of iron homeostasis leading to an increase in iron level in the brain⁵¹. Another explanation is the lack of neuromelanin in albino rats' substantia nigra, which is considered a significant iron storage in SNpc neurons^{52,53}.

Indeed, it is important to clarify that this model has several limitations including the lack of several pathological highlights of PD such as Lewy body pathology, and iron accumulation. It is also known for its variability, observed in the alpha-synuclein propagation pattern we show here, that has not been well documented before in the literature. Moreover, the α -synuclein overexpression

evokes SNCA duplication and triplication mutations, which concerns a small portion of the PD population⁵⁴. It is therefore essential to note that this model has been only used as a first test bed for correlative imaging and histological data, and the translational potential of this study will only be acquired by using the same methodology on other complementary animal models. The fact however remains that correlations between what we see in structural and functional MRI and the tissue modifications at the cellular and molecular level have the potential to confirm MRI markers as biomarkers reflecting pathophysiological changes. This has been corroborated by several studies, including a primate α -synuclein overexpression model, where neuropathology in the substantia nigra correlated with post-mortem MRI data⁵⁵.

One of the most exciting results is the asymmetrical neurodegeneration observed in our bilateral model, with a significantly higher percentage of dopaminergic cell loss in the right substantia nigra compared to the left. This asymmetry was evident in both cohorts and was not due to any experimental bias, as we had two independent experimenters performing the stereotactic surgeries, alternating between the order of injection sides with automatic injection volume delivery, and later, blinded histological analyses. Consistently, a hemispheric asymmetry in nigrostriatal neurodegeneration has been described clinically in the early phases of PD⁵⁶, and one study even unveiled an asymmetrical substantia nigra neuronal loss in PD patients⁵⁷. Some hypotheses have suggested that handedness could play a role in this asymmetry⁵⁸, with the most used side being also the most affected. Others have attributed it to compensatory mechanisms, especially in the early phases of the disease, or a hemispheric lateralization of neuropathological changes such as synuclein propagation^{59–61}. Interestingly, this asymmetry is also revealed in h- α -synuclein spreading assessment, which is more prevalent in the right hemisphere, where we observed higher dopaminergic degeneration.

Overall, this multimodal MRI investigation of the AAV α -synuclein rat model has proved its relevance as a moderate early-stage PD model with mild sensorimotor and non-motor impairments characterized by h- α -synuclein propagation. Indeed, it has shown early brain modifications in several regions closely associated with the behavioural dysfunctions observed and similar to those observed in human imaging (VBM and rs-fMRI) studies^{9,62}, thereby confirming their cross-species translational validity. These same regions modified in MR imaging presented both abnormal connections with other networks and high levels of h- α -synuclein deposits, hence supporting the hypothesis that α -synuclein pathology is involved in the multisystem symptomatology of PD⁶³.

In conclusion, this study highlights the potential of evaluating MRI sequences in animal models of PD, to better understand both the underlying tissue pathology and the associated phenotype. With the use of a whole-brain unbiased approach, and thanks to precise segmentations of a wide range of regions of interest using the same atlas for both imaging and histological analysis, we were able to associate morphological changes and network alterations to the spreading pattern of α -synuclein. The ability to assess α -synuclein pathology using routinely acquired MR images could be an invaluable tool in early diagnosis, staging and monitoring of PD. Future work will aim to validate these imaging markers in other models of PD, and to further develop 3D registration techniques for better correlative studies.

Legends for Figures, Tables:

Figure 1. TH immunoreactivity evaluated 18 weeks p.i., in the left & right dorsal striatum (A) and left & right Substantia nigra pars compacta (B) of ASYN and CTRL rats. The percentage of

dopaminergic neurons (mean \pm SEM) is shown compared to the mean value of CTRL. A. Images and optical density measurements of TH-ir terminals in the dorsal striatum, (* $p < 0.05$). B. Images and stereological evaluation of TH-ir neurons in the substantia nigra, (**** $p < 0.0001$). (ASYN: $n = 28$; CTRL: $n = 18$)

Figure 2. The evaluation of human α -synuclein (h- α -syn) propagation in ASYN group. A. Custom-made 4-level scale defined for each region based on the number of neurons/neurites with h- α -syn. B. 26 sections per brain were spatially registered with the Rat brain atlas (WHS.V4), using QUICKNII software. 222 regions were segmented. C. α -synuclein staining in the Striatum ($\times 20$). D. 3D representation of α -synuclein propagation in the ASYN brain ($n = 13$ brains) with a scalebar from 0 to 30 corresponding to a scaling of the α -synuclein scale (0 to 3).

Figure 3. Assessment of asymmetrical neurodegeneration and α -synuclein accumulation in ASYN animals. A.B. Left and right comparison of TH immunoreactive cells in Substantia Nigra pars compacta (* $p < 0.05$). C. Global h- α -syn score in left versus right hemisphere in 34 regions of interest (* $p < 0.05$). D. Photos of 3 sections from 3 different ASYN brains, showing the asymmetrical spreading of α -synuclein in the secondary motor area, the insular and cingulate cortices, the striatum (caudate putamen), the nucleus accumbens and the basal forebrain region.

Figure 4. Behavioral evaluation of ASYN rats ($n = 14$) compared to CTRL ($n = 9$) over time. A. Forelimb akinesia evaluation at Months 1, 2 3 and 4. Average of number of adjusting steps (Left/Right) over 9 trials in Stepping test. B. Attentional deficits observed in ASYN animals as a

% of correct responses evaluated in the 5CSRT touchscreen task, 16 weeks p.i. C. Touchscreen apparatus and reward paradigm. D, E. Visuo-spatial learning and memory evaluation in the Morris Water Maze test (MWM) at Months 2 & 4. D. Latency to target (platform) on 4 days of training at M2 & M4 for learning assessment. E. Ratio of time spent in target quadrant on probe test day for memory restitution. F. MWM paradigm illustration. * group effect ($p < 0.05$)

Figure 5. Structural changes and α -synuclein spreading in ASYN model. A. Voxel-wise differences in local grey matter in the ASYN group between 2 and 10 weeks p.i. B. between 2 and 18 weeks p.i. C. 2D representation of α -synuclein spreading in the brain of AAV-mediated α -synuclein overexpression rat model, 18 weeks after surgery (average of $n=13$ ASYN rats).

Figure 6. Functional connectivity between brain regions in ASYN animals compared to CTRL at 18-weeks p.i. A. Mean connectivity matrix in ASYN animals. B. Mean connectivity matrix in CTRL animals. C. The difference between the first two panels. Yellow pixels denote statistically significant differences between groups ($p > 0.05$, FDR-corrected for multiple comparisons). D. Glass brain depicting significantly increased functional connectivity between different regions in ASYN rats compared to CTRL rats.

Table 1. Functionally grouped regions used for VBM, fMRI and h- α -syn histological analyses. (A) Average α -synuclein score in 34 regions (left and right) in ASYN brains. * Score using the semi-quantitative scale (B) Detailed VBM ROI with T scores corresponding to significative differences between 2 and 18 weeks p.i. in ASYN group. ** Score from the t-tests using SPM (C)

Detailed rs-fMRI ROI with T scores corresponding to the ASYN/CTRL group comparison of 2 paired ROI, at 18 weeks p.i. using NBS method. *** Score form the NBS analysis (n=13 ASYN n=9 CTRL).

Funding & Acknowledgments:

We thank France Parkinson's association for funding the project and Lille University and Inserm for PhD candidate funding. We thank Florent Auger (Lille In vivo imaging and functional exploration) and Antonino Bongiovanni (BioImaging Center Lille) for their help in *in vivo* and histological imaging.

Relevant conflicts of interests/financial disclosures: Nothing to report.

Supplementary material

Supplementary Figure 1. R2* mapping process. A to F: the multi-echo images (TE=4, 10, 16, 22, 28 and 34 ms). G. The monoexponential fitting allowing to obtain the T2* value for each voxel. H. The R2* map ($R2^* = \frac{1}{T2^*}$).

Supplementary Figure 2. Resting-state Functional MRI analysis process. The pipeline includes pre-processing, spatial registration, parcellation and production of functional connectivity matrices.

Supplementary Figure 3. The evaluation of GFP expression in the whole brain of CTRL rats at 18-weeks post-injection. Represented here are 6 sections covering the main regions of the brain (frontal, striatal, hippocampal, and 2 sections showing the substantia nigra). We observe GFP expression only in the SN (n=18).

References

1. Poewe W, Seppi K, Tanner CM, et al. Parkinson disease. *Nat Rev Dis Primer*. 2017;3(1):1-21. doi:10.1038/nrdp.2017.13
2. Riederer P, Nagatsu T, Youdim MBH, Wulf M, Dijkstra JM, Sian-Huelsmann J. Lewy bodies, iron, inflammation and neuromelanin: pathological aspects underlying Parkinson's disease. *J Neural Transm*. 2023;130(5):627-646. doi:10.1007/s00702-023-02630-9
3. Saeed U, Compagnone J, Aviv RI, et al. Imaging biomarkers in Parkinson's disease and Parkinsonian syndromes: current and emerging concepts. *Transl Neurodegener*. 2017;6(1):8. doi:10.1186/s40035-017-0076-6
4. Heim B, Krismer F, De Marzi R, Seppi K. Magnetic resonance imaging for the diagnosis of Parkinson's disease. *J Neural Transm*. 2017;124(8):915-964. doi:10.1007/s00702-017-1717-8
5. Menke RAL, Szewczyk-Krolikowski K, Jbabdi S, et al. Comprehensive morphometry of subcortical grey matter structures in early-stage Parkinson's disease. *Hum Brain Mapp*. 2014;35(4):1681-1690. doi:10.1002/hbm.22282
6. Péran P, Cherubini A, Assogna F, et al. Magnetic resonance imaging markers of Parkinson's disease nigrostriatal signature. *Brain J Neurol*. 2010;133(11):3423-3433. doi:10.1093/brain/awq212
7. Hopes L, Grolez G, Moreau C, et al. Magnetic Resonance Imaging Features of the Nigrostriatal System: Biomarkers of Parkinson's Disease Stages? *PLOS ONE*. 2016;11(4):e0147947. doi:10.1371/journal.pone.0147947
8. Devos D, Moreau C, Devedjian JC, et al. Targeting Chelatable Iron as a Therapeutic Modality in Parkinson's Disease. *Antioxid Redox Signal*. 2014;21(2):195-210. doi:10.1089/ars.2013.5593

9. Filippi M, Elisabetta S, Piramide N, Agosta F. Functional MRI in Idiopathic Parkinson's Disease. *Int Rev Neurobiol*. 2018;141:439-467. doi:10.1016/bs.irn.2018.08.005
10. Skidmore FM, Yang M, Baxter L, et al. Reliability analysis of the resting state can sensitively and specifically identify the presence of Parkinson disease. *NeuroImage*. 2013;75:249-261. doi:10.1016/j.neuroimage.2011.06.056
11. Yang H, Zhou XJ, Zhang MM, Zheng XN, Zhao YL, Wang J. Changes in spontaneous brain activity in early Parkinson's disease. *Neurosci Lett*. 2013;549:24-28. doi:10.1016/j.neulet.2013.05.080
12. Puchades MA, Csucs G, Ledergerber D, Leergaard TB, Bjaalie JG. Spatial registration of serial microscopic brain images to three-dimensional reference atlases with the QuickNII tool. *PLOS ONE*. 2019;14(5):e0216796. doi:10.1371/journal.pone.0216796
13. Yates SC, Groeneboom NE, Coello C, et al. QUINT: Workflow for Quantification and Spatial Analysis of Features in Histological Images From Rodent Brain. *Front Neuroinformatics*. 2019;13. Accessed May 5, 2023. <https://www.frontiersin.org/articles/10.3389/fninf.2019.00075>
14. Bourdenx M, Dovero S, Engeln M, et al. Lack of additive role of ageing in nigrostriatal neurodegeneration triggered by α -synuclein overexpression. *Acta Neuropathol Commun*. 2015;3(1):46. doi:10.1186/s40478-015-0222-2
15. Van der Perren A, Toelen J, Casteels C, et al. Longitudinal follow-up and characterization of a robust rat model for Parkinson's disease based on overexpression of alpha-synuclein with adeno-associated viral vectors. *Neurobiol Aging*. 2015;36(3):1543-1558. doi:10.1016/j.neurobiolaging.2014.11.015
16. Becker G, Michel A, Bahri MA, et al. Monitoring of a progressive functional dopaminergic deficit in the A53T-AAV synuclein rats by combining 6-[18F]fluoro-L-m-tyrosine imaging and motor performances analysis. *Neurobiol Aging*. 2021;107:142-152. doi:10.1016/j.neurobiolaging.2021.07.012
17. Pawela CP, Biswal BB, Hudetz AG, et al. A protocol for use of medetomidine anesthesia in rats for extended studies using task-induced BOLD contrast and resting-state functional connectivity. *NeuroImage*. 2009;46(4):1137-1147. doi:10.1016/j.neuroimage.2009.03.004
18. Nasrallah FA, Lew SK, Low ASM, Chuang KH. Neural correlate of resting-state functional connectivity under α 2 adrenergic receptor agonist, medetomidine. *NeuroImage*. 2014;84:27-34. doi:10.1016/j.neuroimage.2013.08.004
19. Sierakowiak A, Monnot C, Aski SN, et al. Default Mode Network, Motor Network, Dorsal and Ventral Basal Ganglia Networks in the Rat Brain: Comparison to Human Networks Using Resting State-fMRI. *PLOS ONE*. 2015;10(3):e0120345. doi:10.1371/journal.pone.0120345

20. Sirmpilatze N, Baudewig J, Boretius S. Temporal stability of fMRI in medetomidine-anesthetized rats. *Sci Rep*. 2019;9:16673. doi:10.1038/s41598-019-53144-y
21. Kint LT, Seewoo BJ, Hyndman TH, et al. The Pharmacokinetics of Medetomidine Administered Subcutaneously during Isoflurane Anaesthesia in Sprague-Dawley Rats. *Animals*. 2020;10(6):1050. doi:10.3390/ani10061050
22. Steiner AR, Rousseau-Blass F, Schroeter A, Hartnack S, Bettschart-Wolfensberger R. Systematic Review: Anesthetic Protocols and Management as Confounders in Rodent Blood Oxygen Level Dependent Functional Magnetic Resonance Imaging (BOLD fMRI)—Part B: Effects of Anesthetic Agents, Doses and Timing. *Animals*. 2021;11(1):199. doi:10.3390/ani11010199
23. Wallin DJ, Sullivan EDK, Bragg EM, Khokhar JY, Lu H, Doucette WT. Acquisition of Resting-State Functional Magnet Resonance Imaging Data in the Rat. *J Vis Exp JoVE*. 2021;(174):10.3791/62596. doi:10.3791/62596
24. Suzuki H, Sumiyoshi A, Taki Y, et al. Voxel-based morphometry and histological analysis for evaluating hippocampal damage in a rat model of cardiopulmonary resuscitation. *NeuroImage*. 2013;77:215-221. doi:10.1016/j.neuroimage.2013.03.042
25. Valdes Hernandez P, Sumiyoshi A, Nonaka H, et al. An in vivo MRI Template Set for Morphometry, Tissue Segmentation, and fMRI Localization in Rats. *Front Neuroinformatics*. 2011;5. Accessed May 10, 2023. <https://www.frontiersin.org/articles/10.3389/fninf.2011.00026>
26. Papp EA, Leergaard TB, Calabrese E, Johnson GA, Bjaalie JG. Waxholm Space atlas of the Sprague Dawley rat brain. *NeuroImage*. 2014;97:374-386. doi:10.1016/j.neuroimage.2014.04.001
27. Pell GS, Briellmann RS, Waites AB, Abbott DF, Jackson GD. Voxel-based relaxometry: a new approach for analysis of T2 relaxometry changes in epilepsy. *NeuroImage*. 2004;21(2):707-713. doi:10.1016/j.neuroimage.2003.09.059
28. Jia X, Li Y, Li K, Liang P, Fu X. Precuneus Dysfunction in Parkinson's Disease With Mild Cognitive Impairment. *Front Aging Neurosci*. 2019;10:427. doi:10.3389/fnagi.2018.00427
29. Westphal R, Simmons C, Mesquita MB, et al. Characterization of the resting-state brain network topology in the 6-hydroxydopamine rat model of Parkinson's disease. *PLOS ONE*. 2017;12(3):e0172394. doi:10.1371/journal.pone.0172394
30. Laloux C, Petrault M, Lecoite C, Devos D, Bordet R. Differential susceptibility to the PPAR- γ agonist pioglitazone in 1-methyl-4-phenyl-1,2,3,6-tetrahydropyridine and 6-hydroxydopamine rodent models of Parkinson's disease. *Pharmacol Res*. 2012;65(5):514-522. doi:10.1016/j.phrs.2012.02.008

31. Dauer née Joppe K, Tatenhorst L, Caldi Gomes L, et al. Brain iron enrichment attenuates α -synuclein spreading after injection of preformed fibrils. *J Neurochem*. 2021;159(3):554-573. doi:10.1111/jnc.15461
32. Laloux C, Gouel F, Lachaud C, et al. Continuous cerebroventricular administration of dopamine: A new treatment for severe dyskinesia in Parkinson's disease? *Neurobiol Dis*. 2017;103:24-31. doi:10.1016/j.nbd.2017.03.013
33. Slezak JM, Mueller M, Ricaurte GA, Katz JL. Pharmacokinetic and pharmacodynamic analysis of d-amphetamine in an attention task in rodents. *Behav Pharmacol*. 2018;29(6):551-556. doi:10.1097/FBP.0000000000000409
34. Delattre C, Bournonville C, Auger F, et al. Hippocampal Deformations and Entorhinal Cortex Atrophy as an Anatomical Signature of Long-Term Cognitive Impairment: from the MCAO Rat Model to the Stroke Patient. *Transl Stroke Res*. 2018;9(3):294-305. doi:10.1007/s12975-017-0576-9
35. Lieberman MD, Cunningham WA. Type I and Type II error concerns in fMRI research: re-balancing the scale. *Soc Cogn Affect Neurosci*. 2009;4(4):423-428. doi:10.1093/scan/nsp052
36. Roiser JP, Linden DE, Gorno-Tempini ML, Moran RJ, Dickerson BC, Grafton ST. Minimum statistical standards for submissions to Neuroimage: Clinical. *NeuroImage Clin*. 2016;12:1045-1047. doi:10.1016/j.nicl.2016.08.002
37. Zalesky A, Fornito A, Bullmore ET. Network-based statistic: identifying differences in brain networks. *NeuroImage*. 2010;53(4):1197-1207. doi:10.1016/j.neuroimage.2010.06.041
38. Antony PMA, Diederich NJ, Krüger R, Balling R. The hallmarks of Parkinson's disease. *FEBS J*. 2013;280(23):5981-5993. doi:10.1111/febs.12335
39. Gómez-Benito M, Granado N, García-Sanz P, Michel A, Dumoulin M, Moratalla R. Modeling Parkinson's Disease With the Alpha-Synuclein Protein. *Front Pharmacol*. 2020;11. Accessed March 30, 2023. <https://www.frontiersin.org/articles/10.3389/fphar.2020.00356>
40. Sun X, Yu X, Zhang L, et al. Comparison of the expression and toxicity of AAV2/9 carrying the human A53T α -synuclein gene in presence or absence of WPRE. *Heliyon*. 2021;7(2):e06302. doi:10.1016/j.heliyon.2021.e06302
41. Albert K, Voutilainen MH, Domanskyi A, Airavaara M. AAV Vector-Mediated Gene Delivery to Substantia Nigra Dopamine Neurons: Implications for Gene Therapy and Disease Models. *Genes*. 2017;8(2):63. doi:10.3390/genes8020063
42. Klinkenberg M, Helwig M, Pinto-Costa R, et al. Interneuronal In Vivo Transfer of Synaptic Proteins. *Cells*. 2023;12(4):569. doi:10.3390/cells12040569
43. Dubois B, Pillon B. Cognitive deficits in Parkinson's disease. *J Neurol*. 1996;244(1):2-8. doi:10.1007/PL00007725

44. Zeighami Y, Ulla M, Iturria-Medina Y, et al. Network structure of brain atrophy in de novo Parkinson's disease. Van Essen DC, ed. *eLife*. 2015;4:e08440. doi:10.7554/eLife.08440
45. Summerfield C, Junqué C, Tolosa E, et al. Structural Brain Changes in Parkinson Disease With Dementia: A Voxel-Based Morphometry Study. *Arch Neurol*. 2005;62(2):281-285. doi:10.1001/archneur.62.2.281
46. Rivlin-Etzion M, Marmor O, Heimer G, Raz A, Nini A, Bergman H. Basal ganglia oscillations and pathophysiology of movement disorders. *Curr Opin Neurobiol*. 2006;16(6):629-637. doi:10.1016/j.conb.2006.10.002
47. Delgado-Alvarado M, Gago B, Navalpotro-Gomez I, Jiménez-Urbieto H, Rodríguez-Oroz MC. Biomarkers for dementia and mild cognitive impairment in Parkinson's disease: Biomarkers and Cognition in Parkinson's Disease. *Mov Disord*. 2016;31(6):861-881. doi:10.1002/mds.26662
48. Almaguer-Melian W, Mercerón-Martínez D, Pavón-Fuentes N, et al. Erythropoietin Promotes Neural Plasticity and Spatial Memory Recovery in Fimbria-Fornix-Lesioned Rats. *Neurorehabil Neural Repair*. 2015;29(10):979-988. doi:10.1177/1545968315572389
49. Vervoort G, Alaerts K, Bengevoord A, et al. Functional connectivity alterations in the motor and fronto-parietal network relate to behavioral heterogeneity in Parkinson's disease. *Parkinsonism Relat Disord*. 2016;24:48-55. doi:10.1016/j.parkreldis.2016.01.016
50. Tuovinen N, Seppi K, de Pasquale F, et al. The reorganization of functional architecture in the early-stages of Parkinson's disease. *Parkinsonism Relat Disord*. 2018;50:61-68. doi:10.1016/j.parkreldis.2018.02.013
51. Ficiarà E, Stura I, Guiot C. Iron Deposition in Brain: Does Aging Matter? *Int J Mol Sci*. 2022;23(17):10018. doi:10.3390/ijms231710018
52. Barden H, Levine S. Histochemical observations on rodent brain melanin. *Brain Res Bull*. 1983;10(6):847-851. doi:10.1016/0361-9230(83)90218-6
53. Zecca L, Gallorini M, Schünemann V, et al. Iron, neuromelanin and ferritin content in the substantia nigra of normal subjects at different ages: consequences for iron storage and neurodegenerative processes. *J Neurochem*. 2001;76(6):1766-1773. doi:10.1046/j.1471-4159.2001.00186.x
54. Book A, Guella I, Candido T, et al. A Meta-Analysis of α -Synuclein Multiplication in Familial Parkinsonism. *Front Neurol*. 2018;9:1021. doi:10.3389/fneur.2018.01021
55. Eslamboli A, Romero-Ramos M, Burger C, et al. Long-term consequences of human alpha-synuclein overexpression in the primate ventral midbrain. *Brain J Neurol*. 2007;130(Pt 3):799-815. doi:10.1093/brain/awl382
56. Djaldetti R, Ziv I, Melamed E. The mystery of motor asymmetry in Parkinson's disease. *Lancet Neurol*. 2006;5(9):796-802. doi:10.1016/S1474-4422(06)70549-X

57. Kempster PA, Gibb WR, Stern GM, Lees AJ. Asymmetry of substantia nigra neuronal loss in Parkinson's disease and its relevance to the mechanism of levodopa related motor fluctuations. *J Neurol Neurosurg Psychiatry*. 1989;52(1):72-76. doi:10.1136/jnnp.52.1.72
58. van der Hoorn A, Burger H, Leenders KL, de Jong BM. Handedness correlates with the dominant Parkinson side: A systematic review and meta-analysis. *Mov Disord*. 2012;27(2):206-210. doi:10.1002/mds.24007
59. Blesa J, Juri C, García-Cabezas MÁ, et al. Inter-hemispheric asymmetry of nigrostriatal dopaminergic lesion: a possible compensatory mechanism in Parkinson's disease. *Front Syst Neurosci*. 2011;5. doi:10.3389/fnsys.2011.00092
60. Claassen DO, McDonell KE, Donahue M, et al. Cortical asymmetry in Parkinson's disease: early susceptibility of the left hemisphere. *Brain Behav*. 2016;6(12):e00573. doi:10.1002/brb3.573
61. Blesa J, Foffani G, Dehay B, Bezard E, Obeso JA. Motor and non-motor circuit disturbances in early Parkinson disease: which happens first? *Nat Rev Neurosci*. 2022;23(2):115-128. doi:10.1038/s41583-021-00542-9
62. Gao Y, Nie K, Huang B, et al. Changes of brain structure in Parkinson's disease patients with mild cognitive impairment analyzed via VBM technology. *Neurosci Lett*. 2017;658:121-132. doi:10.1016/j.neulet.2017.08.028
63. Dickson DW, Fujishiro H, Orr C, et al. Neuropathology of non-motor features of Parkinson disease. *Parkinsonism Relat Disord*. 2009;15:S1-S5. doi:10.1016/S1353-8020(09)70769-2

Figure 1

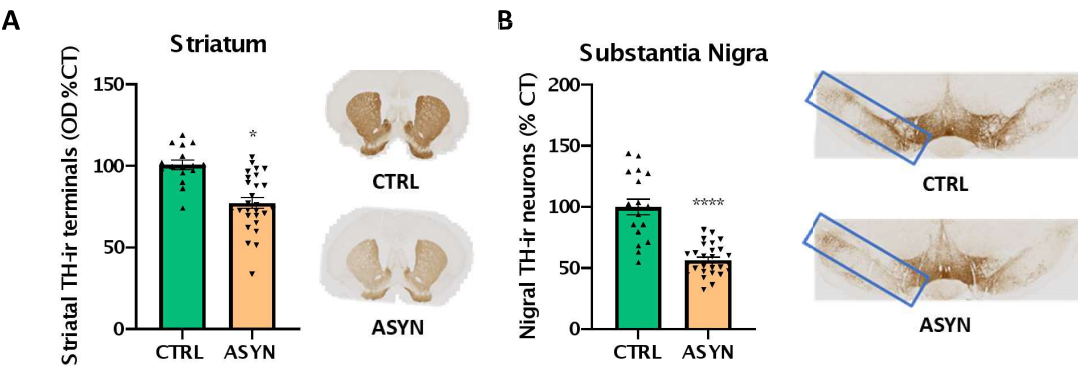


Figure 2

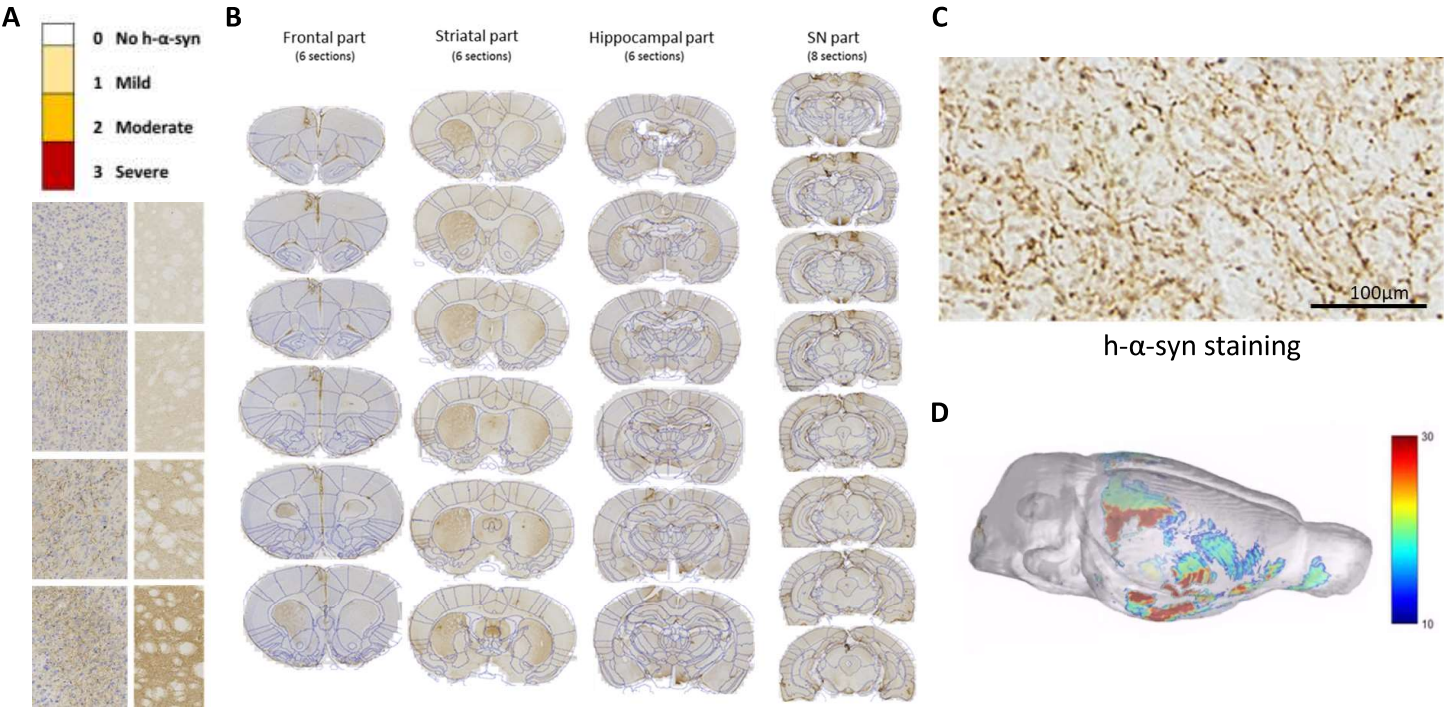


Figure 3

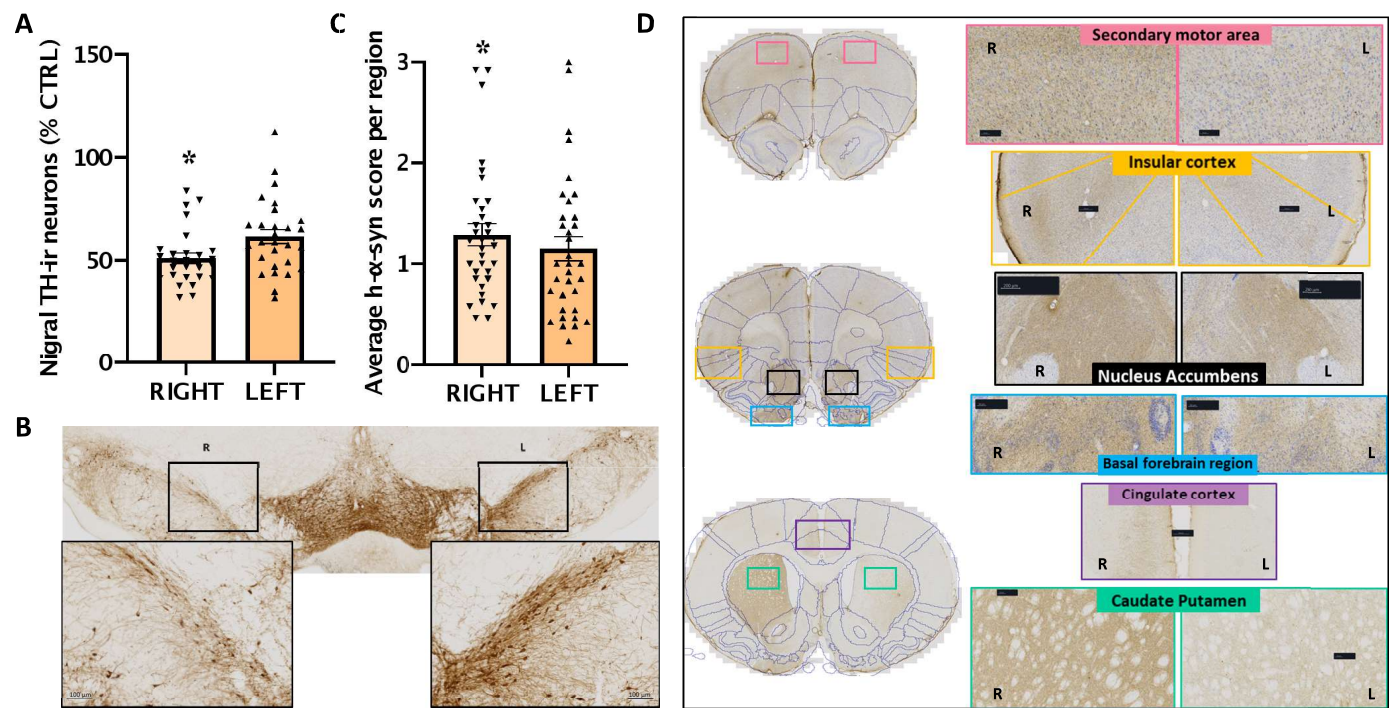


Figure 4

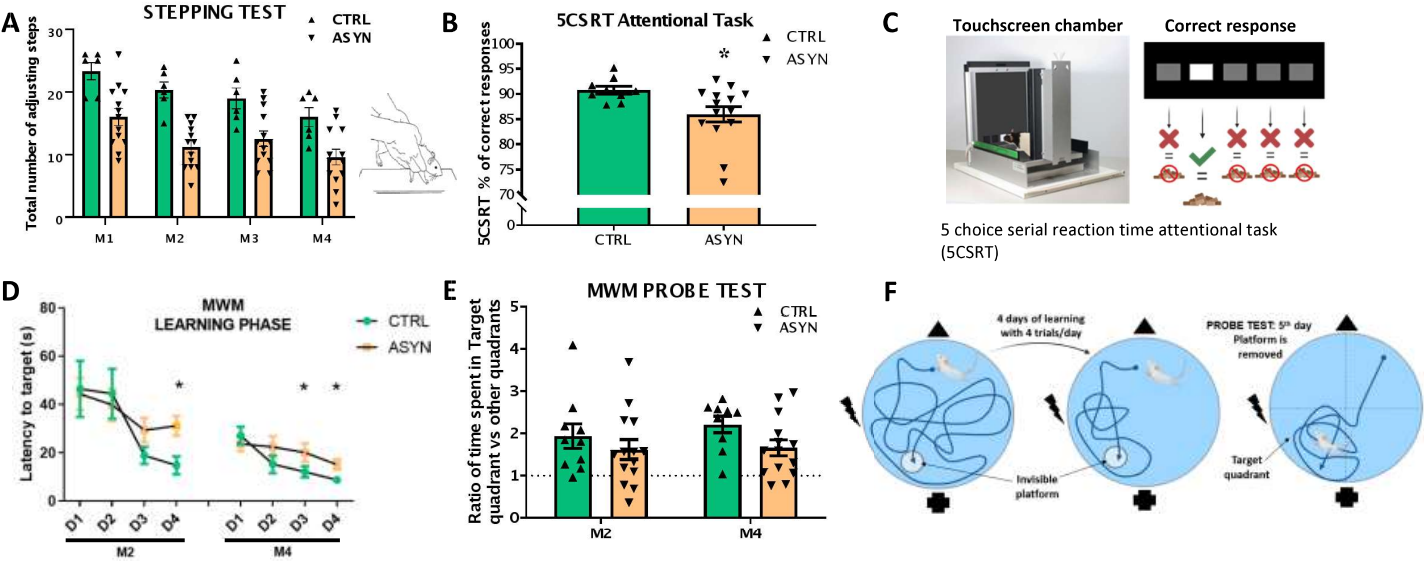


Figure 5

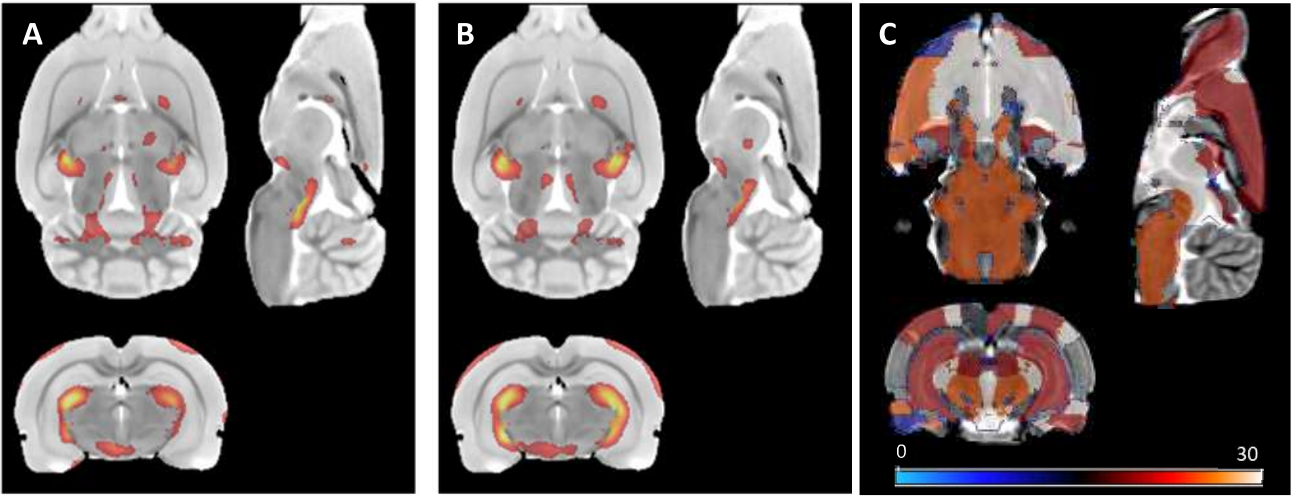


Figure 6

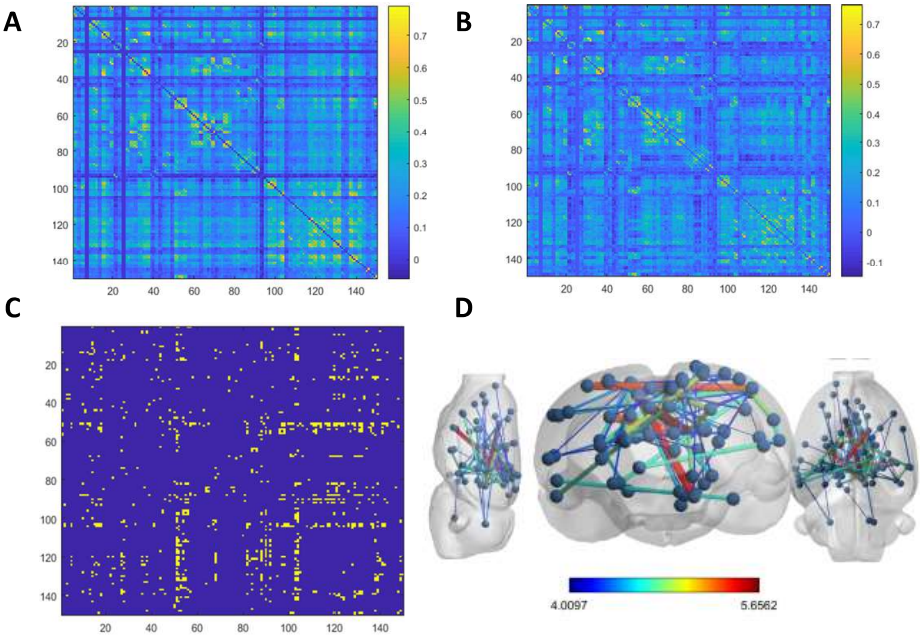


Table 1

	ALPHA5/NUCLEIN HISTOLOGY		VBM of T2w images in ASYN MRIW2-W18		rs-fMRI Connectivity matrices comparisons (W18-W2) in ASYN compared to CTRL		
Functional ROI	ROI	AVERAGE SCORE *	ROI	T score **	ROI 1	ROI2	T score ***
STRIATUM	Striatum = Caudate Putamen L	1.85	striatum L	12.4249	striatum L	secondary visual cortex, lateral area L	411
	Striatum = Caudate Putamen R	2.77	striatum R	11.47665			
SN	Substantia Nigra = [SNpc, R, L] L	1.46	substantia nigra L	14.7528	substantia nigra R	isocortex R	453
	Substantia Nigra = [SNpc, R, L] R	1.15	substantia nigra R	39.0948	substantia nigra R	hindbrain L	415
PALLIDIUM	Globus Pallidus (ext, int) L	0.46	pallidum L	12.37483	substantia nigra L	secondary visual cortex, mediolateral area L	411
	Globus Pallidus (ext, int) R	0.69	pallidum R	11.55522	NO functional connectivity CHANGES IN Pallidum		
	Ventral Pallidum L	0.54					
	Ventral Pallidum R	0.85					
NUCLEUS ACCUMBENS	Nucleus Accumbens (Shell + Core) L	1.00	NO STRUCTURAL CHANGES IN Nacc		accumbens nucleus L	midbrain L	477
	Nucleus Accumbens (Shell + Core) R	1.23					
DIENTEPHALON	Subthalamic Nucleus L	1.25	diencephalon R	13.4412	diencephalon L	prelimbic infralimbic cortex L	415
	Subthalamic Nucleus R	1.25	diencephalon L	11.56524			
	Thalamic Nuclei L	1.00					
	Thalamic Nuclei R	1.08					
	Zona Incerta L	1.31					
	Zona Incerta R	1.62					
HYPOTHALAMUS	Hypothalamic area L	3.00	hypothalamus L	13.59101	hypothalamus L	retrosplenial dysgranular cortex R	411
	Hypothalamic area R	2.92	hypothalamus R	11.49234			
MIDBRAIN			preoptic area L	11.99504			
			preoptic area R	11.49239			
	Periaqueductal gray L	2.31	midbrain R	23.86146	midbrain L	corpus callosum R	535
	Periaqueductal gray R	2.00	midbrain L	12.97527	midbrain L	corpus callosum L	493
	Pretectal region L	1.46			midbrain L	cingulum L	413
	Pretectal region R	1.23			midbrain L	prelimbic infralimbic cortex L	424
	Colliculus (sup, inf) L	1.38			midbrain L	accumbens nucleus L	477
	Colliculus (sup, inf) R	1.31			midbrain R	septum L	427
	Ventral Tegmental Area (VTA) L	1.62			midbrain L	septum L	476
	Ventral Tegmental Area (VTA) R	1.54			midbrain L	fibria R	454
					midbrain R	primary visual cortex L	465
					midbrain L	cingulate cortex, area 2 R	566
					midbrain L	cingulate cortex, area 2 L	403
					midbrain R	cingulate cortex, area 2 L	446
					midbrain R	cingulate cortex, area 1 L	41
					midbrain R	cingulate cortex, area 2 R	41
					midbrain R	medial Ventral lateral dorsolateral orbital cortex L	408

Table 1

Functional ROI	ALPHA SYN NUCLEON HISTOLOGY ^{***}		VBM of T2w images in ASYN MRQ W2-W18 ^{***}		rs-MRQ Connectivity matrices comparisons (W18-W2) in ASYN compared to CTRL ^{***}		
	ROI	AVERAGE SCORE [†]	ROI	T score ^{**}	ROI1	ROI2	T score ^{***}
HIPPOCAMPUS	Hippocampus = DG+CA1+CA2+CA3 L	1.08	hippocampal formation L	12.55708	hippocampal formation L	retrosplenial dysgranular cortex R	4.42
	Hippocampus = DG+CA1+CA2+CA3 R	1.00	hippocampal formation R	11.75813	hippocampal formation R	retrosplenial dysgranular cortex R	4.68
FIMBRIA	Fimbria L	0.85	fimbria L	13.32267	fimbria L	ectothal cortex R	4.21
	Fimbria R	0.85	fimbria R	11.97373	fimbria R	primary somatosensory cortex, hindlimb region L	4.92
					fimbria R	retrosplenial dysgranular cortex R	4.76
					fimbria R	midbrain L	4.54
PFC & INFRA LIMBIC	Prelimbic Area L	0.83	prelimbic infralimbic cortex L	12.28411	prelimbic infralimbic cortex L	primary visual cortex L	4.21
	Prelimbic Area R	0.92	prelimbic infralimbic cortex R	11.38235	prelimbic infralimbic cortex L	isocortex L	4.25
	Infra limbic Area L	0.42			prelimbic infralimbic cortex L	midbrain L	4.24
	Infra limbic Area R	0.58			prelimbic infralimbic cortex L	diencephalon L	4.15
AMYGDALA	Amygdaloid Area L	1.69	amygdala L	12.78413	amygdala L	retrosplenial dysgranular cortex R	4.02
	Amygdaloid Area R	0.92	amygdala R	23.664		dorsolateral entorhinal cortex R	4.62
OLFACTORY	Olfactory bulb L	0.73	olfactory structures L	12.06113	olfactory structures R		
	Olfactory bulb R	1.00	olfactory structures R	12.03226		retrosplenial dysgranular cortex R	4.24
HIND BRAIN	Brainstem L	1.69	hindbrain R	12.96005	hindbrain L	substantia nigra R	4.15
	Brainstem R	1.38	hindbrain L	11.58605	cerebellum L	cingulate cortex, area 2 L	4.4
			cerebellum R	11.41023	cerebellum R	isocortex R	4.22
				11.62313			
BF CHOLINERGIC SYSTEM	Basal forebrain region L	1.38	diagonal domain L	14.0068	diagonal domain L	secondary auditory cortex, ventral area R	4.36
	Basal forebrain region R	1.85				secondary visual cortex, mediolateral area L	4.17
INSULAR CORTEX	Insular cortex (granular, dysg. ag) L	0.85	agranular insular cortex, dorsal part L	23.6874	agranular insular cortex, ventral part R	retrosplenial dysgranular cortex R	5.44
	Insular cortex (granular, dysg. ag) R	1.46	agranular insular cortex, dorsal part R	11.87243	granular insular cortex L	retrosplenial granular cortex, b region R	4.37
			agranular insular cortex, ventral part R	11.63345		secondary auditory cortex, ventral area L	4.33

Table 1

ALPHA-SYNUCLEIN HISTOLOGY			VBM of T2w images in ASYN MRI W2>W18		rs-MRI Connectivity matrices comparisons (W18>W2) in ASYN compared to CTRL		
Functional ROI	ROI	AVERAGE SCORE *	ROI	T score **	ROI1	ROI2	T score ***
RETROSPLENIAL CORTEX	Retrosplenial cortex (granular, dysgranular) L	0.23	retrosplenial dysgranular cortex L	14.57744	retrosplenial dysgranular cortex R	diagonal domain L	5.44
		0.46	retrosplenial dysgranular cortex R	13.70656	retrosplenial dysgranular cortex R	corpus callosum L	4.88
	Retrosplenial cortex (granular, dysgranular) R		retrosplenial granular cortex, c region R	12.72883	retrosplenial dysgranular cortex R	fimbria R	4.76
			retrosplenial granular cortex, b region R	11.65925	retrosplenial dysgranular cortex L	isocortex R	4.71
			retrosplenial granular cortex, c region L	11.56918	retrosplenial dysgranular cortex R	hippocampal formation R	4.68
			retrosplenial granular cortex, b region L	11.53214	retrosplenial dysgranular cortex R	internal capsule L	4.56
					retrosplenial dysgranular cortex R	preoptic area L	4.52
					retrosplenial dysgranular cortex R	corpus callosum R	4.43
					retrosplenial dysgranular cortex R	hippocampal formation L	4.42
					retrosplenial dysgranular cortex R	primary somatosensory cortex R	4.41
					retrosplenial granular cortex, c region R	agranular insular cortex, ventral part R	4.37
					retrosplenial granular cortex, c region R	primary visual cortex L	4.35
					retrosplenial granular cortex, b region L	parietal cortex, posterior area, rostral part L	4.26
					retrosplenial dysgranular cortex R	isocortex R	4.24
					retrosplenial dysgranular cortex R	olfactory structures R	4.24
					retrosplenial granular cortex, b region L	corpus callosum R	4.24
VISUAL CORTEX	Primary visual area L	0.92	primary visual cortex L	11.42267	primary visual cortex R	parietal cortex, posterior area, rostral part L	5.33
	Primary visual area R	0.62	primary visual cortex R	16.45123	primary visual cortex L	midbrain R	4.65
	Secondary visual area medial part L	2.92	secondary visual cortex, lateral area L	13.77167	primary visual cortex L	fimbria R	4.21
	Secondary visual area medial part R	2.92	secondary visual cortex, lateral area R	15.57221	primary visual cortex L	retrosplenial granular cortex, c region R	4.35
			primary visual cortex, binocular area L	11.52233	primary visual cortex, monocular area R	primary somatosensory cortex, oral dysgranular 2o L	4.31
			primary visual cortex, binocular area R	11.36746	primary visual cortex, monocular area L	primary somatosensory cortex, oral dysgranular 2o L	4.16
			primary visual cortex, monocular area L	11.34175	secondary visual cortex, lateral area L	corpus callosum L	4.23
					secondary visual cortex, lateral area L	striatum L	4.11
					secondary visual cortex, lateral area L	internal capsule R	4.68
					secondary visual cortex, lateral area L	primary auditory cortex L	4.85
					secondary visual cortex, lateral area L	primary somatosensory cortex, barrel field R	4.22
					secondary visual cortex, lateral area L	isocortex R	4.17
					secondary visual cortex, mediolateral area L	septum L	4.39
					secondary visual cortex, mediolateral area L	diagonal domain L	4.17
					secondary visual cortex, mediolateral area L	substantia nigra L	4.11

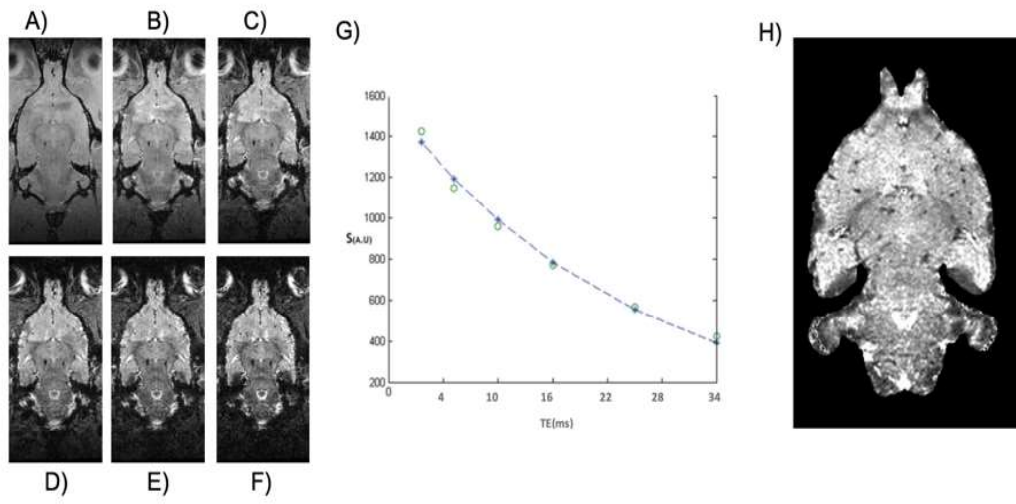
Table 1

Functional ROI	ALPHASYNUCLEIN HISTOLOGY		VBM of T2w images in ASYN MRI W2>W18		rs-fMRI Connectivity matrices comparisons (W18>W2) in ASYN compared to CTRL		
	ROI	AVERAGE SCORE *	ROI	T score **	ROI 1	ROI2	T score ***
MOTOR CORTEX	Primary motor cortex L	0.46	primary motor cortex L	11.65533	secondary motor cortex L	internal capsule L	4.27
	Primary motor cortex R	1.00	primary motor cortex R	11.66815			
	Secondary motor cortex L	0.69	secondary motor cortex L	11.41012			
	Secondary motor cortex R	1.38	secondary motor cortex R	11.94443			
SOMATOSENSORY CORTEX	Primary somatosensory cortex (forelimb, hindlimb, barrel, trunk, dysgranular, faceprep) L	0.38	primary somatosensory cortex, shoulder region R	27.2218	primary somatosensory cortex, hindlimb region R	cingulum R	4.17
		0.77	primary somatosensory cortex, dysgranular zone R	23.90055	primary somatosensory cortex, hindlimb region L	fimbria R	4.92
	Primary somatosensory cortex (forelimb, hindlimb, barrel, trunk, dysgranular, faceprep) R		primary somatosensory cortex, forelimb region R	22.47878	primary somatosensory cortex R	retrosplenial dysgranular cortex R	4.41
			primary somatosensory cortex, oral dysgranular R	17.94628	primary somatosensory cortex R	parietal cortex, posterior area, caudal part R	4.31
			primary somatosensory cortex, hindlimb region R	15.83684	primary somatosensory cortex, oral dysgranular zo L	primary visual cortex, monocular area L	4.16
			primary somatosensory cortex, trunk region R	15.50901	primary somatosensory cortex, oral dysgranular zo L	primary visual cortex, monocular area R	4.31
			primary somatosensory cortex, jaw region R	12.72486	primary somatosensory cortex, barrel field R	secondary visual cortex, lateral area L	4.22
			primary somatosensory cortex, upper lip region R	12.25981	primary somatosensory cortex, hindlimb region L	corpus callosum R	4.09
			primary somatosensory cortex, barrel field R	12.2017			
			primary somatosensory cortex R	11.98039			
			primary somatosensory cortex L	13.05267			
			primary somatosensory cortex, jaw region L	13.05271			
			primary somatosensory cortex, hindlimb region L	12.5678			
			primary somatosensory cortex, forelimb region L	12.52263			
			primary somatosensory cortex, trunk region L	12.24115			
			primary somatosensory cortex, upper lip region L	11.581			
			primary somatosensory cortex, barrel field L	11.55798			
			primary somatosensory cortex, shoulder region L	11.51304			
			primary somatosensory cortex, oral dysgranular zo L	11.39746			
			primary somatosensory cortex, dysgranular zone L	11.38795			

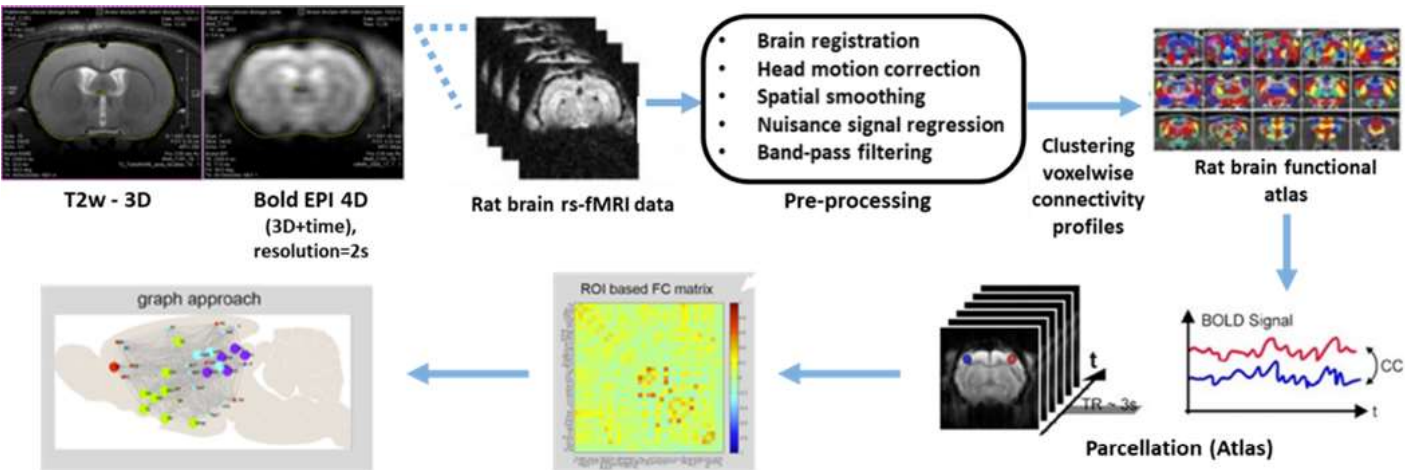
Table 1

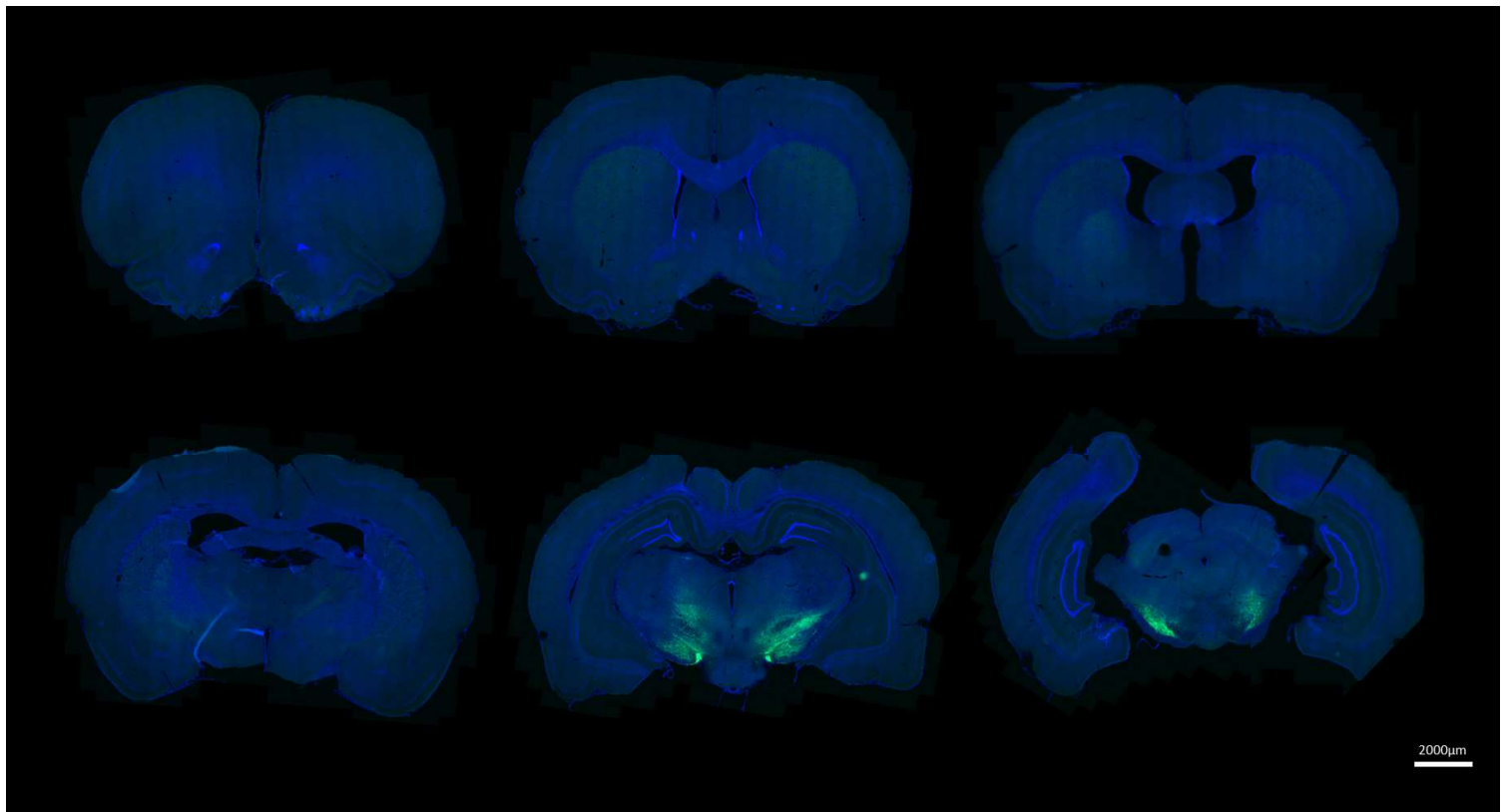
Functional ROI	ALPHASYNNUCLEIN HISTOLOGY	VBM of T2w images in ASYN MRI W2>W18		rs-fMRI Connectivity matrices comparisons (W18>W2) in ASYN compared to CTRL		
	ROI	AVERAGE SCORE	ROI	T score	ROI1	ROI2
AUDITORY CORTEX			primary auditory cortex R	11.72805	primary auditory cortex L	secondary visual cortex, lateral area L
			secondary auditory cortex, dorsal area L	12.13995	primary auditory cortex L	secondary auditory cortex, ventral area L
			secondary auditory cortex, dorsal area R	11.58427	secondary auditory cortex, ventral area L	bed nucleus of the stria terminalis R
			primary auditory cortex L	11.4214	secondary auditory cortex, ventral area L	granular insular cortex L
					secondary auditory cortex, ventral area R	cerebellum R
PARIETAL CORTEX					secondary auditory cortex, ventral area R	retrosplenial dysgranular cortex R
			parietal cortex, posterior area, dorsal part R	18.67093	parietal cortex, posterior area, caudal part R	parietal cortex, posterior area, rostral part L
			parietal cortex, posterior area, rostral part R	17.53633	parietal cortex, posterior area, caudal part R	primary somatosensory cortex R
			parietal cortex, posterior area, caudal part R	14.9858	parietal cortex, posterior area, dorsal part L	retrosplenial dysgranular cortex R
			parietal cortex, posterior area, dorsal part L	11.79073	parietal cortex, posterior area, rostral part L	primary visual cortex R
			parietal cortex, posterior area, caudal part L	11.43439	parietal cortex, posterior area, rostral part L	pituitary L
			parietal cortex, posterior area, caudal part L	11.4745	parietal cortex, posterior area, rostral part L	retrosplenial granular cortex, b region L
			parietal cortex, posterior area, rostral part L		parietal cortex, posterior area, dorsal part L	perirhinal cortex L
CINGULATE CORTEX	Cingulate cortex (area 1,2) L Cingulate cortex (area 1,2) R	0.54 1.31	cingulate cortex, area 1 L	13.65496	cingulate cortex, area 2 R	midbrain L
			cingulate cortex, area 1 R	20.1164	cingulate cortex, area 2 L	dorsal intermediate entorhinal cortex R
			cingulate cortex, area 2 R	17.46389	cingulate cortex, area 2 L	midbrain R
			cingulate cortex, area 2 L	11.38418	cingulate cortex, area 2 L	cerebellum L
					cingulate cortex, area 1 L	midbrain R
ENTORHINAL CORTEX	Entorhinal cortex L Entorhinal cortex R	0.73 1.18			cingulate cortex, area 2 R	midbrain R
			medial entorhinal cortex L	12.9988	cingulate cortex, area 2 L	perirhinal cortex L
			medial entorhinal cortex R	13.30852	cingulate cortex, area 2 L	midbrain L
			dorsolateral entorhinal cortex R	11.51425		
ASSOCIATION CORTEX	Association cortex (frontal, parietal, temporal) L	1.00 1.62	lateral parietal association cortex R	26.18618	NO functional coconnectivity CHANGES	
			lateral parietal association cortex L	12.96581		
PERIRHINAL CORTEX	Perirhinal cortex (35,36) L Perirhinal cortex (35,36) R	2.23 1.92	NO STRUCTURAL CHANGES IN PERIRHINAL CX		perirhinal cortex L	parietal cortex, posterior area, dorsal part L
					perirhinal cortex L	cingulate cortex, area 2 L

Supplementary Figure 1



Supplementary Figure 2



Supplementary Figure 3

Neurobiology of Disease

Textural features of magnetic resonance imaging correlate with tissue changes in a human alpha-synuclein overexpression model of Parkinson's disease --Manuscript Draft--

Manuscript Number:	
Article Type:	Research paper
Keywords:	Texture analysis, magnetic resonance imaging, alpha-synuclein-based Parkinson's disease model, behavioural analysis, anatomo-radiological correlations.
Corresponding Author:	Nacim Betrouni, MD, PhD INSERM U1172 FRANCE
First Author:	Chirine Katrib
Order of Authors:	Chirine Katrib
	David Devos
	Hector Hladky
	Kelly Timmerman
	Nicolas Durieux
	Nathalie DUTHEIL
	Erwan Bezard
	Charlotte Laloux
	Nacim Betrouni, PhD
Abstract:	<p>After successful applications in the oncology field to provide new diagnosis and prognosis in vivo imaging features, texture analysis and more generally radiomics were also reported as having the potential to provide markers of different neurodegenerative processes. Indeed, in neurodegenerative diseases such as Parkinson's disease (PD), there is an immense need for neuroprotective therapies, the development of which will be fundamentally aided by imaging biomarkers capable of inferring tissue changes such as loss of neurons in the nigro-striatal pathway or alpha synuclein aggregates that characterize PD. In this study, we therefore sought to decipher the relationship between signal changes measured using brain MRI texture features and histological changes in a preclinical model based on the overexpression of human alpha-synuclein. Sprague Dawley rats received a double bilateral intranigral injection of adeno-associated virus carrying the human alpha-synuclein gene, then underwent several behavioural tests to evaluate motor and cognitive functions over a 4-month period. Animals then had MR imaging with a T2w sequence evaluation and were sacrificed for histological analyses of the brains. Texture features were measured in different brain structures from in vivo images including the nigrostriatal pathway and the cortex. The association analyses revealed significant correlations between the imaging features measured in the substantia nigra and the striatum with dopaminergic degeneration, as well as significant correlations between texture features in key structures: substantia nigra, striatum, thalamus, hippocampus and associative and cingulate cortices, with LB509-positive α-synuclein quantified in these regions. Texture features in these regions also correlated also with scores from the behavioural analyses. These preliminary results suggest that texture features reflect the underlying tissue changes occurring in the brain as well as the changes in the behavioural phenotype.</p>
Suggested Reviewers:	Patrice Péran patrice.peran@inserm.fr Specialist in PD and imaging
	Deniz Yilmazer-hanke deniz.yilmazer-hanke@uni-ulm.de Specialist in PD and histological analysis

	Manuel Delgado-Alvarado manuel.delgado@eug.es Neurologist, specialist in PD, synuclein and imaging
Opposed Reviewers:	

Textural features of magnetic resonance imaging correlate with tissue changes in a human alpha-synuclein overexpression model of Parkinson's disease

Chirine KATRIB ¹, David DEVOS ¹, Hector HLADKY ¹, Kelly TIMMERMAN ¹, Nicolas DURIEUX ², Nathalie DUTHEIL ³, Erwan BEZARD ³, Charlotte LALOUX ^{1,2} and Nacim BETROUNI ¹

¹ Univ. Lille, INSERM, UMR1172 –Lille Neuroscience & Cognition, F-59000, Lille, France.

² Univ. Lille, CNRS, Inserm, CHU Lille, Institut Pasteur de Lille, UAR2014-US41 - Lille In vivo imaging and functional exploration platform, F-59000 Lille, France.

³ Univ. Bordeaux, CNRS, IMN, UMR 5293, F-33000 Bordeaux, France

Corresponding author:

Nacim Betrouni, PhD., INSERM U1172 – Lille Neuroscience & Cognition Laboratoire de Pharmacologie, Faculté de Médecine 1, Place de Verdun, 59000 – Lille, France.

Tel: +33.3.20.44.63.54; Email: nacim.betrouni@inserm.fr

Declarations of interest: none

Financial disclosures: none

Abstract

After successful applications in the oncology field to provide new diagnosis and prognosis *in vivo* imaging features, texture analysis and more generally radiomics were also reported as having the potential to provide markers of different neurodegenerative processes. Indeed, in neurodegenerative diseases such as Parkinson's disease (PD), there is an immense need for neuroprotective therapies, the development of which will be fundamentally aided by imaging biomarkers capable of inferring tissue changes such as loss of neurons in the nigro-striatal pathway or alpha synuclein aggregates that characterize PD. In this study, we therefore sought to decipher the relationship between signal changes measured using brain MRI texture features and histological changes in a preclinical model based on the overexpression of human alpha-synuclein.

Sprague Dawley rats received a double bilateral intranigral injection of adeno-associated virus carrying the human alpha-synuclein gene, then underwent several behavioural tests to evaluate motor and cognitive functions over a 4-month period. Animals then had MR imaging with a T2w sequence evaluation and were sacrificed for histological analyses of the brains. Texture features were measured in different brain structures from *in vivo* images including the nigrostriatal pathway and the cortex. The association analyses revealed significant correlations between the imaging features measured in the substantia nigra and the striatum with dopaminergic degeneration, as well as significant correlations between texture features in key structures: substantia nigra, striatum, thalamus, hippocampus and associative and cingulate cortices, with LB509-positive α -synuclein quantified in these regions. Texture features in these regions also correlated also with scores from the behavioural analyses.

These preliminary results suggest that texture features reflect the underlying tissue changes occurring in the brain as well as the changes in the behavioural phenotype.

Key words

Texture analysis, magnetic resonance imaging, alpha-synuclein-based Parkinson's disease model, behavioural analysis, anatomo-radiological correlations.

Highlights

- Texture features from T2W MR images correlate with dopaminergic degeneration in a preclinical model of Parkinson's disease.
- Texture features correlate with α -synuclein LB509 staining.
- Texture features correlate with scores from the behavioural analyses.

1. Introduction

The major pathological hallmarks of Parkinson's disease (PD) include dopaminergic neuronal degeneration in the nigrostriatal pathway, abnormal iron build-up and alpha-synuclein accumulation forming Lewy body inclusions (Riederer *et al.* 2023). The dopaminergic loss leads to the appearance of three cardinal motor symptoms: bradykinesia, rigidity, and resting tremor (Kalia & Lang 2016), which allows the clinical diagnosis. Interestingly, studies estimate that the onset of the pathophysiological processes of PD, notably the neuronal loss and the formation of the pathogenic alpha-synuclein aggregation occurs approximately 10 to 20 years prior to the clinical manifestation of the disease (Braak *et al.* 2003; Gaig & Tolosa 2009). On the other hand, the disease also associates different non-motor dysfunctions along with disease progression such as anxiety, depression and cognitive impairment, that largely impact the patients' quality of life (Chaudhuri *et al.* 2006). With no yet neuroprotective treatment available, the early and predictive biomarkers of these pathological mechanisms are key elements to facilitate candidate drug evaluation (Devos *et al.* 2021).

Over the last few decades, structural, functional and molecular neuroimaging studies have provided invaluable insights into the mechanisms underlying PD (Bidesi *et al.* 2021). Among these modalities, magnetic resonance imaging (MRI) with its different exploration methods appeared to be a particularly promising modality. In terms of analysis techniques, region of interest (ROI) - based analysis remains the most applied method. A brain structure is defined by a delineated ROI and a single value is measured: mean or median of the $R2^*$ values or the defined volume/shape of the ROI. In recent years, another analysis method allowing the measurement of more than a single value was successfully applied. Texture analysis permits the extraction of statistical features that describe the signal distribution and variation in a defined image region. The assumption is that some of the measured texture features capture changes related to the disease progression and thus can be clinically meaningful. A 2-year follow-up using T2-weighted images of PD patients (Sikio *et al.* 2015), reported that these features were related to clinical scores of PD severity. The Unified Parkinson's Disease Rating Scale (UPDRS) I score evaluating cognition, behaviour and mood, correlated with texture features extracted from the posterior corona radiata and the substantia nigra. UPDRS-II which scores the self-evaluation of the activities of daily living, correlated with texture features from the putamen, the dentate nucleus and the thalamus, while UPDRS-III score

evaluating motor skills, correlated with features in the basilar pons area. Li and colleagues (Li *et al.* 2019) investigated these features in the substantia nigra using R2* and quantitative susceptibility maps. They successfully distinguished PD patients from controls and significantly outperformed R2* ROI-based (mean values) analysis. Betrouni *et al.* (2020 and 2021) demonstrated that texture features, measured on morphologic T1w images, outperform volumetry to detect slight changes related to both motor and non-motor aspects of the disease. In Betrouni *et al.* 2020, the authors showed that texture features measured in the hippocampus, the thalamus and the amygdala were different between patients cognitively intact, patients with slight cognitive slowing and patients with mild cognitive impairment; while in Betrouni *et al.*, 2021, they showed that texture features from the nigrostriatal pathway accurately separate early-stage PD patients from late-stage patients and correlate with motor handicap.

Taken together, all these results about the application of texture analysis on PD MR images suggest that these features can capture early tissular changes related to the disease progression. This study aims to decipher the relationship between the signal changes measured using texture features and the tissular modifications. A preclinical model of PD relying on the overexpression of alpha-synuclein by adeno-associated virus (AAV) injection in the substantia nigra is used. This model has shown a progressive dopaminergic denervation in time with alpha-synuclein expression and propagation (Bourdenx *et al.* 2015), making it an interesting tool to study the MR imaging signature of these two histopathological hallmarks.

2. Material and Methods

2.1 Animal model and experimental design

Experiments were carried out following institutional and national guidelines for the care and use of laboratory animals. They were approved by the regional and French ethical committees (Authorization number 6281-20 16072517437766).

Sprague Dawley adult male rats (n=19, 6 weeks old, 180–200 g) were randomly assigned to an α -synuclein group (ASYN) (n=13) or a control group (CTRL) (n=6). Rats received two bilateral intranigral injections of 1 μ L at 250 nL/min (Anteroposterior: -4.9 and -5.4 , mediolateral: ± 2.1 , dorsoventral: -7.8 , in mm from bregma) of a recombinant AAV2/9-p.A53T-human- α -syn (7×10^{12} gcp/ml) for the ASYN group or AAV2/9-GFP (7×10^{12} gcp/ml) for the CTRL group (Institut des Maladies Neurodegeneratives UMR 5293, Bordeaux, France). All the interventions were performed under complete general anaesthesia with ketamine (100 mg/kg) and xylazine (5 mg/kg).

Basic motor and sensorimotor skill assessments were conducted, along with a cognitive evaluation including visuospatial learning and memory, pairwise visual discrimination and attentional tasks over 4 months post-injection (PI). At the end of these 4 months, the animals had an MR imaging evaluation and then were sacrificed for histological analyses of the brains.

2.2 Behavioural assessment

2.2.1 Motricity and sensori-motricity

Spontaneous motor activity was recorded over a 10-min period in an actimeter equipped with Actitrack analytical software (Panlab, Barcelona, Spain), to evaluate distance travelled, speed, and rearing behaviour (Laloux *et al.* 2012). Sensori-motricity was assessed using the stepping test, which accounts for the number of left/right forehand adjusting steps during a sliding movement, while the other forehand is blocked. Nine trials were conducted over 3 days (Laloux *et al.* 2017). These tests were performed monthly to follow the evolution of spontaneous locomotion and forelimb akinesia.

2.2.2 Cognitive assessment

Visuo-spatial learning and memory assessment was done using the Morris Water Maze (MWM) test (adapted from Delattre *et al.* 2017). It includes a 4-day training period evaluating spatial

learning, with four trials/day measures of the rat's ability to find a hidden platform in a pool using external spatial cues. The learning phase is followed by a probe test on the fifth day when the platform is removed. Spatial memory encoding is thus evaluated by calculating the time spent in the target quadrant where the platform used to be.

Visuo-spatial discrimination ability was assessed using Pairwise visual discrimination task (PVD), which is conducted in automated touchscreen-based testing chambers (Campden Instruments Limited & Lafayette Instrument Company) over 25 days starting 6 weeks p.i.. Following operant conditioning training in which animals has to nose poke toward the screen to receive a reward, they started the two-choice visual discrimination task in which a pair of stimuli would appear on the screen; one stimulus was the correct S+ and the other the incorrect S-. A nose-poke to the S+ resulted in a magazine light and a reward pellet. The criteria for succeeding in the task was the successful completion of 75 trials, with at least 80% correct responses in a maximum of 45 minutes, during 2 consecutive days (adapted from Kumar *et al.*, 2012).

Attention performances were assessed using the 5-choice serial reaction time task (5CSRT), is also conducted in automated touchscreen-based testing chambers over 35 days starting 12 weeks p.i. (adapted from Slezak *et al.* 2018). This task is based on the operant conditioning paradigm whereby the animal receives a reward when nose poking the correct lit square among 5-windows within a defined time limit. The light duration of the square exposure is gradually decreased over training sessions, therefore increasing the task's difficulty, and mobilizing more attentional resources. The criteria for moving on to the next session is completion of 75 trials, with at least 80% correct responses in a maximum of 45 minutes, during 2 consecutive days.

2.3 Imaging and processing

MRI proton imaging experiments were performed at 7 Tesla in a horizontal bore magnet (Bruker, Biospec®, Ettlingen, Germany). Animals were anaesthetized with isoflurane (2%), and their temperature and breathing rate were monitored during the experiments. Structural T2 weighted (T2w) MR sequence was acquired in Turbo RARE (Rapid Acquisition with Relaxation Enhancement) mode, with the following parameters: spin-echo sequence: TR/TE= 3000/33 ms, field of view (FOV) = 4 cm², voxel size = 0.15x0.15x0.75mm³).

The original T2w images were first corrected for intensity non-uniformity, caused by static field inhomogeneity, using the N3 algorithm (Sled *et al.* 1998) and then spatially registered to the

Waxholm Space Atlas of the Sprague Dawley Rat Brain, to accurately define regions of interest (SCR_017124) (Papp *et al.* 2014) (Figure 1).

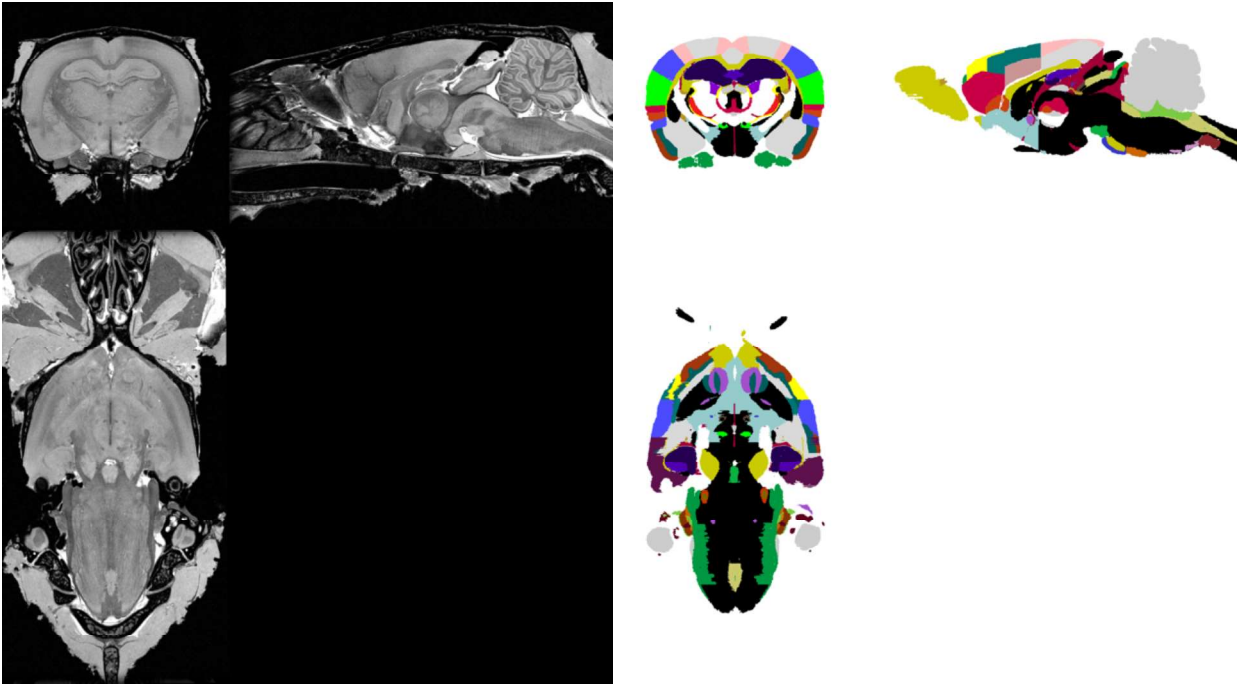


Figure 1: Sprague Dawley Rat Brain atlas: anatomical image and masks of the brain structures.

Using the anatomical delineations of the atlas and by assuming their supposed involvement in the disease's development and progression, the ROIs defining the following anatomical regions were considered: substantia nigra, striatum, thalamus, hippocampus, associative cortex and cingulate cortex.

Overall, and based on previous results (Betrouti *et al.* 2021), 10 texture features including first and second order statistics, were considered and computed in each ROI. The first-order statistics are used to study the voxel value distribution without considering spatial relationships. Four of these features were chosen: Mean grey level; Standard deviation (SD) of grey levels; Kurtosis, which is a measure of whether the data is heavy-tailed or light-tailed in relation to a normal distribution; and Skewness, which also quantifies the asymmetry of signal values in relation to a normal distribution. The second-order statistics describe relationships between pairs of neighbouring voxels in the image, therefore quantifying the spatial relationships between the values. These are mainly computed through the grey level co-occurrence matrix (GLCM) introduced by Haralick *et al.* in 1973. Second-order texture values were derived from the co-

occurrence matrix whose entries represent the number of times that intensity levels i and j occur in two voxels separated by a distance (d) in a specific direction (a). To obtain a full neighbourhood interaction, a matrix was selected to cover 26 connected directions of neighbouring voxels in a 3D space. Seven parameters were considered: Homogeneity (also called angular second moment), which represents uniformity of the texture intensity; Contrast, representing the degree to which the texture intensity levels differ between voxels or local intensity variation; Entropy, (measure of randomness), which represents the degree of uncertainty; Correlation, representing the degree of mutual dependency between voxels; Variance (also called sum of squares), which gives high weights for elements different from the average value; Sum average, measuring the relationship between occurrences of pairs with lower intensity values and occurrences of pairs with higher intensity values; and Inverse difference moment (InvDiff), which measures the difference between the highest and lowest values of a contiguous set of voxels. (Complete description of the computation of the texture features can be found in Betrouni *et al.* 2020 and 2021).

The texture features were computed on the delineated ROIs on both brain hemispheres and the left and right sides values were averaged to obtain global values representative for the structure.

2.4 Histological assessment

Eighteen weeks PI, rats were transcardially perfused with 4% paraformaldehyde (PFA). Brains were fixed overnight in 4% PFA and then cryoprotected in 30% sucrose solution before snap freezing in isopentane and then stored at -80°C . Forty micrometre-thick free-floating coronal sections of the entire brain were prepared using a cryostat (Leica, Nussloch, Germany).

2.4.1 Dopaminergic degeneration

The dopaminergic denervation was assessed by tyrosine hydroxylase (TH) immunostaining of striatal and nigral sections. The brain sections were incubated with 0.3% hydrogen peroxide in a 0.1 phosphate buffer, pH 7.4 (PBS), to quench endogenous peroxidase activity. Then they were incubated in a 0.3% Triton X-100 PBS blocking solution with 10% normal serum. A primary antibody: anti-TH 1:1000 (AB152 Sigma-Aldrich), then a biotinylated secondary antibody goat anti-rabbit (BA1000, VectorLabs) were used. Antibody binding was detected with the avidin–biotin–peroxidase conjugate (Vectastain ABC Elite; VectorLabs) using 3,3'-diaminobenzidine as the chromogen. Finally, sections were dehydrated through graded ethanol solutions, cleared in xylene, and mounted in DPX (DBH Laboratory Supplies).

Images were acquired using a Zeiss Axio Scan Z.1 slide scanner (20× objective) and Zen software, Blue edition (Zeiss, Oberkochen, Germany). Zen Software measured the optical density of TH-ir terminals in the striatum. The number of TH-ir neurons in the substantia nigra was counted by unbiased stereology using Mercator Explora Nova Software, with an optical fractionator method to allow an accurate and efficient estimate of labelled neuron number as previously described (Laloux *et al.*, 2017).

2.4.2 Alpha-synuclein staining

The same immunohistochemistry protocol described above was used for α -synuclein staining, with primary antibody α -synuclein mouse mAb, clone LB509 (180215 Invitrogen) for human α -synuclein (h- α -syn), and secondary antibody horse anti-mouse (BA-2000, Vectorlabs).

After axioscan acquisition, LB509-unravellled α -synuclein was assessed using a custom 4-point scale range from 0 to 3, quantifying the presence and amount of α -synuclein staining (Figure 2A) (adapted from Joppe and colleagues, 2021). Using the QuickNII spatial registration software (Puchades *et al.*, 2019), each region of interest among those described above, was automatically delineated from the Waxholm Space Atlas of the Sprague Dawley Rat Brain (SCR_017124) (Papp *et al.*, 2014) and was scored (Figure 2B&C), allowing, thus to obtain an average score of α -synuclein staining.

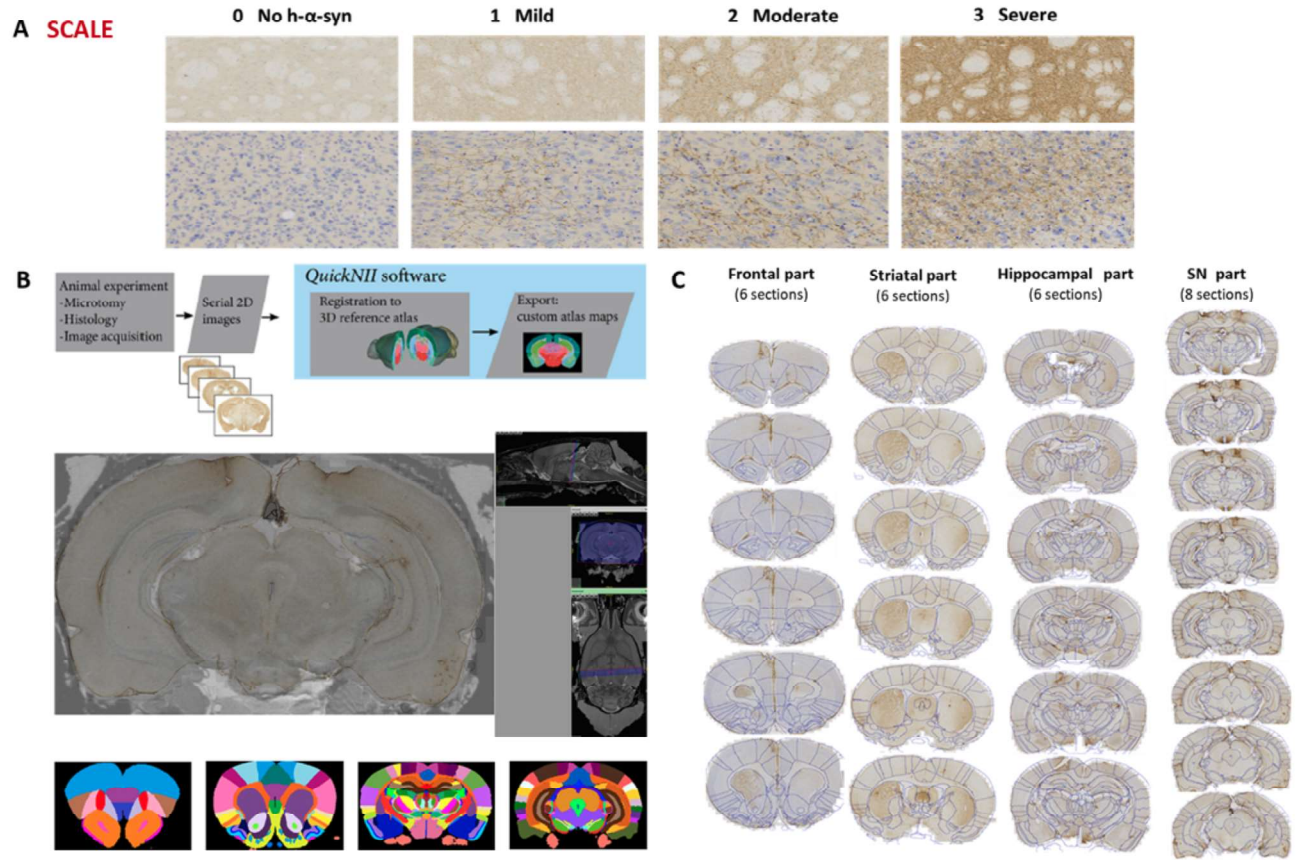


Figure 2. Pipeline for the spatial registration and 3D reconstruction of histological slices. A. The alpha-synuclein quantification 4-level scale used for analysis (0: absence of alpha-synuclein strings; 1: few alpha-synuclein strings; 2: moderate presence of alpha-synuclein strings; 3: Dense alpha-synuclein strings) defined for each region based on the number/density of α -syn strings. **B.** Histological image registration to the WHS MRI atlas, and segmentation, using QUICKNII software. **C.** Application on the rat brain, with a mask representing the ROIs delineation.

2.5 Statistical analysis

2.5.1 Behaviour and histological scores

All data are expressed as mean \pm SEM or as percentage of the CTRL group. Data from behavioural tests were analysed using 2-way ANOVAs followed by Bonferroni post-hoc test for multiple comparisons while histological scores were compared using Mann-Whitney tests.

2.5.2 Texture features

The association between the texture features and the neural density was examined using Spearman's correlation, measured between the imaging features in the substantia nigra and the striatum and the number of neurons or density of neuronal terminals respectively in these structures in both animal groups, while the association between the imaging features and the alpha-synuclein concentration was examined only by considering the ASYN group and using the Spearman's correlation, measured between the texture features in the brain structures indicated above and the corresponding alpha-synuclein distribution scores.

Lastly, the association of texture features with the behavioural scores was examined by measuring the Spearman's correlation between the imaging features in the defined ROIs and the scores.

For all the analyses, significance was fixed at $p\text{-value} < 0.05$. False discovery rate (FDR) correction for multiple testing was applied to correct the significance for each case.

3. Results

3.1 Behavioural assessment

Motor and cognitive tests over the 4 months revealed different outcomes. In terms of motricity, the ASYN model displayed deficits in sensori-motricity but no deficits in general locomotor activity. Indeed, the stepping test, allowed to observe a significant decrease in the number of adjusting steps, in ASYN animals compared to control. The decrease reached 33% 16-weeks post-injection, while the evaluations done using the actimetry test did not find any group differences between ASYN and CTRL animals, in any of the motor activity parameters: mean speed, distance covered, rearing frequency, or resting time.

The training phase of the MWM test allowed to evaluate visuo-spatial learning at 4 and 8 weeks. A significant increase in the latency to reach the escape platform in ASYN animals was observed. This increase in latency showed trouble (a slowing down) in the spatial learning process in the ASYN animals. However, the probe test evaluating the spatial memory did not show differences in the time spent in the target quadrant between the two groups, indicating thus that there are no deficits in spatial memory in ASYN animals.

During the PVD task, we noticed that only 42.9% of ASYN animals were able to reach the criteria for completing the task compared to 70% of the controls after 15 days of learning. This showed that although the ASYN animals did not have trouble discriminating the two images, they needed more time to reach the required criteria, also confirming the deceleration of learning faculties.

Lastly, in the 5CSRT task, nose poking the illuminated aperture was considered as the correct response, while an omission meant the lack of response or nose-poke. The ASYN animals had no differences in omission percentages but a significantly lower percentage of correct answers compared to CTRL animals ($p=0.01$), indicating a deficit in attentional function starting 12 weeks post-injection.

3.2 Histological assessment

Assessment of TH immunoreactivity in the nigrostriatal pathway 4-month post injections revealed a significant reduction of dopaminergic TH-ir neurons in the substantia nigra pars compacta (SNpc) ($p<0.0001$) and of dopaminergic terminals in the striatum ($p=0.02$) in the ASYN group. The percentage of dopamine TH-ir neuron loss was evaluated at an average of 27% in the striatum and 48% in the SNpc, compared to CTRL animals (Figure 3).

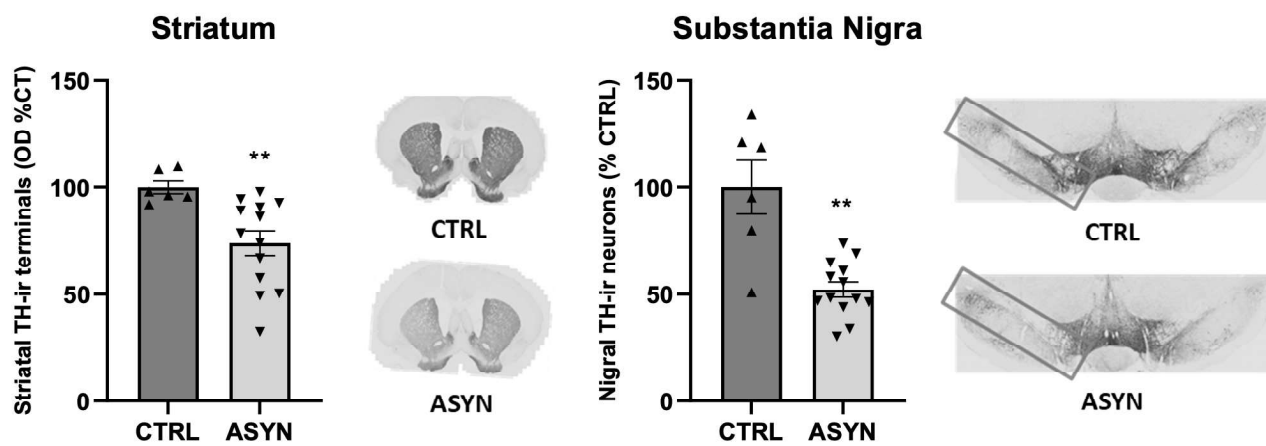


Figure 3. Assessment of the neurodegeneration. Left: dopaminergic terminals in the striatum and right dopaminergic TH-ir neurons in the substantia nigra pars compacta. The percentage of dopaminergic neurons (mean \pm SEM) is shown compared to the mean value of CTRL.

α -synuclein staining was observed both anterior and posterior to the injection site, with the protein reaching the olfactory bulb on one side and the brainstem on the other. The main regions with moderate to severe α -synuclein pathology include the caudate-putamen, the substantia nigra pars compacta, the thalamus, and the hippocampus. Several cortical areas also presented with moderate to severe α -synuclein scores, mainly the cingulate and association cortices (Table 1).

Rat	Substantia-nigra	Striatum	Thalamus	Hippocampus	Associative cortex	Cingulate cortex
1	2.5	2.5	2.5	2	1.25	0.5
2	1.25	1.75	1	3	2.5	0.25
3	2.75	2.5	1.5	0	1.75	1.25
4	2.25	2.5	1.5	1.25	2.25	1.75
5	1.5	2.5	1	0	1	0.5
6	2.5	2.25	0.75	2	1.5	0.5
7	0.25	0.5	1.25	3	0	0
8	2	2.5	0.5	0.25	2.25	1.5
9	2.75	2.5	0	0	1.5	1.5
10	2.5	3	3	2	2.5	1.5
11	1.5	3	2	2	2	2
12	2.5	2.5	1	1	2	2.5
13	2	3	0	0	2	1
Mean	2	2.4	1.2	1.3	1.7	1.1

Table 1: Mean values of the alpha-synuclein scoring in the regions of interest used for the correlations analysis with corresponding MR T2w texture features.

3.3 Texture features and behavioural parameters

The investigation of the association between the texture features and the behavioural scores showed a correlation between different features computed in the striatum and stepping counts, measured at month 4 (standard-deviation of grey levels, Spearman's correlation ratio $r=-0.51$, $p<0.001$, variance $r=0.59$, $p=0.001$, inverse difference moment $r=0.5$, $p=0.008$, and entropy $r=0.60$, $p=0.005$).

Furthermore, texture features from the striatum correlated with variables from visual discrimination learning parameters (PVD task): kurtosis $r=0.51$, $p=0.009$, homogeneity $r=-0.52$, $p=0.009$, contrast $r=-0.50$, $p=0.01$, sumV, $r=0.52$, $p=0.008$ and entropy, $r=0.46$, $p=0.015$.

From visuospatial memory evaluation (MWM), the cumulative duration of time spent in the target quadrant at month 4 correlated with texture features from the thalamus: homogeneity $r=0.6$, $p=0.007$, correlation $r=0.48$, $p=0.01$ and contrast $r=0.5$, $p=0.01$.

The last findings regarding these associations were the significant correlation between the hippocampus's texture features and the cumulative duration of time spent in the target quadrant in MWM at month 4: variance $r=0.48$, $p=0.01$ and sumV $r=0.49$, $p=0.009$.

3.4 Texture features and neurodegeneration

The correlation analysis showed a clear association between the first-order statistics texture feature skewness in both the substantia nigra and the striatum and the corresponding neural density. While in the striatum, the kurtosis features also showed a statistically significant correlation with the measured neural density (in the striatum, skewness $r=-0.55$, $p=0.001$, kurtosis $r=-0.48$, $p=0.009$, in the substantia nigra skewness $r=-0.59$, $p=0.001$, Figure 4).

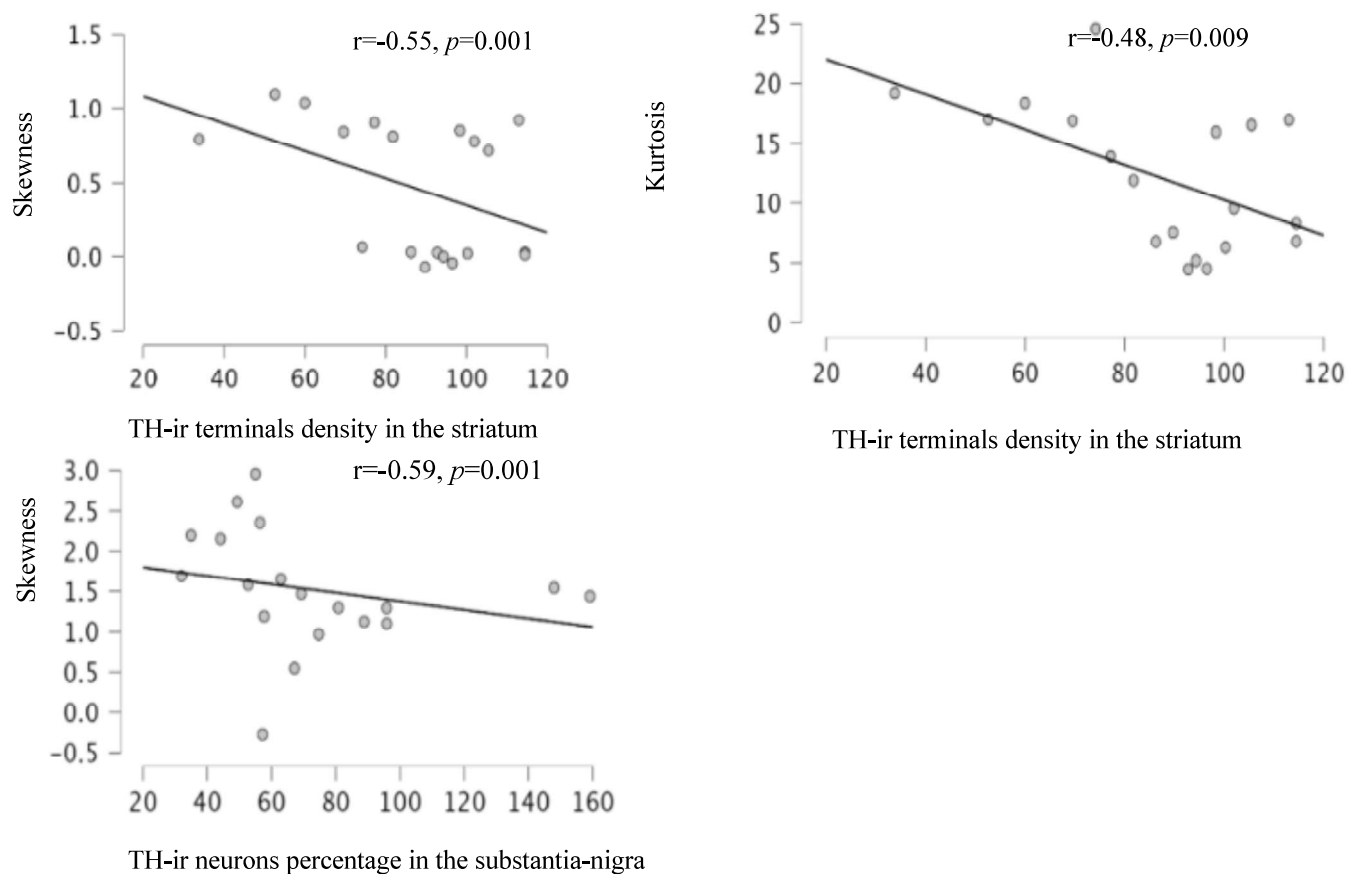


Figure 4: Spearman's correlation of percentage of TH-ir neurons in the substantia-nigra and neuron terminals density in the striatum with texture features in these two regions.

3.5 Texture features and alpha-synuclein overexpression

Associations between texture features and alpha-synuclein overexpression in different brain structures of the animal from the ASYN group showed statistically significant correlations. Table 2 summarises the main findings:

Brain structure	Texture feature	Statistics
Substantia nigra	Standard-deviation	$r=0.81, p=0.001$
	Inverse difference moment	$r=-0.60, p=0.01$
	Entropy	$r=-0.58, p=0.02$
Striatum	Kurtosis	$r=0.62, p=0.002$
	Homogeneity	$r=-0.58, p=0.006$
	Inverse difference moment	$r=-0.63, p=0.002$
	Entropy	$r=-0.63, p=0.002$
Thalamus	Contrast	$r=-0.70, p=0.005$
	Standard-deviation	$r=-0.62, p=0.01$
	Inverse difference moment	$r=0.63, p=0.01$
Hippocampus	Mean gray level	$r=-0.70, p=0.009$
	Sum-Average	$r=-0.65, p=0.01$
	Contrast	$r=-0.60, p=0.01$
	Variance	$r=-0.67, p=0.009$
Associative cortex	Skewness	$r=0.64, p=0.002$
Cingulate cortex	Standard-deviation	$r=0.60, p=0.01$
	Skewness	$r=0.65, p=0.01$

Table 2: Spearman's correlation between alpha-synuclein overexpression and texture features in different brain structures.

4. Discussion

The results reported herein constitute the first application of MR image texture analysis in an animal model of Parkinson's disease. The application of this post-processing method, on *in vivo* structural T2w images has yielded interesting correlative patterns. Indeed, these analyses allowed to make correlations with both histopathological and behavioural scores, hence suggesting that these imaging features could reflect both the underlying tissue changes occurring in the brain, as well as the changes in the behavioural phenotype, progressing overtime.

The behavioural results suggest that this model does not only mimic the early stages of Parkinson's disease with slight sensori-motor deficit, but is also progressive (Decressac *et al.*, 2012). On the other hand, interestingly, texture features in the striatum correlated with the sensori-motor scores evaluated in the stepping test, thereby showing that these subtle image alterations can also reflect the evolution of akinesia overtime in the animals. Furthermore, different texture features from the striatum, the thalamus as well as the hippocampus, brain structures assumed to be involved in the visuo-spatial learning and memory mechanisms, correlated with parameters from the Morris Water Maze and Pairwise Visual Discrimination tasks. These results are in line with of our clinical results (Betrouti *et al.* 2021), where we have showed correlations between texture features computed in regions from the nigrostriatal pathway with MDS-UPDRS III and Hoen-Yahr scores.

In terms of tissular changes, texture features in the nigrostriatal pathway mirrored the dopaminergic degeneration which was observed in both the striatum and the substantia nigra, as shown in the histology measurements. This confirms that ROI-based texture analysis is a sensitive image analysis technique that could detect very subtle changes in the signal, in this case, when the neurodegeneration was valued at 30 to 40 % (Figure 3), and therefore has not yet reached a critical point leading to major morphological changes in the structure. In a clinical context, patients meet the criteria for PD only when 60–70% of the neurons in the substantia nigra have degenerated and approximately 80% of the striatal dopamine content has been lost (Riederer, *et al.* 2023, Diederich *et al.* 2019). Two main texture features from first-order statistics, the kurtosis and the skewness, showed correlations with the dopaminergic neural concentrations in the striatum and the substantia nigra. These two features that globally inform about the signal deviation regarding the normal distribution are particularly sensitive to the signal changes induced by neural density changes. In previous investigations of this method using clinical data, these features were reported as more

sensitive than volumetry to discriminate PD groups with different disease severity (Betrouni *et al.* 2020, Betrouni *et al.* 2021, Devignes *et al.* 2021). Furthermore, and in another context, Colgan *et al.* 2019, carried out an imaging-histological analysis using a preclinical model of Alzheimer's disease and observed significant correlations between tau burden and texture features, mainly skewness in the hippocampus and thalamus.

The other main outcome of this study is the associations between the LB509 immunopositivity for α -synuclein and different texture features measured in key structures from the nigrostriatal pathway and the cortex (Table 2). These results suggest that these changes alter the MR signal and texture features can capture the resulting patterns. Here the features, reporting significant results, were both from the first and second order statistics as inverse difference moment and the entropy. The main difference between these two features categories is about the consideration or not of the neighbourhood. Second-order statistic features provide an information regarding the relationship between the voxels, therefore better demonstrate the intra-ROI heterogeneity. By definition, texture features either from first or second order statistics are strongly correlated between them but bring complementary information about the global and local signal changes in a region. In the oncology field where the first effective clinical applications of texture analysis were reported as for therapies (mainly radiotherapy and chemotherapy) prognosis, these features are usually combined using machine learning methods to build the models (Aerts *et al.*, 2014).

In neurodegenerative diseases, as an early driver of α -synucleinopathies pathogenesis, aggregated α -synuclein could be a suitable imaging biomarker and mainly in PD. However, to date, there is no imaging biomarker for a definitive early diagnosis or prognosis. Nuclear medicine modalities (single-photon emission computed tomography and positron emission tomography) allow only the detection of dopaminergic deficits but not the quantification of the protein as is the case in Alzheimer's disease, with radiotracers having the required sensitivity for tau or beta-amyloid plaques quantification (Alzghool *et al.*, 2022). Efforts to develop these tracers are still underway, but until we have direct measurement methods, indirect measurement using MRI could be a solution. The reported results herein build on this concept can pave the way to this kind of solution. Taken together, the histopathological outcomes may imply that these MR markers can inform about the neurodegeneration as well as alpha-synuclein. Indeed, dopaminergic neurons of the SN show selective neurodegeneration with reduction of dopamine levels in the striatum. The mechanism by which dopaminergic neurons die remains to be fully established and to date there

is no linear relationship between aggregation load of α -synuclein and nigral dopaminergic degeneration (Ghiglieri *et al.*, 2018). Thus, this makes MR imaging biomarkers more adapted to longitudinal follow-up than direct synuclein ligands quantification. Currently, we are investigating the sensitivity of these markers using data from the FAIRPARK-II clinical trial (<https://www.fairpark2.eu>) (Devos *et al.*, 2022). This longitudinal trial investigates the effects of an iron chelation therapy on the progression of handicap in PD.

In 2016, Robert Gillies (Gillies *et al.*, 2016) wrote: “Images Are More than Pictures, They Are Data”. But they can only become data, and to a certain extent, possible biomarkers, when we find a way to interpret the underlying anatomical, cellular and molecular changes that are reflected in images. This process remains a challenge, especially in neurology, because unlike the oncology field, where we can readily have biopsies of the tissue, the brain’s histological signature remains a mystery and only the association of clinical cohorts with brain biobanks could afford the kind of analysis at the human level.

References

- Aerts HJ, Velazquez ER, Leijenaar RT, Parmar C, Grossmann P, Carvalho S, Bussink J, Monshouwer R, Haibe-Kains B, Rietveld D, Hoebbers F, Rietbergen MM, Leemans CR, Dekker A, Quackenbush J, Gillies RJ, Lambin P. Decoding tumour phenotype by noninvasive imaging using a quantitative radiomics approach. *Nat Commun*. 2014 Jun 3;5:4006.
- Alzghool OM, van Dongen G, van de Giessen E, Schoonmade L, Beaino W. α -Synuclein Radiotracer Development and In Vivo Imaging: Recent Advancements and New Perspectives. *Mov Disord*. 2022;37(5):936–48.
- Betrouni N, Lopes R, Defebvre L, Leentjens AFG, Dujardin K. Texture Features of Magnetic Resonance Images: A Marker of Slight Cognitive Deficits in Parkinson's Disease. *Mov Disord*. 2020 Mar;35(3):486–94.
- Betrouni N, Moreau C, Rolland AS, Carrière N, Chupin M, Kuchcinski G, et al. Texture-based markers from structural imaging correlate with motor handicap in Parkinson's disease. *Sci Rep*. 2021 Feb 1;11(1):2724.
- Bidesi NSR, Vang Andersen I, Windhorst AD, Shalgunov V, Herth MM. The role of neuroimaging in Parkinson's disease. *J Neurochem*. 2021;159(4):660–89.
- Bourdenx M, Dovero S, Engeln M, Bido S, Bastide MF, Duthiel N, et al. Lack of additive role of ageing in nigrostriatal neurodegeneration triggered by α -synuclein overexpression. *Acta Neuropathol Commun*. 2015 Dec;3(1):46.
- Braak H, Del Tredici K, Rüb U, de Vos RAI, Jansen Steur ENH, Braak E. Staging of brain pathology related to sporadic Parkinson's disease. *Neurobiol Aging*. 2003;24(2):197–211.
- Chaudhuri KR, Healy DG, Schapira AH. Non-motor symptoms of Parkinson's disease: diagnosis and management. *Lancet Neurol*. 2006 Mar 1;5(3):235–45.
- Colgan N, Ganeshan B, Harrison IF, Ismail O, Holmes HE, Wells JA, et al. In vivo imaging of Tau pathology using magnetic resonance imaging textural analysis. *Front Neurosci*. 2017;11:599.
- Decressac M, Mattsson B, Lundblad M, Weikop P, Björklund A. Progressive neurodegenerative and behavioural changes induced by AAV-mediated overexpression of α -synuclein in midbrain dopamine neurons. *Neurobiol Dis*. 2012 Mar;45(3):939–53.
- Delattre C, Bournonville C, Auger F, Lopes R, Delmaire C, Henon H, et al. Hippocampal Deformations and Entorhinal Cortex Atrophy as an Anatomical Signature of Long-Term Cognitive Impairment: from the MCAO Rat Model to the Stroke Patient. *Transl Stroke Res*. 2018 Jun;9(3):294–305.
- Devignes Q, Viard R, Betrouni N, Carey G, Kuchcinski G, Defebvre L, et al. Posterior Cortical Cognitive Deficits Are Associated With Structural Brain Alterations in Mild Cognitive Impairment in Parkinson's Disease. *Front Aging Neurosci* [Internet]. 2021 [cited 2023 Oct 14];13. Available from: <https://www.frontiersin.org/articles/10.3389/fnagi.2021.668559>

Devos D, Hirsch E, Wyse R. Seven Solutions for Neuroprotection in Parkinson's Disease. *Mov Disord*. 2021 Feb;36(2):306-316.

Devos D, Labreuche J, Rascol O, Corvol JC, Duhamel A, Guyon Delannoy P, et al. FAIRPARK-II Study Group. Trial of Deferiprone in Parkinson's Disease. *N Engl J Med*. 2022 Dec 1;387(22):2045-2055.

Diederich NJ, James Surmeier D, Uchihara T, Grillner S, Goetz CG. Parkinson's disease: Is it a consequence of human brain evolution? *Mov Disord*. 2019 Apr;34(4):453-459.

Gaig C, Tolosa E. When does Parkinson's disease begin? *Mov Disord Off J Mov Disord Soc*. 2009;24 Suppl 2:S656-664.

Gillies RJ, Kinahan PE, Hricak H. Radiomics: Images Are More than Pictures, They Are Data. *Radiology*. 2016 Feb;278(2):563-77.

Ghiglieri V, Calabrese V, Calabresi P. Alpha-Synuclein: From Early Synaptic Dysfunction to Neurodegeneration. *Front Neurol*. 2018 May 4;9:295.

Haralick RM, Shanmugam K, Dinstein I. Textural Features for Image Classification. *IEEE Trans Syst Man Cybern*. 1973 Nov;SMC-3(6):610-21.

Kalia LV, Lang AE. Evolving basic, pathological and clinical concepts in PD. *Nat Rev Neurol*. 2016 Feb;12(2):65-6.

Kumar G, Talpos J, Steckler T. Strain-dependent effects on acquisition and reversal of visual and spatial tasks in a rat touchscreen battery of cognition. *Physiol Behav*. 2015 May 15;144:26-36. Laloux C, Petrault M, Lecointe C, Devos D, Bordet R. Differential susceptibility to the PPAR- γ agonist pioglitazone in 1-methyl-4-phenyl-1,2,3,6-tetrahydropyridine and 6-hydroxydopamine rodent models of Parkinson's disease. *Pharmacol Res*. 2012 May;65(5):514-22.

Laloux C, Petrault M, Lecointe C, Devos D, Bordet R. Differential susceptibility to the PPAR- γ agonist pioglitazone in 1-methyl-4-phenyl-1,2,3,6-tetrahydropyridine and 6-hydroxydopamine rodent models of Parkinson's disease. *Pharmacol Res*. 2012 May;65(5):514-22.

Laloux C, Gouel F, Lachaud C, Timmerman K, Do Van B, Jonneaux A, et al. Continuous cerebroventricular administration of dopamine: A new treatment for severe dyskinesia in Parkinson's disease? *Neurobiol Dis*. 2017 Jul;103:24-31.

Li G, Zhai G, Zhao X, An H, Spincemaille P, Gillen KM, et al. 3D texture analyses within the substantia nigra of Parkinson's disease patients on quantitative susceptibility maps and R2* maps. *NeuroImage*. 2019 Mar;188:465-72.

Papp EA, Leergaard TB, Calabrese E, Johnson GA, Bjaalie JG. Waxholm Space atlas of the Sprague Dawley rat brain. *NeuroImage*. 2014 Aug 15;97:374-86.

Puchades MA, Csucs G, Ledergerber D, Leergaard TB, Bjaalie JG. Spatial registration of serial microscopic brain images to three-dimensional reference atlases with the QuickNII tool. *PLOS ONE*. 2019 mai;14(5):e0216796.

Riederer P, Nagatsu T, Youdim MBH, Wulf M, Dijkstra JM, Sian-Huelsmann J. Lewy bodies, iron, inflammation and neuromelanin: pathological aspects underlying Parkinson's disease. *J Neural Transm.* 2023 May 1;130(5):627–46.

Riederer P, Wuketich St. Time course of nigrostriatal degeneration in parkinson's disease. *J Neural Transm.* 1976 Sep 1;38(3):277–301.

Sikiö M, Holli-Helenius KK, Harrison LC, Ryymin P, Ruottinen H, Saunamäki T, et al. MR image texture in Parkinson's disease: a longitudinal study. *Acta Radiol.* 2015 Jan;56(1):97–104.

Sled JG, Zijdenbos AP, Evans AC. A nonparametric method for automatic correction of intensity nonuniformity in MRI data. *IEEE Trans Med Imaging.* 1998 Feb;17(1):87–97.

Slezak JM, Mueller M, Ricaurte GA, Katz JL. Pharmacokinetic and pharmacodynamic analysis of d-2amphetamine in an attention task in rodents. *Behav Pharmacol.* 2018 Sep;29(6):551–6.

ENGLISH ABSTRACT

Parkinson's disease (PD) is the second most common neurodegenerative disorder worldwide. It is characterized by the progressive loss of dopaminergic neurons in the substantia nigra pars compacta (SNpc) and the accumulation and aggregation of alpha-synuclein in the brain. While there are many symptomatic therapies being developed and used to improve the patient's quality of life, there are still no available therapies that can alter the underlying neurodegenerative process. This absence of cure is mainly due to the lack of complete understanding of PD's pathophysiology, but also, the late diagnosis of the disease. Indeed, the diagnosis of PD relies on the assessment of characteristic motor symptoms, which typically manifest when the neurodegenerative process is already significantly advanced with the loss of up to 60% of SNpc neurons. However, research advances have demonstrated that patients with PD exhibit non-motor symptoms in the earlier stages of the disease, ranging from cognitive to neuropsychiatric impairments that aren't necessarily related to the dopaminergic loss and could be associated with the toxic alpha-synuclein accumulation.

Interestingly, alterations in the whole brain's structure and networks have also been described in PD patients using Magnetic resonance imaging (MRI). However, we still don't know the significance of such alterations on a biological level, and their relation to specific symptoms and phenotypes of the disease. The aim of this thesis is to study the MRI structural and functional alterations observed in animal models of PD, and extracting imaging features to correlate with the different histological and behavioral phenotypes of the animals.

To do so, we conducted longitudinal studies on several cohorts of the AAV alpha-synuclein rat model of PD, where we evaluated motor, cognitive and psycho-behavioral functions, along with three MRI timepoint explorations including morphological and functional sequences, and a fine histological analysis post-mortem.

With 30 to 40% dopaminergic denervation and a progressive alpha-synuclein accumulation, the AAV alpha-synuclein rat model also exhibited sensori-motor but not severe motor deficits, as well as learning and attentional impairments, thus establishing it as a moderate early-phase PD model, and making it interesting for the study of early non-motor symptoms and their relation to alpha-synuclein deposits.

As for structural and functional MRI, we observed morphological alterations and abnormal connectivity, which was not limited to the nigro-striatal pathway, but included several other regions of the midbrain, the diencephalon and the cortex. These regions are associated with the behavioral deficits observed, and display a significant amount of alpha-synuclein deposits. We also extracted texture features from the structural MRIs that were correlated with the dopaminergic denervation and some behavioral parameters.

In addition to being the first non-exhaustive MRI characterization of this animal model, the originality of this study relies on the technical spatial registration used to compare the MRI data and the histological data, which allowed a whole brain evaluation without preconceptions or having to target specific regions.

Its detailed quantification of alpha-synuclein deposits in the entire brain was correlated with imaging features extracted from several regions of the brain.

In conclusion, this work highlights the potential of using clinically relevant MRI sequences and analyses, in the evaluation of early-phase animal models of PD, to reveal the histological signature of certain imaging markers, such as texture features, which, when correlated with behavioral phenotypes, could constitute interesting biomarkers for the early diagnosis of the disease.

ENGLISH ABSTRACT FOR NON-SCIENTISTS

Parkinson's disease (PD) is the second most common neurodegenerative disorder worldwide, affecting nearly 10 million people. As the population ages, these numbers will increase, presenting a major economic and societal challenge in patient care. The lack of curative treatments is due to the limited knowledge of PD's pathophysiology and its late diagnosis. Magnetic resonance imaging (MRI) constitutes an interesting non-invasive tool for PD characterization. Recent studies have shown that new analysis methods allow the extraction of imaging markers that could improve diagnosis and disease monitoring. This project aims to study animal models of PD to establish links between imaging markers and histopathological markers, therefore improving our understanding of the underlying pathological mechanisms. The goal is to make MRI an essential tool for early diagnosis, disease monitoring, and evaluation of therapy effectiveness.

RESUME FRANCAIS

La maladie de Parkinson (MP) est une pathologie neurodégénérative caractérisée par la perte progressive de neurones dopaminergiques dans la substantia nigra pars compacta (SNpc) ainsi que par l'accumulation et l'agrégation d'alpha-synucléine dans le cerveau. Bien qu'il existe de nombreux traitements symptomatiques utilisés pour améliorer la qualité de vie des patients, il n'y a toujours pas de thérapies disponibles qui peuvent modifier le processus neurodégénératif sous-jacent. Cette absence de traitement curatif est principalement due au manque de compréhension complète de la pathophysiologie de la MP, mais également au diagnostic tardif de la maladie. En effet, le diagnostic de la MP repose sur l'évaluation de symptômes moteurs caractéristiques, qui se manifestent généralement lorsque le processus neurodégénératif est déjà significativement avancé avec une dégénérescence dopaminergique évaluée à 60 % dans la SNpc. Cependant, nous savons aujourd'hui que les patients atteints de MP présentent des symptômes non moteurs aux stades précoces de la maladie, allant des troubles cognitifs aux altérations neuropsychiatriques, et qui ne sont pas nécessairement liées à la perte dopaminergique, mais pourraient être associées à l'accumulation toxique d'alpha-synucléine dans le cerveau. De manière intéressante, des altérations de la structure et des réseaux de l'ensemble du cerveau ont également été décrites chez les patients atteints de MP à l'aide de l'imagerie par résonance magnétique (IRM), mais nous ne connaissons toujours pas la signification de telles altérations sur le plan biologique, ni leur lien avec des symptômes spécifiques et les différents phénotypes de la maladie. L'objectif de cette thèse est d'étudier les altérations structurelles et fonctionnelles de l'IRM observées chez les modèles animaux de la MP, et d'extraire des caractéristiques d'imagerie pour les corrélérer avec les différents phénotypes histologiques et comportementaux des animaux.

Pour ce faire, nous avons mené une étude longitudinale de plusieurs cohortes du modèle de rat AAV alpha-synucléine de la MP, avec l'évaluation des fonctions motrices, cognitives et psycho-comportementales, ainsi qu'une exploration IRM à trois temps différents, comprenant des séquences morphologiques et fonctionnelles, et une fine analyse histologique post-mortem.

Avec une dénervation dopaminergique de 30 à 40 % et une accumulation progressive d'alpha-synucléine, le modèle de rat AAV alpha-synucléine présentait également des déficits sensorimoteurs mais pas de déficits moteurs sévères, ainsi que des dysfonctionnements d'apprentissage et d'attention, ce qui en fait un modèle modéré mimant la phase précoce de la MP, et donc intéressant pour l'étude des symptômes non moteurs précoces et de leur relation avec les dépôts d'alpha-synucléine. De plus, nous avons extrait des paramètres de texture dans ces IRM structurelles qui ont été corrélées avec la dénervation dopaminergique et certains paramètres comportementaux.

En plus d'être la première caractérisation non exhaustive par IRM de ce modèle animal, l'originalité de ce travail repose sur l'enregistrement spatial utilisé pour comparer les données IRM et les données

histologiques, qui a permis une évaluation du cerveau entier sans a priori. La quantification détaillée des dépôts d'alpha-synucléine dans tout le cerveau a été corrélée avec les paramètres de textures extraits de plusieurs régions du cerveau.

En conclusion, ce travail met en évidence le potentiel de l'utilisation de séquences et d'analyses IRM cliniquement pertinentes dans l'évaluation de modèles animaux de la maladie de Parkinson à un stade précoce, pour révéler la signature histologique de certains marqueurs fins en imagerie, tels que les textures, qui, corrélés avec des phénotypes comportementaux, pourraient constituer des biomarqueurs intéressants pour le diagnostic précoce de la maladie.

RÉSUMÉ GRAND PUBLIC

La maladie de Parkinson (MP) touche près de 10 million de personnes dans le monde. Avec le vieillissement de la population, ces chiffres vont encore augmenter, constituant donc un défi sociétal et économique majeur. L'absence de traitements curatifs est dû à une connaissance limitée de la physiopathologie de la MP, et à son diagnostic tardif.

L'imagerie par résonance magnétique (IRM) constitue un outil non-invasif intéressant pour la caractérisation de la MP, notamment avec les nouvelles méthodes d'analyses des images, permettant l'extraction de marqueurs fins en IRM.

Ce projet vise à étudier des modèles animaux de la MP pour établir des liens entre ces marqueurs IRM et les marqueurs histopathologiques cérébrales, améliorant ainsi notre compréhension des mécanismes pathologiques sous-jacents. L'objectif est de faire de l'IRM un outil essentiel pour le diagnostic précoce, le bon suivi de l'évolution de la maladie et de l'efficacité des thérapies.